Volume 52
Number 16
21 August 2023
Pages 5345–5804

Chem Soc Rev

Chemical Society Reviews

rsc.li/chem-soc-rev

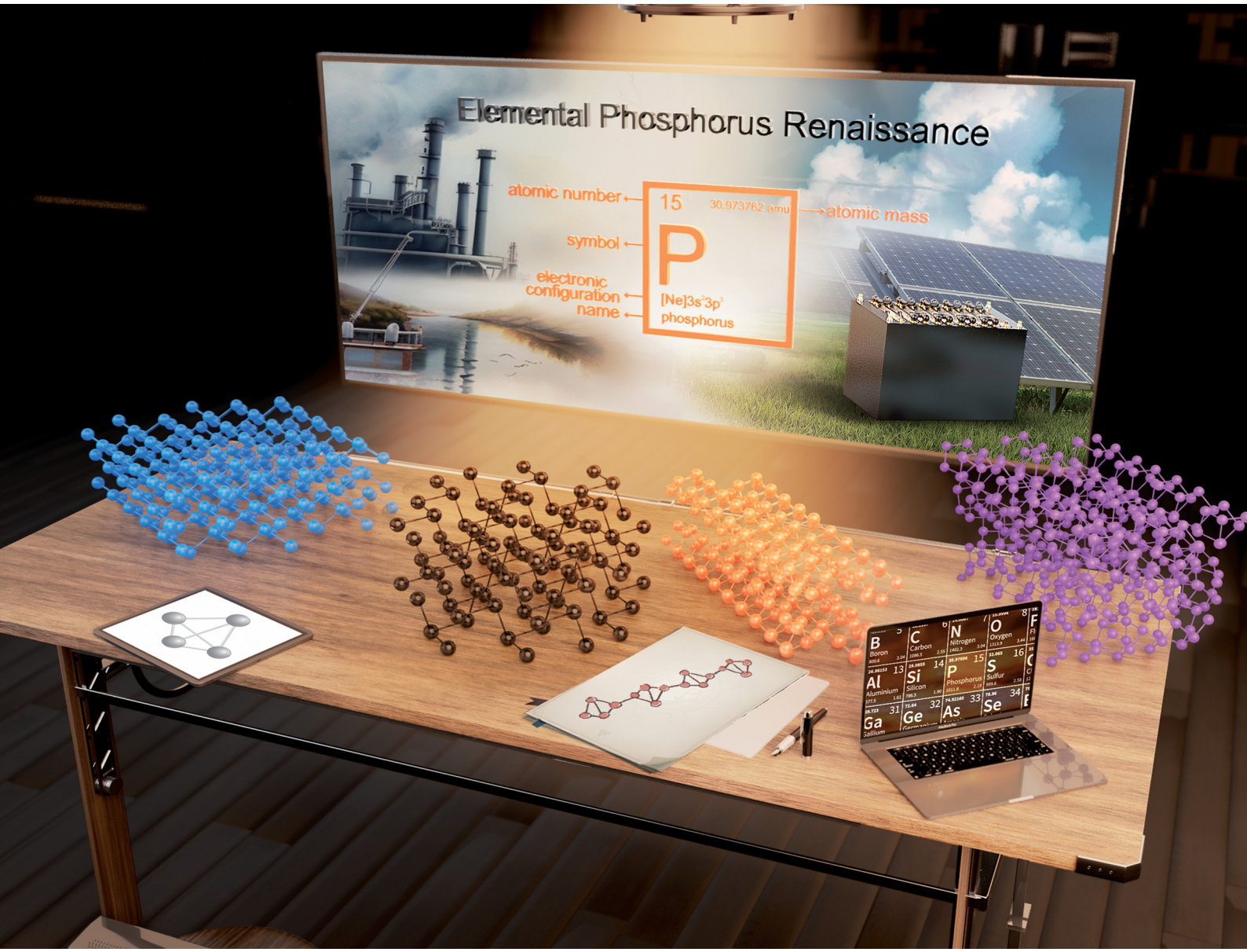

ISSN 0306-0012

ROYAL SOCIETY OF CHEMISTRY

REVIEW ARTICLE

Jiahong Wang, Guangbo Qu, Xue-Feng Yu *et al.*
Renaissance of elemental phosphorus materials: properties, synthesis, and applications in sustainable energy and environment

Chem Soc Rev

REVIEW ARTICLE

View Article Online
View Journal | View Issue

Cite this: *Chem. Soc. Rev.*, 2023, **52**, 5388

Renaissance of elemental phosphorus materials: properties, synthesis, and applications in sustainable energy and environment

Haijiang Tian, [ac] Jiahong Wang, *[bhi] Gengchang Lai, [bi] Yanpeng Dou, [bh] Jie Gao, [ad] Zunbin Duan, [bh] Xiaoxiao Feng, [b] Qi Wu, [ad] Xingchen He, [bh] Linlin Yao, [a] Li Zeng, [a] Yanna Liu, [a] Xiaoxi Yang, [a] Jing Zhao, [ad] Shulin Zhuang, [c] Jianbo Shi, [adi] Guangbo Qu, *[adi] Xue-Feng Yu, *[bhi] Paul K. Chu [efg] and Guibin Jiang [acdi]

The polymorphism of phosphorus-based materials has garnered much research interest, and the variable chemical bonding structures give rise to a variety of micro and nanostructures. Among the different types of materials containing phosphorus, elemental phosphorus materials (EPMs) constitute the foundation for the synthesis of related compounds. EPMs are experiencing a renaissance in the post-graphene era, thanks to recent advancements in the scaling-down of black phosphorus, amorphous red phosphorus, violet phosphorus, and fibrous phosphorus and consequently, diverse classes of low-dimensional sheets, ribbons, and dots of EPMs with intriguing properties have been produced. The nanostructured EPMs featuring tunable bandgaps, moderate carrier mobility, and excellent optical absorption have shown great potential in energy conversion, energy storage, and environmental remediation. It is thus important to have a good understanding of the differences and interrelationships among diverse EPMs, their intrinsic physical and chemical properties, the synthesis of specific structures, and the selection of suitable nanostructures of EPMs for particular applications. In this comprehensive review, we aim to provide an in-depth analysis and discussion of the fundamental physicochemical properties, synthesis, and applications of EPMs in the areas of energy conversion, energy storage, and environmental remediation. Our evaluations are based on recent literature on well-established phosphorus allotropes and theoretical predictions of new EPMs. The objective of this review is to enhance our comprehension of the characteristics of EPMs, keep abreast of recent advances, and provide guidance for future research of EPMs in the fields of chemistry and materials science.

Received 9th April 2023

DOI: 10.1039/d2cs01018f

rsc.li/chem-soc-rev

1. Introduction

Phosphorus (P) is one of the elements serving as the foundation for life on Earth. The Earth's crust contains around 1200 mg P kg^{-1}, ranking it as the eleventh most plentiful element.[1] Phosphorus plays a significant part in global biogeochemical cycles in conjunction with other bioactive elements such as carbon (C), nitrogen (N), and trace metals.[2,3] It has direct and indirect impacts on the rock cycle,[4] marine biogeochemistry,[5,6] biomass accumulation,[7] and nutrient availability.[8,9] Phosphorus is also crucial to numerous technological applications, including optical engineering and communication,[10,11] electronics,[4,12] biomedicine and drug delivery,[13–15] agriculture and food,[16] cosmetics,[17] and textiles,[18] and the development of cost-effective phosphorus-based materials for environmental and energy applications has been rapid recently.[19–21] This is because of the ability of phosphorus to self-bond and form bonds with many metal and

[a] *State Key Laboratory of Environmental Chemistry and Ecotoxicology, Research Center for Eco-Environmental Sciences, Chinese Academy of Sciences, Beijing 100085, P. R. China. E-mail: gbqu@rcees.ac.cn*
[b] *Shenzhen Institute of Advanced Technology, Chinese Academy of Sciences, Shenzhen 518055, P. R. China. E-mail: jh.wang1@siat.ac.cn, xf.yu@siat.ac.cn*
[c] *Key Laboratory of Environment Remediation and Ecological Health, Ministry of Education, College of Environmental and Resource Sciences, Zhejiang University, Hangzhou 310058, P. R. China*
[d] *School of Environment, Hangzhou Institute for Advanced Study, University of Chinese Academy of Sciences, Hangzhou 310024, P. R. China*
[e] *Department of Physics, City University of Hong Kong, Tat Chee Avenue, Kowloon, Hong Kong, China*
[f] *Department of Materials Science and Engineering, City University of Hong Kong, Tat Chee Avenue, Kowloon, Hong Kong, China*
[g] *Department of Biomedical Engineering, City University of Hong Kong, Tat Chee Avenue, Kowloon, Hong Kong, China*
[h] *Hubei Three Gorges Laboratory, Yichang, Hubei 443007, P. R. China*
[i] *University of Chinese Academy of Sciences, Beijing 100049, P. R. China*

non-metal elements with different orbital hybridization, thus resulting in a myriad of physical and chemical properties as well as structural diversity of phosphorus compounds and molecules.

Among the diverse materials containing phosphorus, elemental phosphorus materials (EPMs) are the fundamental materials and origin of many complex products.[22–24] The

Haijiang Tian

Haijiang Tian is currently a PhD student at the College of Environmental & Resource Sciences, Zhejiang University, and a joint student at the Research Center for Eco-Environmental Sciences (RCEES), Chinese Academy of Sciences (CAS). He received his bachelor's degree in chemistry at School of Chemistry and Chemical Engineering, Shandong University in 2021. His research interests are the synthesis of low-dimensional phosphorus-based materials and the evaluation of their biological effects.

Jiahong Wang

Jiahong Wang is an associate professor in the Shenzhen Institute of Advanced Technology (SIAT), CAS. He obtained his PhD in Optics from Wuhan University in 2016. His major research interests are crystal growth and electronic or energy applications. Currently, Dr. Wang focuses on the growth and anodic performance of phosphorus-based materials, such as black phosphorus.

Guangbo Qu

Guangbo Qu is a professor in RCEES, CAS. He obtained his PhD in environmental science at RCEES, CAS in 2011. His major research interests are the evaluation of the biological effects of emerging nanomaterials and halogenated organic pollutants, as well as their molecular mechanisms. Prof. Qu is working on the chemico–physical properties of phosphorus materials as well as biological effects induced by phosphorus materials.

Xue-Feng Yu

Xue-Feng Yu is a professor and director of Materials and Interfaces Center at SIAT, CAS. He received his PhD degree in physics from Wuhan University in 2008, and then worked at Wuhan University and City University of Hong Kong. He leads an interdisciplinary research group focused on the synthesis and applications of nanomaterials. He has coauthored more than 100 publications in SCI-indexed journals with over 16 000 citations.

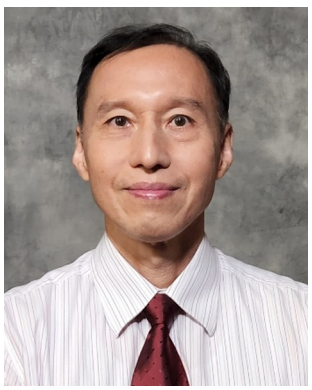

Paul K. Chu

Paul K. Chu is Chair Professor of Materials Engineering in the Department of Physics, Department of Materials Science and Engineering, and Department of Biomedical Engineering at City University of Hong Kong. He obtained his PhD in chemistry from Cornell University in 1982. He is fellow of the APS, AVS, IEEE, MRS, Hong Kong Institution of Engineers, and the Hong Kong Academy of Engineering Sciences. His research interests are quite diverse spanning plasma surface engineering, materials science and engineering, surface science, and functional materials. He is a highly cited researcher and his papers have been cited more than 100 000 times.

Guibin Jiang

Guibin Jiang is a full professor at RCEES, CAS. He obtained his PhD at RCEES, CAS in 1991. Prof. Jiang is an academician of the Chinese Academy of Sciences and the Academy of Sciences of Developing Countries. He won the 2021 Outstanding Achievements in Environmental Science & Technology Award for his basic and translational research, leadership, and service to understand and manage POPs and other emerging contaminants. His research focuses on environmental analysis and toxicology, including environmental occurrence, processes, toxicology and health effects of environmental toxic substances.

polymorphism of EPMs arises from different types of phosphorus clusters serving as the building blocks. Phosphorus allotropes such as tetrahedral white phosphorus (white-P), puckered honeycomb-like black phosphorus (black-P), and polygonal chain-like red phosphorus (red-P) have distinctive micro and nanostructures resulting from the diverse covalent bonding nature and arrangement of phosphorus atoms. Different crystal structures lead to different physicochemical properties including the bandgap, optical absorption, electrical conductivity, redox activity, and material stability. For example, white-P consisting of tetrahedral P_4 molecules is the most active allotrope.[25] Black-P is composed of irregular honeycomb interlayers and is the most thermodynamically stable allotrope.[26] Amorphous red-P is the most versatile phosphorus allotrope. Because of its low cost, environmental friendliness, availability, and stability, it finds applications in various fields such as flame retardants,[27] energy harvesting,[23,28] ion storage,[29] and pollution sensing.[30,31] During the synthesis of red-P, Hittorf and Thurn *et al.* observed the formation of plate-like and fiber bundles of phosphorus crystals, namely, violet phosphorus (violet-P) and fibrous phosphorus (fibrous-P), respectively.[32,33] In earlier studies, violet-P and fibrous-P were often mentioned as two of the red-P modifications (type V and type IV).[34,35] However, violet-P and fibrous-P have been shown to have several unique properties by unambiguous structural characterization, and a growing number of researchers prefer to use the names violet phosphorus and fibrous phosphorus instead of type IV or type V red-P.[36,37] It is recommended to use the term "red-P" only to describe type I amorphous red-P, since it is often produced under mild crystallization conditions. In this review, unless otherwise noted, red-P refers to amorphous red phosphorus.

EPMs are unusual in the elemental material family because their allotropes do not exist in nature and must be produced artificially.[38] Each EPM is "made" rather than "found", and the target allotrope needs to artfully match the structural motif assembly with the achievable reaction conditions. They are witnesses to the development of modern synthetic chemistry. Before 2010, studies in this field seemed to be dominated by inorganic chemists or physicists, probably due to the complicated and risky manufacturing procedures of EPMs. The majority of research has focused on the improvement of synthetic approaches and crystal quality of EPMs. For example, Percy Williams Bridgman, who received the Nobel Prize in Physics in 1946, sought to prepare black-P crystals using high-temperature or high-pressure approaches,[39,40] and subsequently Akimoto *et al.* obtained black-P single crystals with diameters up to $4 \times 2 \times 0.2$ mm^3.[41] Nilges' group developed Sn-based mineralizers to alleviate the harsh conditions for synthesizing high-quality black-P crystals.[42–44] Phosphorene, one of the structural analogs of graphene, was regarded as a purely theoretical material for a very long time. In 2014, however, black-P was successfully scaled down to phosphorene by mechanical exfoliation, spurring the advance of EPM synthetic chemistry to the nanoscale.[45,46] Synthetic low-dimensional EPMs are a developing class of intriguing atomic structures with amazing materials properties. On the heels of a comprehensive understanding of the physicochemical properties of black-P based materials, researchers have extended their curiosity to rediscover other EPMs. Amorphous red-P, violet-P, and fibrous-P can also be scaled down to form low-dimensional sheets, ribbons, and dots with exciting properties.[28,47,48] Concurrently, researchers have predicted the existence of new fancy EPMs such as blue phosphorus (blue-P, also known as gray phosphorus) and green phosphorus (green-P) based on *ab initio* density functional theory (DFT) calculations.[49–51] In 2016, Zhang *et al.* fabricated blue-P on Au(111),[52] and Wang *et al.* synthesized greenish phosphorus on carbon substrates in 2021.[53] A developing trend is the use of computational simulation to assist the synthesis of EPMs. Since 2018, several research groups have employed machine learning-based atomic simulations to predict new EPMs or attempt to answer fundamental structural questions (for instance, the precise structure of amorphous red-P).[54–58] It is expected that more computational simulation systems will be developed with artificial intelligence for structural analysis and prediction.

The development of new materials has the potential to address the challenges faced by humanity today.[59] Among the pressing challenges of the 21st century, energy crisis and environmental pollution are most critical. As the global population continues to grow, the current energy consumption of 12.8 TW is projected to more than double to 28–35 TW by 2050 and triple by 2100.[60–62] This increase in energy demand is limited by the availability of fossil fuels, which currently account for 77% of energy consumption and are associated with a 16% rise in anthropogenic carbon dioxide (CO_2) emissions by 2040.[28,63] The International Panel on Climate Change (IPCC) estimates that by 2100, the atmosphere will contain up to 570 ppm of CO_2, resulting in an average global temperature rise of approximately 1.9 °C.[64,65] The consequences of global warming will severely impact agriculture, labor productivity, human health, and economic development.[66,67] To meet the growing global energy demand, sustainable and inexpensive energy sources must be developed as alternatives to fossil fuels. Moreover, due to the intermittent nature of renewable energy, cost-effective and high-performance energy storage devices are urgently needed for electric vehicles and scalable energy storage.[68] Environmental stewardship is also important in aiming for sensitive sensing and complete removal of pollutants, or selectively converting pollutants into useable chemicals. Synthetic EPMs have the potential to address both sustainable energy and environmental remediation challenges. Although traditional EPMs (white-P, black-P, red-P, violet-P, and fibrous-P) are not novel materials, the recent progress in synthesizing high-quality, large-size bulk crystals and various low-dimensional structures has enabled the rediscovery of many previously unknown physicochemical properties, including chemical sensing, tunable bandgaps, and anisotropic mobility.[36,48,69–72] At the same time, theoretical studies have identified several unique photoelectric properties of new EPMs (blue-P and green-P).[73–75] The implementation of these EPMs will offer innovative opportunities and new approaches for energy conversion, energy storage, and environmental remediation.

EPMs are experiencing a renaissance in the post-graphene era. Researchers have explored various phosphorus allotropes

and synthesized corresponding nanostructures to date. This rich variety of materials allows for the construction of a library of elemental phosphorus materials to facilitate the selection of specific phosphorus allotropes and corresponding micro/nanostructures and to address practical needs for particular applications. Although black-P and red-P have been reviewed in recent years, there is still a lack of comprehensive understanding regarding the differences and relationships between numerous EPMs, their intrinsic physical and chemical properties, synthesis of specific structures, and selection of suitable EPMs for specific applications. To fill this gap, we herein provide a comprehensive review of the physicochemical properties, synthetic methods, and sustainable applications of EPMs (white-P, red-P, black-P, fibrous-P, violet-P, blue-P, and green-P), as illustrated in Fig. 1. The aim of this review is to not only describe the latest research advancements in black-P, red-P, and other emerging EPMs, but also summarize the intrinsic properties of elemental phosphorus by examining the broader research context of this field, which will guide future materials design and applications. It is important to note that EPMs are a

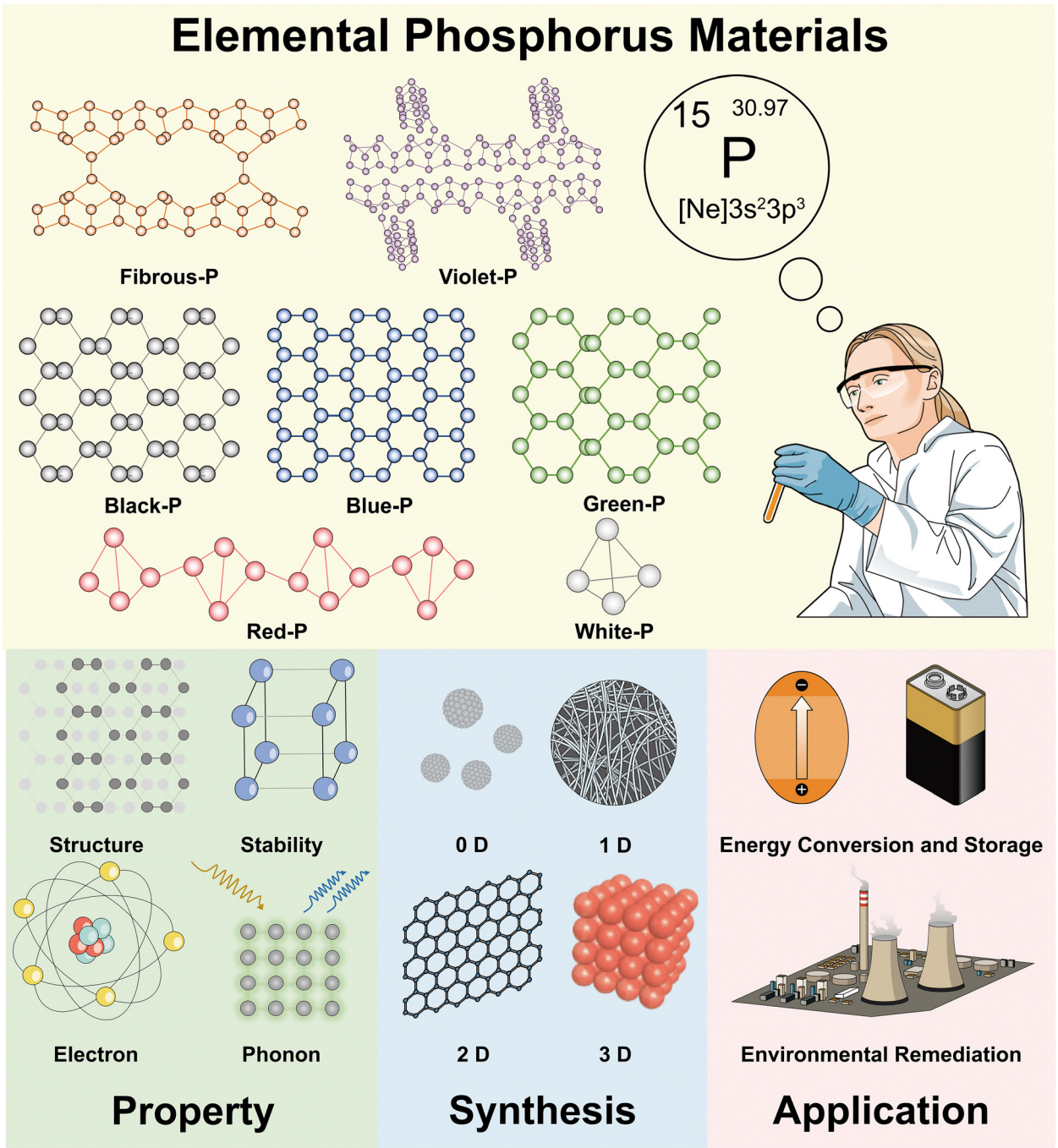

Fig. 1 Overview of the properties, synthesis, and sustainable applications of elemental phosphorus materials.

big family of phosphorus materials that also include theoretically predicted materials such as phosphorus fullerenes,[76] crimson phosphorus,[77] phosphorus nanotubes,[78] and others. However, owing to the challenges associated with chemical synthesis and their limited practical applications, these materials are not covered in this review.

This review is organized as follows. We start with a concise overview of the discovery of common phosphorus bulk crystals and phosphorene. The latest studies on machine learning-driven stimulations that aid the description and prediction of EPM structures are described in this part (Section 2). The structural, electron, and phonon properties of EPMs which are theoretically and/or experimentally studied are described in Section 3. The comparisons of building blocks, material stability, bandgaps, and charge carrier mobility among different EPMs are highlighted. Section 4 critically discusses the synthesis of EPMs and their nanostructures with different dimensions (0D, 1D, 2D, or 3D). The advantages and disadvantages of different synthetic routes are discussed and characterization of the corresponding products is described. In Section 5, recent advancement in EPMs and EPM-derived systems for energy conversion (photocatalytic/electrocatalytic HER, OER, CO_2RR, and NRR), energy storage (hydrogen storage, LIBs, SIBs, PIBs, and SCs), and environmental remediation (sensing and gas/liquid/soil treatment) is summarized. In each area, the mechanisms, advantages of EPMs, performance comparison among EPMs, and modification strategies are emphasized. The conclusions and outlook are finally presented to provide guidance for future research in this burgeoning field.

2. Development of elemental phosphorus materials

As the fifteenth element in the periodic table, phosphorus derives its name from the Greek words '*phôs*' and '*phoros*', translating literally to ''light-bearer''.[79] The first isolated form of the element glows and emits visible light. The origin of phosphorus is unknown. Some investigations demonstrate that phosphorous might have been used in the Roman era, but this record was lost over time.[80] However, elemental phosphorus in its molecular form was only isolated in the 17th century and afterwards, scientists inaugurated the age of synthetic EPMs.

Between the 17th and 20th centuries, researchers synthesized several elemental phosphorus bulk crystals. Self-styled doctor Hennig Brand discovered a strange substance (white-P) from human urine in 1669 and Anton Schrötter von Kristelli presented red-P before the Vienna Academy of Sciences in 1847. The first black-P crystals were fabricated at a high pressure by the Nobel prize winner Percy Williams Bridgman in 1914.[81] At the turn of the 21st century, the rapid development of nanosynthesis and characterization technology enabled researchers to expand their interest into low-dimensional materials, and phosphorene, corresponding to the elemental phosphorus bulk crystals, was isolated one after another. Concurrently, breakthroughs in computational chemistry have enabled chemists to discover metastable phosphorus allotropes that can be a potent supplement to common EPMs in technological applications.[82,83] Fig. 2 demonstrates the development of phosphorus crystals and phosphorene, highlighting key milestones such as the discovery of allotropes and low-dimensional materials. In addition, artificial intelligence has gained traction in materials science over the last few years, and atomistic simulations of phosphorus can now be achieved using machine learning-based algorithms.[54,55] This section reviews the discovery of bulk crystals and phosphorene, renowned scientists, and recent progress in machine learning-driven stimulations for structural description and prediction of EPMs.

2.1 History of phosphorus allotropes

EPMs cannot exist in nature alone because of the high chemical reactivity and must be synthesized chemically. Their synthesis dates back to the end of the renaissance and physicists and chemists made great contributions to the discovery of phosphorus allotropes (Fig. 3).

White-P is the first known phosphorus allotrope, and its discovery is intrinsically related to medieval alchemy. In 1669, Hennig Brand, a German alchemist and a self-styled doctor, was in search of the mythical Philosopher's Stone, which was believed to have the power to turn ordinary metals into gold.[80,84] Brand condensed 50 barrels of urine by heating and distillation. Surprisingly, he did not get the magical stone with mutant powers, but did find the pure form of flammable phosphorous, which gave out a faint green glow in the dark. After a period of keeping his discovery a secret, Brand revealed the discovery of white-P in 1675, and his colleague alchemist Daniel Kraft gained fame and fortune by exhibiting this enigmatic new light source to European nobles. Later in the 19th century, chemists developed white-P matches,[85] but these matches were extremely reactive to fire and generated noxious fumes. Due to its pyrophoric properties, white-P was subsequently used as a bombing agent during World War II, causing severe harm to human health, and its usage became obsolete after the war. White-P is now mostly used as an industrial intermediate for the production of phosphorus-containing compounds such as herbicides, fertilizers, and food additives.[86]

Red-P is the second known phosphorus allotrope, and Anton Schrötter von Kristelli is the acknowledged discoverer of this allotrope, even before other scientists had this substance in their hands.[87] In 1844, chemist Berzelius reported that when white-P is exposed to sunshine, it could be transformed into a red modification that would not spontaneously oxidize or ignite. However, many chemists recognized this red modification as phosphorus oxide. This controversy was settled by Schrötter's work. He presented his findings to the Vienna Academy of Sciences on December 9, 1847. He discovered that white-P could be converted to red-P by exposure to sunlight, even in the absence of moisture and atmospheric oxygen. The red substance was isolated by treating the residual white-P with carbon disulfide. It could also be produced from white-P by heating it to $\sim$250 °C in an inert atmosphere. Heating to a higher temperature would reconvert red-P back to white-P.

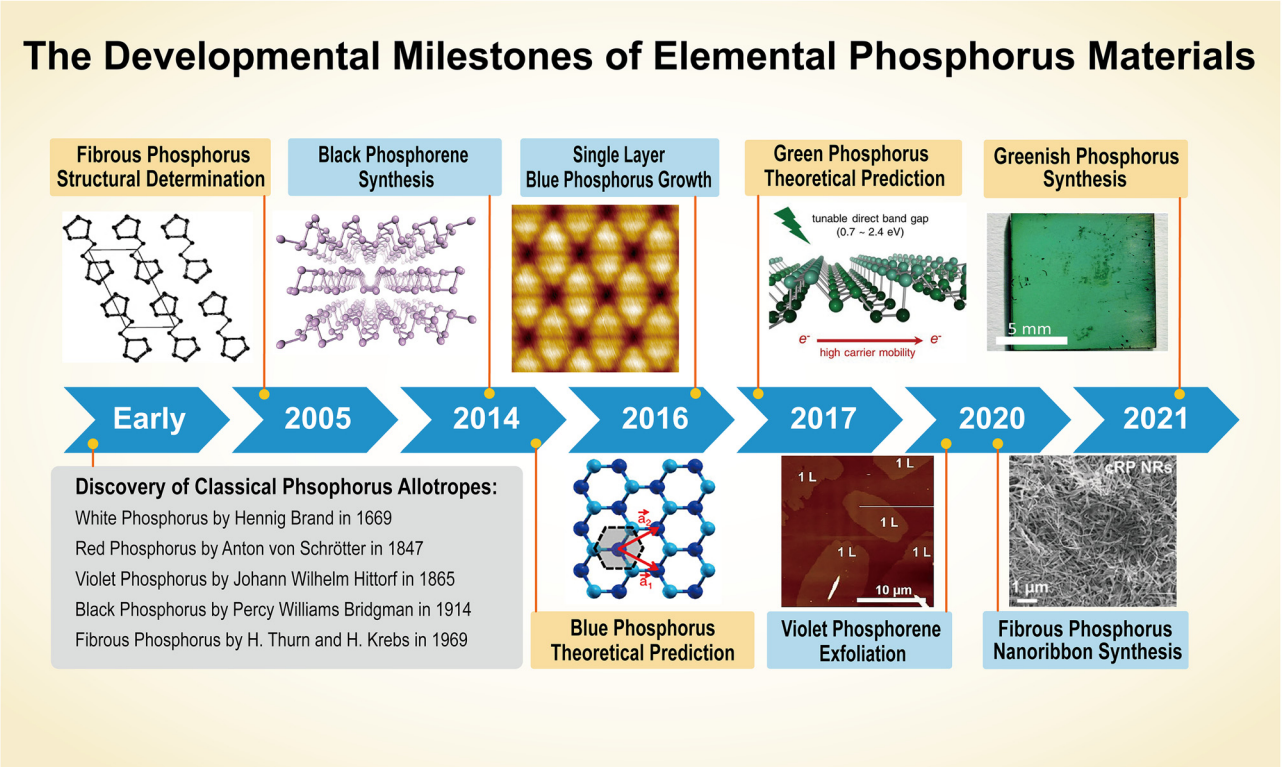

Fig. 2 Timeline of the developmental milestones of elemental phosphorus materials (bulk crystals and phosphorene). Inset images are reproduced from the following sources: fibrous phosphorus structural determination, reproduced with permission from ref. 88. Copyright 2005 John Wiley and Sons. Black phosphorene synthesis, reproduced with permission from ref. 45. Copyright 2014 Nature Publishing Group. Blue phosphorus prediction, reproduced with permission from ref. 49. Copyright 2014 American Physical Society. Blue phosphorus synthesis, reproduced with permission from ref. 52. Copyright 2016 American Chemical Society. Green phosphorus prediction, reproduced with permission from ref. 50. Copyright 2017 American Chemical Society. Violet phosphorene synthesis, reproduced with permission from ref. 48. Copyright 2020 John Wiley and Sons. Fibrous phosphorus nanoribbon synthesis, reproduced with permission from ref. 47. Copyright 2020 John Wiley and Sons. Greenish phosphorus synthesis, reproduced with permission from ref. 53. Copyright 2021 Royal Society of Chemistry.

Schrötter emphasized the potential of this allotrope in the match industry. This was confirmed by the creation of safe Swedish matches made of red-P, which only ignited upon friction with a rough surface and did not generate harmful fumes like white-P matches.[85,87] Red-P (amorphous form) is now a widely used industrial allotrope along with white-P. Its commercial chemical, with a purity of around 90%, sells for USD 2–10 per kilogram in the Chinese market.[22] In addition, research on the atomic structure of amorphous red-P has advanced over the decades, and this part will be discussed later.

Violet-P, also known as Hittorf's phosphorus (or α-metallic phosphorus), is the third known allotrope of phosphorus that can be produced by annealing white-P/red-P above 500 °C. This phosphorus form was first observed in 1865 by Johann Wilhelm Hittorf, who noted that recrystallizing phosphorus from molten lead resulted in red-to-violet colored platelets.[32] Furthering this discovery, Thurn and Krebs synthesized violet-P and identified its structure in 1969.[33]

In the same year, Thurn and Krebs also made an intriguing observation of formations resembling capillary fibers beside plate-like violet-P crystals in the reaction kettle.[33] These fibrous formations, later referred to as fibrous phosphorus (fibrous-P), appeared to possess a structure that was similar yet distinct from violet-P. Based on X-ray rotation images of the fibers, they proposed the layout of tubes of the same sort as in violet-P but bound to double tubes in parallel. Ruck and colleagues validated the presumed structure of fibrous-P using single-crystal XRD and TEM in 2005.[88]

The discovery of black-P can be traced back to 1914, when American physicist Percy Williams Bridgeman attempted to convert commercial white-P into red-P by applying high hydrostatic pressure at a temperature below the transition point that occurs with an appreciable velocity at atmospheric pressure.[39] The density of the obtained black-P was 2.691 kg m^{-3}, which was greater than those of white-P (1.83 kg m^{-3}) and red-P (2.05–2.34 kg m^{-3}) at ambient temperature. Percy Williams Bridgman won the 1946 Nobel Prize in Physics for his pioneering work on the physics of high pressures.[89] He subsequently made several improvements to the reaction conditions for the synthesis of black-P. For example, he developed a room-temperature method for converting red-P into black-P crystals, although extremely high pressure (8.0 GPa) was required in the process.[40] Today, black-P has become a promising elemental material and plays an important role in materials science, chemistry, condensation physics, engineering, and biomedical applications.

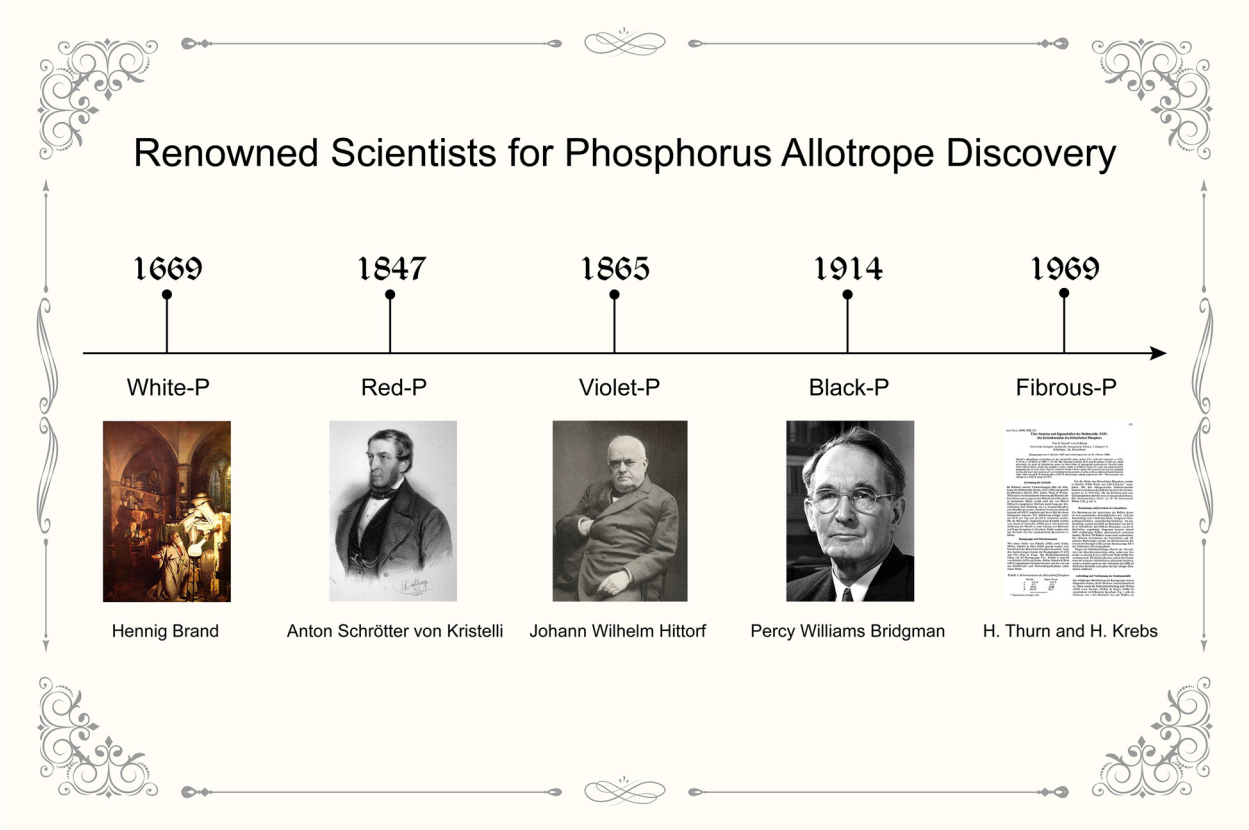

Fig. 3 Timeline of the discovery of white phosphorus, red phosphorus, violet phosphorus, black phosphorus, and fibrous phosphorus bulk crystals as well as renowned scientists. Painting of Hennig Brand taken from "*The Alchymist, In Search of the Philosopher's Stone*" by Joseph Wright of Derby. Portrait of Anton Schrötter von Kristelli taken from Smithsonian Archives by Adolf Dauthage. Portrait of Johann Wilhelm Hittorf taken from the special issue in honour of the 80th anniversary of Hittorf's birth, Leipzig: Barth 1904. Portrait of Percy Williams Bridgman taken from ref. 81. Copyright 1946 The Nobel Foundation. For H. Thurn and H. Krebs, the discoverers of fibrous phosphorus, in absence of their photographs, we have chosen to represent them with the first page of their original research paper published in 1969 documenting the discovery. The research paper taken from ref. 33. Copyright 1969 International Union of Crystallography.

2.2 Emergence of phosphorene

In the 1960s, the interest in superconductivity brought attention to phosphorus-rich phase diagrams.[90] However, because of the narrow bandgaps and harsh synthetic conditions of crystalline phosphorus, the research on EPMs remained lukewarm for a long time. Black phosphorus, for example, was mentioned in only about 150 research publications before 2014. Since the successful exfoliation of graphene layers using Scotch tape, scientists have turned to other elemental crystals that can be layered through van der Waals (vdW) forces, and the fabrication of atomic-layered elemental nanomaterials has gained popularity.[91] For this reason, research interests in EPMs, particularly black-P, have been reignited.

In 2014, atomic-layered black-P was synthesized for the first time, and this breakthrough launched a new section in research on what came to be known as phosphorene.[45,46] Liu and colleagues referred to single- or few-layered black-P as "phosphorene" with the suffix "-ene," emphasizing its structural similarity to graphene.[46] However, the designation of single- or few-layered black-P is still a subject of debate. As Favron and co-workers have pointed out,[92] the term phosphorene does not correlate with the IUPAC nomenclature since the suffix "-ene" is allotted to systems having sp^2 hybridized orbitals. They suggested renaming a single layer of black-P as 2D-phosphane to ensure consistency with other sp^3-hybridized monolayers such as graphane and germanane. Gusmão *et al.*,[93] on the other hand, argued that the term phosphane should be reserved for saturated phosphorus hydrides with the general formula P_nH_{n+2}, and is inappropriate for designating the black-P monolayer. They preferred the term "black-P single sheet" to directly designate single-layered black-P. However, the term phosphorene has surfaced in an increasing number of publications in the past few years, and the majority of academics have embraced this designation. Nowadays, the term phosphorene encompasses not only black phosphorene, but also blue phosphorene, violet phosphorene, fibrous phosphorene, and other atomic-layer allotropes of the phosphorus family.[94]

The discovery of phosphorene *in silico* was encouraged by the development of structural prediction algorithms. Zhu *et al.* first proposed an in-plane hexagonal structure termed blue phosphorus (blue-P) in 2014,[49] and this new phase is almost as stable as black phosphorene. In the side view, blue phosphorene displays less puckered zigzag ridges, in contrast to the

armchair ridges of the black counterpart. The structural shift from the black to blue counterpart can be viewed as flipping every fourth row of phosphorus atoms, transforming all armchair ridges into zigzag ridges.[49,50] In 2016, Zhang *et al.* reported the growth of atomic-layered blue-P on Au(111),[52] and its fabrication encouraged other metastable phosphorene discoveries. One year later, Han *et al.* predicted the presence of green phosphorene (λ-P) combining both armchair and zigzag ridges, indicating that its structure is a hybrid of black and blue phosphorene.[50] The structural shift from the black to green counterpart can be viewed as flipping every twelfth row of phosphorus atoms following the dislocation of every fourth row.[50] Other materials with honeycomb-like structures such as γ-P and δ-P, have also been predicted based on *ab initio* DFT calculations, and both of them are semiconductors.[76] While these theoretical transformations provide valuable insights into the exploration of potential phosphorus allotropes, it is important to note that the actual synthesis process is often more complex. The transformation from one phosphorus allotrope to another in practice requires precise control over reaction conditions, highlighting the necessity to understand the phosphorus phase diagram in detail.

Apart from the honeycomb lattice structures, Wu *et al.* presented four distinct structural phosphorenes, named ε-P, ζ-P, η-P, and θ-P, and these allotropes are dynamically stable based on phonon-spectrum calculations.[95] Each building block unit in ε-P and ζ-P comprises two P_4 squares which, when viewed from the side, resembles the armchair and zigzag ridges found in black and blue phosphorene, respectively. For η-P and θ-P, each unit is composed of two P_5 units oriented in opposing directions, and pentagonal blocks are arranged in a chain along a certain direction, forming a monolayer. Each pentagonal block contains four intrachain bonds and one interchain bond.[95] Among the four phosphorene allotropes mentioned, θ-P has been proven to be energetically close to black phosphorene with a relative energy disparity of less than 0.01 eV per atom, suggesting its theoretically stable nature. In principle, new kinds of phosphorene can be created by reorganizing different unit blocks, which can considerably expand the family of atomic-layer EPMs. It is envisaged that other types of phosphorene with hybridized building blocks will be predicted and eventually synthesized.

2.3 Machine learning for prediction of phosphorus materials

Classical phosphorus allotropes such as black, red, and white phosphorus were discovered directly by chemical synthesis, normally relying on chemists' extraordinary intuition and wealth of experience. However, direct synthesis can be difficult to accomplish when we attempt to predict crystal structures that go beyond chemical intuition. At this point, DFT-based computational chemistry techniques come in handy, enabling us to effectively predict complex structures (*e.g.*, ε-P, ζ-P, η-P, and θ-P).[95] Of note, quantum-mechanical DFT computations entail solving the Schrödinger equations for the electronic structures of molecules and periodic systems, limiting them to systems with small unit cells and high symmetry.[54,96,97] However, for sophisticated systems with numerous atoms per cell and low symmetry (*e.g.*, violet-P and fibrous-P), DFT-based calculations become prohibitively costly and time-consuming.

To circumvent this issue, application of machine learning (ML) in atomic-scale simulations and predictions is emerging. By "learning" small structures commonly generated from DFT results, ML-based force field method achieves high accuracy but are orders of magnitude faster.[97–99] ML modeling differs from empirically fitted force fields in that it does not make any assumptions about the interatomic potential and instead gathers all information from a large reference database. Building an appropriate reference database is vital for ML-based force field training, which should include enough atomic configurations while having a manageable number of entries. Following that, an appropriate mathematical representation of the atomic structure is required as input for the ML algorithm and ultimately, ML methodology involves regression or "learning" for materials simulations.[97] In 2020, Deringer *et al.* achieved notable success in building a reference database for phosphorus and using it to develop an ML-based Gaussian approximation potential (GAP) model that accurately depicts various bulk crystalline allotropes, liquid structures, and nanostructured phases of phosphorus (Fig. 4).[55] This GAP can even be utilized to explore the local structure of amorphous phosphorus's and how it changes under pressure.[58] In 2022, Koneru *et al.* presented a multi-reward reinforcement learning algorithm for training flexible and high-fidelity bond-order potential models for 2D phosphorene.[57] The resulting ML-based model accurately portrays various properties of diverse phosphorene polymorphs such as the structure, energetics, transformation barriers, equation of state, elastic constants, and phonon dispersions.[57] This work paves a way for the dynamic simulation of low-dimensional EPMs on a mesoscale, leading to faster design and discovery.

Atomic-level simulations offer significant advantages in studying materials with complex structures. ML-based force field method is rapidly emerging as a powerful tool in materials

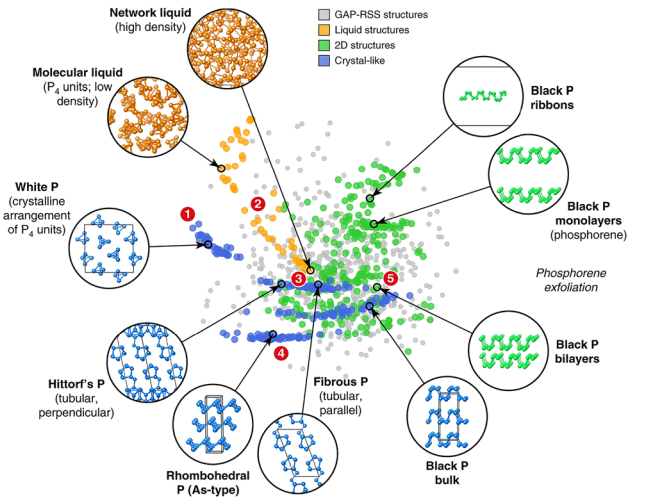

Fig. 4 GAP (Gaussian approximation potential) fitting database designed for elemental phosphorus. Reproduced with permission from ref. 55. Copyright 2020 Nature Publishing Group.

modeling, capable of solving a wide range of materials science challenges. However, ML modeling for phosphorus-based materials is still in its infancy, and the academic community must solve several algorithmic and adaptability issues. For instance, ML-based force fields that are trained to be very accurate for a certain set of configurations will not be highly accurate elsewhere.[97] Thus, a reference database with representative configurations is needed to balance simulation accuracy and versatility. In addition, balancing precision and speed in describing the diverse and complex structures of phosphorus-based materials is crucial. We expect that in the future, ML-based force field method will tackle key issues in phosphorus materials science, and data-driven structure searching will reveal more structural allotropes of phosphorus.

In summary, this section has delved into the development of EPMs, tracing the discovery of classic allotropes to the emergence of phosphorene and the use of machine learning in this field. As we forge ahead, future work should leverage a multidisciplinary approach to discover new phosphorus allotropes, further investigate the properties of newly predicted phosphorene allotropes, and advance the use of machine learning models for predicting and simulating these materials. This integrated approach could open new frontiers in EPM research. Importantly, it is crucial to note that every claim of a newly discovered phosphorus allotrope must be substantiated by solid crystallographic data from free-standing samples, such as single-crystal X-ray diffraction, single-crystal neutron diffraction, and electron diffraction.

3. Fundamental physicochemical properties of elemental phosphorus materials

The characteristics of materials such as electronic, optical, and mechanical properties are not solely determined by the chemical composition but are also significantly influenced by allotropes, which refer to the arrangement of atoms within the lattice structure. EPMs that possess different crystal lattices have been investigated and demonstrated to exhibit fascinating properties, such as structural polymorphism, moderate carrier mobility, adjustable bandgaps, as well as in-plane anisotropic electronic and phonon properties. These properties are both structure-dependent and versatile, favoring potential applications of EPMs. In this section, we analyze these properties which have been theoretically and/or experimentally studied (Fig. 5). In particular, there are commonalities and differences among various EPMs and the comparisons of building blocks, materials stability, bandgaps, and charge carrier mobility of EPMs are highlighted. In addition, we briefly introduce the passivation techniques for improving the materials stability by, for example, doping, encapsulation, and surface functionalization.

3.1 Atomic structure

Many intriguing properties of EPMs are intimately related to the geometric configuration of phosphorus atoms. As shown in Fig. 6, EPMs possess different building blocks that can be divided into three categories: (1) white-P containing tetrahedral P_4 cages; (2) black-P and its derivatives with a puckered honeycomb structure; and (3) red-P allotropic modifications composed of chain-like and polygonal connected rings. In the following parts, we will discuss these categories in greater detail, providing insights into their unique geometries and the consequent impacts on the properties of EPMs.

3.1.1 Tetrahedral P_4. White-P has a cubic structure composed of 58 tetrahedral P_4 units per cell and is formed by condensation of P_4 vapor.[100] The bonds within the P_4 units are covalent, while the interactions between tetrahedra are the weaker vdW forces. The P–P bond length in the P_4 tetrahedron has been the subject of debate, with quantum mechanical calculations indicating it to be 2.194 Å, but the results obtained from Raman scattering (2.2228(5) Å) and electron diffraction (2.21 Å at 470 K) differ.[101–104] White-P exists in three crystalline phases (α-, β-, and γ-form) at different temperatures and pressures.[105,106] The α-form is a plastic crystal that exists at ambient temperature. The reversible transition from the α-form to β-form occurs at a temperature below 196 K or a pressure of over 1.0 GPa. β-Form crystallizes in the space group Pī with three molecules in the asymmetric unit with a P–P bond length of 2.209(5) Å. When the α-form is cooled to 88 K, it transitions to the γ-form. The γ-form transitions to the β-form at 153 K, while the β-form to γ-form transition is uncommon. White-P displays the highest chemical reactivity among all known phosphorus allotropes due to its atomic structure. The four phosphorus atoms form a tetrahedral shape with six bonds, yielding three bonds connecting each atom to neighboring atoms. These bonds derived from non-hybridized 3p orbitals typically form at a 90-degree angle; however, because of the pyramidal geometry of white-P, the bonds are bent rendering the structure of white-P unstable.[107,108] In addition, each atom holds a lone pair of electrons thereby making it capable of undergoing strong redox reactions with other chemicals.

3.1.2 Puckered honeycomb. Black-P and its derivatives (blue-P and green-P) have a puckered layer structure and the P_4 units in these allotropes should be opened to form sp^3 hybrid bonds. The phosphorus atoms are covalently bonded with adjacent atoms to form continuous layers that are held together by vdW forces. Each atom forms three hybrid bonds in the layer leaving a lone pair of electrons that protrude from the layer at an angle different from the bonding angle, resulting in the formation of a puckered structure.

Bulk black-P exists in three crystalline phases, orthorhombic, simple cubic, and rhombohedral, and the most intriguing is the semiconducting orthorhombic phase belonging to the space group *Cmca*(64) with eight phosphorus atoms per cell.[109] Orthorhombic black-P can change its structure reversibly at a high pressure morphing into the denser rhombohedral or simple cubic forms.[110] However, these two forms are unstable under normal conditions and are not suitable for use in practice. In this review, unless specified, black-P refers to the orthorhombic phase which is the focus of most research. The lattice constants *a*, *b*, and *c* of black-P crystals, determined by time-of-flight neutron powder diffractometry by Cartz *et al.*, are

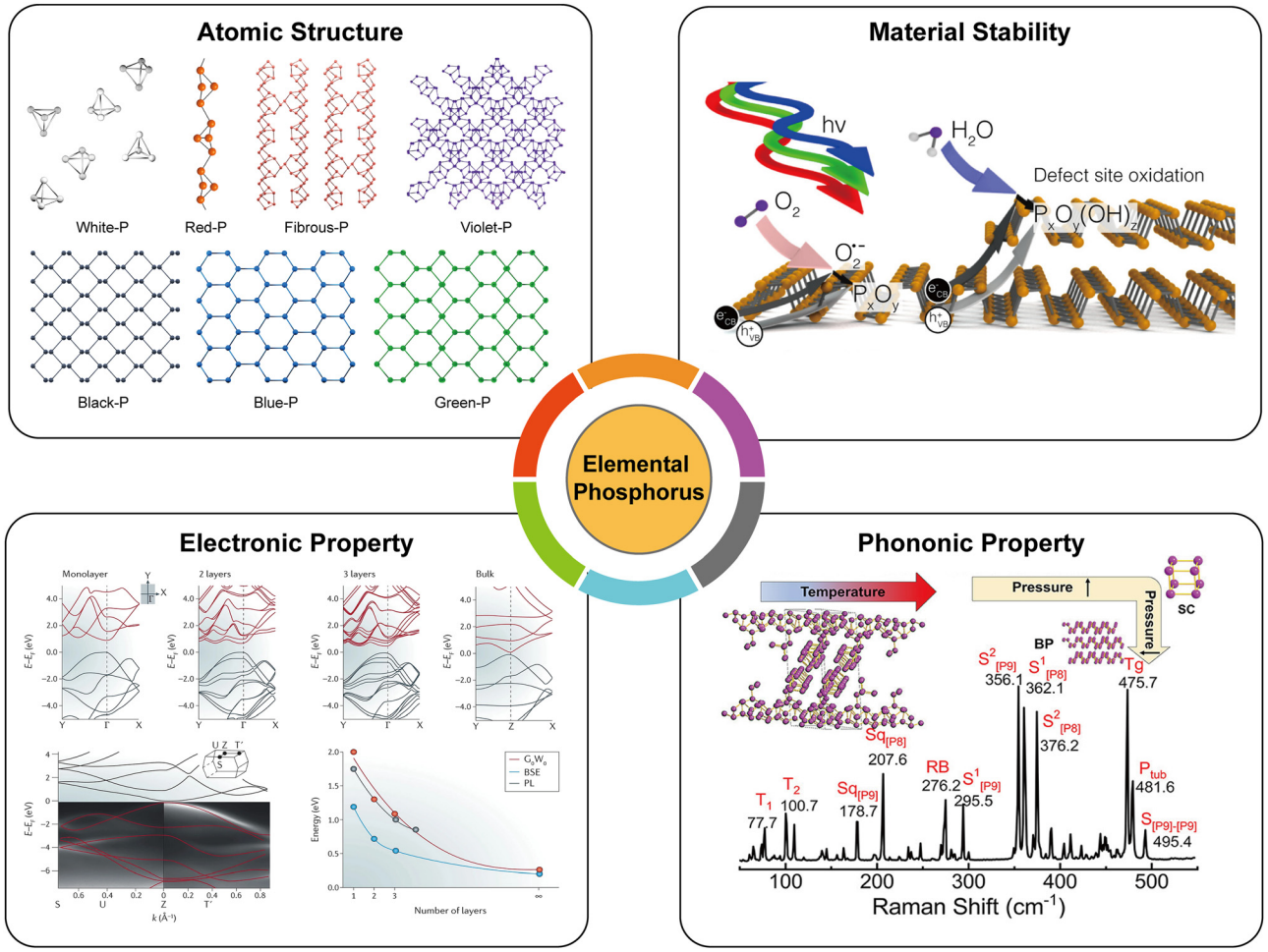

Fig. 5 Fundamental physicochemical properties of elemental phosphorus materials. Atomic structure, originally drawn by our group. Material stability, reproduced with permission from ref. 72. Copyright 2017 American Chemical Society. Electronic property, reproduced with permission from ref. 112. Copyright 2016 Nature Publishing Group. Phonon property, reproduced with permission from ref. 173. Copyright 2021 American Chemical Society.

4.374(2), 3.3133(9), and 10.473(5) Å, respectively.[111] Owing to orbital hybridization, black-P has a nonplanar bilayer structure with two different bond angles ($\alpha = 96.34^\circ$ and $\beta = 103.09^\circ$). From the side view, there are two types of P–P bonds, a short bond (2.224 Å) and a long bond (2.244 Å) connecting two close atoms in different sublayers.[112] This results in anisotropy between the zigzag (y) and armchair (x) directions and the crystalline symmetry of single-layered black-P is two-fold rotational (D_{2h}), which is far less than the six-fold rotational (D_{6h}) symmetry observed in single-layered graphene, which has a flat hexagonal lattice.[71] The reduction in crystalline symmetry is fundamental to the various chemical and physical properties. For instance, the band structure of black-P exhibits anisotropy irrespective of the thickness, giving rise to in-plane anisotropic properties in charge transport, thermal conductivity, and optics.[113,114] The interlayers are held together by vdW forces with a layer spacing of 3.214–3.729 Å,[115] depending on different stacking orders. The relatively weak vdW forces make black-P suitable for exfoliation to prepare phosphorene and allow for property turnability.

The atomic structure of the blue-P monolayer, as discussed in Section 2, can be viewed as the flipping of specific atoms, transforming the armchair ridges into zigzag ridges in the black-P monolayer without altering the local bond angles. This leads to a non-planar but isotropic structure for single-layered blue-P, a significant difference from the anisotropic structure of its black counterpart. Zhu *et al.* noted the possibility of a new phosphorus phase resulting from a certain dislocation of black-P and conducted *ab initio* calculations to investigate the basic properties of the allotrope.[49] They dubbed this new allotrope blue phosphorus (blue-P) with the color defined by its fundamental bandgap. Blue-P atoms are covalently bonded in the layer with a bond length of 2.27 Å, and a weak interlayer interaction of 6 meV per atom keeps the layered structure intact with an interlayer distance of 5.63 Å.[49] The optimized blue-P monolayer has a hexagonal unit cell with lattice vectors of $|\vec{a}| = |\vec{b}| = 3.33$ Å. The interlayer interaction shows little effects on the in-layer structure, causing only a slight shift in the lattice vector from 3.324 Å in bulk to 3.326 Å in the monolayer. The free-standing bulk crystals of blue-P do not exist, although single-layered blue-P has been reported to grow on several noble metals.[52]

Green-P is a metastable EPM that combines features of armchair-ridged black-P and zigzag-ridged blue-P. Han *et al.*

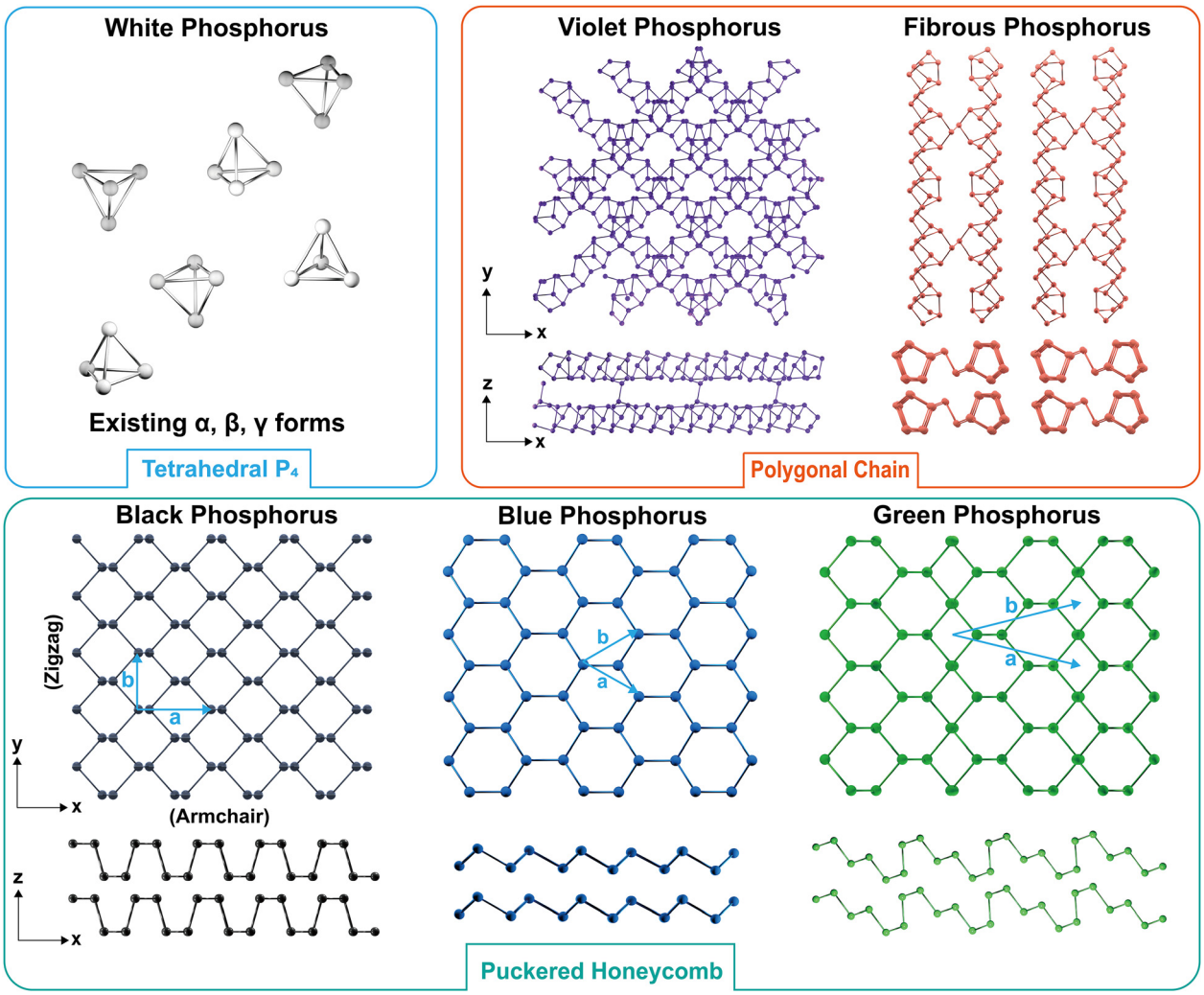

Fig. 6 Atomic structures of white, violet, fibrous, black, blue, and green phosphorus. Three categories are divided by the building blocks: tetrahedral P_4 (white phosphorus), polygonal chain (violet and fibrous phosphorus), and puckered honeycomb (black, blue, and green phosphorus).

were the first to report the structural and electronic properties *in silico*.[50] Bulk green-P has a monoclinic $C2/m$ structure with six atoms per unit cell and in-plane lattice constants of $a = b =$ 7.13 Å. Green-P exhibits the greatest layer thickness (2.91 Å) among the three allotropes due to the presence of three slightly curved sublayers in each layer, compared to 2.11 Å for black phosphorene and 1.24 Å for blue phosphorene. All the atoms in green-P are three-fold bonded with in-plane lengths of 2.23 Å and out-of-plane bond lengths of 2.26 Å. The AB stacking order is energetically preferred and the interlayer distance is 2.16 Å. Although green-P has a shorter interlayer distance than black-P and blue-P, the interaction between green-P layers at 74 meV per atom is similar to that of Black-P (79 meV per atom), indicating its potential for mechanical exfoliation. Moreover, the buckled structure of green phosphorene aligns well with corrugated Au and Ag substrates, suggesting that epitaxial growth is favored with this allotrope.[50]

3.1.3 Polygonal chains. Unlike the EPMs mentioned above, the structure of red-P crystalline phases is challenging to characterize due to its polymorphism, resulting in various proposed molecular geometries including amorphous and fibrous structures.[116] X-ray diffraction and Raman scattering have revealed that red-P is a mid-range order semiconductor made up of multiple subunits forming a chain-like network.[117] The subunits exist in various configurations, and the particular crystallographic phase of red-P depends on synthesis conditions as well as terminal group and chain length variations. Roth *et al.* have suggested a numbering system, labelling the different red-P modifications as type I to V, based on the thermal stability.[34]

The structure of type I amorphous red-P has been the subject of debate and two main models are currently being considered.[28] Model 1 postulates that it consists of chain-like pentagonal nanotubes resembling monoclinic violet-P,[118,119] while model 2 proposes a layered structure similar to that of orthorhombic black-P.[120–122] Model 2, which explains the alterations in the intermediate-range order in phosphorus layers based on growth factors,[120] has been widely adopted

and accepted by many studies. However, several structural studies using Raman spectroscopy and XPS have found evidence of the presence of pentagonal tubes in the microstructure of amorphous red-P,[100,118] suggesting that model 1 may also play a role.

In recent years, innovative methodologies have been employed to determine the microstructure of amorphous red-P. Zhang *et al.*[123] discussed the four possible linear molecular structures of amorphous red-P that were previously proposed by chemists (Fig. 7a). These included the double triangle P_4 (1) proposed by Pauling and Simonetta in 1952,[108] the zigzag ladder P_4 (2) proposed by Salzmann *et al.*,[124] as well as [P8]P2[(3) and [P10]P2[(4) suggested by Häser and colleagues.[125,126] Through their single-molecule studies, they discovered that amorphous red-P is a straight-chain inorganic polymer with a zigzag ladder structure, which aligns more closely with structure (2). However, Deringer *et al.* adopted ML-based simulations to visualize the local structure and pressure-induced changes in amorphous red-P at the atomic scale.[58] They inferred that amorphous red-P is an open network of covalently connected phosphorus clusters. They analyzed the types and counts of cluster fragments, finding that P_5 rings, P2[P3]P2 and P3]P2[P3 clusters, and P_{10} cages are the dominant building units, whereas P_3 rings and P_4 tetrahedra are much less abundant (Fig. 7b). The precise molecular structure of amorphous red-P still awaits verification through further computational and experimental investigation.

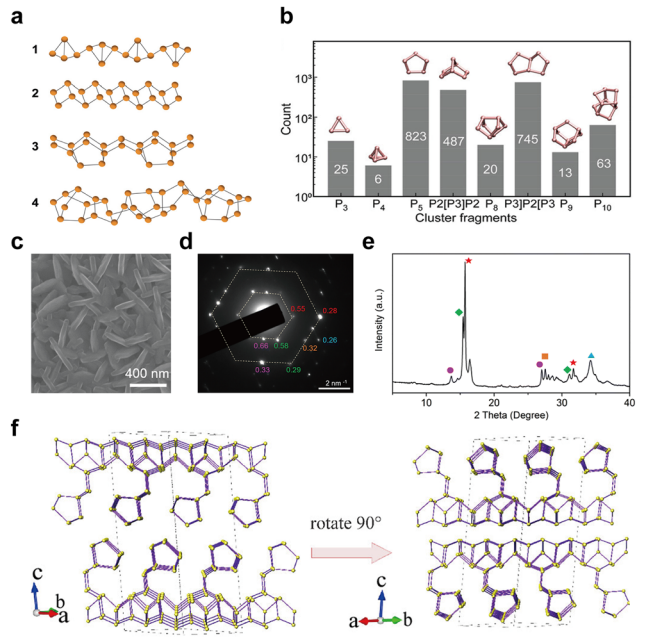

Fig. 7 Structure and characterization of type I amorphous red-P, type II crystalline red-P, and violet-P_{11}. (a) Possible linear molecular structures of amorphous red-P. Reproduced with permission from ref. 123. Copyright 2019 John Wiley and Sons. (b) Counts of relevant cluster fragments in the simulated model. Reproduced with permission from ref. 58. Copyright 2021 John Wiley and Sons. (c) SEM image of type II crystalline red-P. (d) SAED pattern of type II crystalline red-P with interplanar spacings. (e) XRD peaks marked with the same colour as spots in (d) represent a set of corresponding lattice planes with primary and secondary diffraction peaks. Reproduced with permission from ref. 129. Copyright 2021 Royal Society of Chemistry. (f) Crystal structure of violet-P_{11} viewed along two directions. Reproduced with permission from ref. 136. Copyright 2023 American Chemical Society.

Roth *et al.*[34] were the first to observe type II and III crystalline red-P using differential thermal analysis. In 1966, Rubenstein and Ryan[127] verified the presence of type II crystalline red-P by annealing in an inert atmosphere and matching the powder XRD patterns with Roth's findings. Nechaeva *et al.*[128] later produced type II crystalline red-P by chemical vapor deposition and identified the monoclinic structure with specific lattice parameters. Recently, Yan and colleagues have produced type II red-P crystals with a platelet morphology using a solution phase synthesis method (Fig. 7c).[129] The high crystallinity of the product is evident from the XRD results, with the most intense peak at 15.66° and a plane spacing of 5.66 Å, which is in close agreement with the results obtained by Roth and colleagues in 1947.[34,129] The nearly hexagonal symmetrical SAED pattern of the crystal suggests a monoclinic crystal system, and the plane spacing is consistent with the XRD pattern (Fig. 7d and e). However, so far, limited structural information is available for type III crystalline red-P. It is imperative to develop reliable methods for synthesizing type III crystalline red-P to facilitate the analysis of its crystal structure.

The structures of two other types of crystalline red-P have been studied.[23,28] Type IV fibrous-P and type V violet-P have been confirmed to consist of repeating polymeric tubes with a pentagonal segment arranged in a regular pattern of [P9]P2 [P8]P2[. The key difference between fibrous-P and violet-P lies in the manner the double tubes are connected. Violet-P consists of two interpenetrating tube systems that run perpendicular to each other, forming double stacks held together by vdW forces in the *c* direction. The double tubes in fibrous-P, on the other hand, are parallel and held together by vdW forces in both the *a* and *c* directions, making it a member of the unique 1D vdW crystal family with distinct bonding behavior and anisotropic physical properties.[36] The structural parameters of violet-P and fibrous-P are available. By using single-crystal XRD, Zhang *et al.*[48] have determined the lattice constants of violet-P crystals to be 9.210, 9.128, and 21.893 Å for the parameters *a*, *b*, and *c*, respectively. Meanwhile, Du *et al.*[36] have used XRD to show that the lattice constants of fibrous-P crystals are 12.198, 12.986, and 7.075 Å for *a*, *b*, and *c*, respectively, which are consistent with theoretical simulation results. Although both fibrous-P and violet-P have similar plate-like shape and color, they can be differentiated through mechanical stress tests, in which fibrous-P crystals break down into thin filaments, while violet-P crystals shatter into smaller platelets.[88] Furthermore, high-resolution TEM shows distinct morphological differences between the two crystalline phases.

Bulk crystals of violet-P can be peeled into few- or single-layered violet phosphorene by applying external forces. DFT calculation has been used to compute the binding energy per layer needed for complete exfoliation of the bulk crystal into monolayers. The binding energy of violet phosphorene is 0.35 J m^{-2}, which is comparable to that of graphene (0.34 J m^{-2}) but lower than that of black phosphorene (0.40 J m^{-2}) or blue

phosphorene (0.42 J m^{-2}).[130] This indicates that exfoliating violet phosphorene is easier than other types of phosphorene. In 2020, violet phosphorene was synthesized and characterized as a 2D nanobelt composed of tubular strands with an interlayer spacing of 11 Å in AB stacking.[48] Regarding fibrous phosphorene, Hu and Guo have confirmed that fibrous-P bulk crystals have a layered structure along the (001) direction and can be exfoliated experimentally.[131] Each layer consists of four [P9]P2 [P8]P2[polytubes with 84 phosphorus atoms held together by vdW interactions. The average interlayer distances along the (001) and (200) facets are 5.83 Å and 5.57 Å, respectively. The binding energy for fibrous phosphorene, calculated to be 0.88 J m^{-2},[132] is at least two times greater than that of violet phosphorene, making exfoliation of fibrous-P more challenging. However, fibrous phosphorene is held together by vdW interactions in two directions (*a* and *c*) similar to selenene and tellurene[133–135] and can be fabricated by epitaxy or other methods.

Very recently, Cicirello and colleagues synthesized a new two-dimensional allotrope of violet phosphorus, dubbed violet-P_{11}, using a salt flux method in the presence of bismuth.[136] The crystal structure of this allotrope from different views is shown in Fig. 7f. The structure of violet-P_{11} is similar to that of violet-P. However, violet-P_{11} possesses a higher structural symmetry compared to that of violet-P. The asymmetric unit of violet-P_{11} is entirely occupied by 11 distinct phosphorus atoms, while that of violet-P comprises 21 different phosphorus atoms. Single-crystal XRD has revealed that violet-P_{11} crystallizes in the monoclinic space group $C2/c$(15), with unit cell parameters of 9.166(6), 9.121(6), and 21.803(14) Å for *a*, *b*, and *c*, respectively.[136] Violet-P_{11} exhibits substantial stability in ambient air even after being exfoliated for at least an hour.

3.2 Electronic properties

Understanding the electronic properties of a material is pivotal for unraveling the mechanisms underlying its applications in catalysis, ion storage, sensing, and environmental remediation. In the following parts, we will discuss the differences and interrelationships in the band structure and charge mobility among different EPMs.

3.2.1 Band structure. The bandgap of materials affects the effectiveness in photo-/electrocatalysis and ion storage. White-P exhibits an insulating nature making it unsuitable for these applications.[100,137,138] The electronic properties of white-P are associated with the electronic arrangement of a P_4 molecule, which possesses a HOMO–LUMO bandgap of 3.9 eV,[116] making it susceptible to activation by many nucleophiles and electrophiles. Other EPMs have demonstrated the characteristics of semiconductors with moderate and adjustable bandgaps. Among the five crystalline allotropes (black, green, blue, fibrous, and violet), black-P and green-P bulk crystals have direct bandgaps of 0.3 and 0.68 eV, respectively.[50,139] The bandgaps in their monolayer forms were determined to be 2.0 and 2.42 eV, respectively. Tran *et al.*[139] have demonstrated different methods for the bandgap evolution of black-P, as depicted in Fig. 8a. The direct gap in bulk black-P is located at the *Z* point, while in bulk green-P, it is located at the *L* point. As the layer decreases, both gaps shift to the Γ point of the Brillouin zone. Liang *et al.* determined the bandgap of the black-P monolayer to be 2.05 eV by scanning tunneling spectroscopy in an ultrahigh vacuum (Fig. 8b),[140] which is very close to theoretical calculations. The research on the electronic properties of green-P is still in the theoretical stage, and its bandgap has been calculated using quasiparticle approximation, which is one of the most reliable first-principles electrical structure approaches for bandgap determination.[112] Both black-P and green-P are layer-independent direct semiconductors that provide advantages in optoelectronic applications such as higher solar energy conversion efficiency without the need for phonons or other elementary excitations.[141] Furthermore, the bandgap of black and green phosphorene is substantially larger than that of the bulk structure, allowing for wider bandgap tuning. Nonetheless, precise experimental control of the number of layers remains a challenge.

Fibrous-P and atomically layered blue-P have indirect bandgaps. Du *et al.* have plotted the electronic band structures of bulk fibrous-P and shown an indirect bandgap of approximately 1.57 eV (Fig. 8c).[36] The conduction band minimum (CBM) and valence band maximum (VBM) can be found around the *L* and Γ/Y points of the Brillouin zone, respectively. To correct for the underestimated value, they applied the modified Becke–Johnson functional, resulting in an indirect bandgap range of $\sim$1.80 to 2.11 eV. The 3D mapping of the Fermi surface reveals weak dispersion in the valence band (Fig. 8d), which is caused by electron confinement in one dimension. Lu *et al.* used the HSE06 hybrid functional and determined the indirect bandgap of fibrous-P bulk crystals and monolayers to be 2.25 and 2.46 eV, respectively.[132] The bandgap of a fibrous-P bilayer is 2.34 eV, which is only slightly narrower than that of the monolayer, indicating that the number of stacked layers has minimal effects on the bandgap of fibrous-P. This makes fibrous-P based materials ideal for catalysis because bulk crystals can be directly used without the need for extra exfoliation or precise control over layer numbers. Zhou *et al.*[142] have assessed the evolution of quasiparticle bandgaps in few-layered blue-P (Fig. 8e and f). The indirect bandgap diminishes as the layer count rises starting at 3.41 eV for the monolayer, reaching 1.09 eV for the penta-layer, and finally changing into a metallic bandgap in the bulk form. The bandgap calculated using PBE is significantly smaller than that determined using quasiparticle approximation, yet the degree of band dispersion remains largely unchanged. This suggests that the bandgap width of blue-P is larger than that of black-P and green-P, and bulk blue-P even exhibits metallic characteristics. However, whether bulk blue-P is semiconducting or metallic is controversial,[49,142,143] and further theoretical studies on the electrical structure of blue-P crystals are required. Experimentally, the bandgap of 4 × 4 blue phosphorene on Au(111) is measured to be approximately 1.10 eV by angle-resolved photoemission spectroscopy,[144] which is significantly lower than the theoretical bandgap of free-standing blue phosphorene. This results from the strong in-layer strain caused by the interaction between phosphorene and the Au(111) substrate,[52,145] which disturbs the lattice symmetry of free-standing blue-P, hence impacting the electrical characteristics.

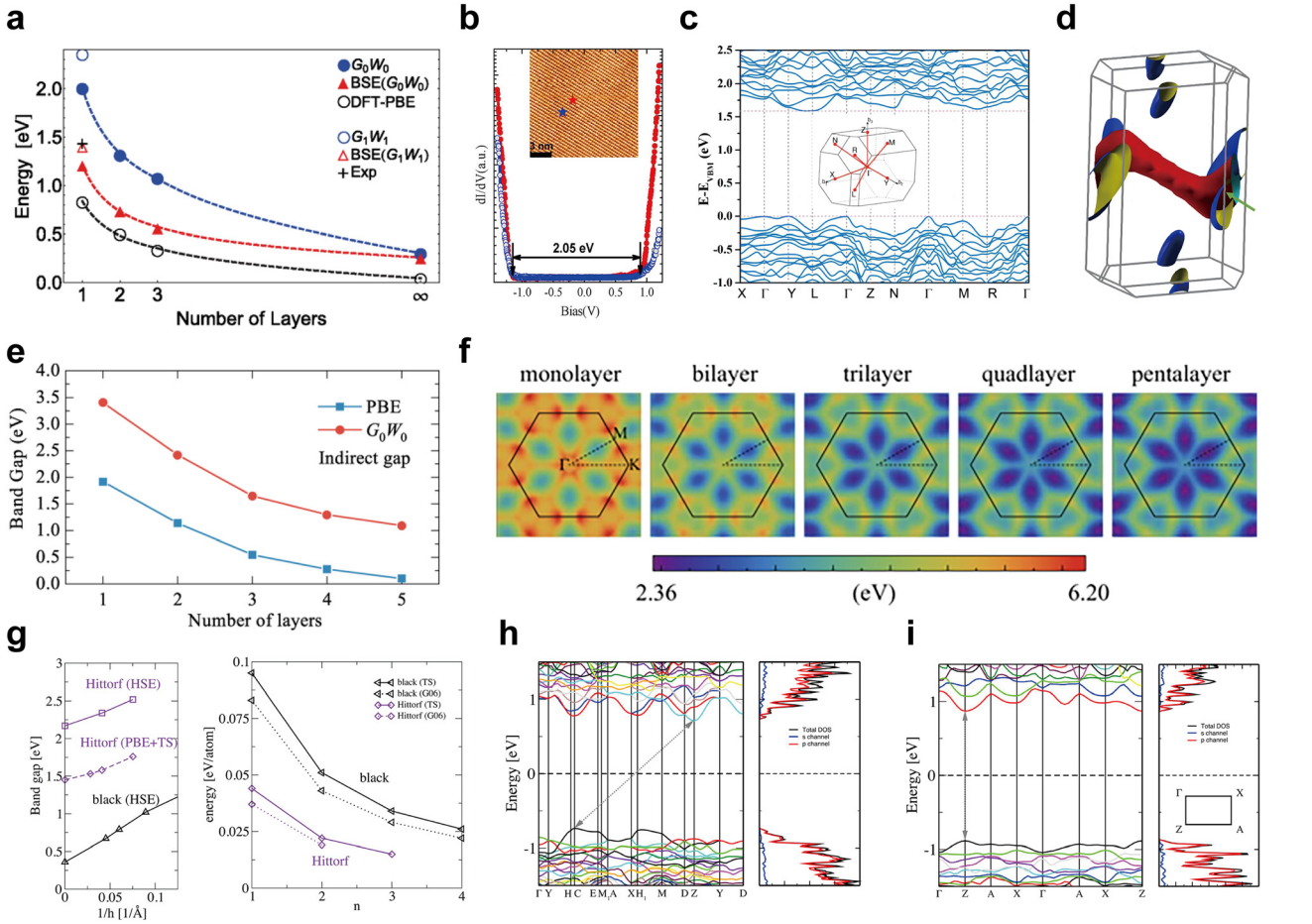

Fig. 8 Electronic band structures of black, violet, fibrous, blue, and green phosphorus. (a) Layer dependence of bandgaps for black-P as calculated by various methods. Reproduced with permission from ref. 139. Copyright 2014 American Physical Society. (b) Spectroscopic measurement of the bandgap for black-P. Reproduced with permission from ref. 140. Copyright 2014 American Chemical Society. (c) Theoretical band structure and (d) the mapping of the Fermi surface of bulk fibrous-P. Reproduced with permission from ref. 36. Copyright 2021 Nature Publishing Group. (e and f) Layer dependence of quasiparticle bandgaps for few-layered blue-P. Reproduced with permission from ref. 142. Copyright 2021 American Physical Society. (g) Layer-dependent bandgaps and relative energy of violet-P and black-P. The electronic band structure of the violet-P monolayer (h) and bulk form (i). Reproduced with permission from ref. 130. Copyright 2016 American Chemical Society.

Violet-P differs from the other four allotropes as it undergoes an indirect-to-direct bandgap cross-over when downscaling from the bulk to monolayers. This cross-over is also found in many semiconducting transition metal dichalcogenides (TMDs),[146–148] making it a useful way to tune the electronic properties of layered semiconductors. Schusteritsch *et al.*[130] have developed several calculation methods for determining the electronic band structure of Violet-P (Fig. 8g). The PBE method with dispersion corrections shows the bandgap of bulk violet-P to be 1.45 eV, while monolayer violet-P exhibits a direct bandgap of 1.76 eV at the *Z* point in the Brillouin zone (Fig. 8h–i).[130] A more accurate HSE(TS) hybrid calculation gives wider bandgaps of 2.17 and 2.52 eV for the violet-P bulk form and monolayer, respectively. UV/vis diffuse reflectance spectroscopy reveals an optical bandgap of 1.7 eV for violet-P crystal powder, similar to 1.77 eV obtained in photoluminescence of single-crystal violet-P.[48] The optical bandgap is narrower than the calculated value because it is measured on a substrate-supported sample rather than in vacuum.[112] Both fibrous-P and violet-P have similar bandgaps that are not greatly affected by the number of layers due to similarities in the atomic structures.[88] Further research is needed to fully explain why violet-P has an indirect-to-direct cross-over instead of an indirect bandgap like fibrous-P.

The bandgaps of the aforementioned EPMs are influenced by the number of layers, and the bandgap becomes smaller with increasing number of layers due to the influence of vdW interactions between the layers. As the layer number increases, the interlayer interaction becomes stronger to increase band dispersion and produce a narrower band gap.[11,149,150] Single- and few-layered phosphorene displays pronounced quantum confinement, and the valence and conduction bands mimic those of a quantum-well structure. However, in the bulk counterpart, energy dispersion becomes densely packed, causing the discrete energy bands to turn into quasi-continuous subbands.[11] In addition, the bandgaps of phosphorus allotropes are sensitive to electric fields,[151] molecule adsorption,[152] and tensile strain.[153] These external factors offer significant control

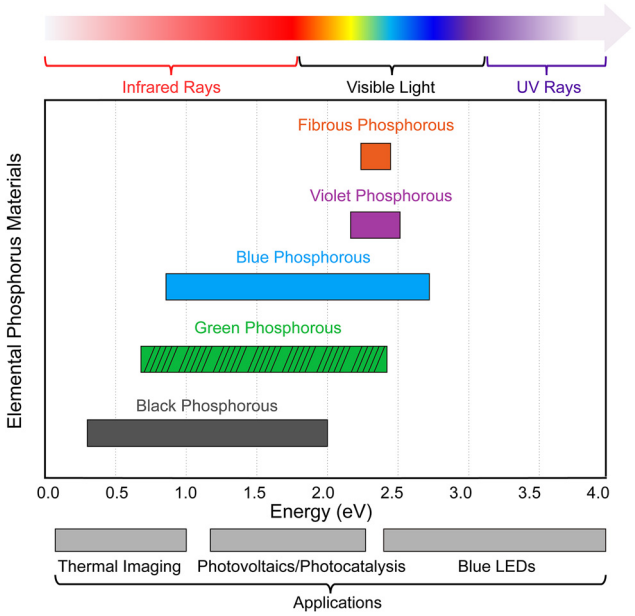

Fig. 9 Comparison of the bandgaps of different EPMs and potential applications. The horizontal bars displaying a range of bandgap values indicate that the bandgap can be adjusted by changing the number of layers. The bandgap of green-P is currently based on theoretical calculations. Bandgap values are taken from ref. 50, 130, 132, 139, and 143.

over the bandgap, particularly in the single-and few-layered structures. As shown in Fig. 9, EPMs with tunable and layer-dependent bandgaps cover a wide range of energy and exhibit strong interaction with electromagnetic waves across the mid-infrared, near-infrared, visible, and near-ultraviolet frequencies, making them suitable for various applications such as thermal imaging (0.1–1.0 eV), photovoltaics/photocatalysis (1.2–2.2 eV), and blue LED techniques (2.5–2.9 eV).

3.2.2 Charge mobility. In addition to the band structure, the mobility of charge carriers also plays a significant role in determining the electronic properties of semiconductors. Although graphene shows high carrier mobility, its transistors generally have an on–off ratio of less than 10 because of the gapless dispersion.[154,155] The discovery of single- and few-layered TMDs has sparked scientific interests and single-layered MoS_2 is a prime example with a direct bandgap and an ultra-high on–off ratio (10^8–10^{10}).[156] However, the carrier mobility is around 200 $cm^2\ V^{-1}\ s^{-1}$, with potential improvements of up to 500 $cm^2\ V^{-1}\ s^{-1}$,[156] which is still significantly lower than that of graphene. Fortunately, elemental phosphorus semiconductors with moderate bandgaps offer high mobility and unusual in-plane anisotropy, making them suitable for optoelectronic applications. Table 1 summarizes the electron and hole mobility values and relevant physical variables of different elemental phosphorus monolayers along the *x* and *y*-axis.

Black-P and violet-P exhibit intrinsic p-type conductivity with a positive Hall coefficient, indicating that conductivity is primarily driven by holes.[37,69] Based on Qiao's phonon-limited scattering model, the hole and electron mobility of black-P can be extended to 10 000–26 000 $cm^2\ V^{-1}\ s^{-1}$ and 1100–1140 $cm^2\ V^{-1}\ s^{-1}$, respectively, which are comparable to those of graphene and greater than those of 2D TMDs.[69] Black-P shows in-plane anisotropic carrier mobility with electron mobility along the *x*-axis being greater than that along the *y*-axis. Regarding the hole mobility, the preference for migration along the *x* or *y*-axis depends on the number of layers. In the few-layered black-P, the hole mobility along the *y*-axis is about half that along the *x*-axis. In a monolayer, the hole mobility along the *y*-axis is surprisingly 16–38 times greater than along the *x*-axis, that is, 10 000–26 000 $cm^2\ V^{-1}\ s^{-1}$ *versus* 640–700 $cm^2\ V^{-1}\ s^{-1}$, indicating that the *y*-axis is the direction of enhanced hole conductivity.[69] Despite the carriers being relatively heavy ($6.35m_0$), the high mobility in a monolayer is due to the low deformation potential (0.15 ± 0.03 eV).[69] Several people have designed black-P based field-effect transistors (FETs) and examined the charge carrier mobility.[45,46,109,157] Violet-P has been predicted to have hole mobilities between 3000–7000 $cm^2\ V^{-1}\ s^{-1}$ based on theoretical calculations.[130] Applying PBE without dispersion corrections, the effective masses of electrons and holes are found to be greater along the *y*-axis and the effective mass of electrons along the *x*-axis ($0.69 \pm 0.01m_0$) is the smallest. The hole deformation potential along the *y*-axis is nearly 7 times smaller than the value along the *x*-axis, that is, 0.18 ± 0.05 eV *versus* 1.26 ± 0.06 eV, resulting in a significant hole mobility of $\sim$7000 $cm^2\ V^{-1}\ s^{-1}$ along the *y*-axis. However, when PBE with dispersion corrections (PBE + TS)

Table 1 Calculated effective mass (m^*), deformation potential (E_1, in eV), 2D elastic modulus (C_{2D}, in J m^{-2}), and electron and hole mobility (μ_{2D}, in 10^3 $cm^2\ V^{-1}\ s^{-1}$) along the *x* and *y* axis of various phosphorus allotrope monolayers at 300 K

System	m_x^*/m_0	m_y^*/m_0	E_{1x}	E_{1y}	C_{x_2D}	C_{y_2D}	μ_{x_2D}	μ_{y_2D}
Black-P(e)	0.17	1.12	2.72 ± 0.02	7.11 ± 0.02	28.94	101.60	1.10–1.14	~0.08
Black-P(h)	0.15	6.35	2.50 ± 0.06	0.15 ± 0.03	28.94	101.60	0.64–0.70	10–26
Violet-P(e)	0.69 ± 0.06	3.58 ± 0.14	1.40 ± 0.03	0.66 ± 0.01	49.70 ± 0.2	49.92 ± 0.4	0.50 ± 0.02	0.43 ± 0.03
Violet-P(h)	1.24 ± 0.03	2.45 ± 0.06	1.26 ± 0.06	0.18 ± 0.05	49.70 ± 0.2	49.92 ± 0.4	0.31 ± 0.02	7.68 ± 4.3
Fibrous-P(e)	0.41	0.56	3.98	0.64	9.96	91.65	0.07	17.7
Fibrous-P(h)	2.95	0.44	0.56	1.83	9.96	91.65	0.19	1.17
Green-P(e)	0.27	0.20	−5.02	2.35	26.5	84.9	0.355	7.02
Green-P(h)	0.21	1.71	−9.93	7.71	26.5	84.9	0.048	0.024
Blue-P*(e)	0.130	0.132	−2.289	−2.261	42.826	47.248	10.263	11.429
Blue-P*(h)	2.231	1.587	−1.007	−1.005	42.826	47.248	0.215	0.335

e, electrons; h, holes; Blue-P*, 4 × 4 phosphorene on Au(111). Data extracted from ref. 69, 75, 130, 132, and 144.

is employed, the hole mobility is reduced to $\sim$3000 cm^2 V^{-1} s^{-1} as PBE + TS calculates a magnitude of the deformation potential that is twice that of PBE. Recently, Ricciardulli *et al.* have created a FET using exfoliated violet-P thin films and found that the hole mobility of the film is 2.25 cm^2 V^{-1} s^{-1} at room temperature.[37] Although charge transport in films may be impeded by inter-flake resistances and structural defects caused by the exfoliation process,[158] this work experimentally demonstrates the potential of violet-P as a p-type semiconductor.

Dominated by high electron mobilities, fibrous-P and green-P are potential materials for n-type devices.[50,132] In the fibrous-P monolayer, the effective masses of electrons (holes) along the *x*- and *y*-axis are calculated to be 0.41 (2.95) and 0.56 (0.44)m_0, respectively.[132] The deformation potential (E_1) and elastic modulus (C_{2D}) are highly anisotropic in the plane. The calculated deformation potentials of electrons along the *x*- and *y*-axis are approximately 3.98 and 0.64 eV, respectively, with an anisotropy ratio greater than 6. C_{2D_y} is almost nine times larger than C_{2D_x}. This results in a significant electron mobility of $\sim$17 700 cm^2 V^{-1} s^{-1} along the *y*-axis, which is comparable to that of other layered semiconductors like black phosphorene,[69] violet phosphorene,[130] and Al_2C monolayers.[159] However, the FET made from fibrous-P nanoribbons has a lower hole mobility (236.7 cm^2 V^{-1} s^{-1}),[160] which is far less than expected. This may be due to the high contact resistance between the channel materials and electrodes. High mobility can be improved by modifying the contact electrodes or using high-*k* materials as the gate layer.[156,160] In green phosphorene, the effective masses of electrons (holes) along the *x*- and *y*-axis are predicted to be 0.274 (0.166) and 0.162 (1.333)m_0, respectively.[50] This suggests that the hole mobility is highly anisotropic, while the electron mobility is nearly isotropic. For a carrier concentration of 5×10^{12} cm^{-2}, the electron mobility is determined to be around 200 cm^2 V^{-1} s^{-1} at 300 K, which is higher than the hole mobility ($\sim$60 cm^2 V^{-1} s^{-1}). This relatively high electron mobility is a result of lower scattering rates near the CBM.

Zhuang *et al.* have investigated the carrier mobility characteristics of 4 $\times$ 4 blue phosphorene on Au(111) theoretically.[144] The effective mass of holes is slightly greater along the *x*-axis than along the *y*-axis (2.231m_0 *versus* 1.587m_0), whereas the effective mass of electrons along both axes is very close and small ($\sim$0.130m_0). This small effective mass leads to high electron mobility, which can reach up to 11 429 cm^2 V^{-1} s^{-1}. The limited anisotropy in carrier mobilities of 4 $\times$ 4 blue phosphorene on Au(111) is related to the more symmetrical atomic structure, but even minor changes in the structure of layered materials can produce significant variations in the electronic properties. The strong in-layer strain caused by the blue-P–Au(111) interaction greatly influences the electron mobility.[144,161] Therefore, they have also calculated the carrier mobilities of 4 $\times$ 4 blue phosphorene in the absence of tensile strain.[144] The effective mass of electrons increases significantly in free-standing blue phosphorene, which greatly reduces the electron mobility by one or two orders of magnitude.

So far, studies on the carrier mobility of elemental phosphorus semiconductors, excluding black-P, have mainly been theoretical. In general, theoretical calculations for the room-temperature carrier mobilities (μ_{2D}) of layered materials use an acoustic phonon limited method and the following expression:[69,162]

$$\mu_{2D} = \frac{e\hbar^3 C_{2D}}{k_B T m_e^* m_d \left(E_1^i\right)^2}$$

The factors that impact the mobility most significantly are the deformation potential (E_1) and elastic modulus (C_{2D}) in the direction of the longitudinal acoustic wave. This is why single-layered phosphorene tends to have higher carrier mobility. In single-layered phosphorene, the absence of interlayer and stacking-induced intralayer overlap for valence or conduction band wavefunctions leads to a minimal deformation potential in a specific direction, leading to remarkable hole or electron mobility.[163] However, experimental results for carrier mobility of EPMs have shown significant discrepancies with theoretical predictions. For example, no experimentally measured black-P monolayer has a hole mobility greater than 10 000 cm^2 V^{-1} s^{-1}. The unmanageable layer number and structural defects in preparation as well as the interface resistance in detection should be ascribed to the discrepancy.

3.3 Phonon properties

Phonons are the quantized vibrational modes of the material's lattice structure and strongly influence its thermal and mechanical properties as well as electronic behavior.[164–166] To obtain a comprehensive understanding of the performance of low-dimensional EPMs in various applications including nanoelectronics, optoelectronics, and spintronic devices, it is necessary to conduct systematic investigations of the phonon-related properties. Raman spectroscopy serves as an important characterization tool for acquiring information about the phonon band structure and properties of materials. To comprehend the Raman scattering and Raman selection rules in EPM crystals, it is essential to understand the crystal symmetry, lattice vibration, and phonon dispersion.[167]

Generally, group theory can be employed to predict the normal modes in crystals and classify lattice vibrations based on the irreducible representations of the corresponding crystal symmetry groups.[168] Recent theoretical and experimental investigations have primarily focused on characterizing the vibrational properties of three phosphorus allotropes: black-P, blue-P, and violet-P. Considering that there is an extensive literature discussing the vibrational modes of bulk black-P,[169–171] here we primarily focus on the vibrational modes of black-P monolayers. Black-P monolayers belong to the D_{2h}^7 space group and the primitive cell consists of four atoms. This space group exhibits 12 phonon branches including 3 acoustic and 9 optical modes.[172] The irreducible representations for the black-P monolayer are as follows: $\Gamma = 2\Gamma_1^+ + \Gamma_2^+ + 2\Gamma_3^+ + \Gamma_4^+ + \Gamma_1^- + 2\Gamma_2^- + \Gamma_3^- + 2\Gamma_4^-$, where the acoustic modes are Γ_2^-, Γ_3^-, and Γ_4^-. The remaining optical modes in the one-dimensional representations Γ_1^+, Γ_2^+, Γ_3^+, and Γ_4^+ are Raman active, while Γ_2^- and Γ_4^-, are infrared active. The associated non-normalized eigenvectors for black-P monolayer lattice vibration modes are shown in Fig. 10a.

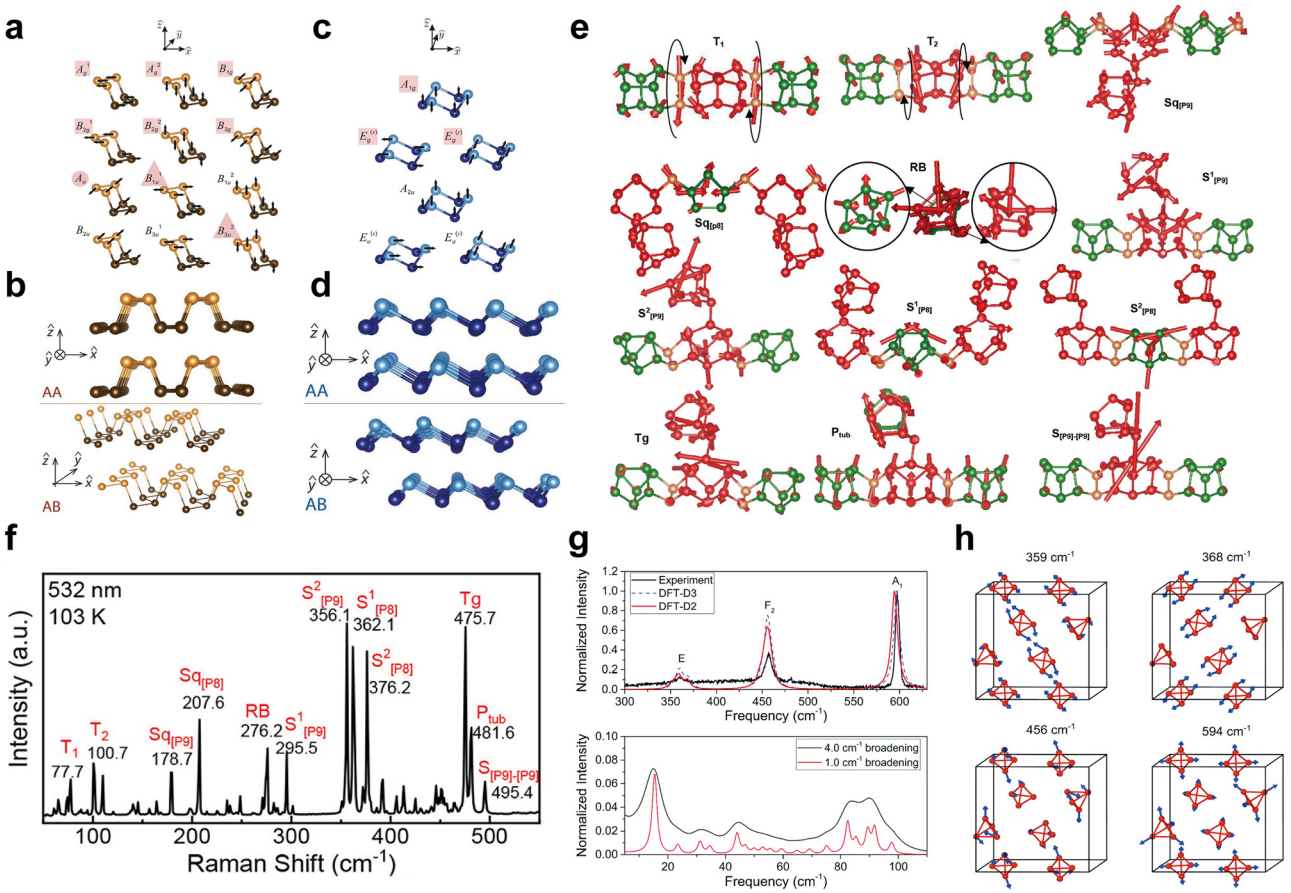

Fig. 10 Phonon-related properties of EPMs. (a) Non-normalized eigenvector representations for Black-P monolayer vibrational modes. (b) Side view of the AA and AB stacking arrangements for the Black-P bilayer. (c) Non-normalized eigenvector representations for blue-P monolayer vibrational modes. (d) Side view of the AA and AB stacking arrangements for the blue-P bilayer. Reproduced with permission from ref. 172. Copyright 2015 American Physical Society. (e) Vibrations of the typical Raman modes of bulk violet-P. (f) Raman spectra of violet-P single crystals at 103 K. Reproduced with permission from ref. 173. Copyright 2021 American Chemical Society. (g) DFT calculated the Raman spectrum of bulk white-P together with the recorded experimental spectrum and (h) calculated eigenvectors of key Raman active modes. Reproduced with permission from ref. 174. Copyright 2021 Royal Society of Chemistry.

Different numbers of layers and different stacking arrangements can also give rise to variations in the symmetry and lattice vibration modes. When multiple layers of black-P are stacked in the AA manner as shown in Fig. 10b, the space group is always D_{2h}^{7} (*Pbmn*, #53), irrespective of the odd or even number of stacked layers. The corresponding irreducible representations are as follows: $\Gamma = 2N(\Gamma_1^+ + \Gamma_3^+ + \Gamma_2^- + \Gamma_4^-) + N(\Gamma_2^+ + \Gamma_4^+ + \Gamma_1^- + \Gamma_3^-)$, where $\Gamma_2^- + \Gamma_3^- + \Gamma_4^-$ are acoustic modes, $2N(\Gamma_1^+ + \Gamma_3^+) + N(\Gamma_2^+ + \Gamma_4^+)$ are Raman active, $(2N-1)(\Gamma_2^- + \Gamma_4^-)(N-1)\Gamma_3^-$ are infrared active, and $N\Gamma_1^-$ are silent. In contrast, when multiple layers of black-P are stacked in the AB manner, odd and even layers exhibit distinct vibrational modes. For odd-numbered layers, the space group and irreducible representations remain consistent with those stacked in the AA manner. However, for even-numbered layers, the lattice vibration belongs to the D_{2h}^{11} (*Pbmn*, #57) space group, and the irreducible representations are as follows: $\Gamma = 2N(\Gamma_1^+ + \Gamma_3^+ + \Gamma_2^- + \Gamma_4^-) + N(\Gamma_2^+ + \Gamma_4^+ + \Gamma_1^- + \Gamma_3^-)$, where the acoustic and optical modes are the same as in the space group of D_{2h}^{7} (*Pbmn*, #53).

Blue-P has a lattice structure similar to that of Black-P. Especially, the blue-P monolayer primitive unit cell comprises two atoms and belongs to the D_{3d}^{3} subgroup, which has the triple rotational symmetry. The irreducible representations of the blue-P monolayer are as follows: $\Gamma = \Gamma_1^+ + \Gamma_3^+ + \Gamma_2^- + \Gamma_3^-$, where $\Gamma_2^- + \Gamma_3^-$ are acoustic modes. The remaining optical modes in the one-dimensional representations Γ_1^+ and Γ_3^+ are Raman active with no infrared activity. The corresponding non-normalized eigenvectors for blue-P monolayer lattice vibration modes are shown in Fig. 10c. However, when dealing with multiple layers of blue-P, the lattice vibration modes differ. For layers stacked in the AA manner, as shown in Fig. 10d, the lattice vibration belongs to the D_{3d}^{3} ($P\bar{3}m1$, #164) group, and irreducible representations are as follows: $\Gamma = N(\Gamma_1^+ + \Gamma_3^+ + \Gamma_2^- + \Gamma_3^-)$, where $\Gamma_2^- + \Gamma_3^-$ are acoustic modes, $N(\Gamma_1^+ + \Gamma_3^+)$ are Raman active, and $(N-1)(\Gamma_2^- + \Gamma_3^-)$ are infrared active. In contrast, when multiple layers of blue-P are stacked in the AB manner, odd and even layers exhibit distinct vibrational modes. For odd-numbered layers, the lattice vibration belongs to the C_{3v}^{1} ($P3m1$, #156) group and the irreducible representations are

as follows: $\Gamma = 2N(\Gamma_1 + \Gamma_3)$, where $\Gamma_1 + \Gamma_3$ are acoustic modes and $(2N-1)(\Gamma_1 + \Gamma_3)$ are both Raman active and infrared active. For even-numbered layers, the space group and irreducible representations are consistent with the AA stacking pattern.[172]

Violet-P in its bulk form has the monoclinic lattice structure with a space group of $P2/n$ (13, $C2h(2/m)$).[173] The lattice vibrations of bulk violet-P at the center of the Brillouin zone involve 252 phonon modes, consisting of 3 acoustic modes and 249 optical modes. These modes can be represented as follows: $\Gamma = (A_u + 2B_u) + 63(A_g + B_g) + (62A_u + 61B_u)$, where $A_u + 2B_u$ are the acoustic modes, $63(A_g + B_g)$ are both Raman and infrared active, and $62A_u + 61B_u$ are inactive in terms of both Raman and infrared. Based on this information, 12 primary vibration modes can be identified (Fig. 10e) and the corresponding Raman features of violet-P will be discussed further below.

Raman scattering is a straightforward, nondestructive, and efficient technique to examine crystal lattice vibrations. During Raman scattering in a crystal, the incident photons can either absorb or emit crystal phonons and subsequently scatter in various directions at different angles.[165] By detecting and analyzing the scattered light that has gained or lost phonon energy, one can determine the relevant phonon properties of the materials. Additionally, since the Raman intensity is proportional to the derivative of the dielectric tensor concerning vibrational coordinates, DFT calculations can be combined with Raman scattering experiments to conduct in-depth studies. Impellizzeri *et al.*[174] applied the Placzek approximation to DFT calculations and combined it with experiments to simulate Raman spectra for various phosphorus allotropes including bulk and low-dimensional structures. The simulated Raman spectrum of white-P (Fig. 10g and h) reveals three different modes: a bending mode E at 371.5 cm^{-1}, and symmetrical stretching modes F_2 and A_1 at 459.5 cm^{-1} and 602.1 cm^{-1}, respectively. The simulated Raman spectra for bulk and monolayer black-P display three unique peaks at 357.3 cm^{-1}, 425.2 cm^{-1}, and 453.5 cm^{-1}, corresponding to the A_g^1, B_{2g}, and A_g^2 modes associated with out-of-plane, zigzag, and armchair vibrations, respectively. Violet-P with its more intricate crystal structure produces a more complex Raman spectrum than white-P and Black-P. The monolayer blue-P simulated Raman spectrum exhibits only two prominent Raman peaks, reflecting its higher symmetry relative to black-P. The E_g mode at 422 cm^{-1} corresponds to the longitudinal displacement in the plane direction, while the A_{1g} mode at 534 cm^{-1} arises from out-of-plane vibrations. Although DFT calculations are effective in simulating Raman spectra to discern the vibrational modes of phosphorus allotropes, refinements are necessary to achieve a closer match with experimental results. Raman spectroscopic studies of bulk violet-P have been reported by Zhang's group.[173] As shown in Fig. 10e and f, the 12 peaks correspond to the 12 main vibrational modes, ranging from strong to moderate intensity.

The thermal properties of phosphorus allotropes are heavily influenced by the crystal orientation due to structural anisotropy. For instance, the thermal conductivity of black-P demonstrates a significant dependence on the thickness and high degree of anisotropy.[166] Theoretical calculations indicate that the thermal conductivity of monolayer phosphorene is lower than that of bulk black-P,[175] showing that the thermal conductivity tends to increase as the black-P thickness increases. However, defects can result in thermal conductivity values lower than the intrinsic ones. Single-crystal black-P exhibits strong in-plane anisotropy in the thermal conductivity across the zigzag and armchair directions, with the armchair direction having lower thermal conductivity values—up to half---compared of those in the zigzag direction.[176] This anisotropy primarily originates from the anisotropic dispersion of phonons and, to a lesser extent, the phonon–phonon scattering rate. Ge *et al.* have investigated the lattice vibrational properties and thermal expansion of blue phosphorene through DFT calculations.[177] Slight buckling of the blue phosphorene atoms in the *Z*-direction disrupts the mirror symmetry, resulting in hybridization of ZA and ZO modes with other modes. Consequently, a phonon band gap develops and the phonon group velocity decreases, effectively reducing the thermal conductivity.

3.4 Materials stability

The stability of EPMs under ambient conditions is crucial to applications because the presence of small molecules like water and oxygen can be problematic.[178] Prolonged exposure to the environment can cause significant changes in the physicochemical properties of phosphorene, including a rougher surface, higher ohmic resistance, and reduced charge mobility due to the formation of a surface oxide layer.[179,180] The detrimental modifications negatively impact the efficiency of catalysts and electrodes. Therefore, comprehending the vulnerabilities of EPMs and potential factors that may interfere with their performance is important for designing more durable EPM-based materials that can be used under industrial conditions.

The stability of materials is influenced by the intrinsic atomic and electronic structures. First, layered EPMs generally have an elevated surface area-to-volume ratio, which accelerates the rate of surface chemical reactions and makes them susceptible to deterioration. Second, the valence electron configuration of phosphorus atoms ($3s^23p^3$) results in the formation of covalent bonds with three neighboring atoms, leaving a lone electron pair that is highly reactive to ambient components such as oxygen and water.[181] Recently, Lyu and colleagues have conducted a systematic evaluation of the relative stability of 10 layered EPMs with a focus on structure and bonding and found that the *gauche* effect is essential in determining the stability of these materials.[182] Based on DFT calculations, violet-P has the lowest energy relative to other structures and is deemed the most stable (Fig. 11a). Analysis of the torsion-bonding strength relationship reveals that the majority of the P–P bonds in violet-P fall into the *gauche* region (Fig. 11b), indicating that these bonds predominantly exhibit the *gauche* conformation. The phosphorus atom in the layered structure is sp^3 hybridized with a lone electron pair, which contributes to the stability of the *gauche* conformation. This is because the orbitals of two adjacent lone pairs are positioned near each other's nodal planes (Fig. 11c), thus avoiding strong interaction.[183–185] The energetically

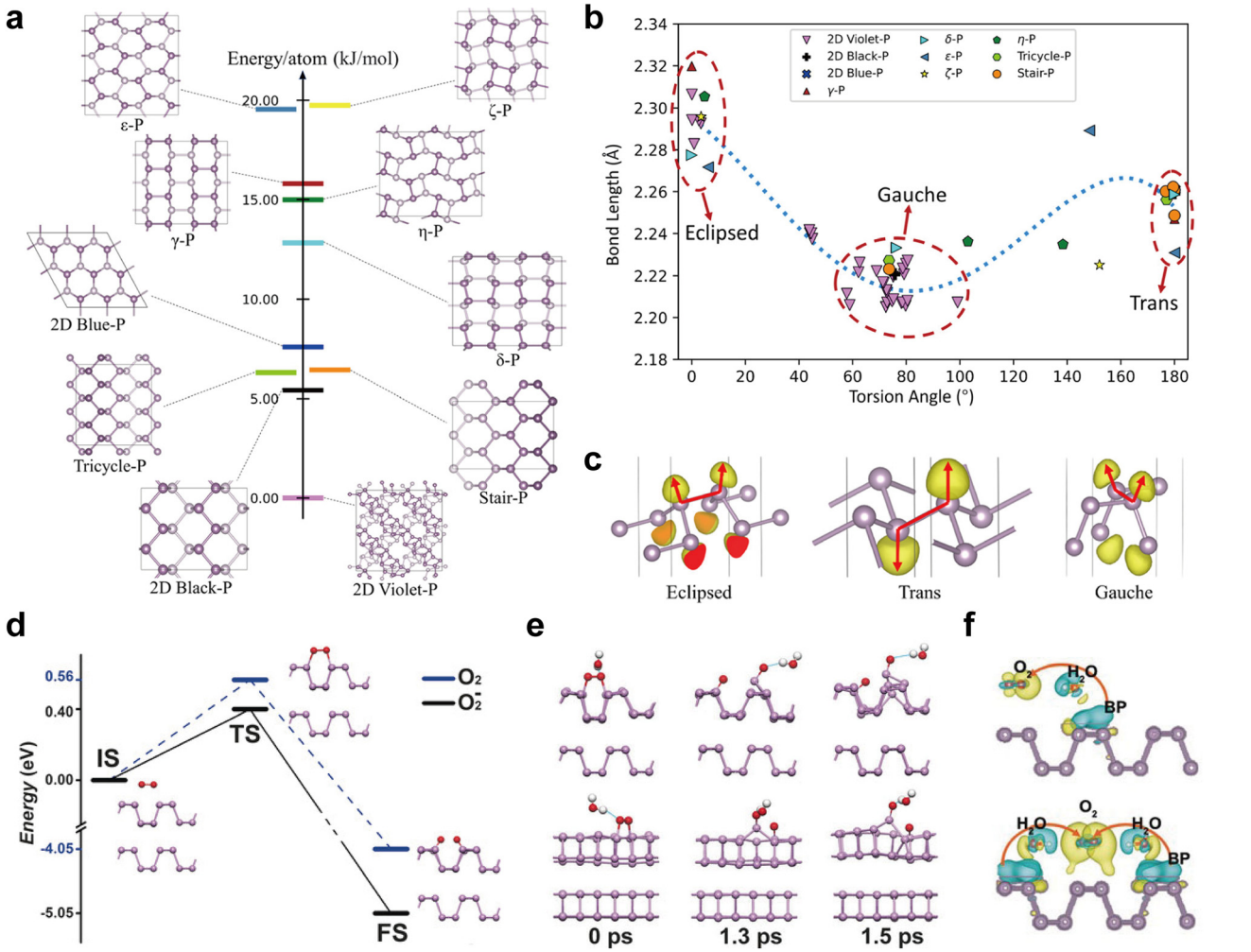

Fig. 11 Theoretical calculations of the stability of EPMs. (a) The relative energy of 10 layered EPMs. (b) Torsion-bonding strength relationship of all P–P bonds in 10 layered EPMs. (c) Eclipsed, trans, and *gauche* conformations of P–P bond in layered EPMs. Reproduced with permission from ref. 182. Copyright 2022 American Chemical Society. (d and e) The oxidization and disintegration process of bilayer black-P. Reproduced with permission from ref. 192. Copyright 2016 John Wiley and Sons. (f) The formation of water–oxygen clusters on the black-P surface. Reproduced with permission from ref. 195. Copyright 2017 John Wiley and Sons.

favorable structure of EPMs has a greater proportion of *gauche* bonds, and an increase in the proportion of eclipse or *trans* conformations will result in a corresponding rise in the energy of the ground state.[182] Other structural factors that can impact the stability include bond length, bond angle, and vdW interactions, and some studies have also evaluated the stability of EPMs from these perspectives.[75,186,187]

Under environmental conditions, the stability of EPMs is also influenced by the thickness and form of crystals. Single-layered phosphorene, composed entirely of surface phosphorus atoms with fully exposed lone-pair electrons, show more surface defects than thicker crystals.[188] Thinner phosphorene tends to degrade from the edges inward due to edge effects, while bulk crystals primarily degrade on the surface, and surface oxidation can extend the overall stability of the materials.[189–191] Additionally, as the thickness decreases, the phosphorene bandgap moves to higher energies due to quantum confinement, bringing the valence and conduction bands closer to O_2 acceptor states.[192] As a result, thinner phosphorene has lower stability and is more susceptible to oxidative degradation than thicker ones. EPMs with different crystal forms also show variations in their degradation under environmental conditions. Fali *et al.* have studied chemical degradation of violet-P flakes and compared surface oxidation with that of black-P under ambient conditions with time.[193] Initially, both violet-P and black-P show similar degradation patterns with random nanoparticles appearing on the surface shortly after exfoliation. However, the sustained growth kinetics of the nanoparticles differs between the two allotropes. In black-P, the degradation area expands rapidly along an S-shaped curve due to merging of neighboring nanoparticles, but no noticeable merging is observed in violet-P, and the deteriorated surface elements have minimal impact on the non-degraded surface elements. As a result, the degradation rate of violet-P is nearly 9 times slower than that of black-P under the same ambient conditions. This work provides experimental proof of the superior stability of violet-P.

External factors that impact the stability of EPMs include light, oxygen, and water. However, the exact degradation mechanism remains a subject of debate. The degradation mechanism of black-P has been extensively investigated under various environmental conditions. Martel's group[92] and Wang's group[192] have put forth a light-induced oxidation mechanism based on *in situ* Raman spectroscopy and theoretical calculations, in which the superoxide anions on the surface, triggered by light exposure, are critical in the degradation of black-P. This light-induced degradation process can be divided into three stages: (1) ambient light promotes the generation of superoxide anions through a charge transfer reaction; (2) the superoxide anions dissociate on the surface and form two P–O bonds with black-P, resulting in the formation of a native surface oxide; and (3) water molecules interact with the bonded O and remove P atoms from the surface *via* hydrogen bonding, leading to the deterioration of the top layer and further oxidation of the inner layer. Throughout the process, superoxide anions stride over a small potential barrier through a triplet–singlet transition, generating dangling O atoms on the surface (Fig. 11d). As a result, the surface becomes hydrophilic, causing the O adsorbed phosphorene to dissolve in water (Fig. 11e).[192] Huang *et al.* have performed isotopic labeling and wetting experiments to confirm the effects of O_2 on the surface hydrophilicity.[194] The pristine Black-P is hydrophobic, but with dissociative chemisorption of O_2, the surface becomes progressively more hydrophilic. Interestingly, a distinctive degradation mechanism for the water-catalyzed oxidation of a few-layered black-P in the absence of light has been proposed.[195] This theory suggests that water and oxygen molecules co-adsorb on the surface of black-P to generate water–oxygen clusters (Fig. 11f), and then electron transfer from black-P to oxygen initiates oxidation even in the absence of light. This can be attributed to the strong polarization effect of water molecules, which significantly enhances the electron affinity of oxygen to improve the capacity to accept electrons. Yu *et al.* recently found that persistent generation of reactive oxygen species on the surface of few-layered black-P also plays a significant role in the dark degradation.[196] Zhao *et al.* have studied the degradation kinetics of fibrous-P nanoribbons under four different exposure conditions.[197] They found that fibrous-P nanoribbons deteriorate rapidly in both oxygenated and deoxygenated water, while deterioration is slower in the absence of light, suggesting that the degradation behavior of fibrous-P differs from that of black-P. For black-P, the influence of light on the degradation kinetics is insignificant and oxygen plays a substantial role.[198] It is also necessary to study the degradation kinetics of other EPMs as the degradation mechanisms may be different from those of black-P.

A variety of physical and chemical protection techniques such as capping layers,[199] liquid protection,[200] surface functionalization,[201] and doping with other elements,[202] have been developed to passivate EPMs. However, in practical applications, striking a balance between material stability and performance is crucial, as blindly pursuing stability at the expense of performance is not a viable option. Our group has proposed a metal-ion modification strategy that can improve both the stability and performance of black-P sheets.[203] The strategy involves the cation–π interaction between metal ions (Ag^+) and the conjugated π bond formed by the lone pair electrons of phosphorus atoms in each layer (Fig. 12a). The high-resolution Raman spectra confirm that the surface of black-P is modified with Ag^+ and no noticeable P_xO_y characteristic peaks are observed (Fig. 12b–d). The intensity of the typical black-P peak at 360.9 cm^{-1} progressively increases until 60 minutes and then stabilizes as a result of saturated adsorption (Fig. 12e),[203] indicating that modifying black-P with Ag^+ *via* cation–π interaction is a manageable and straightforward process. As shown in Fig. 12f–i, the modification process improves the stability of black-P sheets, allowing them to remain unchanged in the air with a relative humidity of up to 95% for several days and without any major alterations in the surface morphology or roughness, despite only a slight increase in thickness (~9.5 nm) compared to the pristine black-P sheets (~8.2 nm). Furthermore, the modified black-P FET exhibits improved hole mobility and ON/OFF ratios. The hole mobility reaches 1666 $cm^2\ V^{-1}\ s^{-1}$, which is more than double the value for pristine black-P. The ON/OFF ratio improves to 2.6×10^6, which is 44 times greater than that of pristine black-P. This strategy has the added advantage of allowing control over the ion concentration and modification time, and it can be extended to other metal ions also. In the future, it is expected that more innovative methods will be developed, which will not only secure the stability of EPMs in practical applications but also enhance their performance.

In summary, this section have offered an in-depth analysis of the fundamental physicochemical properties of EPMs, elucidating the differences and interrelationships among their atomic structures, electronic and phonon properties, and material stability. The section underscored the unique features of these materials and ongoing debates in the field. A specific point of focus, moving forward, should be the structural intricacies of EPMs, particularly surface and edge structures. Despite the advances made in the research of bulk crystals, our comprehension of surface or edge reconstruction and amorphization remains limited. The arrangement change of the surface or edge atoms would bring about significant modifications in physicochemical properties. Furthermore, there is a noticeable lack of emphasis on the structural phase transitions occurring at the sub-nanometer scale, and associated structure–property relationship studies are still insufficient. Further research should also focus on the exotic properties of phosphorene, potentially revealing novel phenomena and applications. In addition, several fundamental debates remain unresolved, including the precise atomic structure of amorphous red-P and type II and III crystalline red-P, the disparity between theoretical predictions and actual measurements of carrier mobility in diverse "violet-P", and the different degradation behavior observed in various EPMs. Addressing these issues will provide a more solid foundation for the field and guide the design and application of these intriguing materials.

4. Synthetic strategies of elemental phosphorus materials

Phosphorus is a versatile element in the periodic table that exists in a variety of allotrope forms and sizes, ranging from

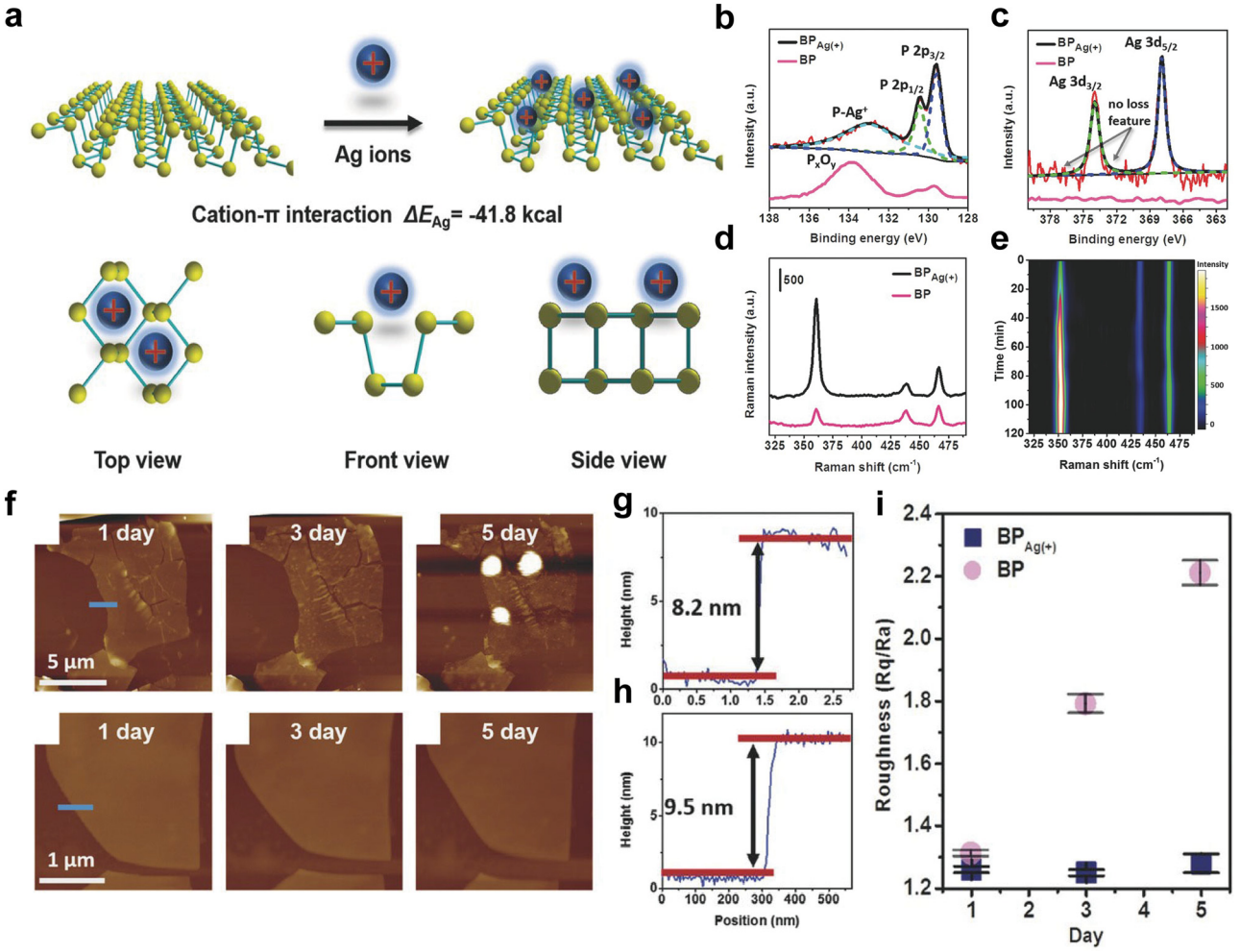

Fig. 12 Metal-ion modified black-P with enhanced stability. (a) Schematic illustration of the interaction of Ag ions with black-P. (b) High-resolution XPS spectra of P 2p and (c) Ag 3d. (d) Raman spectra of a black-P sheet before and after Ag^+ modification. (e) Series of Raman spectra of a black-P sheet after Ag^+ modification for 0 to 120 min. (f) AFM images of pristine (top) and modified (bottom) black-P sheets exposed to air for several days. (g) Corresponding height profile of pristine and (h) modified black-P sheet. (i) Surface roughness of the modified and pristine black-P sheet with exposure time. Reproduced with permission from ref. 203. Copyright 2017 John Wiley and Sons.

bulk crystals to layered sheets, nanoribbons, and quantum dots. Synthetic EPMs provide a broad range of properties that can be tailored through the choice of constituent allotropes and reaction conditions. To fully realize the potential of EPMs and their "on-demand" properties, it is necessary to develop and optimize the synthetic methods. High-quality, uniform, and mass-producible synthesis of EPMs is crucial to applications. Currently, the synthesis of white-P still relies on pyrolysis of phosphate ores using the J. B. Readman electrothermal approach reported in 1888.[104] However, new and improved synthesis methods have been developed for other EPMs such as black-P, red-P, fibrous-P, and violet-P. These methods have enabled the synthesis of high-quality 3D bulk crystals as well as low-dimensional (0D, 1D, and 2D) nanostructures. Bulk crystals of blue-P have not yet been synthesized, but 2D blue phosphorene has been prepared. Additionally, recent reports have described the synthesis of new nanostructured EPMs. The varying dimensional material structures that have been demonstrated for each of the phosphorus allotropes are summarized in Fig. 13. This section critically discusses the synthesis of EPMs and their nanostructures. The advantages and disadvantages of different synthetic routes are discussed and characterization of the corresponding products is described.

4.1 Synthesis of black phosphorus

4.1.1 Black phosphorus in the bulk form. The traditional methods for synthesizing black-P bulk crystals often require high pressure to facilitate phase transition. As mentioned in Section 2, the high-pressure synthetic method for black-P was first established by Percy Williams Bridgeman,[39] who attempted to convert white-P into a new crystal phase using a high-pressure apparatus with a pressure greater than 1 GPa and at a temperature of 200 °C. However, for safety reasons, the method was later refined by using a more stable red-P as the precursor and a belt-type apparatus.[204] Nevertheless, these methods result in incomplete phase transitions at relatively low temperature, and only produce

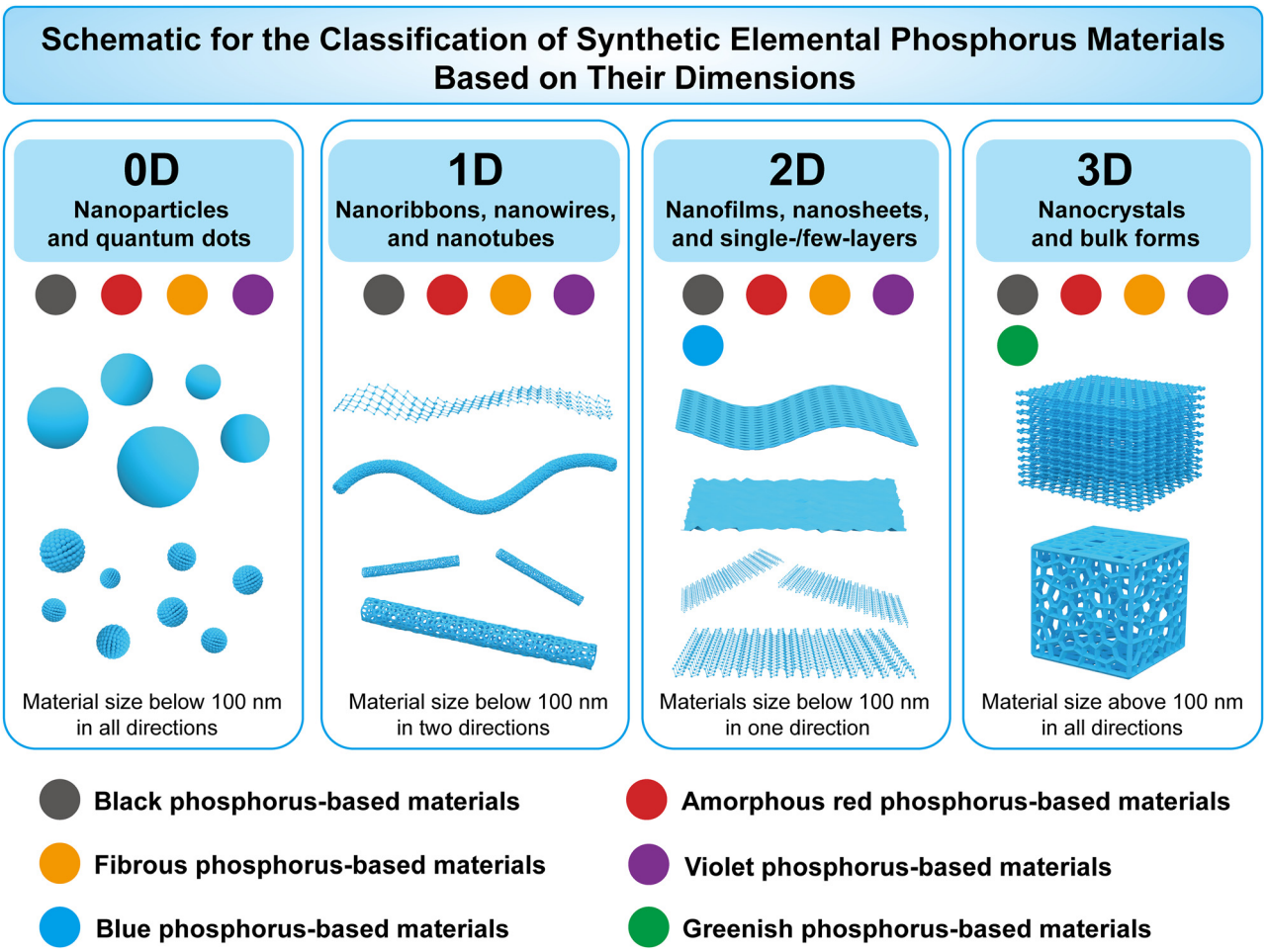

Fig. 13 Schematic diagram showing classification of synthetic elemental phosphorus materials based on the dimensions and structural examples for each dimension. Elemental phosphorus materials (EPMs) are classified into three categories: zero-dimensional (0D) EPMs (nanoparticles and quantum dots), one-dimensional (1D) EPMs (nanoribbons, nanowires, and nanotubes), two-dimensional (2D) EPMs (nanofilms, nanosheets, and single-/few-layers), and three-dimensional (3D) EPMs (nanocrystals and bulk forms). Each coloured circle within the EPM structural box is indicative of different phosphorus allotropes reported with corresponding dimensional structures in the literature. It should be noted that the EPM nanotubes have not been experimentally synthesized so far, but the synthesis of black or blue phosphorus nanotubes is theoretically feasible.

small and low-quality crystals, making it challenging to separate them from impurities. The development of wedge-type and multianvil-type apparatus has made a great contribution to the production of large-scale and high-quality black-P crystals. In 1981, Shirotani *et al.* made a breakthrough in the high-pressure synthesis of black-P crystals, achieving successful growth of black-P single crystals.[41] Using a cubic anvil apparatus, they obtained crystals up to $4 \times 2 \times 0.2$ mm^3 from red-P at a temperature of 270 °C and a pressure of 3.8 GPa. Despite these advances, the potential safety issues of the high-pressure process remain, prompting researchers to seek milder methods for synthesizing black-P bulk crystals.

To address the requirement for high-pressure conditions in black-P crystal production, mercury flux or bismuth flux was introduced as supplementary catalysts.[205–207] In 1955, Krebs and his colleagues reported that under high-temperature conditions (370–410 °C), addition of 30 to 40 atomic percent of mercury would initiate the transition of white-P into black-P.[205] The reaction was found to take a few days to complete, yielding Black-P crystals as the final product. However, the use of mercury or bismuth as catalysts is associated with several drawbacks, including mercury contamination, bismuth toxicity, prolonged reaction times, and limited yield, making the mercury or bismuth flux method far from ideal. Despite the limitations, this method of introducing additional catalysts seems to provide insights into the later-developed chemical vapor transport (CVT) method, which efficiently produces black-P crystals at moderate temperature and pressure through the addition of transfer agents. CVT refers to a chemical reaction that transforms a condensed phase into a gaseous phase in the presence of a transfer agent, followed by deposition elsewhere and eventual formation of a crystalline structure.[208] In 2007, Nilges and colleagues introduced a pioneering CVT-based approach for the preparation of black-P crystals at low pressure in evacuated silica ampules.[42] By heating red-P with a mixture of Au, Sn, and SnI_4 as transport agents, they were able to produce black-P crystals, where a sample batch was grown on the surface of the Au_3SnP_7/AuSn materials (Fig. 14a). One year later, this research

group improved the previous reaction system by using the AuSn alloy instead of Au and Sn metals.[43] This change, along with the optimal temperature program, reduced the crystal growth time to 32.5 hours and increased the crystal size to 1.5 cm in diameter. However, the cost of synthesis remained high due to the use of noble metals. In 2014, they further refined the synthetic procedure by eliminating expensive Au and substituting it with Sn/SnI_4 as transfer agents, which significantly reduced costs and the number of impurities.[44] Building on these advances, Nilges *et al.* recently utilized DFT calculations to probe the formation mechanism of black phosphorus and phosphorene.[209] They discovered that the gaseous species P_4 and SnI_2 play a crucial role in the gas-phase growth of black phosphorus and phosphorene, with SnI_2 directly inserting into the P–P bonds of P_4. This work not only contributes to the optimization of the gas-phase growth system for black-P crystals but also aids in understanding the principles of epitaxial growth of phosphorene on substrates, which will be discussed further below.

In contrast to Nilges' CVT growth approach,[42,43] which requires a temperature gradient for long-distance transport (LDT), Liu's group have devised an efficient short-distance transport (SDT) growth method that utilizes a uniform temperature.[210] As shown in Fig. 14c and d, a substantial number of black-P crystals formed during the SDT process, with 98% of red-P being converted to black-P, while only a limited number of black-P crystals formed during the LDT process. The comparison of the yield and purity of black-P synthesized by different methods including high-pressure high temperature (HPHT) methods, sonochemistry, flux methods, and CVT methods is shown in Fig. 14b, and the results indicate that this work has achieved the highest yield and purity of black-P crystals among the compared methods. Two key factors for obtaining high black-P production yields are the short-distance transport and uniform temperature.[210] As the temperature in the quartz ampoule rises, the reactants (red-P, Sn, and SnI_4) start vaporizing and fill the ampoule. This results in a reaction between gaseous phosphorus and Sn and SnI_4 gases, forming P–Sn–I complexes that accumulate at the bottom of the ampoule. These complexes act as nucleation sites for further crystal growth. The transport agent aids in the crystallization and growth of black-P during the gradual cooling process until all the gaseous phosphorus is transformed into black-P crystals. However, the Sn/SnI_4/red-P reaction system still faces several challenges, such as the time-consuming synthesis of SnI_4 and the requirement for precise temperature control. The amount of red-P loading, ampoule capacity, and Sn/SnI_4 proportion all play crucial roles in the synthesis of black-P crystals. Scaling up the production of black-P necessitates appropriate modification of the experimental conditions, as excessive red-P loading can cause ampoule breakage, while inadequate loading results in the production of only white-P or violet-P.[93] In addition, this method can introduce iodine- or tin-doped impurities during the crystallization process of black-P. However, the ability to dope black-P allows for the alteration of properties, thereby offering potential to broaden the range of applications.

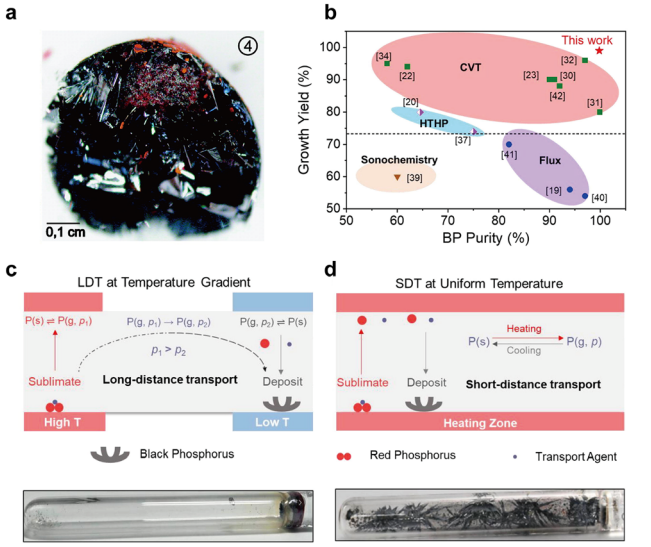

Fig. 14 CVT-based methods for black-P bulk crystal preparation. (a) Photographs of the obtained black-P crystals. Reproduced with permission from ref. 42. Copyright 2007 American Chemical Society. (b) A comparison of the yield and purity of black-P synthesized by different methods, including high-pressure high temperature (HPHT) methods, sonochemistry, flux methods, and CVT methods. (c) Schemes of the LDT method and (d) SDT method to grow black-P crystals and their corresponding photographs of the resulting products. Reproduced with permission from ref. 210. Copyright 2020 Elsevier.

4.1.2 Black phosphorene

Top–down methods. Inspired by the successful mechanical exfoliation of graphene, few- and single-layered black phosphorene was first prepared by a micro-mechanical cleavage method in 2014.[45,46] When the Scotch tape is repeatedly detached from bulk crystals, single-layered phosphorene with a thickness of ~0.85 nm can be obtained and transferred onto a Si/SiO_2 substrate.[46] Although this method can produce controllable layers of black phosphorene by recycling the detaching process at different times, adhesive contamination and low yields must to be addressed. A modified mechanical exfoliation method has been developed to improve the yield of atomically thin black-P flakes.[211] In this method, the commercially available black-P bulk crystals are repeatedly exfoliated using blue Nitto tape and the thinnest region of the flake has a thickness of 1.6 nm equivalent to three layers of black phosphorene. The use of sticky tape coupled with a viscoelastic polydimethylsiloxane substrate increases the yield of the products and reduces contamination.

Dry and wet ball milling methods are commonly used mechanical techniques to grind bulk black-P powders into few-layered phosphorene.[212] Zhu *et al.* have developed a solid-state ball milling method to prepare ultrathin black-P nanosheets (Fig. 15a).[213] They mixed 300 mg of black-P powder with 700 mg of anhydrous LiOH powder in a vessel brimming with an Ar atmosphere and ball milled for 24 hours,[213] resulting in the formation of black-P nanosheets with lateral sizes ranging from 30–60 nm and a thickness of ~0.7–6 nm. Addition of LiOH plays a crucial role in the ball milling process by functionalizing the nanosheet edges with hydroxyl groups, which improves the stability of nanosheets. Without LiOH, the exfoliated black-P

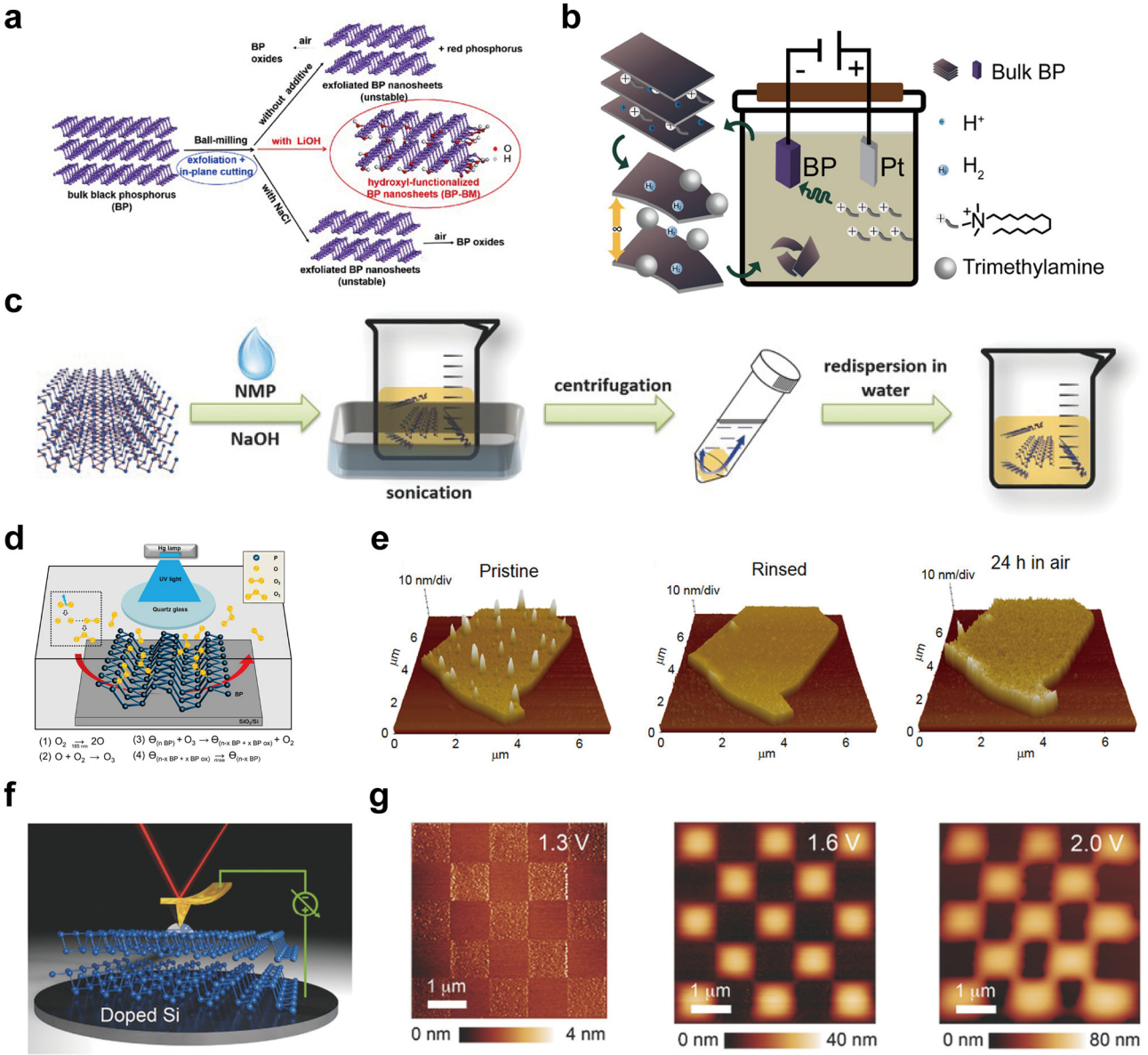

Fig. 15 Typical top–down methods for the black phosphorene preparation. (a) Scheme of solid-state ball milling process of black-P with or without additives. Reproduced with permission from ref. 213. Copyright 2017 John Wiley and Sons. (b) Scheme of cathode exfoliation of few-layered black-P. Reproduced with permission from ref. 234. Copyright 2019 American Chemical Society. (c) Scheme of basic NMP exfoliation of black phosphorene. Reproduced with permission from ref. 218. Copyright 2015 John Wiley and Sons. (d) Scheme of the ozone etching method for black phosphorene preparation. (e) 3D AFM height images of black-P flakes before and after rinsing with water. Reproduced with permission from ref. 240. Copyright 2016 American Chemical Society. (f) Scheme of CAFM patterning setup for black-P. (g) Tapping-mode AFM images of checkerboard patterns created under various sample biases. Reproduced with permission from ref. 241. Copyright 2016 John Wiley and Sons.

nanosheets exhibit instability, and some of them are converted into red-P. Liu *et al.* have used wet ball milling to prepare a few-layered black-P and evaluated the impact of different organic solvents.[214] Dimethylformamide (DMF), *N*-methyl-2-pyrrolidone (NMP), and dimethyl sulfoxide (DMSO) are more effective solvents than absolute ethanol (AE) and ethylene glycol (EG), with DMSO being the optimal solvent for 3–5 layers of black-P. However, ball milling requires extended processing to achieve high yield, and the irregular movement of hard balls induces high stress that leads to the fragmentation of bulk crystals into nanosheets with reduced lateral dimensions. To tackle these challenges, Liu's group introduced glue-assisted grinding for exfoliating large-size 2D materials and obtained hexagonal boron nitride nanosheets with an average lateral size of 2.18 μm.[215] Similar methods are expected to be developed for the production of large-size black phosphorene.

Liquid-phase exfoliation is another widely used method to produce black phosphorene, with NMP being the first solvent used for this purpose.[200] The process involves immersing bulk black-P into NMP (5 mg mL^{-1}) and exfoliating it in an

ultrasonic bath (820 W, 37 kHz) for 24 hours. The resulting phosphorene nanosheets had dimensions of *ca.* 200 × 200 nm and a thickness of 3.5–5 nm. To date, NMP has been the most widely utilized solvent for black-P exfoliation, with the size of the resulting black phosphorene nanosheets ranging from 0.6 to 60 nm depending on the time (from 1.5 to 24 hours) and power (from 200 to 820 W) of ultrasonication.[216] In NMP exfoliation, the functional groups work as ''scissors'', cleaving bulk black-P into phosphorene through sharing of electron pairs from the exposed phosphorus atoms and oxygen from NMP.[217] The surface tension of NMP is comparable to that of black phosphorene, which effectively disperses the exfoliated nanosheets and prevents restacking and aggregation. However, pure NMP exfoliation leads to surface contamination with NMP and instability of phosphorene in water. To address this, our group has developed a basic-NMP solvent process, in which bulk black-P is added to a NaOH-saturated NMP solution to perform liquid exfoliation (Fig. 15c). The resulting phosphorene exhibits improved water stability and controllable size and number of layers.[218] Addition of OH^- to the solution adsorbed on the surface of phosphorene makes it negatively charged (−30.9 mV) and further increases the stability in water. Other polarized solvents have been also used to synthesize black phosphorene, including DMF, DMSO, isopropyl alcohol (IPA), *N*-cyclohexyl-2-pyrrolidone (CHP), bis(2-methoxyethyl) ether (DIGLYM), acetonitrile (AN), distilled water, tetrahydrofuran, ethanol, benzonitrile, acetone, chloroform, and hexane.[219–230] Liquid-phase exfoliation is more scalable than mechanical exfoliation for the preparation of black phosphorene. However, Young's modulus of phosphorene is smaller compared to other 2D materials, and strong ultrasonic treatment results in nanosheets that are smaller than a few hundred nanometers.[231] Long-term sonication can also lead to fragile crystallinity and irreversible surface damage. Therefore, it is important to develop a large-scale method for the liquid synthesis of high-quality black phosphorene.

Electrochemical exfoliation is considered to a more efficient and controllable method that allows for the production of black phosphorene with precise control over the size and thickness by applying different voltages for different time. This method can be divided into anode and cathode exfoliation, depending on the location of the exfoliating materials. In 2015, Erande and colleagues were the first to use anode exfoliation to produce black phosphorene.[232] After applying a positive bias voltage of +7 V and a current of ∼0.2 A to the working electrode for 50 minutes,[232] black phosphorene displayed a nanosheet-like characteristic with lateral dimensions ranging from 5 to 10 μm and a thickness of around 1.4 nm. Different from anode exfoliation, cathode exfoliation does not involve the generation of oxygen-containing free radicals, leading to the formation of phosphorene products with no visible surface defects or oxidative damage.[233] Cationic surfactant hexadecyltrimethylammonium chloride (CTAC) can be used as an intercalating agent to exfoliate bulk black-P in water at a cathodic potential (Fig. 15b), resulting in the formation of few-layered black-P flakes within 20 seconds.[234] Delamination of bulk black-P is primarily driven by intercalation of large-sized hexadecyltrimethylammonium cations (CTA^+) into the interlayer of black-P, which then decompose into gaseous bubbles at a negative potential, further improving the cathodic exfoliation of black-P.[235,236] The interface-assisted strategy is useful for the synthesis of 2D materials.[237] Our group has developed a cathodic electrochemical exfoliation method which uses the plasma–liquid interface to facilitate the transfer of active species and initiate chemical reactions in solution.[238] This method allows for mass production of few-layered black phosphorene in pure *N*,*N*-dimethylformamide (DMF) without any intercalating agents. The entire exfoliation process can be completed in merely five minutes with a yield of ∼63%. During exfoliation, the plasma and DMF molecules interact strongly to form a series of cationic species. These species are drawn towards the cathode black-P crystals under the action of electric field and intercalated into the interlayer. Afterwards, these cationic species decompose into gaseous bubbles, causing the black-P crystals to expand and the phosphorene nanosheets to separate. The plasma–liquid exfoliation system has the advantage of being easily scalable and cost-effective, making it a viable option for commercial production of black phosphorene.

Plasma etching is an alternative strategy for preparing large-size black phosphorene. Lu *et al.* have reported a combination approach of mechanical cleavage and Ar^+ plasma treatment to produce stable monolayer phosphorene.[239] Subsequently, ozone etching has been used to prepare black phosphorene for efficient and precise control over the thickness of Black-P flakes (Fig. 15d).[240] By adjusting the flow velocity of O_2 in the reactor vessel, an average etching rate of 12 ± 2 nm h^{-1} or 0.40 ± 0.07 layer min^{-1} can be achieved, allowing for near-monolayer control.[240] However, ozone molecules generated by O_2 photolysis partially oxidize black-P, necessitating an additional step of oxide removal to obtain pristine black phosphorene. This can be accomplished by rinsing with deionized water and then blow-drying with N_2. This clean-up procedure also results in phosphorene with good resistance to ambient oxidation (Fig. 15e). However, plasma etching operates on a large scale, and laser oxidation is spatially constrained by optical diffraction, resulting in either the unavailability or significant difficulty in achieving nanoscale thinning and patterning.[241] Scanning probe nanolithography is well known for its high spatial resolution, which makes it a potential solution to overcome the limitations of plasma etching and laser oxidation.[242] Liu *et al.* have used conductive force microscopy (CAFM) to accomplish lateral nanopatterning and layer-by-layer thinning of black-P (Fig. 15f), and the checkerboard pattern is produced on a newly exfoliated black-P crystal.[241] The height of the pattern protrusions increases in proportion to the applied bias voltage during contact-mode CAFM scanning (Fig. 15g). However, inevitable oxidation of black-P during the process as well as the high cost of CAFM probe consumption limit the widespread use of this technology.

Bottom–up methods. Chemical vapor deposition (CVD) is a commonly used bottom–up method to synthesize high-quality thin films of 2D materials. This requires volatile precursors in controlled reactions or decomposition onto the substrate

surface under specific atmospheres, temperatures, and pressures.[243] Smith *et al.* have demonstrated an *in situ* CVD method for growing black-P films on a silicon substrate.[244] Initially, an amorphous red-P film is vapor-deposited onto the substrate, which is then heated in the presence of an Sn/SnI_4 (10 mg) mineralizer under an Ar atmosphere and high pressure (27.2 atm).[244] This process results in the direct growth of black-P films with varying thicknesses on the silicon substrate. Nevertheless, this method may encounter uncontrolled nucleation and incomplete conversion issues throughout the growth process. To achieve effective nucleation and spatial control, Zhang's group have utilized polyphosphide Au_3SnP_7 as nucleation seeds to grow large-area black-P thin films on silicon substrates (Fig. 16a).[245] Au_3SnP_7 is a suitable nucleation seed for black-P epitaxial growth because its lattice plane (010) matches the (100) plane of black-P. The process involves three stages: precursor evaporation, Au_3SnP_7 formation, and black-P nucleation and growth. The process begins by depositing a gold film on the silicon substrate and heating it with precursors (Red-P, Sn, and SnI_4) to 750 °C for 1 hour in an evacuated quartz tube, where red-P evaporates and transforms into P_4 molecules, and SnI_4 decomposes into Sn and I_2. The temperature is then lowered to 500 °C, leading to the formation of dispersed Au_3SnP_7 (Fig. 16b) on the silicon substrate through a series of chemical reactions between excessive red-P, Sn, and gold films. Due to lattice plane matching, vaporous P_4 molecules are continuously deposited on the surface of Au_3SnP_7, completing the nucleation of black-P (Fig. 16c). As the temperature decreases, P_4 molecules fully transform into black-P, and small black-P nanosheets spatially grow over the nucleation center (Fig. 16d), expanding and fusing to ultimately form a large-area black-P thin film with a lateral size of over 200 μm and a thickness of ~150 nm (Fig. 16e). The resulting black-P films have a flawless orthogonally symmetrical structure with high crystallinity and purity, as well as an exceptional field effect and Hall mobility of over 1200 $cm^2 V^{-1} s^{-1}$ and 1400 $cm^2 V^{-1} s^{-1}$ at room temperature, respectively.[245] Researchers have addressed the nucleation challenge of black-P films on substrates. However, controlling the lateral growth of these films is difficult due to the complexities in managing the vapor pressure of P_4 molecules, leading to limited domain sizes of only a few hundred nanometers. To resolve this issue, the group has recently implemented a sustained feedstock release strategy for synthesizing single-crystal black-P thin films, focusing on promoting the lateral growth mode at low nucleation rates.[246]

Under quasi-static equilibrium conditions and a continuous, stable P_4 supply, individual domains progressively expand into millimeter-sized single-crystal black-P films. Subsequently, these films merge to form centimeter-sized, continuous black-P films, covering nearly the entire Si/SiO_2 substrate. The as-grown black-P single-crystal film exhibits outstanding single crystallinity, as evidenced by the full-width at half-maximum of the (040) reflection rocking curve, measured at ~0.08° using high-resolution XRD.[246] Furthermore, the film has a remarkable carrier mobility of around 6500 $cm^2 V^{-1} s^{-1}$ at low temperature. This study marks the first observation of Shubnikov-de Haas oscillations in directly grown black-P films.

Pulsed laser deposition (PLD) is an approach that involves a laser to irradiate the target to deposit materials onto a substrate, resulting in the formation of a thin film or multilayer structure.[247] By employing a pulsed laser, large black-P clusters can be formed within the transported physical vapor, which reduces the formation energy and allows for the growth of centimeter-scale black-P thin films.[248,249] Yang *et al.* have used the PLD approach to fabricate wafer-scale black-P films with controllable thicknesses ranging from 2 to 10 nm.[250] During the synthesis process, the substrate temperature is held at 150 °C. A KrF pulsed laser operating at a repetition rate of 5 Hz is used to irradiate the black-P bulk crystals. To achieve uniform film growth, both the black-P crystals and substrate are continuously rotated. However, structural characterization reveals that the as-synthesized black-P films are highly disordered and have an amorphous nature. By utilizing a black-P single crystal as the target source, Wu *et al.* have developed a controlled PLD method to grow centimeter-scale black-P ultra-thin films on mica substrates, as demonstrated in Fig. 16f.[249] The resulting black-P films are firmly deposited onto the 1 cm^2 mica surfaces and the thickness can be accurately modulated by varying the number of laser pulses (Fig. 16g). Throughout the growth process, the vaporous black-P clusters generated by laser irradiation are uniformly dispersed over the homogenous mica surface, facilitating the thermodynamically-driven unidirectional growth and intermingling of small black-P nanosheets to form a large-area film. As observed by high-resolution TEM, the as-grown black-P film exhibits high ordering of phosphorus atoms with no apparent crystal defects (Fig. 16h). The lattice constants in the zigzag and armchair directions were measured to be 3.30 and 4.55 Å, respectively, indicating an orthorhombic phase for the black-P film (Fig. 16i). The selected-area electron diffraction (SAED) pattern confirms the presence of a typical orthorhombic lattice of black-P with the homologous fourfold symmetry (Fig. 16j). This work addresses three critical challenges that have impeded the production of high-quality black-P thin films by deposition-based methods. First, traditional deposition methods often yield black-P films that are relatively thick (>10 nm), suggesting that the resulting black-P has bulk crystal properties rather than the desired two-dimensional features. This work, however, successfully produces few-layered black-P films with a thickness of ~1.1 nm for the bilayer. Second, earlier attempts in growing black-P films resulted in films with limited crystallinity, whereas the lattice structure of the black-P films grown in this work is highly ordered and devoid of significant crystal defects. Third, this work extends the lateral area of high-quality black-P films to the centimeter scale, facilitating the manufacture of wafer-scale optoelectronic and electrical devices based on black-P.

Wet chemical synthesis is an effective bottom–up approach known for its ease of use, versatility, high yield, and remarkable reproducibility.[251] Some studies have claimed successful synthesis of black-P nanosheets by this method.[252–254] However, the wet chemical method for synthesizing black-P nanosheets often encounters challenges of partial oxidation and poly-phosphorous phase complexes. XRD analysis of the resulting structures commonly

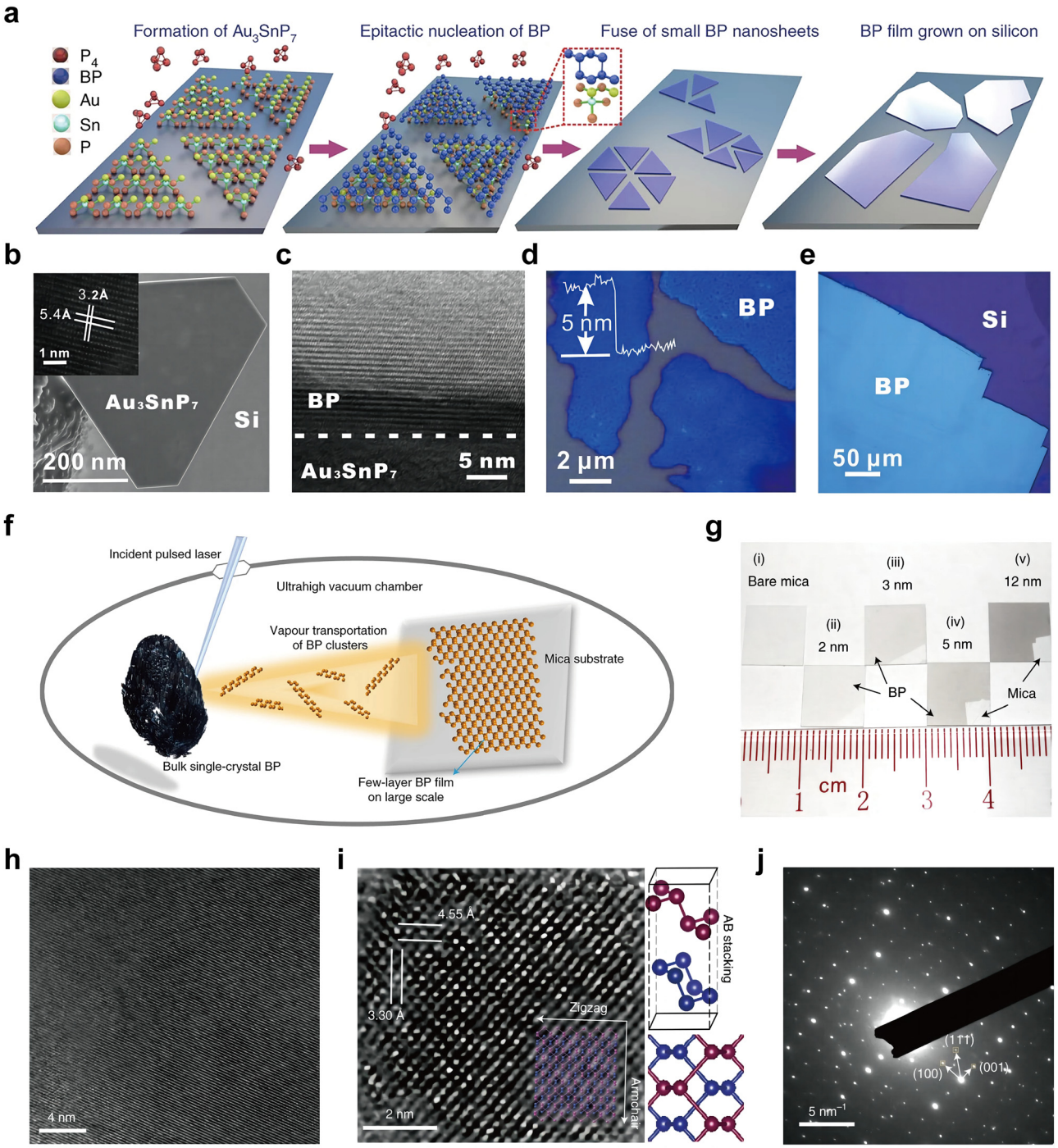

Fig. 16 Typical bottom–up methods for black-P film preparation. (a) Scheme of epitaxial nucleation and lateral growth process of black-P films. (b) SEM image of Au_3SnP_7 grown on a silicon substrate. The inset shows the lattice structure of Au_3SnP_7. (c) Cross-sectional HRTEM image of a layered black-P nanosheet grown on Au_3SnP_7. (d) Optical image of the fusion of small black-P nanosheets to form a large-area film. (e) Optical image of a black-P film grown on a silicon substrate with a lateral size over 200 μm. Reproduced with permission from ref. 245. Copyright 2020 Nature Publishing Group. (f) Scheme of a controlled PLD method for few-layered black-P film growth. (g) Photographs of bare mica and as-synthesized centimetre-scale black-P films of different thicknesses. (h) Plan-view HRTEM image of a few-layered black-P film. (i) Detailed HRTEM image of the lattice structure of black-P films. (j) The corresponding SAED pattern of black-P films. Reproduced with permission from ref. 249. Copyright 2021 Nature Publishing Group.

reveals broad peaks with amorphous features, indicating the presence of impurities. Consequently, the synthesized nanosheets cannot be considered strictly crystalline black-P. To the best of our knowledge, currently there is a lack of definitive XRD and TEM characterization results demonstrating the efficacy of wet chemical synthesis in producing crystalline black-P nanosheets.

4.1.3 Black phosphorus nanoribbons. Shaping materials into one-dimensional nanoribbons subjects two of their dimensions to

quantum confinement effects to bring forth novel phenomena and applications. Black phosphorene is an unusual anisotropic two-dimensional material that exhibits exceptional anisotropic properties in thermal conductivity and carrier transport.[166] Top–down or bottom–up synthesis often produces black phosphorene with narrow and uniform widths.[255] To explore the exotic properties of black phosphorene in particular orientations, precise and efficient separation of black-P nanoribbons with specific chirality is crucial. However, synthesizing black-P nanoribbons is a challenging task, as many methods developed to produce graphene nanoribbons are not directly applicable to black-P nanoribbons due to their intrinsic chemical reactivity. Fortunately, researchers have made progress in developing three different types of methods for synthesizing black-P nanoribbons, namely nano-etching, liquid-based exfoliation, and CVT.

Nano-etching of black-P nanoribbons is achieved by electron beam lithography, reactive ion etching, and scanning TEM nano-sculpting techniques. In 2015, Lee *et al.* reported the successful fabrication of black-P nanoribbons with desired width and length through the use of electron beam lithography and reactive ion etching.[176] The process involved placing an exfoliated black-P flake on a SiO_2 substrate, followed by spin-coating PMMA on the flake for electron beam lithography in either the armchair or zigzag direction. Reactive ion etching (90% SF_6 and 10% O_2) was then used to eliminate the exposed black-P stripes, and PMMA protective stripes were removed with acetone to obtain black-P nanoribbons (Fig. 17a). However, the produced nanoribbons had a thickness of $\sim$50 nm and width within the range of 500 nm, resulting in their electronic properties being similar to those of black-P in its bulk form. To produce atomic-thick black-P nanoribbons, a scanning TEM nano-sculpting technique has been reported to synthesize sub-10 nm wide black-P nanoribbons composed of a few layers.[256] However, this method has low throughput, making it challenging to produce black-P nanoribbons in large quantities. Feng *et al.* have utilized reactive ion etching to prepare anisotropic black-P nanoribbon field-effect transistors (Fig. 17b).[257] This process allows for precise positioning of the nanoribbon and control of its width ($\sim$60 nm) and height ($\sim$3 nm) (Fig. 17c). However, the reliance on exfoliated black-P flakes and need for crystallographic alignment still limit the potential of this etching technique in practice.

In 2019, Watts and colleagues introduced a novel approach for synthesizing high-quality black-P nanoribbons on a large scale.[258] Their method relied on the combination of lithium intercalation and liquid exfoliation and involved two steps.

Black-P bulk crystals are first immersed in an aprotic lithium-ion solution at -50 °C for 24 hours, resulting in the intercalation of lithium into black-P. After ammonia is removed, the intercalated black-P is transferred to a glovebox and added to a vial containing NMP. The resulting mixture is sonicated for 1 hour and then centrifuged at a low speed to obtain a black-P nanoribbon solution (Fig. 17d). These nanoribbons exhibit a predominantly monolayer thickness, widths ranging from 4–50 nm, lengths up to 75 μm, and aspect ratios of up to 1000 (Fig. 17e and f). The nanoribbons are highly ordered and align well along the zigzag crystallographic orientation (Fig. 17g and h). The responsible mechanism for the formation of black-P nanoribbons involves the difference in diffusion kinetics between the armchair and zigzag directions.[259,260] Specifically, the preferred diffusion of alkaline metal ions in the zigzag direction creates a strain between intercalated and non-intercalated regions. This strain eventually leads to the breakage of the longer armchair P–P bonds, resulting in the formation of stripes oriented in the zigzag direction. Using this method, McDonald *et al.* synthesized black-P nanoribbons and utilized the nanoribbons in photovoltaic devices.[261] A recent report demonstrated an alternative method for the synthesis of black-P nanoribbons, utilizing an electrochemical-based sodium intercalation process. The resulting nanoribbons have a constrained width of 10.3 ± 3.8 nm and a length of 250 ± 156 nm. The width of the nanoribbons obtained by this method is narrower compared to that of the nanoribbons prepared by Watts *et al.*[258] Furthermore, this electrochemical-based method eliminates the requirement for cryogenic conditions (-50 °C), making it more cost-effective and readily scalable for the synthesis of black-P nanoribbons. Other electrochemical-based exfoliation approaches have also been developed to synthesize black-P nanoribbons. For example, Liu *et al.*[262] have synthesized zigzag-phosphorene nanobelts by an electrochemical method with oxygen-driven BF_4^- intercalations. Yu *et al.*[263] have optimized the electrochemical exfoliation conditions and employed two different types of quaternary ammonium salt cations (TPA and THA) as intercalating agents in the preparation of zigzag black-P nanoribbons with a yield of over 80%.

The bottom–up CVT method has been recently reported as an alternative to the top–down synthesis methods to produce black-P nanoribbons. Wang's group developed a one-step CVT method for the synthesis of black-P nanoribbons under mild conditions.[264] The process involves heating commercial red-P with iodine precursors at a rate of 2 K min^{-1} in a sealed quartz ampoule to 873 K. The temperature is maintained for 2 hours, followed by cooling to 738 K after 490 minutes and keeping for another 2 hours before natural cooling to room temperature. Ultimately, the black-P nanoribbons are grown at the bottom of the ampoule. The nanoribbons are several tens of microns in length, $\sim$400 nm in width, and $\sim$20 nm in thickness. Macewicz *et al.* optimized the CVT synthesis method of producing black-P nanoribbons and introduced a two-step process involving CVT growth of black-P columns, followed by ultrasonic treatment and centrifugation.[265] The process is initiated by placing red-P, Sn, and SnI_4 precursors at one end of a vacuum quartz ampoule with the silicon substrate being positioned on the other end (Fig. 17i). To maintain the CVT process, a temperature gradient of 50 °C is maintained between the precursor and silicon substrate during heating (Fig. 17j). After the reaction, a uniform layer of columnar black-P is formed on the substrate surface. The columnar black-P is then transferred to a beaker containing DMF and sonicated for 10 minutes (Fig. 17k), after which black-P nanoribbons are collected by centrifugation. The black-P nanoribbons have an aspect ratio in the range of a few hundred with the majority of the columns having a width of up to 1.5 μm and length of more than 500 μm.

Overall, nano-etching is capable of producing black-P nanoribbons with different crystallographic orientations, but achieving

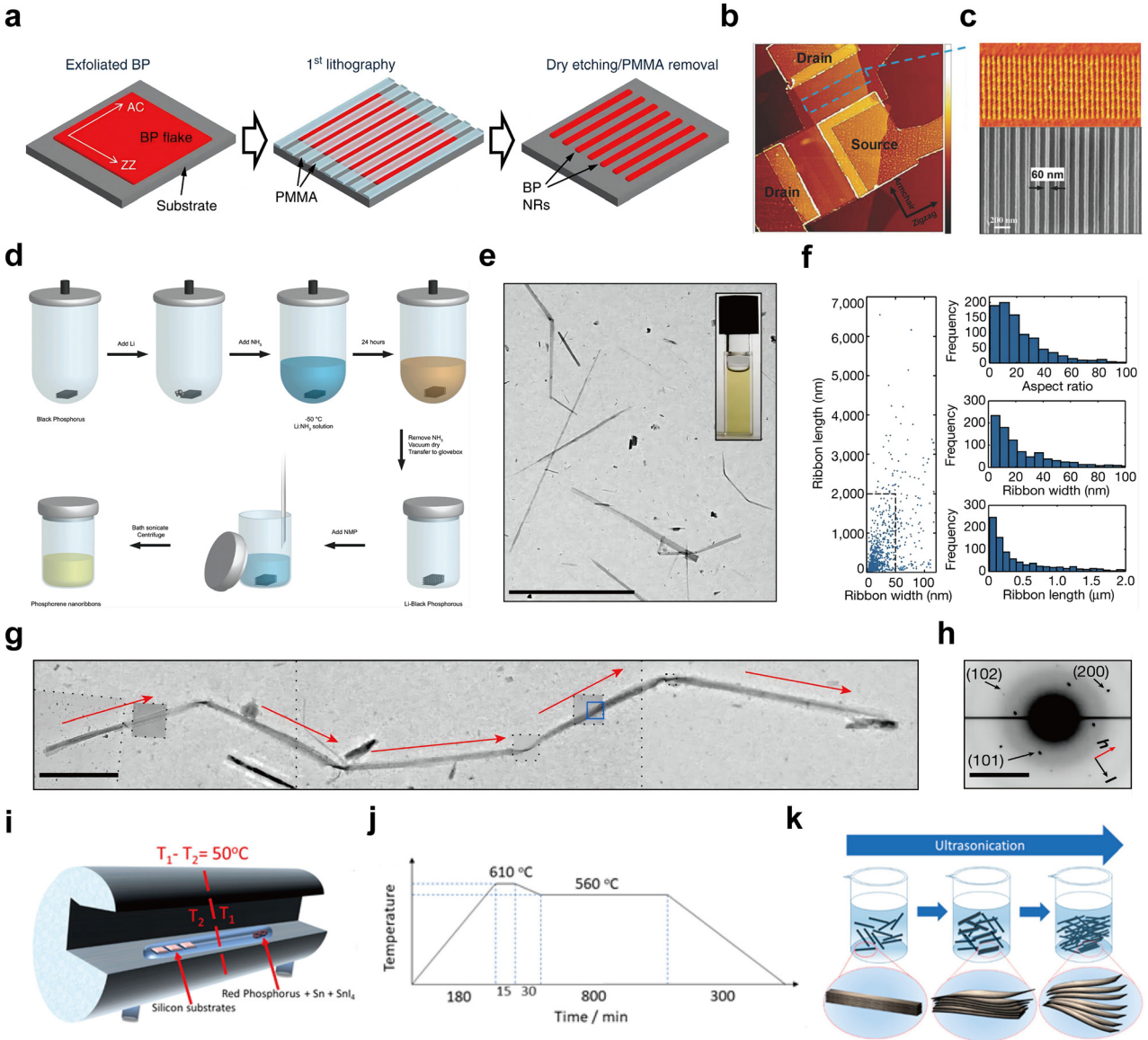

Fig. 17 Synthesis and characterization of black-P nanoribbons. (a) Scheme of electron beam lithography and reactive ion etching process of black-P nanoribbons. Reproduced with permission from ref. 176. Copyright 2015 Nature Publishing Group. (b) AFM image of the black-P nanoribbon field-effect transistor along the armchair and zigzag directions. (c) An enlarged AFM image of the nanoribbons (top) and SEM image showing the nanoribbon width of 60 nm (bottom). Reproduced with permission from ref. 257. Copyright 2018 John Wiley and Sons. (d) Schematic diagram of phosphorene nanoribbon production by lithium intercalation and liquid exfoliation. (e) TEM image of phosphorene nanoribbons drop-cast from the liquid dispersion shown in the inset. Scale bar is 10 μm. (f) Scatter diagram depicting the relationship between the widths and lengths of 940 phosphorene nanoribbons (left); aspect ratios (top right), widths (middle right), and lengths (bottom right) of only those nanoribbons falling within a dashed rectangle located in the scatter diagram. (g) A combined TEM image of a phosphorene nanoribbon with an approximate length of 11 μm. The crystallographic direction in the zigzag direction, identified by SAED, is indicated by the use of red arrows. The scale bar is 1 μm. (h) SAED pattern corresponding to the blue box shown in (g). The scale bar is 5 nm^{-1}. Reproduced with permission from ref. 258. Copyright 2019 Nature Publishing Group. (i) Scheme of CVT-growth of black-P columns. (j) Temperature profile of the CVT heating process. (k) Scheme of nanoribbon formation through ultrasonic treatment. Reproduced with permission from ref. 265. Copyright 2021 American Chemical Society.

precise control over the thickness and width at the atomic level remains challenging. Liquid-based exfoliation methods, including ion intercalation and electrochemical exfoliation, can lead to the fabrication of high-quality black-P nanoribbons on a large scale, but the nanoribbons obtained are predominantly oriented along the zigzag direction. CVT synthesis offers a relatively straightforward experimental procedure, but effectively separating the nanoribbons from impurities during crystal growth is an obstacle. It is anticipated that further improvement of existing methods or emergence of new ones will hasten the incorporation of black-P nanoribbons into real-world applications.

4.1.4 Black phosphorus quantum dots. Ultra-small quantum dots (QDs) have three dimensions on the nanometer scale and possess distinctive electronic and optical properties as a

result of high quantum confinement and edge effects.[266] In 2015, Zhang's group reported ultrasonic exfoliation for preparing black phosphorus quantum dots (BPQDs).[267] In the standard synthetic procedure, 5 mg of black-P crystal powder is ground with 1 mL of NMP solvent for 20 minutes. The mixture is placed into a glass vial with 3 mL of NMP and sonicated in an ice bath at 200 W for 3 hours. Subsequently, the product is separated from the reactants by centrifugation. The as-synthesized BPQDs display a stable dispersion in NMP and their lateral size and thickness are determined to be 4.9 ± 1.6 nm and 1.9 ± 0.9 nm, respectively. However, ultrasmall BPQDs exhibit partial oxidation as evidenced by the presence of an O signal in XPS. This can be attributed to the air instability of black-P, particularly in the case of quantum dots.[268] Our group has also developed a two-step sonication method to prepare a water-stable suspension of BPQDs with an average lateral size of ~2.6 nm and a thickness of ~1.5 nm (Fig. 18a–c).[269] The process begins with probe sonication of black-P crystal powders in an NMP solution to obtain black-P nanosheets. The nanosheets are then exfoliated into BPQDs through ice-bath sonication and transferred to a water solution for further PEGylation. The combination of probe and ice-bath sonication significantly increases the product yield, while using only one of them results in the formation of uneven black-P nanosheets. This work resulted in the successful synthesis PEG-modified BPQDs with improved stability for the BPQDs in physiological environments (Fig. 18d), including phosphate-buffered saline (PBS) and cell culture media. This makes them highly promising in biomedical applications.[15,270–272] In addition to NMP, several organic solvents have been utilized in the preparation of BPQDs, for example, dimethyl-formamide (DMF),[273] isopropanol (IPA),[274] and N-vinyl pyrrolidone (NVP).[275]

Electrochemical exfoliation with bipolar electrodes for the synthesis of BPQDs has been developed. In 2016, Mayorga-Martinez and co-workers devised a simple electrochemical exfoliation-based approach to prepare black-P nanoparticles,

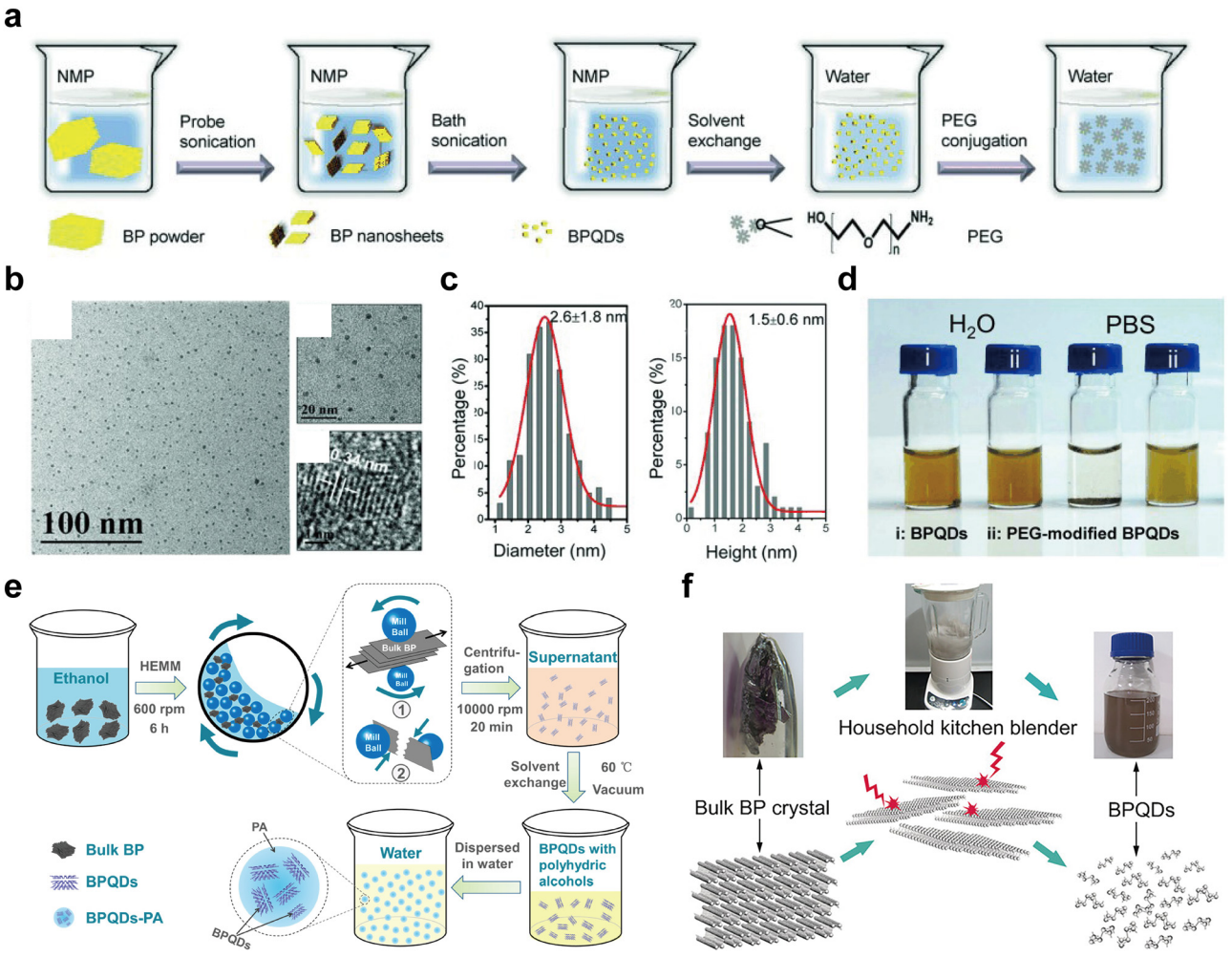

Fig. 18 Synthesis and characterization of black-P quantum dots. (a) Scheme of the two-step sonication method for BPQD preparation and modification. (b) TEM images of BPQDs. (c) Lateral sizes (right) and heights (left) of BPQDs. (d) BPQDs and PEG-modified BPQDs in H_2O and PBS. Reproduced with permission from ref. 269. Copyright 2015 John Wiley and Sons. (e) Scheme of the HEBM process of BPQDs and modification. Reproduced with permission from ref. 278. Copyright 2020 American Chemical Society. (f) Scheme of the synthesis of BPQDs by using a household kitchen blender. Reproduced with permission from ref. 279. Copyright 2016 John Wiley and Sons.

yielding nanoparticles with a size ranging from 40 to 200 nm.[276] Two years later, Tang *et al.* succeeded in preparing fluorinated BPQDs (F-BPQDs) using an electrochemical exfoliation and synchronous fluorination technique.[277] This process involves using black-P bulk crystals as the working electrode in a sealed three-electrode electrochemical system, where 1-ethyl-3-methylimidazolium tetrafluoroborate ([EMIM][BF_4])/acetonitrile (MeCN) serves as the electrolyte.[277] Application of a +8 V voltage against a Ag wire anode initiates a series of chemical reactions in solution, leading to gradual exfoliation of black-P and electrolysis of BF_4^- to generate BF_3 molecules and F^- anions. The resulting BF_3 molecules form donor–acceptor bonds with MeCN, while the F^- anions synchronously exfoliate BPQDs. The as-synthesized BPQDs exhibit robust environmental stability, allowing them to withstand persistent ambient exposure for up to 7 days due to the hindrance of charge transfer from the phosphorus atoms to external oxygen, induced by fluorine adatoms.[277]

Ball milling is a viable choice for the synthesis of BPQDs. Ren *et al.* have developed a liquid-phase high energy ball milling (HEBM) and centrifugal separation process to synthesize brown transparent BPQDs ethanol suspensions, as shown in Fig. 18e.[278] First, the HEBM approach is used to prepare black-P powders from amorphous red-P which are then placed in a sealed stainless ball milling jar containing ethanol and milling balls. The milling procedure is carried out at 600 revolutions per minute for 6 hours. After centrifugation and dispersion, the BPQD solution is mixed with various polyhydric alcohols to enhance the stability in aqueous environments. The as-prepared BPQDs show stable dispersion in ethyl alcohol and ethylene glycol, with an average lateral size of 6.5 ± 3 nm and a thickness of 3.4 ± 2.6 nm. Interestingly, BPQDs can also be fabricated by utilizing a household kitchen blender to generate a high turbulent shear rate for layer-by-layer disassembly (Fig. 18f).[279] Using DMSO as a stabilized solvent, black-P bulk crystals are processed for 40 minutes in a household kitchen blender set to 17 000–21 000 rpm. The high-shear turbulence gradually peels off and disintegrates the black-P, ultimately resulting in the formation of the BPQDs suspension.

Pulsed laser ablation with high peak power densities (usually $>10^{13}$ W cm^{-2}) and ultra-short periods (femto- and nanosecond) has been applied for the exfoliation of 2D materials and production of their low-dimensional structures.[268] Some studies have demonstrated that this approach can be utilized to prepare BPQDs. Ge *et al.* have synthesized phosphorene quantum dots (PQDs) by pulsed laser ablation of a bulk black-P target in diethyl ether.[280] Diethyl ether molecules are cleaved by laser ablation to passivate the surface and edges of the phosphorene domains. The PQDs exhibit strong photoluminescence in the blue–violet range, with an average lateral size of ~7 nm. Ren and co-workers have fabricated a few-layered BPQDs using pulsed laser ablation of black-P bulk crystal in isopropyl ether.[281] A neodymium-doped yttrium aluminum garnet (Nd:YAG) pulsed laser with a repetition rate of 10 Hz and wavelength of 1064 nm is used in the experiment.[281] The ablation process lasts for about 30 minutes and the BPQDs exhibit a higher photoluminescence quantum yield (~20.7%) than PQD (11.92%),[280] showing potential in cell bioimaging.

4.2 Synthesis of red phosphorus

4.2.1 Red phosphorus in the bulk form. Currently, amorphous red-P is the most commercially available EPM. This section centers on the synthesis of amorphous red-P, but it should be noted that the earlier literature on red-P synthesis may have included a mixture of crystalline red-P, as the confirmation of its lattice structures and phonon properties has only recently been established.[48,88,129]

Using white-P as starting materials, early synthesis of red-P often involves the pyrochemical method, which requires temperatures over 250 °C in the absence of air.[87] Vvedenskii and Frost studied the reaction kinetics of thermal conversion and claimed that the conversion of melted white-P to red-P followed a first-order reaction in the temperature range of 176–373 °C.[282] However, the increasing trend of constants with a rise in the percentage conversion at temperature below 263 °C suggests an autocatalytic conversion. To validate this phenomenon, DeWitt and co-workers conducted more experiments on the reaction kinetics in 1946.[282] The reaction mixture initially comprises red-P particles suspended in white-P. As the reaction progresses and the percentage conversion reaches approximately 50%, the particles grow in number and size forming a semi-fluid before forming a solid product. The reaction in the temperature range of 250–350 °C strictly follows a first-order rate law, with an activation energy of 37 800 calories per mole. In addition, it is noted that addition of iodine or sulfur has a significant accelerating effect on the thermal conversion process. However, this effect is only noticeable in the initial stages and rapidly diminishes, resulting in the conversion proceeding at a rate similar to that without accelerators.

In contrast to the pyrochemical method of red-P synthesis, electromagnetic radiation utilizes a gentler synthetic approach to convert white-P to red-P (Fig. 19a, route a).[283] Linus Pauling had proposed that red-P can be formed from white-P by cleaving a single bond in each P_4 molecule, resulting in an expansion of the unit into a figure comprising two equilateral triangles with a shared base.[108] The two apical phosphorus atoms in each P_4 unit can then bond with similar phosphorus atoms in neighboring P_4 complexes, leading to the formation of long chains of bonded atoms and ultimately the formation of red-P. The formation of red-P from white-P is easier than that of black-P because breaking a single bond is sufficient to convert each P_4 unit into red-P, whereas the formation of black-P requires breaking of three out of the six bonds in each P_4 unit.[108] A. Pedler and G. Rathenau have published two seminal papers demonstrating how light triggers the conversion of white-P to red-P.[284,285] These studies reveal two mechanisms that drive the transformation through light activation. One mechanism involves the symmetry cleavage of the P_4 tetrahedron and subsequent rearrangement of P_2 into the final polymeric red-P.[285] The other mechanism, which occurs in non-polar media, involves a radical process.[286] The dispersed phase also influences the concentrations of P_4 and P_2. When white-P is heated to 1000–1500 °C in an inert atmosphere, the resulting gas is a mixture of P_4 and P_2 molecules, with their vapor

pressure ultimately reaching equilibrium (Fig. 19a, route f),[283,287] but when the dispersed phase is a solution at room temperature, P_4 molecules are photolyzed to P_2.[288] M. Kraft and V. Parini have described a photochemical reaction between white-P and alkyl iodides at 20 °C, yielding a small quantity of red-P containing organic molecules.[289] D. Perner and A. Henglein have carried out a similar reaction of white-P with alkyl (or aryl) iodides in CCl_4 under γ-^{60}Co at temperatures ranging from 20 to 140 °C.[290] The primary product is red-P (79%) at 25 °C, but the primary product is alkyl-phosphorylated derivatives (80%) at 130 °C. However, when white-P is subjected to visible light up to 100 °C, red-P becomes the primary product. There seems to be a more

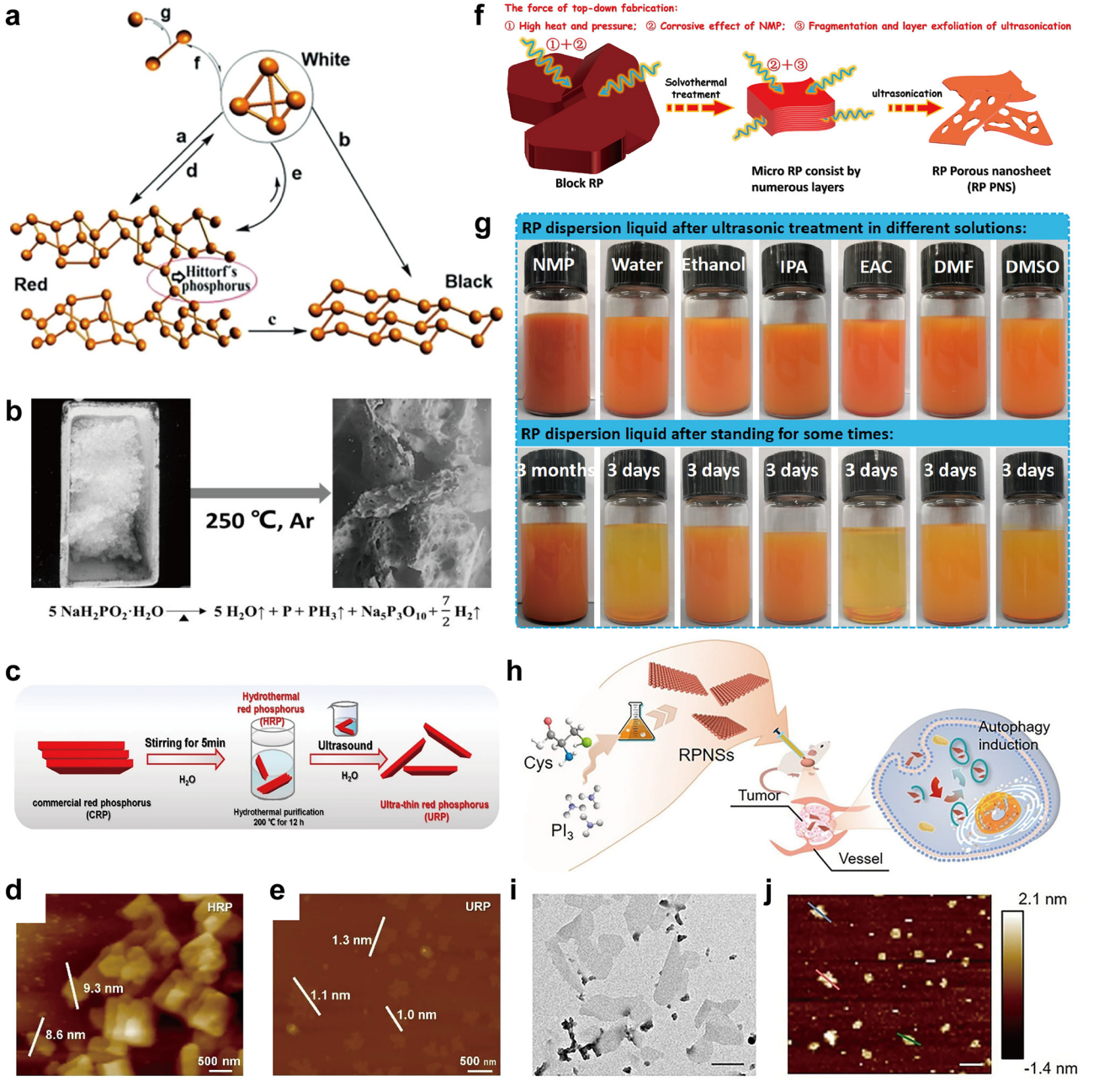

Fig. 19 Synthesis and characterization of the red-P bulk form and nanosheets. (a) Scheme of the conversion of the main significant phosphorus allotropes through different routes. Reproduced with permission from ref. 283. Copyright 2014 John Wiley and Sons. (b) Images of samples before and after thermal decomposition. Reproduced with permission from ref. 292. Copyright 2018 Elsevier. (c) Scheme of the fabrication procedure of ultra-thin red-P. (d) and (e) AFM images of samples before and after sonication. Reproduced with permission from ref. 293. Copyright 2021 Springer. (f) Scheme of the fabrication procedure of red-P porous nanosheets. (g) Photographs of the red-P dispersion after ultrasonic treatment in different solvents and after standing for some days. Reproduced with permission from ref. 294. Copyright 2020 Elsevier. (h) Scheme of the synthesis of red-P nanosheets and their potential anticancer applications. (i) TEM image of the obtained red-P nanosheets. The scale bar is 200 nm. (j) AFM image of the as-synthesized red-P nanosheets. The scale bar is 500 nm. Reproduced with permission from ref. 298. Copyright 2021 John Wiley and Sons.

sophisticated mechanism behind the transformation of white-P into red-P through electromagnetic radiation, and a further study is necessary.

4.2.2 Red phosphorus nanosheets. The thermal decomposition method can lead to the preparation of nano-powders with particular morphologies by decomposing substances at high temperatures.[291] Thermal decomposition can be used to fabricate ultrathin red-P nanosheets.[292] For instance, 5 g of sodium hypophosphite monohydrate ($NaH_2PO_2{\cdot}H_2O$) is sealed in a quartz tube with silicon wool at both ends and then calcined at a heating rate of 3 °C min^{-1} for 2 hours at 250 °C (Fig. 19b). The samples have a disordered structure with no apparent lattice fringe, indicating an amorphous nature. However, TEM reveals only partial layered structures at the edge and wrinkles on the surface, suggesting aggregation of nanosheets, which would hinder practical use due to insufficient separation.

Ultrasound-assisted liquid exfoliation can be utilized to prepare highly dispersed red-P nanosheets. Water exfoliation is carried out to produce ultra-thin red-P from commercial red-P (Fig. 19c), with the resulting nanosheets being highly dispersed and having an average thickness of ~1 nm (Fig. 19d–e).[293] When a similar liquid exfoliation process is conducted using probe ultrasonication in the NMP solvent, red-P porous nanosheets are produced (Fig. 19f).[294] This is because of the strong synergistic effects of NMP and ultrasonication facilitating layered exfoliation and partial surface fragmentation of bulk red-P, leading to the formation of nanosheets with porous topologies. In contrast, bulk red-P exfoliated in a water solution displays insufficient fragmentation and fails to form porous structures. To further assess the suitability of red-P nanosheets with dispersants and the role of NMP in ultrasonication, other solvents are used in exfoliating nanosheets (Fig. 19g).[294] However, the nanosheets are found to be unstable in these solvents and visible deposition occurs to varying degrees after three days. On the other hand, the nanosheets can remain stable in the NMP solvent for over three months, thus confirming the superior stability of NMP in the red-P exfoliation systems. However, the specific interaction between bulk red-P and solvents of varying polarity requires further elucidation.

While red-P nanosheets prepared by liquid exfoliation have shown potential for a variety of applications, they suffer from issues such as sheet-edge corrosion and uncontrollable size. Fortunately, an alternative method using amine-induced wet chemical synthesis has made significant progress in the production of red-P nanosheets.[295–297] This method involves a nucleophilic attack on phosphorus sources, which triggers the breakage of the P–P bond and the formation of polyphosphoric ions (P_n^-). Subsequent treatment with water and acid replaces external ions with electrophiles, resulting in the decomposition of P_n^- to form red-P nanosheets. Recently, Mo and colleagues have described a unique wet-chemical approach for the synthesis of red-P nanosheets through a cysteine-mediated redox reaction and demonstrated their potential for anticancer applications (Fig. 19h).[298] In this method, phosphorus triiodide (PI_3) serves as the phosphorus source, while L-cysteine (L-Cys) acts as the reductant. The confinement material CATB and stabilizer PVP are also employed. Through a mild redox reaction between PI_3 and L-Cys, phosphorus atoms are gradually released and then assembled into nanosheets. The optimal concentration of CATB is critical in the process, since it suppresses red-P natural 3D growth, allowing for 2D growth instead. The weakened reduction, combined with the appropriate confinement material, enables a mild reaction equilibrium, resulting in the formation of high-quality red-P nanosheets. TEM and AFM reveal that the RPNSs are atomically flat with a thickness of around 1.7 nm (Fig. 19i and j). Moreover, this method enables doping of metal atoms in red-P nanosheets to regulate the basic properties and expand the applications.

4.2.3 Red phosphorus quantum dots. Ultrasonic exfoliation is a common method to synthesize red phosphorus quantum dots (RPQDs). Compared to black phosphorus quantum dots, RPQDs exhibit moderate reactivity, making them suitable for composite formation and providing excellent stability under ambient conditions. RPQDs show significant potential in energy and biomedicine applications highlighting their versatility.

Song *et al.* have developed a drug delivery platform by constructing a nanocomposite of bismuthene and RPQDs for synergistic photothermal/photodynamic/chemotherapy.[299] The nanocomposite is synthesized through an electrostatic assembly of exfoliated bismuth nanosheets and RPQDs, followed by PEGylation and loading of the organic drug molecule DOX (Fig. 20a). RPQDs are prepared by dispersing 0.5*g* of red-P powder and 0.2*g* of triphosphate in water and subjecting them to sonication in an ice bath for 10 hours, followed by centrifugation and filtration. The resulting RPQDs are then PEGylated to make them more suitable for physiological conditions and the average diameters of RPQDs before and after PEGylation are around 2.5 and 55 nm, respectively. The combination of bismuthene and RPQDs exhibits synergistic effects achieving photothermal conversion efficiencies of 54.2% and 38.5% upon 1064 nm and 808 nm (1.5 W cm^{-2}) laser irradiation, respectively.

Jia and colleagues have reported *in situ* growth of single-atom nickel on the surface of RPQDs using the ultrasonic method.[300] In the process, commercial bulk red-P is first ground into fine particles, followed by hydrothermal treatment to remove the oxide layer from the surface. The purified red-P and $NiCl_2{\cdot}6H_2O$ are introduced to 100 mL of NMP and sonicated in an ice bath for 48 h to form the nanocomposite Ni-RPQD (Fig. 20b). TEM demonstrates successful synthesis of a homogeneous nanocomposite with a particle size of around 2.7 nm (Fig. 20c and d). The uniform distribution of single-atom Ni is attributed to the unique coordination of single atoms docked with P vacancies on the RPQD surface, which is supported by significant reduction of the electron paramagnetic resonance signal and high-angle shift in the XRD patterns (Fig. 20e and f). The Ni–P bond potentially serves as an electronic antenna to promote facile extraction and transfer of charges. Furthermore, incorporation of Ni single atoms reduces the bandgap and enhances light absorption to improve photocatalytic activity under visible light irradiation.[300]

4.3 Synthesis of fibrous phosphorus

4.3.1 Fibrous phosphorus in the bulk form. CVT is a straightforward and efficient approach to synthesize high-quality bulk

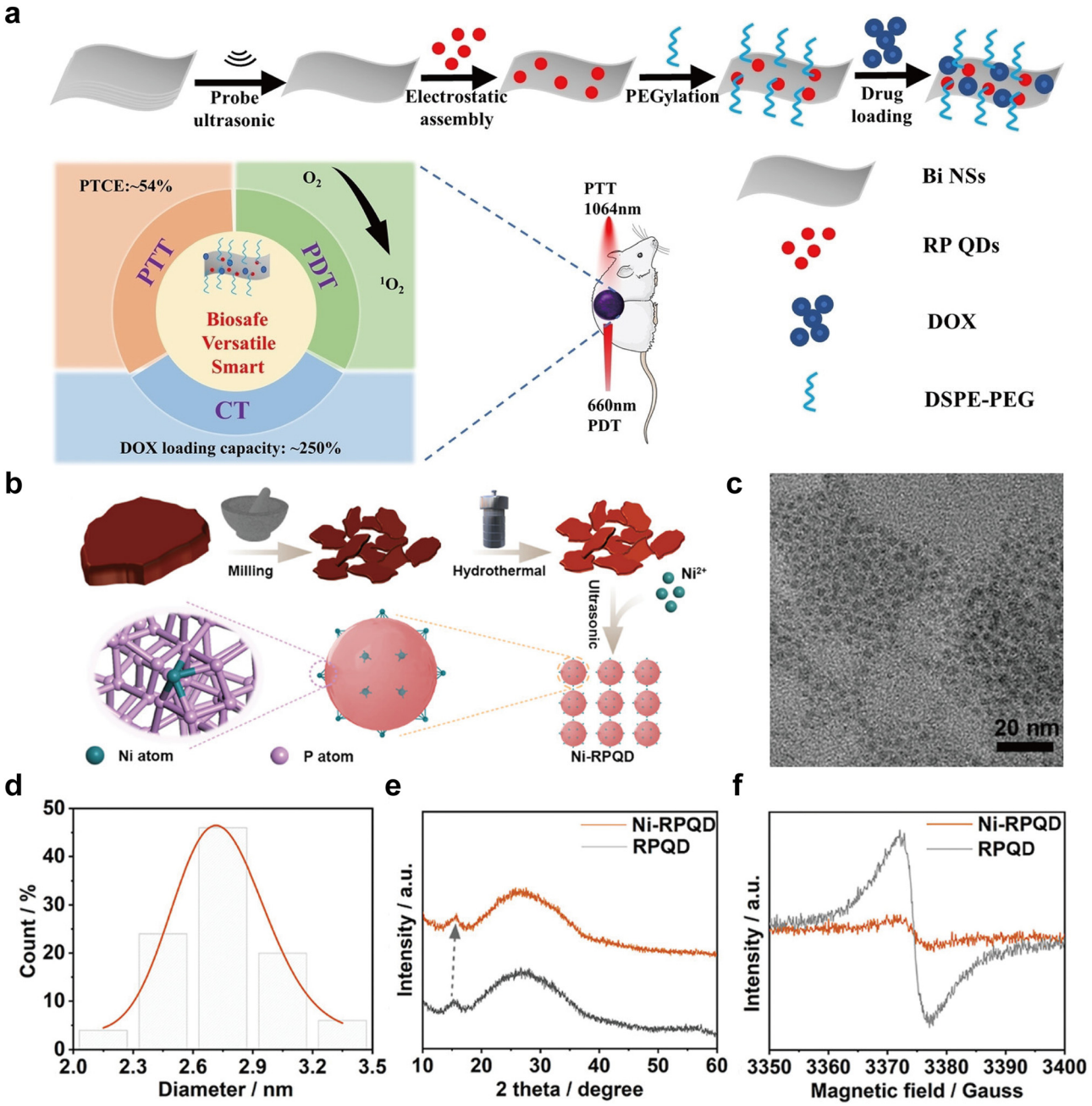

Fig. 20 Synthesis and characterization of RPQD-based materials. (a) Scheme of the fabrication procedure of Bi@RP-PEG-DOX. Reproduced with permission from ref. 299. Copyright 2022 John Wiley and Sons. (b) Scheme of the synthesis of Ni-RPQD. (c) XRD pattern of Ni-RPQD and RPQD. (d) TEM image of Ni-RPQDs. (e) Statistical analysis of Ni-RPQD diameters. (f) EPR spectra of Ni-RPQD and RPQD. Reproduced with permission from ref. 300. Copyright 2022 John Wiley and Sons.

crystals of fibrous-P. In the process, the source (amorphous red-P) is transported to the substrate or inner wall of the ampule in the low-temperature zone, where it crystallizes with the aid of transport agents. These agents are generally pure halogen elements or their compounds, which chemically interact with the source to form easily vaporizable compounds for efficient crystallization.[301] In 1969, Thurns *et al.* were the first to develop a method for red-P fiber production by annealing white-P at temperatures of up to 580 °C for a few months.[33] They noticed the formation of red-P bundles, which took the form of capillary fibers, alongside plate-like violet-P crystals in the reaction kettle. Afterwards, Ruck and co-workers produced dark red fibrous-P needles by the iodine-catalyzed recrystallization of red-P resources.[88] To obtain optimal products, a mixture of 1.0 g of red-P and 40 mg of I_2 is heated in a fused-silica ampule in the temperature range of 570–590 °C for a few days. Although red-P sublimation is possible without catalysts, it occurs more slowly due to the kinetic hindrance of gas phase formation.

The fibrous-P crystals obtained were subjected to single-crystal XRD and TEM characterization to verify the fiber structural model previously proposed by Thurns *et al.*[33,88]

Ruck's detailed experimental synthesis procedure for fibrous-P bulk crystals using the CVT approach has become a widely adopted practice. Researchers have utilized various iodine-containing transport agents in experiments to improve the short-distance transport reaction and obtain high-purity fibrous-P crystals. Smith *et al.* developed a two-step method for producing ultra-long and uniform fibrous-P nanowires.[302] They first prepared thin films of red-P on a SiO_2/Si wafer, and then heated a mixture of purified red-P (110 mg), SnI_4 (15 mg), and Sn powder (30 mg) in a sealed ampoule with the red-P-coated silicon wafer plate to 630 °C for 1 hour, followed by programmed cooling. The resulting fibrous-P nanowires have a diameter of 300–800 nm and a length of over 1 mm. However, the nanowires are found to be sensitive to air due to their larger specific surface area and the presence of other crystalline forms of red-P. Other iodine-containing transporters such as CuI and SbI_3 are also found to produce other phosphorus allotropes besides fibrous-P. To obtain single-phase fibrous-P crystals, Nilges' group substituted the iodine-containing transport agents with chloride compounds and used $CuCl_2$ as an assisting agent.[303] They designed a temperature-control program that involves heating the precursors to 550 °C within 8 hours, followed by holding the temperature for 15 hours, cooling to 275 °C within 75 hours, maintaining this temperature for 1 hour, and finally cooling to room temperature within 75 hours.[303] This method leads to the production of fibrous-P crystals in high yield with reasonable quality. However, not all products synthesized by the CVT method have well-defined fibrous structures and some crystals instead show different morphologies such as bunches-like, nanowire, and urchin-shaped structures.[302–305] These diverse morphologies may be attributed to the complex phase transformation that occurs during the gas phase process and the dispersion interaction between each tubular unit.

Aside from the transport agent, the vapor transport process is highly influenced by the reaction conditions. Our group has developed a low-temperature CVT method that effectively produces high-quality fibrous-P crystals on a large scale (Fig. 21a).[47] In this process, amorphous red-P is transported in the presence of iodine from a high-temperature region (480 °C) to a low-temperature region (450 °C), where crystallization occurs within a day. Compared to previous reports in which the typical temperature is over 550 °C and annealing time lasts several days to weeks, our method greatly reduces the overall reaction temperature and annealing time. In a single preparation, we are able to obtain a total amount of 9.937 g crystals with a yield exceeding 99% (Fig. 21b and c). Mass production of fibrous-P bulk crystals allows for exfoliation of fibrous-P nanoribbons, which will be discussed in the next part. Yan's group has investigated the impact of growth kinetics on the crystallinity of fibrous-P in the CVT reaction and found that the kinetics of CVT is regulated by the rate-determining steps of gas convection and diffusion. To obtain high-quality crystalline fibrous-P, it is important to

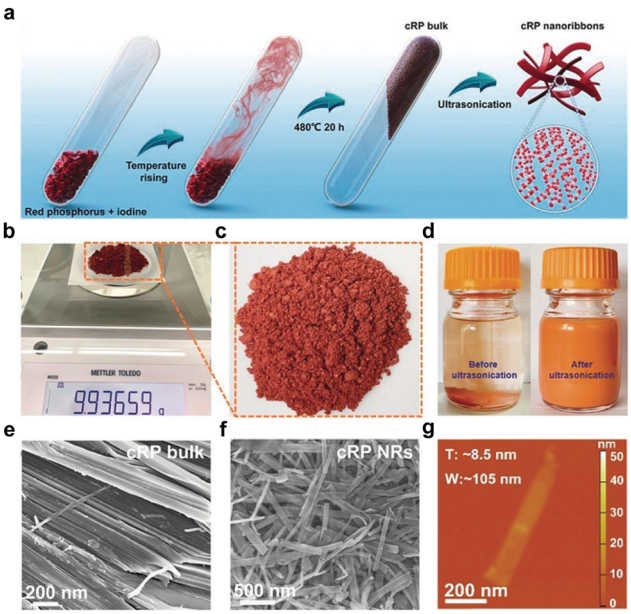

Fig. 21 Low-temperature CVT method for the preparation of fibrous-P bulk crystals and nanoribbons. (a) Scheme of the low-temperature CVT method. (b) Photograph and weight of the fibrous-P bulk powder. (c) Photograph of the bulk powder under high magnification. (d) Photograph of the fibrous-P dispersion before and after exfoliation. (e) TEM image of fibrous-P bulk crystals and (f) nanoribbons. (g) AFM image of a representative fibrous-P nanoribbon. For the sake of consistency, it should be noted that the term "fibrous-P" is used throughout this review to refer to the "triclinic crystalline red phosphorus (cRP)" mentioned in the original text. Reproduced with permission from ref. 47. Copyright 2020 John Wiley and Sons.

slow down gas convection and diffusion. To achieve this, there are several strategies including reducing the amount of red-P during the reaction, increasing the length of the ampoule, lowering the average reaction temperature, and designing a "neck" on the ampoule to reduce the cross-sectional area and slowing down the reaction rate (Fig. 22a).[160] These measures are effective in modifying the growth kinetics of the CVT reaction, ultimately leading to the production of high-quality and well-crystallized fibrous-P crystals. Recently, Zhang *et al.* have developed a low-pressure CVT approach for the production of centimeter-scale fibrous-P micropillar arrays without the use of transport agents.[306] The approach utilizes directional phase transformation of amorphous red-P at a specific temperature and pressure to generate fibrous-P micropillar arrays by self-assembly. In contrast to traditional transport agent-assisted CVT methods, this approach avoids nucleation aggregation induced by transport agents, paving the way for the bottom–up synthesis of fibrous-P microstructures and nanostructures.

Solution-based deposition of elemental phosphorus is an alternative method to prepare low-cost and scalable fibrous-P thin films. Ban *et al.* have demonstrated a wet chemical process that utilizes soluble polyphosphides as precursors to generate fibrous-P through moderate heating without the need for external agents.[307] Amorphous red-P is the source in the polyphosphide synthesis and reacts with potassium ethoxide to

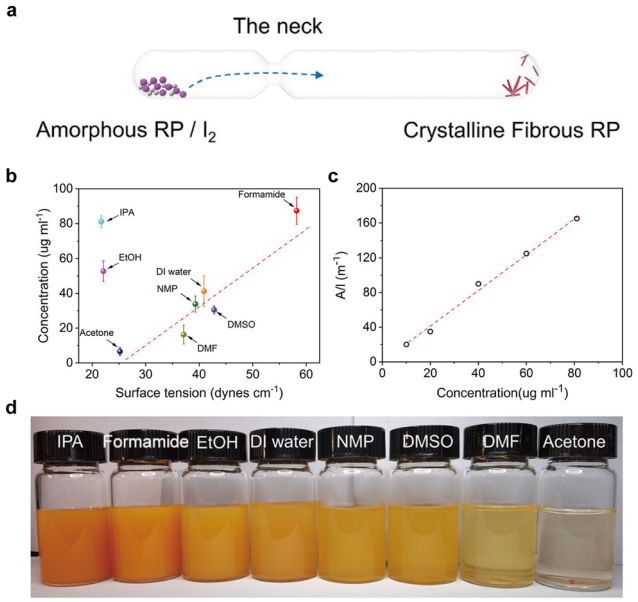

Fig. 22 Modification of the growth kinetics in the CVT reaction for the preparation of fibrous-P bulk crystals and nanoribbons. (a) Scheme of a "neck" on the ampoule in the CVT reaction. (b) Dispersion concentration of fibrous-P nanoribbons *versus* solvent surface tensions. (c) Lambert–Beer's plot at λ = 650 nm of fibrous-P nanoribbons in IPA. (d) Photograph of fibrous-P nanoribbon dispersions in different solvents. Reproduced with permission from ref. 160. Copyright 2021 American Chemical Society.

produce a potassium mixture of polyphosphide powder. The resulting polyphosphide powder is then refined by ethanol dispersion and insoluble precipitate removal to eliminate unreacted precursors and by-products. To fabricate fibrous-P thin films, the polyphosphide solution is spin-coated or drop-cast onto glass or Si/SiO_2 substrates followed by annealing for 30 minutes at 250 °C. The Raman signals of fibrous-P films formed on glass and Si/SiO_2 substrates are almost identical, indicating that fibrous-P formation is mainly due to the precursor itself rather than the precursor–substrate interaction. However, similar to the issues encountered during the preparation of black-P crystals by wet chemical methods,[252] fibrous-P produced by this method lacks obvious lattice structures and may contain mixed phosphorus phases. Hence, investigation of the interaction between phosphorus clusters and solvents is necessary to better understand the dynamic growth process of crystalline phosphorus in solutions.

4.3.2 Fibrous phosphorus nanoribbons. Fibrous-P is an intrinsic one-dimensional vdW material in which electrons are confined in 1D sub-units.[36] In contrast to black-P, preparation of fibrous-P nanoribbons does not require deliberate control over the size of the plane width. Instead, an external force can be applied to break the vdW forces between the interlayers to form unique nanoribbons.

Liquid-phase exfoliation is currently the primary method to fabricate fibrous-P nanoribbons due to its scalability and high-yield production. As aforementioned in the preceding section, our group has developed a low-temperature CVT method for mass production of high-quality fibrous-P bulk crystals.[47] After dispersing these crystal powders in absolute ethanol and performing probe sonication, the resulting supernatant changes from colorless to a uniform orange color (Fig. 21d), indicating the formation of a stable fibrous-P colloid solution. The fibrous-P nanoribbons obtained from this solution are compact, micro-pillar-like lumps, which are quite distinct from the micrometer-scale fiber structures of the bulk materials (Fig. 21e and f). The width of the nanoribbons is approximately 120 nm and lengths range from hundreds of nanometers to several micrometers. The majority of the fibrous-P nanoribbons have an aspect ratio greater than 10, with some having an aspect ratio close to 100. AFM reveals that the thickness of a representative fibrous-P nanoribbon is ~8.5 nm (Fig. 21g), indicating that liquid-phase exfoliation can lead to the production of few-layered fibrous-P nanoribbons. Hu *et al.* have proposed the concept of fibrous phosphorene based on the feature that fibrous-P can be exfoliated.[131] Using *N*-cyclohexyl-2-pyrrolidone (CHP) as the liquid-sonication solvent, they were able to prepare fibrous phosphorene along the [001] direction with a thickness of roughly 1.67 nm. Given that the [001] facet has an average spacing of 0.583 nm,[131] the fibrous phosphorene should consist of three layers. NMP is also used to exfoliate bulk fibrous-P. In the process, single-layered phosphorene is observed, indicating that NMP may have a greater exfoliation capability than CHP. This study demonstrates that the choice of solvents plays a critical role in the exfoliation of Fibrous-P.

To investigate the impact of solvents on the efficiency of fibrous-P exfoliation, Yan's group selected eight solvents with different surface tensions, including isopropanol (IPA), DMSO, NMP, DMF, formamide, ethanol, deionized water, and acetone (Fig. 22d).[160] Each solvent shows a different exfoliation efficiency and there is a broad linear relationship between the dispersed concentration of nanoribbons and solvent surface tension (Fig. 22b). Solvents with higher surface tension tend to have stronger phosphorus–solvent adhesion, which stabilizes the nanoribbon surface for a higher exfoliation efficiency.[308] However, IPA and ethanol, which have relatively low surface tension, also show efficient exfoliation due to the appropriate molecular interaction with fibrous-P interlayers.[309] Although formamide has the highest exfoliation concentration, IPA is recommend as the primary solvent for fibrous-P exfoliation due to its high efficiency, low boiling point, ease of handling, and cost-effective features. The yield of exfoliated nanoribbons in IPA is 16%, and the dispersion extinction coefficient is measured to be ~2087 L g^{-1} m^{-1} under 650 nm incident light (Fig. 22c).[160] Liu *et al.* have used the Hansen solubility parameters (HSPs) to quantify the effects of the solvents on the exfoliation efficiency of fibrous-P nanoribbons.[310] The HSP approach considers three key parameters: δD (intermolecular dispersion force), δH (intermolecular hydrogen bond), and δP (intermolecular polar force).[311] The desired exfoliating solvent should have HSPs that closely match those of fibrous-P. After comparing 19 common solvents, acetone and 1,3-dimethyl-3,4,5,6-tetrahydro-2(1*H*)-pyrimidinone (DMPU) were found to be more suitable for fibrous-P exfoliation. Moreover, the HSPs of a solvent can be modified by varying the solvent ratios. The water/acetone

mixture is chosen as the solvent because it covers the HSPs of Fibrous-P, and both water and acetone are easy to remove without leaving a residual solution. The optimal solvent mixture for fibrous-P exfoliation is determined to be 10% water and 90% acetone, which yields 40% nanoribbons with a thickness of less than 10 nm and 70% with a thickness of less than 20 nm. These results demonstrate the potential of HSP modeling in identifying suitable solvents for exfoliating 2D materials and highlight the importance of solvent selection in the exfoliation process.

4.3.3 Fibrous phosphorus quantum dots. The ability to downscale fibrous-P crystals from the bulk scale to the one-dimensional nanoribbon scale has spurred interest in exploring the potential to further downscale this material to zero-dimensional quantum dots. This investigation provides a more comprehensive understanding of the nanostructures of fibrous-P. With this in mind, Amaral *et al.* have attempted to downscale fibrous-P bulk crystals to the 0D nanoscale by synthesizing fibrous phosphorus quantum dots (FPQDs).[312] Fig. 23a illustrates the FPQD preparation process which includes grinding 30 mg of fibrous-P bulk crystal into powder and adding it to a centrifugal tube containing 35 mL of NMP. The solution is probe sonicated for 7 hours at 300 W in an ice bath and subsequently centrifuged to segregate the FPQDs by size. As shown in Fig. 23b and c, the FPQDs have an average lateral size of 3.8 ± 0.9 nm and a thickness of 2.7 ± 1.3 nm. High-resolution TEM reveals the good crystallinity of FPQDs with a lattice spacing of 0.22 nm. However, both XPS and FTIR indicate that the surface of FPQDs is more susceptible to oxidation manifested by formation of P_xO_y salts compared to the bulk crystals (Fig. 23d and e).[312] This is because the nano-edges of the quantum dots expose more lone electron pairs of the phosphorus atoms making them more vulnerable to oxidation. Nevertheless, the O 1s XPS intensity of FPQDs is lower than that of BPQDs,[267,312] suggesting that FPQDs are more stable in air than BPQDs. The FPQDs dispersed in NMP stored at room temperature remain stable for over two months without aggregation. Even when exposed to air and light for 15 days, the fluorescence intensity from the FPQDs only decreases by 6% (Fig. 23f).[312] This work provides important insights into the synthesis and stability of FPQDs and potential applications to the energy and environmental fields.

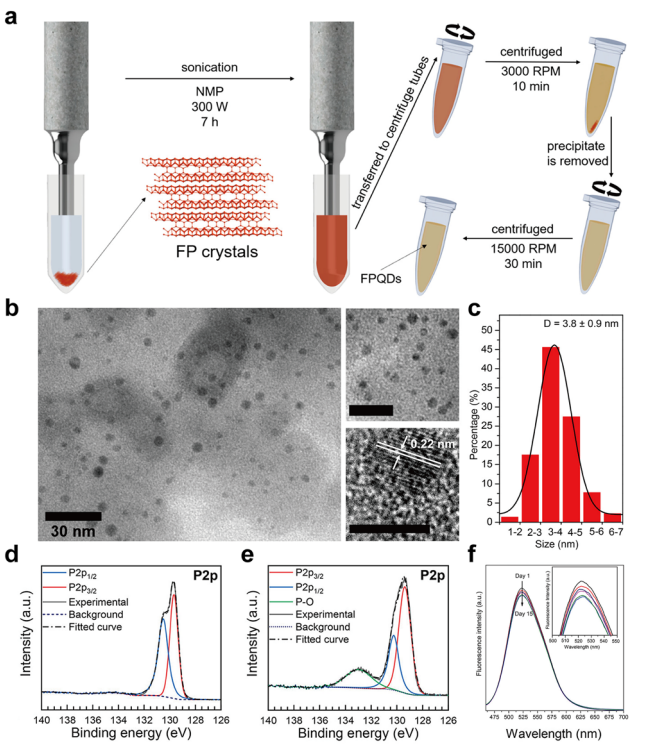

Fig. 23 Synthesis and characterization of FPQDs. (a) Scheme of the fabrication procedure of FPQDs. (b) TEM, high-resolution TEM images, and (c) statistical analysis of the size of FPQDs. The middle–upside and middle–downside images have scale bars of 20 and 5 nm, respectively. (d) XPS spectra of bulk fibrous-P and (e) FPQDs. (f) Photoluminescence intensity of FPQDs was measured over 15 days, with excitation at λ = 370 nm. The inset is a magnified view of the photoluminescence peak. Reproduced with permission from ref. 312. Copyright 2020 American Chemical Society.

4.4 Synthesis of violet phosphorus

4.4.1 Violet phosphorus in the bulk form. The synthesis of violet-P bulk crystals can be traced back to Johann Hittorf's thermal conversion experiment in 1865.[32] In the experiment, white-P is heated to 530 °C in a sealed vessel in contact with lead while the top vessel temperature is maintained at 444 °C. The opaque rhombohedral or monoclinic reddish-violet crystals sublimate, and phosphorus recrystallizes from the molten lead producing the red/violet allotropes.[28,32] The growth of violet-P crystals is facilitated by molten lead which reduces nucleation vacancies and grain boundaries due to the high mobility of atoms on the liquid metal surface.[313] However, on account of the toxicity of lead, it is crucial to identify alternative, low-toxic, or non-toxic liquid metals for the synthesis of violet-P crystals.

In 2019, Yu's group developed a thermal evaporation method that utilized liquid bismuth nanodroplets to produce large quantities of single-crystal violet-P microbelts measuring up to 100 × 10 × 0.3 μm^3 (Fig. 24a).[314] The growth mechanism of microbelts is shown in Fig. 24c. The process involves the sealing of appropriate amounts of red-P and Bi powders in vacuum quartz capsules and heating to 550 °C, inducing the sublimation of the red-P precursor while Bi melts. At this temperature, the molecular motion of the phosphorus vapor becomes highly turbulent producing quick disturbances within the capsule to impinge into the Bi droplets and stretch then into nanodroplets. As the temperature drops to 300 °C, the sublimed phosphorus progressively adsorbs onto the surface of the Bi nanodroplets and nucleates, forming seed crystals that eventually grow into nanorods.[315] Due to the high surface energy of the nanodroplets, they tend to consolidate, causing the nanorods to cohere and form a thicker crystal that gradually expands into a microbelt. The Bi nanodroplets may depart during growth and after cooling to ambient temperature, most of them aggregate, with only a few droplets condensing singly on the microbelts.[316,317] The XRD pattern of violet-P microbelts reveals a high-intensity peak at 15.66 degrees from the (013)

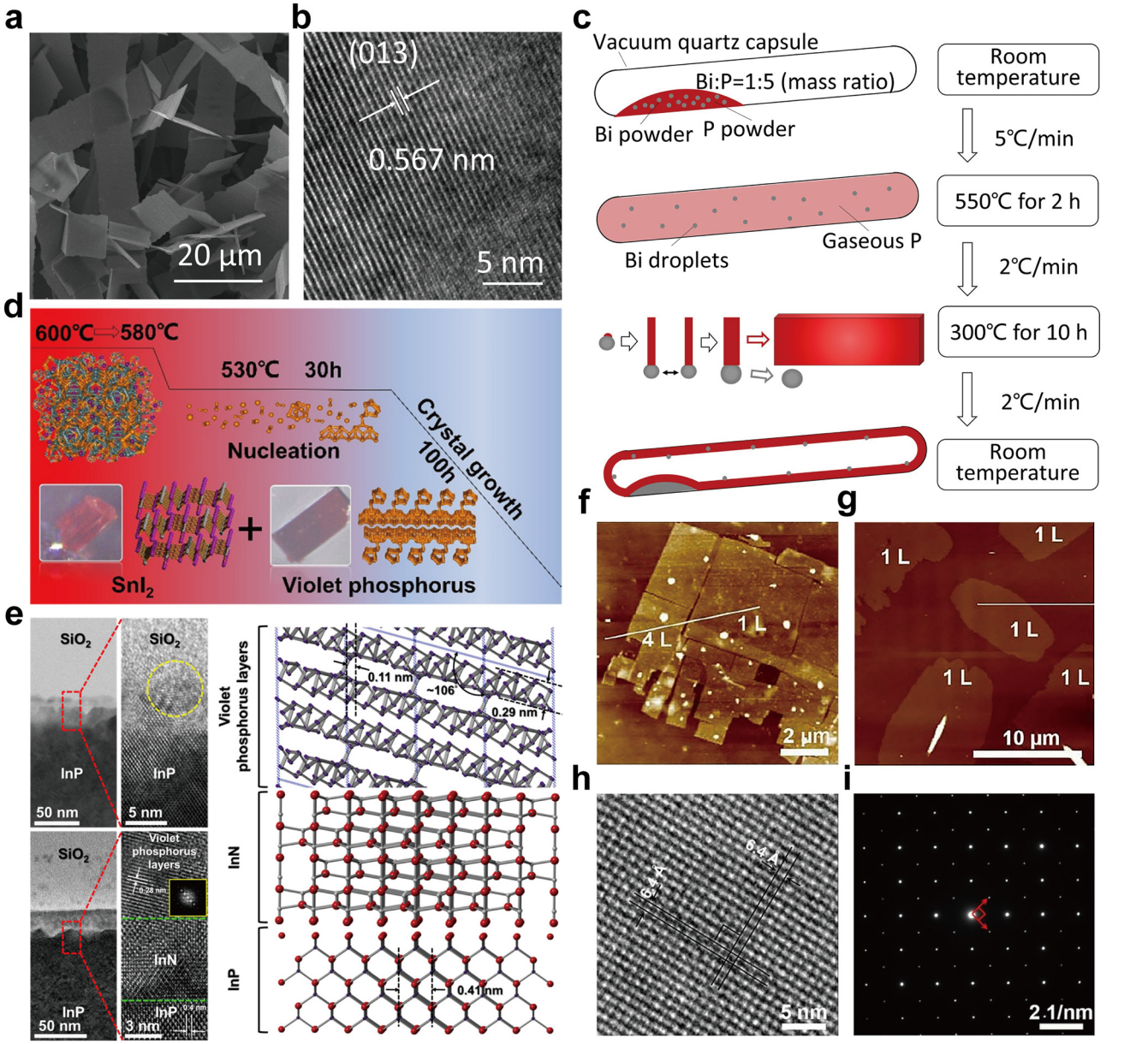

Fig. 24 Synthesis and characterization of the violet-P bulk form and phosphorene. (a) SEM image and (b) high-resolution TEM patterns of violet-P microbelts. (c) Scheme of the growth mechanism of microbelts initiated by liquid Bi through thermal vaporization. Reproduced with permission from ref. 314. Copyright 2019 Elsevier. (d) Scheme of the fabrication procedure of violet-P crystals through an improved CVT method. Reproduced with permission from ref. 319. Copyright 2020 American Chemical Society. (e) TEM images and atomic model of the violet-P/InN/InP layered structure. Reproduced with permission from ref. 320. Copyright 2015 American Chemical Society. (f) AFM images of violet phosphorene from mechanical and (g) liquid exfoliation. (h) High-resolution TEM image of a violet-P nanobelt. (i) SAED pattern corresponding to (h) with the zone axis of [001]. Reproduced with permission from ref. 48. Copyright 2020 John Wiley and Sons.

facet. This peak is markedly distinct from the corresponding peak in the standard violet-P bulk crystal with low intensity. The difference in the peak intensity suggests the specific orientation of facets within the crystal.[314] Additionally, high-resolution TEM shows a well-resolved interference fringe spacing of 5.67 Å along the crystal's edge (Fig. 24b), which is in good agreement with the interplane distance between the (013) planes of violet-P.[314] These findings provide evidence of successful synthesis of high-quality violet-P microbelts with the exposed active (013) facets.

Different from direct thermal evaporation, CVT typically involves separate heating zones, which allow for the movement of gaseous intermediates in defined directions.[318] Zhang's group has made contributions to the synthesis of high-quality violet-P bulk crystals using the CVT method. In 2020, they obtained single-crystal violet-P and conducted a detailed analysis of its structure.[48] This achievement is of great significance, as it represents the first experimental determination of the lattice structure of violet-P and provides valuable information about

the properties and potential applications of violet-P. However, the violet-P crystals obtained in this study contain a mixture of black-P with a yield of only about 36% after separation. To address this issue and improve the production yield, the CVT process has been optimized by using 10 mg of Sn and 18 mg of SnI_4 as the transport agents and 470 mg of amorphous red-P as the source materials in a vacuum quartz tube.[319] As shown in Fig. 24d, the tube is heated slowly in a three-zone muffle furnace for 8 hours to reach 600 °C at the sample end (source zone) and 580 °C at the other end (reaction zone).[319] After 5 hours, the tube is cooled for 10 hours to 550 °C in the source zone and 530 °C in the reaction zone. The tube is kept at these temperatures for 30 hours before slowly cooling to room temperature for about 100 hours. The violet-P crystals are produced with a high yield of ~80%. The holding time of 550–530 °C and cooling time to room temperature are critical for violet-P crystal nucleation and growth.[319] A long holding time at 550–530 °C increases the nucleation of violet-P, with nucleation peaking at approximately 30 hours. Longer cooling time results in larger crystal formation with crystal size reaching its maximum at around 100 hours.[319] The ability to produce high-quality and high-yield violet-P bulk crystals serves as the foundation for the subsequent synthesis of nanostructured violet-P.

4.4.2 Violet phosphorene. Violet-P has the potential to be scaled down to few- or single-layered flakes due to its layered nature. When the thickness is downsized to the atomic scale, violet-P is referred to as violet phosphorene.[48] In 2015, Tsai *et al.* reported the plasma-assisted synthesis of atomically layered violet-P on an InP substrate (Fig. 24e) through N_2 plasma exposure followed by annealing for 1.5 hours at 500 °C and 400 Torr.[320] This produces a 20 nm thick violet-P layer on the surface of InP. However, there are some issues, including insufficient structural characterization of the prepared violet phosphorene and relatively simple explanation of the formation mechanism based solely on the substantial discrepancy in Gibbs free energy. To validate the lattice structure of the prepared violet phosphorene in detail, more analytical results by for example, XRD, are required.

To date, violet phosphorene has been fabricated by both mechanical and liquid exfoliation of violet-P single crystals.[48,321–323] Zhang's group has demonstrated that violet phosphorene can be produced by immersing single-crystal violet-P ($\sim 0.30 \times 0.23 \times 0.13$ mm^3) in 30 mL of ethanol and treating it by tip sonication at room temperature.[48] They also utilized Scotch tape to peel violet-P crystals into thin flakes several times and then transferred them to SiO_2/Si substrates. Fig. 24f and g show the AFM images of violet phosphorene prepared by both mechanical and liquid exfoliation methods. Mechanical exfoliation produces single-layered violet-P with a thickness of ~1.9 nm, but most of the flakes are multi-layered. On the other hand, liquid phase exfoliation can more easily produce thin violet-P flakes (~2.2 nm), but the edges of the flakes are irregular due to defects generated during liquid exfoliation. However, the internal lattice in the liquid-exfoliated flakes remains intact and high-resolution TEM shows that most flakes have two sets of crystal planes intersecting at an angle of 90° (Fig. 24h) consistent with the (110) and (1$\bar{1}$0) lattice planes determined by single-crystal XRD.[48] The SAED pattern obtained from the flake with the zone axis [001] in Fig. 24i clearly demonstrates the high degree of crystallinity in the as-prepared phosphorene. Furthermore, EDS confirms the high stability of violet phosphorene by showing no detectable oxygen signal. These findings make a significant contribution to the development of high-quality violet phosphorene materials and potential applications in various fields.

4.4.3 Violet phosphorus quantum dots. Another type of nanostructured violet-P is the violet phosphorus quantum dots (VPQDs) which possess distinctive optical and electronic properties attributable to the edge effects and quantum confinement.[268] In 2022, Zhang's group synthesized VPQDs for the first time using a simple solvothermal approach.[324] The process involves dispersing ground violet-P crystals into NMP solvent, followed by sonicating the mixture in an ice bath for 2 hours. The sonicated dispersion is subjected to a solvothermal reaction in a muffle furnace. The VPQDs have a single-layered structure with an average height of 1.81 ± 0.57 nm and a lateral size of 3.16 ± 0.78 nm. It is worth noting that an appropriate solvothermal temperature can promote surface atom rearrangement, which helps to eliminate surface defects. However, an excessively high or low reaction temperature may lead to sluggish or hasty reaction kinetics, respectively, producing excessive non-radiative defects.[325] To investigate the influence of solvothermal temperature and time on the morphology of VPQDs, experiments have been conducted. The average lateral size and height of the VPQDs decrease as the temperature is increased from 150 to 180 °C, but then increase slightly upon further temperature increase, suggesting that an excessively high solvothermal temperature may cause VPQD aggregation. Moreover, the average lateral size and height of the VPQDs decrease steadily as the reaction time is increased from 12 to 24 hours. Therefore, it is concluded that in NMP, a long solvothermal reaction at 150 °C can lead to the production of smaller VPQDs.

The VPQDs synthesized in NMP emit a high fluorescence intensity. To rule out the possibility that the fluorescence originates from the NMP solvent, the excitation wavelength is set at 430 nm, as fluorescence from NMP disappears completely at excitation wavelengths longer than 430 nm. Upon 430 nm excitation, a robust fluorescence band at 522 nm is observed from the VPQDs.[324] The VPQDs emit strong green light compared to conventional QDs such as BPQDs (450 nm) and MoS2 QDs (414 nm),[326,327] which emit light in the blue–violet range. Conventional QDs emitting blue–violet light penetrate biological tissues poorly due to the predominantly blue luminescence of biological tissues thus limiting *in vivo* optical imaging of deep tissues.[328] However, the green fluorescence emitted by VPQDs may greatly mitigate this issue. The fluorescence quantum yield of VPQDs is determined to be 7.02% and the fluorescence properties have been demonstrated to be adjustable by varying the solvothermal temperature and time conditions, making them potential candidates for nanosensors in biology and medicine.[324,329]

In addition to the solvothermal temperature and reaction time, Zhang's group demonstrated that the solvent used in the VPQD synthesis influences the fluorescence properties.[330] They used six different solvents, including DMF, NMP, H_2O, 1,3-dimethyl-2-imidazolidinone (DMI), isopropanol (IPA), and

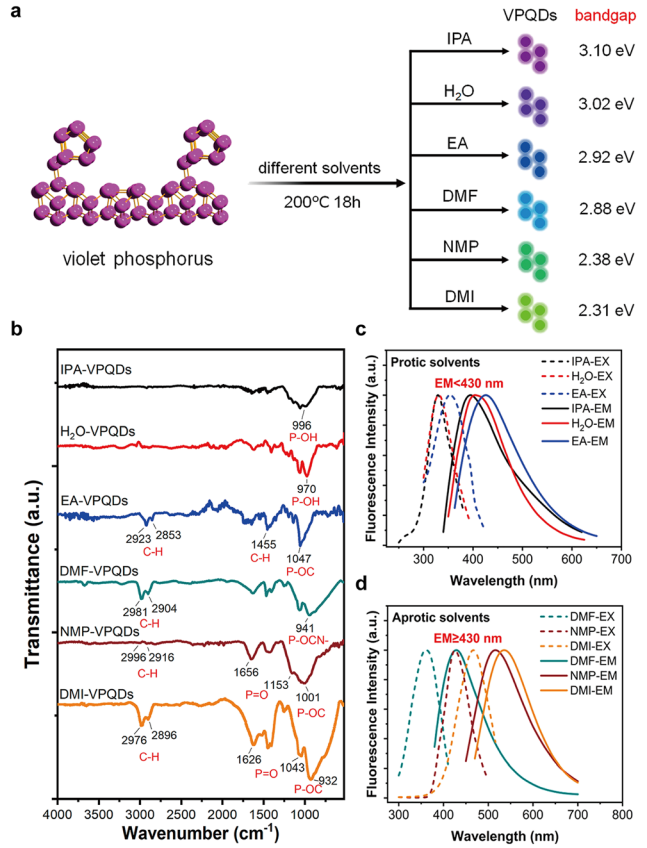

Fig. 25 Synthesis and characterization of VPQDs in various solvents. (a) Scheme of the synthesis of VPQDs with tunable bandgaps by using different solvents. (b) Fourier transform infrared spectroscopy analysis of VPQDs in different solvents. (c) Fluorescence emission spectra of VPQDs in protic solvents and (d) in aprotic solvents. The excitation spectrum is represented by the dotted line, and the emission spectrum is represented by the solid line. Reproduced with permission from ref. 330 Copyright 2022 American Chemical Society.

ethanol (EA), to prepare VPQDs based on the solvothermal method (Fig. 25a).[330] The quantum dots prepared in the six solvents had the characteristic lattice structure of violet-P with similar lateral dimensions (2.5–4.0 nm) and thickness (1.5–2.0 nm). However, FTIR reveals that the VPQDs have different oxygen-containing functional groups in different solvents (Fig. 25b), which can stabilize the edge-dangling phosphorus bonds of VPQDs during synthesis. This modification affects the bandgap size of VPQDs, and thus their fluorescence properties. By functionalizing the edge-dangling phosphorus bonds with different reaction solvents, fluorescence from VPQDs can be adjusted from 400 nm (3.10 eV) to 536 nm (2.31 eV) to span the violet to green spectrum.[330] The VPQDs prepared in protic solvents (IPA, H_2O, and EA) exhibit shorter emission wavelengths (<430 nm) than those prepared in aprotic solvents (DMF, NMP, and DMI), suggesting larger bandgaps for VPQDs prepared in protic solvents (Fig. 25c and d).[330] Theoretical calculations show that different functional groups can alter the HOMO and LUMO positions of VPQDs. In protic solvents, hydroxyl groups are ionized, leading to the formation of P–O bonds between the O atoms of solvent molecules and the edge-dangling phosphorus bonds. This results in significant changes in the HOMO–LUMO bandgaps. Functionalizing the edge-dangling phosphorus bonds with different reaction solvents to adjust the bandgap properties is a simpler and more feasible method than traditional doping and particle size control methods, thereby expanding the potential optoelectronic applications of the VPQDs.

4.5 Synthesis of blue phosphorus

Since Zhu *et al.* predicted the existence of blue-P using DFT calculations,[49] *in silico* research on the structure and properties of this allotrope has been intense. However, to confirm theoretical proposals of blue-P, it is necessary to explore the practical properties through experiments. One method to synthesize 2D inorganic materials with precise control over the deposition rate, composition, and thickness is molecular-beam epitaxy (MBE).[331,332] This technique involves depositing a directed beam of atoms or molecules onto the substrate in an ultrahigh vacuum environment. The beam of atoms or molecules is generated by heating the source in a chamber and the substrate is typically heated to promote the growth of the thin film. MBE has been the primary method for the synthesis of atomically layered blue-P. However, synthesis of blue-P bulk crystals has not been achieved so far.

In 2016, Chen's group reported the growth of single-layered blue-P on Au(111) using MBE under ultrahigh-vacuum conditions.[52] They deposited the black-P precursor on a heated Au(111) surface (230 °C) to produce a highly organized hexagonal superstructure of blue phosphorene on Au(111). Low-temperature scanning tunneling microscopy (STM) shows that this structure consists of a dark center surrounded by six equilateral triangles (Fig. 26a) with an average distance of 14.7 Å between the dark

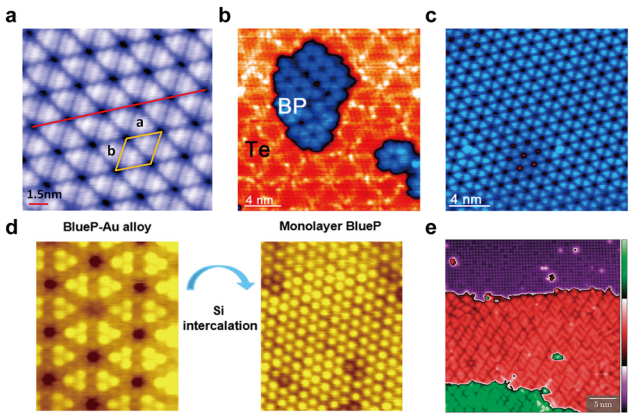

Fig. 26 Synthesis and characterization of blue phosphorene. (a) High-resolution STM image of single-layered blue-P on Au(111). Reproduced with permission from ref. 52. Copyright 2016 American Chemical Society. (b-c) STM images of single-layered blue-P on the tellurium layer. Reproduced with permission from ref. 145. Copyright 2017 American Chemical Society. (d) STM images of blue-P grown on Au(111) before and after Si intercalation. Reproduced with permission from ref. 334. Copyright 2020 American Chemical Society. (e) STM image of the two different phosphorus phases (purple and red domains). Reproduced with permission from ref. 336. Copyright 2021 IOP Publishing.

centers. DFT calculations show that the hexagonal surface structure is derived from the 4 × 4 blue-P supercell, which highly matches with the 5 × 5 Au(111) supercell. When the precursor is annealed at a lower temperature of 150 °C for 60 minutes, phosphorus clusters with a regular geometric structure are formed on the substrate surface instead of the blue-P layer. The edges of the phosphorus clusters are found to exhibit a preferential orientation towards the [110] direction of the Au(111) surface.[52] STM cross-line scanning reveals that the height of the monolayer phosphorus cluster was 2.3 Å, which is consistent with the height of monolayer blue-P. Therefore, the growth of blue phosphorene entails the initial formation of triangular phosphorus clusters at a lower temperature followed by gradual merging to form a blue-P monolayer at a higher temperature.

The substrate is critical in the MBE growth of blue phosphorene and regulating the interactions between the substrate and phosphorus source is necessary to form the desirable structures.[333] Chen's group has developed a two-step deposition strategy to grow quasi-free-standing single-layered blue-P on tellurium (Te) functionalized Au(111).[145] In this approach, a well-defined tellurium layer is deposited on Au(111) as a buffer layer, followed by the deposition of phosphorus onto the Te/Au(111) surface at 250 °C by evaporating the black-P precursor at 290 °C.[145] The single-layered blue-P film has a low degree of contact with the underlying tellurium layer (Fig. 26b and c), indicating that inserting Te atoms between the phosphorus and Au surface can reduce their interaction. Alternatively, intercalation is a powerful technique to modify interfacial interactions by *in situ* introduction of an atomic layer between the surface and substrate. The same group has synthesized a pure blue-P monolayer by silicon intercalation (Fig. 26d).[334] In contrast to the tellurium-layer intercalation described above, a blue-P–Au alloy is first formed by directly depositing the black-P precursor on pure Au(111). Si is then evaporated and intercalated beneath the blue-P–Au alloy to form a gold silicide buffer layer. This results in P–Au bond breakage and re-establishment of P–P bonds between nearby blue-P nanoclusters. These nanoclusters eventually fuse into a solid 1 × 1 blue-P monolayer on the buffer layer. The band structure related to the blue-P–Au alloy disappears and a new feature corresponding to 1 × 1 blue-P appears. Angle-resolved photoemission spectroscopy shows that the band maximum at the Γ point is about −1.2 eV with a parabolic shape, consistent with the theoretical band characteristics of the free-standing blue-P monolayer at the Γ point.[334]

The choice of the substrate is also crucial to blue phosphorene growth, and several experiments have explored different substrates. The Ag(111) surface is a fundamental substrate for the synthesis of a variety of elemental materials such as silicene, germanene, and borophene. Yang *et al.* used the Ag(111) substrate and high-quality bulk red-P as the precursor to produce phosphorus films consisting of regular 2D blue phosphorene clusters with a buckled 1 × 1 lattice.[335] The average lattice constant of this film is 3.08 Å, which is smaller than the theoretical lattice constant of free-standing blue phosphorene (3.28 Å) but contradicts the lattice constant of Ag(111) (2.88 Å).[335] This stems from compression of the phosphorus domains and formation of twisted blue phosphorene clusters due to the lattice mismatch with the Ag(111) substrate. Schaal *et al.* found that growing phosphorus on the Au(100) surface forms two phases depending on the phosphorus coverage (Fig. 26e).[336] A low-density 2 × 2 phosphorous superstructure is observed in the low coverage regime. By increasing the phosphorus amount, the 2 × 2 superstructure vanishes and a roughly hexagonal structure emerges. The lattice constant of the latter phase (3.4(2) Å) resembles that of free-standing blue-P (3.33 Å).[49] However, the unit cell angle of this structure is different from 120°, indicating that it is not completely hexagonal. The domains in this structure are extended, likely as a consequence of on-line epitaxy and strain occurring in diverse directions.[337] Some theoretical studies on the growth of blue phosphorene on different substrates have also contributed to our understanding of the growth process.[338–341]

The most promising method to prepare atomically layered blue-P is MBE-based evaporative thermal decomposition of black-P and deposition on selected and highly ordered single-crystal metal surfaces.[342] This approach produces a complete structure of blue phosphorene with relatively low total energy required for the atomic arrangement. However, the interfacial behavior between phosphorus and substrate requires further experimental investigation. Moreover, the MBE technique involves a sophisticated experimental procedure requiring precise temperature control and ultrahigh vacuum conditions,[343] thereby hindering the cost-effective and large-scale production of blue-P. Currently, the synthesized blue phosphorene remains on the nanoscale level in terms of lateral size. Top–down approaches, such as mechanical or liquid exfoliation, can be utilized to scale up the manufacture of blue phosphorus/phosphorene, but producing blue-P bulk crystals remains a challenge.

4.6 Synthesis of other phosphorus allotropes

The discovery of new phosphorus allotropes is promising but challenging, requiring a combination of experimental synthesis and theoretical calculations. Researchers have gained a better understanding of phosphorus clusters that constitute EPMs, and theoretical studies have predicted a variety of energetically supported allotropes such as phosphorus fullerenes and nanotubes,[76] crimson phosphorus,[77] Haeckelite phosphorus,[344] and phosphorene derivatives.[345–347] However, despite these predictions, most of these allotropes are still in the theoretical stage lacking effective experimental synthetic methods. This section focuses on the experimental synthesis of three uncommon EPMs, namely, phosphorus nanorods, greenish phosphorus, and one-dimensional phosphorus nanostructures confined within carbon nanotubes.

At the dawn of the 21st century, several inorganic chemists uncovered the potential of copper halides as a unique synthetic tool for the creation of compounds featuring novel phosphorus-based structures.[348–350] This was achieved by reacting a stoichiometric mixture of copper halides and elemental phosphorus, which led to the synthesis of polymeric phosphorus chains that

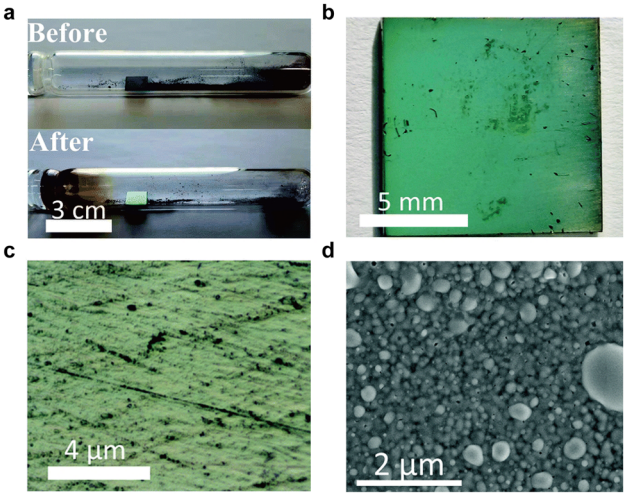

Fig. 27 Synthesis and characterization of greenish phosphorus. (a) Photograph of the sealed quartz tube before and after the deposition of greenish phosphorus onto glassy carbon. (b) Photograph, (c) optical microscopy image, and (d) SEM image of greenish phosphorus on glassy carbon. Reproduced with permission from ref. 53. Copyright 2021 Royal Society of Chemistry.

were complexed with copper halide adducts. Leveraging these studies, Pfitzner *et al.*, in 2004, successfully extracted pure phosphorus nanorods that displayed deep red/brown colors from two distinctive adducts, $(CuI)_8P_{12}$ and $(CuI)_3P_{12}$.[351] These allotropes were identified by their unique repeating units, [P8]P4(4)[and [P10]P2[, respectively.

After the prediction of blue-P in 2014,[49] a new phosphorus allotrope called green-P was predicted in 2017.[50] However, due to its complicated structure, no experimental synthesis of green-P has been reported to date. Nevertheless, it is noteworthy that "greenish phosphorus" on carbon substrates was prepared by the CVD method in 2021 with red-P being the source which was encapsulated in a quartz tube with a glassy carbon substrate under a vacuum of 0.1 MPa.[53] The mixture is heated to 480 °C in a tube furnace to sublimate phosphorus and then cooled to 260 °C to generate greenish phosphorus. The quartz tube holding red-P and the glassy carbon substrate before and after deposition is shown in Fig. 27a. Many nanoparticles are deposited on the substrate, and most of the phosphorus particles show a diameter of ~100 nm, while a few are bigger with a diameter of about 700 nm (Fig. 27b–d). By sonication or scraping, the greenish phosphorus is hardly removed from the substrate, demonstrating strong interactions between phosphorus and the substrate. Other substrates such as carbon paper and silicon wafer have been investigated for the synthesis of greenish phosphorus. Greenish phosphorus can be deposited on carbon paper but not the silicon wafer. The partial pressure and edge structure of carbon materials plays essential roles in the production of this allotrope. The Raman spectra, XRD patterns, and lattice fringes observed by TEM confirm that greenish phosphorus has an atomic structure distinct from those of existing phosphorus allotropes including amorphous red-P, fibrous-P, black-P, and blue-P. Although the synthesis of greenish phosphorus on carbon substrates is promising, some questions remain unanswered. The structural analysis of greenish phosphorus is incomplete, and there is a lack of detailed analysis of the grazing incidence XRD data. Moreover, the name "greenish phosphorus" is given based on the observed color of the materials on the substrate, but this color may be a structural color caused by thin film interference.[352] Therefore, additional structural characterization is necessary to establish that this is indeed a new phosphorus allotrope.

Carbon nanotubes (CNTs) have been shown to be efficient nanoreactors to synthesize nanostructured materials for confined and specific orientation material growth. The type of phosphorus precursor and the wall layer and inner diameter of the CNTs significantly influence the nanostructured phosphorus. Using white-P as a precursor, Hart *et al.* have polymerized melted P_4 molecules inside single-walled CNTs at 50 °C to form a single-stranded phosphorus zigzag chain (Fig. 28a–e).[124,353] This polymerized chain may be an intermediate between white-P and red-P referred to as "pink phosphorus",[354] although its true color remains unknown. Zhang *et al.*[355] prepared sp^3 hybridized ring-shaped phosphorus nanostructures inside multi-walled CNTs using red-P as a precursor by the CVT method at 500 °C. They observed a ring with a diameter of 5.30 nm in a multi-walled CNT with an inner diameter of 5.90 nm, comprising 23 P_8 and 23 P_2 units with 230 phosphorus atoms, and a distance of 6.4 Å between adjacent rings (Fig. 28f and g).[355] Under similar reaction conditions, they obtained a square columnar phosphorus structure with an intersectional size of less than 1.4 nm inside single-walled CNTs with an inner diameter of ~1 nm (Fig. 28h and i), while planar zigzag black-P nanoribbons were formed inside multi-walled CNTs with an inner diameter of ~4.1 nm (Fig. 28j and k),[356] indicating that the host size of the CNTs plays a more significant role than the synthesis conditions in determining the structure of the encapsulated phosphorus.

Identification of motif fragments of one-dimensional red-P chains confined in CNTs is crucial to understand the relationship between the host size of CNTs and phosphorus nanostructures. Recently, Rybkovskiy *et al.*[357] have obtained one-dimensional red-P-based chains in intermediate-diameter (1.6–2.9 nm) single-walled CNTs, and identified the main phosphorus clusters comprising the nanochains by combining experimental characterization and theoretical calculations. By screening six potential phosphorus chain types based on previously reported fibrous-P, $(CuI)_nP_m$ crystals and free-standing vdW bonded chain crystals (Fig. 28l), they have simulated the associated phosphorus using DFT calculations to match the product morphology obtained from high-resolution TEM observations. The obtained one-dimensional red-P-based chains in CNTs are derived from a mixture of fibrous-P building blocks P8]P2 and crl-[P8]P2[P9]P2[. This chain can be the most common nanostructure for encapsulating red-P within CNTs with inner diameters of at least ~1 nm and represents a new phosphorus phase. Additionally, based on previous reports and their findings, a phosphorus phase diagram is constructed to illustrate the behavior in 1D channels with varying diameters. In narrow channels with diameters less than 0.8 nm,

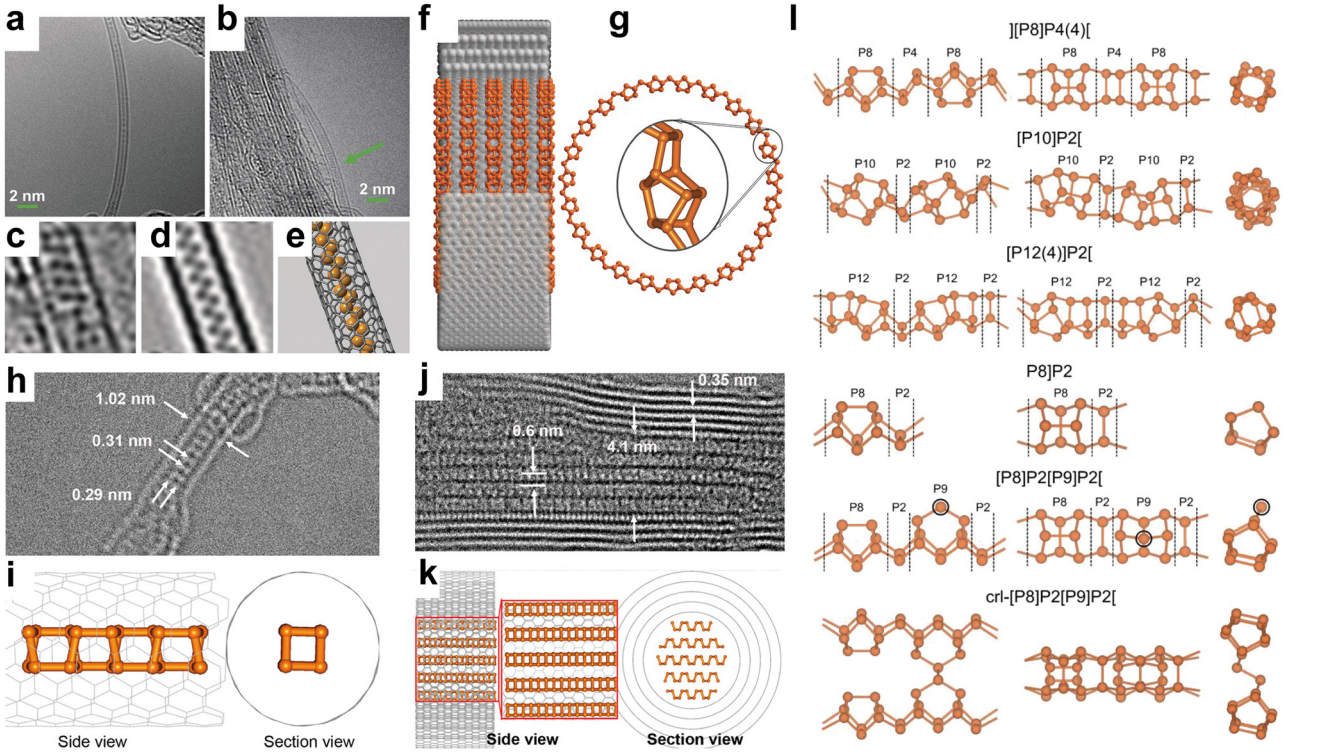

Fig. 28 Synthesis and characterization of 1D phosphorus nanostructures confined within CNTs. (a and b) High-resolution TEM images of polymerized P_4 chain within single-walled CNTs. (c) Noise-filtered high-resolution TEM image of the region highlighted in (b). (d) Simulated high-resolution TEM image and (e) the corresponding atomic structure of a polymerized P_4 chain within a single-walled CNT. Reproduced with permission from ref. 124. Copyright 2017 John Wiley and Sons. (f) Structural model of ring-shaped phosphorus inside a multi-walled CNT. (g) Side view of ring-shaped phosphorus. The inset shows the repeating units. Reproduced with permission from ref. 355. Copyright 2017 John Wiley and Sons. (h) Negative spherical aberration imaging and (i) structural model of square columnar phosphorus inside a single-walled CNT. (j) Negative spherical aberration imaging and (k) structural model of planar zigzag Black-P nanoribbons inside a multi-walled CNT. Reproduced with permission from ref. 356. Copyright 2020 American Chemical Society. (l) Side, top, and end views of six potential phosphorus chain types. Reproduced with permission from ref. 357. Copyright 2022 American Chemical Society.

phosphorus prefers to form zigzag chains. In the diameter range of 0.8–1 nm, tetrahedral P_4 cages and their polymeric derivatives are formed.[124,353] As the diameter increases beyond 1 nm, a thermodynamically stable single P8]P2 chain is confined within the larger cavity, which then forms bundles of P8]P2 chains and paired cross-linked counterparts as the cavity size increases.[357] In larger cavities, [P8]P2 nanorings are formed possibly due to different synthesis conditions and the natural curvature of the P8]P2 chains.[355] This study is of great significance for the predictable growth of phosphorus materials confined within tube-related nanostructures.

The future trend in synthesizing new phosphorus allotropes involves integrating nanotechnology with artificial intelligence-based theoretical calculations. Specifically, machine learning-driven theoretical calculations can accelerate the exploration of phosphorus motif fragments and enable the assembly of diverse architecture types based on identified phosphorus cluster configurations obtained from experiments.[56] After the desired nanostructures are designed, specific cavity nanoreactors such as CNTs, metal-organic frameworks (MOFs), and covalent organic frameworks (COFs) with various dimensions are selected for the confined growth of nanostructures. This synthetic route is expected to facilitate the experimental synthesis of more phosphorus allotropes and requires exploring diverse phosphorus phase diagrams for different confined materials.

In summary, this section has discussed the synthesis of each EPMs across various dimensions. Looking ahead, efforts should be directed towards optimizing reaction conditions for the production of high-quality single crystals and large-scale thin films, and establishing reliable synthesis methods for low-dimensional structures such as phosphorene. Despite the multitude of synthesized allotropes, only a few, notably white-P and amorphous red-P, have reached industrial-scale production of thousands of tons. This underscores the urgency and importance of enhancing growth techniques for black-P, with the goal of achieving ton-level production in a single batch, which would significantly propel the evolution of the future phosphorus chemical industry.

5. Applications of elemental phosphorus materials to sustainable energy and environment

Growing concerns about energy sustainability and security arise from the rapid depletion of fossil fuels and their adverse

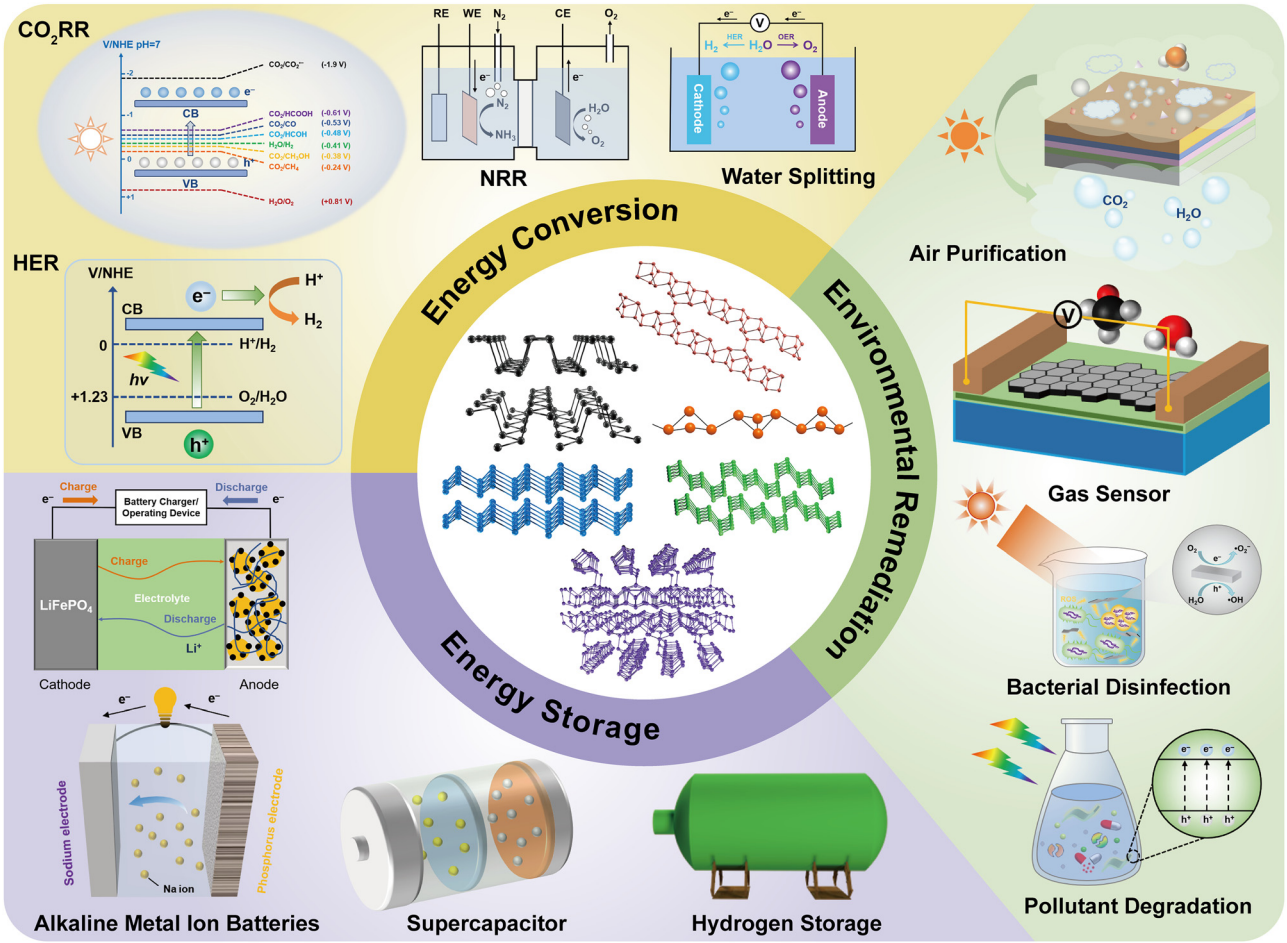

Fig. 29 Diverse applications of elemental phosphorus-based materials in the fields of energy conversion, energy storage, and environmental remediation.

environmental effects,[358] and developing novel, stable, and efficient materials for green energy exploitation, storage, and environmental remediation is crucial.[68,359,360] EPMs with diverse microstructures and nanostructures have emerged as versatile toolkits offering a range of application possibilities. The electron-rich nature of EPMs facilitates interactions with a variety of metal and non-metal materials, promoting the development of advanced composite systems. These elemental phosphorus-based materials exhibit exciting and tunable physicochemical properties including bandgaps, carrier mobility, and ion absorption. Consequently, EPMs demonstrate significant potential in applications such as chemical sensing, ion storage, photo(electro)catalysis, and energy conversion (Fig. 29). In this section, we systemically discuss the functional performance of EPMs and their derivatives in applications of energy conversion, energy storage, and environmental remediation. For each type of application discipline, the analysis of reaction mechanisms, the unique advantages of EPMs in specific scenarios, and strategies for enhancing material performance are emphasized.

5.1 Energy conversion applications

5.1.1 Photocatalytic hydrogen generation. Hydrogen is widely recognized as an environmentally friendly and efficient fuel due to its emission-free properties and high calorific value of nearly 143 MJ kg^{-1}.[361,362] Currently, hydrogen generation mainly relies on biomass gasification, water electrolysis, natural gas steam reforming, and coal combustion.[363–365] However, these conventional methods inevitably produce unwanted by-products during hydrogen preparation, with carbon dioxide emissions resulting from partial methane oxidation contributing to the greenhouse effect and climate change.[366,367] Therefore, there is a pressing need to explore green and sustainable methods for hydrogen production. Since the discovery of photo(electro)catalytic water splitting for hydrogen production in 1972,[368] it has been recognized as one of the most potent and environmentally friendly techniques to generate hydrogen.

Photocatalysis is a process in which the photoreaction is accelerated in the presence of a semiconductor photocatalyst.[369] The semiconductor absorbs solar photons and converts the reactant into the final product without depletion.[370] The overall mechanism of photocatalysis involves three steps. First, solar photons excite electrons in the semiconductor, allowing them to move from the valence band to the conduction band, generating charge-negative electron (e^-) and charge-positive hole (h^+) pairs. Second, the photoexcited electrons and holes move to the

semiconductor surface, where they act as redox agents. Third, the transfer of electrons leads to the formation of superoxide radicals ($^{\bullet}O_2^-$) or initiates reduction events with a corresponding reduction potential. Hole transfer, on the other hand, generates hydroxyl radicals ($^{\bullet}OH$) or initiates oxidation events with an appropriate oxidation potential. The two critical steps in a photocatalytic process are light absorption and charge carrier excitation, and the application of this process in energy conversion is largely dependent on the light radiation intensity and the semiconductor's bandgap. To achieve photocatalytic hydrogen generation, the semiconductor bandgap should be greater than 1.23 eV with a suitable conduction band position for the H^+/H_2 potential. Several common semiconductors such as TiO_2 and MoS_2[371,372] have been reported for photocatalytic water splitting to generate hydrogen. However, as these metal oxides consist of rare elements with relatively high manufacturing costs, their widespread industrial use is restricted. Moreover, these semiconductors have wider bandgaps (>3.2 eV), resulting in the primary absorption of ultraviolet light (<400 nm), which corresponds to only $\sim 4\%$ of the solar spectrum, leaving a significant portion of the solar spectrum unused. Consequently, these disadvantages significantly limit the practical applications of conventional semiconductors and necessitate the development of innovative and cost-effective photocatalysts for hydrogen production.

EPMs are promising materials in the mono-elemental family, with the potential to serve as metal-free photocatalysts for hydrogen generation. First, phosphorus is one of the most earth-abundant elements on the earth,[373,374] and so the production cost of phosphorus-based catalysts is relatively low. Second, EPMs have narrow bandgaps (<2.7 eV), making them suitable for absorbing solar photons primarily in the visible light region and even down to the near-infrared region, with their conduction band minimum position being more negative than the water reduction potential. Third, EPMs have several layered allotropes with tunable bandgaps, allowing the selection of different allotropes in bulk or few-layered nanosheet forms for specific photocatalytic situations. Apart from black-P, amorphous red-P, fibrous-P, violet-P, and blue-P have all demonstrated their viability as candidates for photocatalytic hydrogen generation, both theoretically and experimentally.[21,23,375–377] Table 2 summarizes the progress made in EPMs and EPM-based systems for photocatalytic hydrogen generation.

Although theoretical studies suggest that pristine bulk EPMs may serve as photocatalysts for water splitting,[75,378,379] their inadequate catalytic efficiency limits the competitiveness compared to conventional photocatalysts. This is due to their narrow bandgaps, limited catalytic sites, and elevated recombination of photogenerated electron–hole pairs. As discussed in the electronic property section, exfoliation of EPM bulk crystals into few-layered nanosheets or phosphorene leads to a positive shift in the valence band and a negative shift in the conduction band, resulting in a significant increase in the bandgap. This promotes the efficient generation of strongly oxidative holes, preventing undesirable photoinduced charge pair recombination. In addition, the exfoliation process provides a large surface area and increases the molecule absorption space and active sites. As a result, low-dimensional EPMs are becoming increasingly popular for photocatalytic hydrogen generation. Zhu *et al.* conducted a systematic study of the visible-light photocatalytic efficiency of black-P bulk powder and nanosheets and found that black-P nanosheets exhibit an 18-fold greater hydrogen generation activity compared to the bulk form ref. 205. It is noteworthy that anhydrous LiOH powder is added during the synthetic process, and the photocatalytic hydrogen generation rate of black-P nanosheets in the presence of LiOH is 512 μmol h^{-1} g^{-1}, which is greater than that of bulk black-P (28 μmol h^{-1} g^{-1}) and well-known metal-free photocatalyst g-C_3N_4 (107 μmol h^{-1} g^{-1}).[380] After illumination for 9 hours with 420 nm homochromatic light, the apparent quantum yield of hydrogen generation is calculated to be approximately 0.47%. However, another study also using black-P nanosheets for photocatalytic hydrogen generation showed a lower generation rate.[213,381] This discrepancy may arise from the different fabrication methods (liquid exfoliation and ball milling, respectively) and addition of LiOH, which terminates the reactive black-P nanosheet edges and provides a stable structure for photocatalytic reaction.

Amorphous red-P boasting a lower manufacturing cost and well-established production technique compared to black-P has attracted a considerable interest due to its great photocatalytic characteristics. Chen and co-workers investigated the photocatalytic hydrogen generation efficiency of ultra-thin amorphous red-P nanosheets produced by liquid exfoliation.[293] The nanosheets exhibited a good hydrogen generation activity of 180 μmol h^{-1} g^{-1}, which is 2.88 times higher than that of bulk red-P. The apparent quantum efficiency of amorphous red-P nanosheets is approximately 0.28%. Cycling stability measurements show that the amorphous red-P nanosheets retain 89.1% of their original catalytic activity after three irradiation cycles, indicative of great chemical stability. The primary advantage is the low cost of the raw materials and environmentally friendly preparation process, boding well for commercializing. Zhang *et al.*[294] used a probe ultrasonication technique to synthesize porous red-P nanosheets with a significantly higher photocatalytic hydrogen generation rate of 1169.4 μmol h^{-1} g^{-1}. The BET-specific surface area of the porous nanosheets reach 84.37 m^2 g^{-1} and this vast surface area significantly increases the number of reactive sites and molecule adsorption areas, leading to higher hydrogen production efficiency. Furthermore, other red-P derivatives such as fibrous phosphorene (1021 μmol h^{-1} g^{-1}),[131] and violet-P microbelts (553.4 μmol h^{-1} g^{-1})[396] have also delivered excellent performance in photocatalytic hydrogen generation.

However, low-dimensional EPMs are not invincible, and they also face some challenges in photocatalytic hydrogen generation. Experimental findings show that the quantum efficiency of two-dimensional EPMs is relatively low due to the poor stability of pristine phosphorene. The electron-rich nature of the phosphorene surface and the presence of multiple unpaired lone pairs of electrons leads to the recombination of layers, preventing the materials from maintaining a long-term stability in the photocatalytic process. To overcome these issues, three potential

Table 2 Summary of photocatalytic hydrogen generation performance of elemental phosphorus-based materials

Allotropes	Materials	Methodology	Light source	H_2 generation rate	Ref.
Black phosphorus	BP-BM	Ball milling	300 W Xe lamp with a 420 nm cut-off filter	512 μmol h^{-1} g^{-1}	213
	BP nanosheets and nanoparticles	Liquid phase exfoliation	300 W Xe lamp with a 420 nm cut-off filter	64 μmol from the two cycles for-nanosheets/45 μmol h^{-1} g^{-1} for nanoparticles	381
	BPQDs/g-C_3N_4	Sonication approach	300 W Xenon lamp with a 420 nm cut-off filter	271 μmol h^{-1} g^{-1}	382
	Ni_2P/BP	Solvothermal process	150 W Xe arc lamp l	406.08 μmol h^{-1} g^{-1}	383
	BP-10000/MoS_2	Solvothermal method	300 W Xenon lamp with a UV cutoff filter ($\lambda > 420$ nm)	1286 μmol h^{-1} g^{-1}	384
	BP/CN	High-energy ball milling	Blue LED lamp (λ = 440–445 nm)	786 μmol h^{-1} g^{-1}	385
	FPS/CS	Mechanical mixing	300 W Xenon arc lamp with a UV-cutoff filter ($\lambda \geq 420$ nm)	11 192 μmol h^{-1} g^{-1}	386
	BP/PCN-HKM	Ultrasonication and wet-chemical self-assembly	300 W Xenon lamp with an optical filter ($\lambda > 400$ nm)	7380 μmol h^{-1} g^{-1}	387
	BP/MBWO	Sonication	300 W Xenon lamp	21 042 μmol g^{-1}	388
Amorphous red phosphorus	URP	Liquid exfoliation	300 W Xe lamp with a UV-cut 420 nm filter	180 μmol h^{-1} g^{-1}	293
	RP PNS	Solvothermal treatment-coupled ultrasonic exfoliation	300 W Xe lamp	1169.4 μmol h^{-1} g^{-1}	294
	Red-P/g-C_3N_4	Solid state annealing	300 W Xenon lamp with a UV cut-off filter ($\lambda > 420$ nm)	310 μmol h^{-1} g^{-1}	389
	Hierarchical P/YPO_4 hollow microspheres	Hydrothermal method	300 W Xenon lamp with a 400 nm cut-off filter	65 μmol h^{-1} g^{-1}	390
	g-C_3N_4/Red-P hybrid nanosheets	Sono-chemical treatment	300 W Xenon lamp with a 420 nm cut-off filter	1691 μmol h^{-1} g^{-1}	391
	Co_2P/RP	Hydrothermal method	300 W Xe lamp irradiation	5992.5 μmol h^{-1} g^{-1}	392
Fibrous phosphorus	Micro-fibrous P/SiO_2 and smashed-fibrous P	CVD and ultrasonication	300 W Xenon lamp	633 and 684 μmol h^{-1} g^{-1}, respectively	393
	Red P/g-C_3N_4	One-step CVD	300 W Xenon lamp equipped with L40 cutoff filter	2565 μmol h^{-1} g^{-1}	394
	Fibrous phosphorene	Ultrasonication	300 W Xenon lamp	1021 μmol h^{-1} g^{-1}	131
Violet phosphorus	Violet phosphorus	CVT	300 W Xenon lamp	553 μmol h^{-1} g^{-1}	395
	CRPMR	CVT	Solar simulator-300 W Xenon lamp	324.2 μmol h^{-1} g^{-1}	396
	PCN@HP	CVD	300 W Xe lamp with an AM 1.5G filter as simulated sunlight ($\lambda > 300$ nm) or a 420 nm cutoff filter as visible light ($\lambda > 420$ nm)	33.2 and 17.5 μmol h^{-1} g^{-1} for simulated sunlight and visible light, respectively	397

strategies can be applied to improve the photocatalytic efficiency. First of all, chemical modification of phosphorene with hydroxyl (–OH) or pseudo-halogen (–CN and –OCN) functional groups can passivate the phosphorene surface and improve the durability.[213,398] Second, phosphorene can be utilized as a matrix to load photocatalytically active electron mediators (Ag/Au nanoparticles)[399,400] to produce co-catalytic effects in photocatalysis. Third, metal/nonmetal doping and heterostructure construction are powerful methods for regulating the electronic structure and mechanical strength of phosphorene.[401,402]

Heterostructures play an important role in promoting the spatial separation of electrons and holes and the photocatalytic activity of materials like black-P. Zhu *et al.* have designed a binary nanohybrid composed of black-P nanoflakes and graphitic carbon nitride nanosheets to investigate the photocatalytic hydrogen performance in the presence of methanol as a hole quencher.[403] At the interface between black-P and graphitic carbon nitride, a type-I heterojunction is formed. Under light irradiation above 420 nm, graphitic carbon nitride is the main excited materials generating electrons and holes in the conduction band and valence band, respectively. Black-P serves as an electron acceptor and accepts electrons from the conduction band of adjacent graphitic carbon nitride, while the transferred holes in black-P are quenched by methanol (Fig. 30a). This process inhibits recombination of electron–hole pairs in graphitic carbon nitride. Electrons and holes in black-P recombine rapidly under irradiation (lifetime of less than 1 ps) to prevent black-P from functioning as a photocatalyst. However, this type-I heterojunction can produce hydrogen under light irradiation above 780 nm. Time-resolved diffuse reflectance spectroscopy indicates that the P–N coordination bond at the interface between Black-P and graphitic carbon nitride can act as a trap site for electrons and captures electrons in the conduction band of black-P to generate hydrogen. This strong interfacial interaction and effective charge transfer between black-P and graphitic carbon nitride improves the photocatalytic efficiency by inhibiting the recombination of photogenerated charges in black-P. This demonstrates that the interfacial P–N coordination bond plays a critical role in photocatalytic hydrogen generation in both visible and near-infrared regions. Zhu *et al.* constructed 2D black-P/$BiVO_4$ heterostructures as a novel Z-scheme photocatalyst for overall water splitting.[404] Under >420 nm light irradiation, the photocatalyst generates H_2 and O_2 yields of approximately 160 and 102 μmol h^{-1} g^{-1}, respectively, without the need for any sacrificial agents or external bias. The staggered band positions of black-P and $BiVO_4$ facilitate separation of charges, leading to the reduction and oxidation of water on black-P and $BiVO_4$, respectively. In addition to binary heterostructures, researchers have constructed ternary nanostructures for photocatalytic hydrogen generation. Black-P–Au/$La_2Ti_2O_7$ shows high efficiency as a photocatalyst over a broad spectrum of wavelengths spanning the ultraviolet to near-infrared regime.[405] The optimal hydrogen generation rates of black-P–Au/$La_2Ti_2O_7$ are 0.74 and 0.30 mmol h^{-1} g^{-1} at wavelengths longer than 420 nm and 780 nm, respectively. This work highlights that the strong surface plasmon resonance absorption of gold nanoparticles in the hybrid nanostructure can transform incident photon energy into plasma energy and transmit electrons to the semiconductor to induce charge separation (Fig. 30b), thus improving the photocatalytic performance. Furthermore, the strong optical absorption of black-P and plasma gold nanoparticles in the region from ultraviolet to near-infrared, along with the interfacial interaction of black-P and Au/$La_2Ti_2O_7$, enables effective electron transfer to $La_2Ti_2O_7$ by excited black-P and Au.

The low-dimensional black-P materials exhibit powerful multibody effects resulting in strong exciton that dominates the photoexcitation process.[219,406,407] To enhance the photocatalytic effects of black-P, it is crucial to make reasonable use of these excitons. Xie's group has proposed a strategy to modulate exciton dissociation by heterojunction engineering,[408] which combines black-P nanosheets with poly(3-hexylthiophene) (P3HT) leading to the construction of type-II heterojunctions (Fig. 30c). This strategy weakens the stability of excitons in black-P and promotes the dissociation and conversion to free carriers. The internal electric field generated at the heterojunction interface due to the difference in the band structure further promotes directional transfer of holes to P3HT and electrons to black-P (Fig. 30d), consequently increasing the output of the loaded carriers. Benefiting from this, the black-P/P3HT heterojunction shows efficient exciton dissociation and greatly improved photoresponsive properties of black-P such as a photocurrent switching ratio of approximately 18.3. Excitons can undergo resonant transfer between systems possessing compatible spin states and energy levels.[409] In 2021, Xie's group proposed an exciton-mediated energy transfer strategy in heterojunction engineering for efficient infrared-light-driven photocatalysis.[410] They constructed a black-P/polymeric carbon nitride heterojunction in which black-P acted as an infrared light absorber and transferred its energy to activate polymeric carbon nitride through exciton interaction (Fig. 30e). The excitons in carbon nitride separated into free charge carriers at the heterojunction interface, where holes were further transferred into black-P and electrons were transferred into carbon nitride to achieve great photocatalytic efficiency under infrared light irradiation.

The strategy has also been widely used for other EPMs, and Yu's group has made contributions in the preparation of crystalline red-P composites to promote sustainable application of low-cost and effective materials in photocatalysis. In 2016, they used different synthetic methods to prepare two kinds of fibrous-P-based materials, namely, micro-fibrous-P/SiO_2 composites and smashed-fibrous-P crystals.[411] These materials show stable and high hydrogen release rates of 633 μmol h^{-1} g^{-1} and 684 μmol h^{-1} g^{-1}, respectively. The high photocatalytic efficiency is due to the high conduction band minimum of fibrous-P (-0.9 eV *vs.* NHE) and the favorable full contact of the small-size microstructure with water. One year later, they developed a crystalline red-P/g-C_3N_4 composite with a record-high hydrogen generation rate of 2565 μmol h^{-1} g^{-1}.[394] The apparent quantum yield of the red-P/g-C_3N_4 composite is 13.8% at 420 nm, which is about 3.5 times that of pristine g-C_3N_4 (3.9%).[394] The great catalytic performance of the composite is attributed to the formation of chemical bonds between red-P (fibrous phase phosphorus)

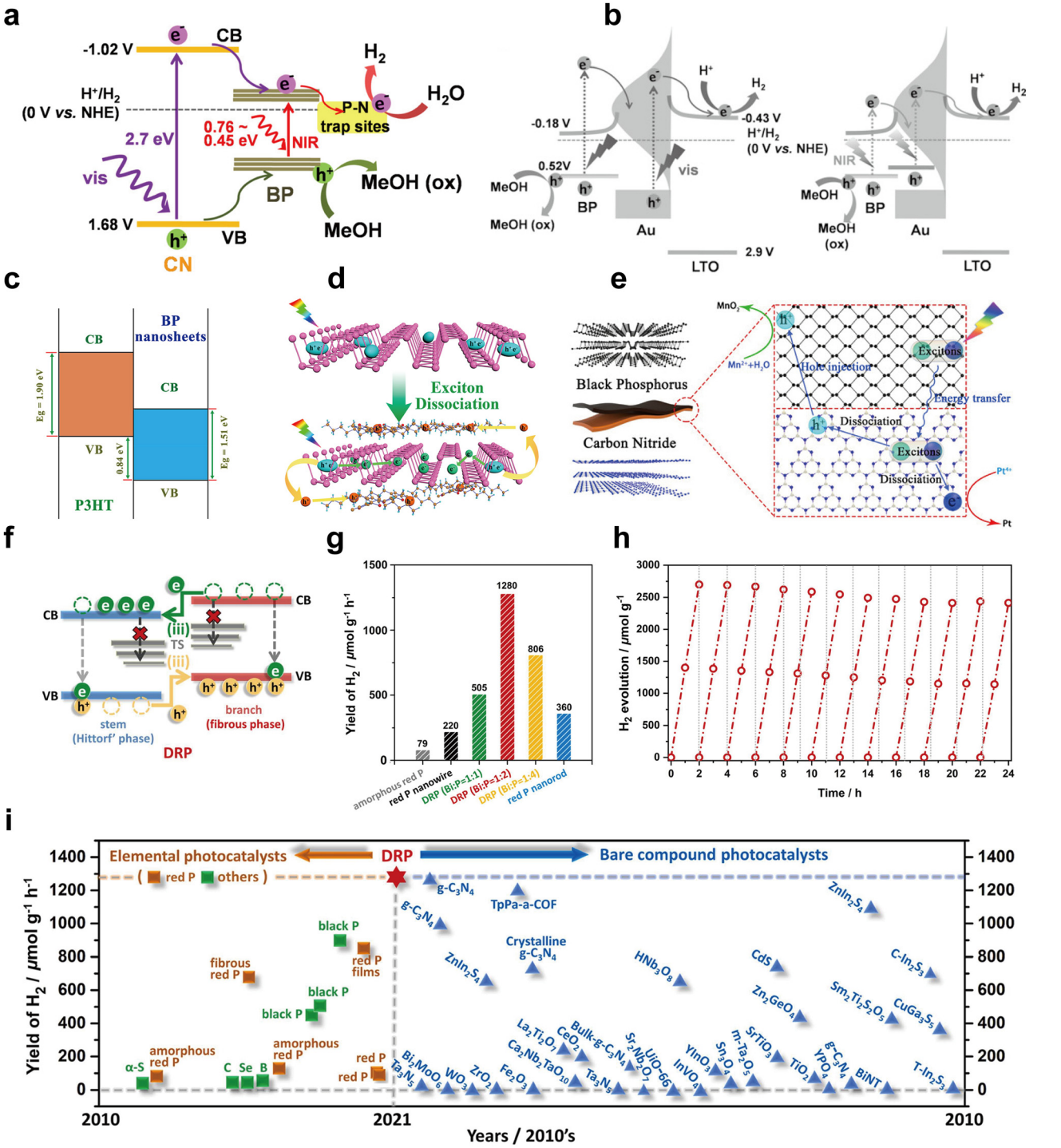

Fig. 30 Applications of elemental phosphorus materials to photocatalytic hydrogen generation. (a) Proposed mechanism of photocatalytic hydrogen generation for the black-P/graphitic carbon nitride (CN) heterostructure under visible and near-infrared irradiation in the presence of methanol. Reproduced with permission from ref. 403. Copyright 2017 American Chemical Society. (b) Proposed mechanism of photocatalytic hydrogen generation for the black-P–Au/$La_2Ti_2O_7$ (LTO) composite under visible (left) and near-infrared (right) irradiation in the presence of methanol. Reproduced with permission from ref. 405. Copyright 2017 John Wiley and Sons. (c) Band alignment of black-P/P3HT type-II heterojunctions. (d) Charge transfer at the heterojunction interface. Reproduced with permission from ref. 408. Copyright 2019 American Chemical Society. (e) Photoexcitation processes in black-P/carbon nitride heterojunctions. Reproduced with permission from ref. 410. Copyright 2021 John Wiley and Sons. (f) Proposed photocatalytic process of dendritic red-P (DRP). (g) Photocatalytic hydrogen evolution yield of DRP and red-P-based materials under visible light irradiation. (h) Photocatalytic stability of DRP. (i) Comparison of the visible-light photocatalytic hydrogen generation rate between DRP and other bare elemental/compound photocatalysts. Reproduced with permission from ref. 412. Copyright 2022 Elsevier.

nanoparticles and g-C_3N_4, which reduces the number of structural defects in g-C_3N_4. This, in turn, inhibits the inactive charge capture and prolongs the lifetime of the active charge in g-C_3N_4, resulting in improved photocatalytic activity. Recently, Yu's group[412] has developed a bismuth-catalyzed CVD method to prepare violet-fibrous hetero-phase dendritic structures from amorphous red-P for photocatalytic hydrogen generation (Fig. 30f). The hetero-phase dendritic catalyst shows stable and efficient photocatalytic activity such as a hydrogen generation rate of 1280 μmol h^{-1} g^{-1}, which is about 16 times greater than that of amorphous red-P and exceeds those of many elemental and bare compound photocatalysts (Fig. 30g–i). The alignment of band structures between two crystalline phases and intimate heterojunction binding at the stem-branch intersection contributes to the construction of a well-organized structure that reduces the interfacial resistance, promotes charge transfer, and inhibits charge trapping and recombination. Other phosphorus-based composites have also been explored for photocatalytic hydrogen generation, for example, red-P/YPO_4,[390] fibrous-P/TiO_2,[413] violet-P/polymeric C_3N_4,[414] blue-P/$Mg(OH)_2$,[415] blue-P/g-C_3N_4,[416] and green-P/$MoSe_2$.[75]

5.1.2 Photocatalytic carbon dioxide conversion. Consumption of fossil fuels has given rise to worldwide energy depletion and excessive carbon dioxide emissions. As a greenhouse gas, carbon dioxide plays a major role in global warming.[417–419] Hence, it is critical to create sustainable technologies that can tackle both the energy crisis and greenhouse gas emissions, ultimately aiming for a net-zero carbon footprint.[420,421] Fortunately, CO_2 reduction catalysis can address these challenges simultaneously and transform waste into resources. Since the discovery of photo-electrocatalytic CO_2 conversion in 1979,[422] artificial CO_2 reduction has attracted considerable interest. Photocatalytic CO_2 reduction mimics the natural carbon cycle by converting CO_2 to hydrocarbon fuels through a chemical reaction. Photocatalytic reduction has several advantages over electrocatalysis such as direct utilization of inexhaustible solar power and minimized secondary energy waste.

Photocatalytic CO_2 conversion is more challenging than photocatalytic H_2 generation. CO_2 is a non-polar linear molecule with a symmetric structure, and the C═O bond energy is 804.4 kJ mol^{-1} at 298 K, indicating that a large amount of energy is required to break the bond.[423,424] Eqn (1)–(5) show the electrode equations and potentials (V *vs.* NHE) for CO_2 reduction to free radicals and typically produced compounds.[425,426] Although CO_2 can form a free radical by accepting one electron directly as shown in eqn (1), the reduction potential of −1.90 V is substantially negative, indicating a higher positive Gibbs free energy required, which is thermodynamically unfavorable. As a result, photocatalytic CO_2 reduction generally occurs *via* a proton-coupled multielectron transfer process.[425] The typical reduction products are methane, methanol, carbon monoxide, and formic acid (eqn (2)–(5)). In addition to producing photoexcited electrons and delivering them to adsorbed carbon dioxide molecules for activation and reduction, the photocatalyst also plays a crucial role in stabilizing the corresponding intermediates in their respective reduction pathways, thus increasing the reaction selectivity.[427]

$$CO_2(g) + e^- \rightarrow CO_2^{\bullet -} \quad \varphi^\circ_{redox} = -1.90\ V \qquad (1)$$

$$CO_2(g) + 2H^+ + 2e^- \rightarrow HCOOH(l) \quad \varphi^\circ_{redox} = -0.61\ V \qquad (2)$$

$$CO_2(g) + 2H^+ + 2e^- \rightarrow CO(g) + H_2O(l) \quad \varphi^\circ_{redox} = -0.52\ V \qquad (3)$$

$$CO_2(g) + 6H^+ + 6e^- \rightarrow CH_3OH(l) + H_2O(l) \quad \varphi^\circ_{redox} = -0.38\ V \qquad (4)$$

$$CO_2(g) + 8H^+ + 8e^- \rightarrow CH_4(g) + 2H_2O(l) \quad \varphi^\circ_{redox} = -0.24\ V \qquad (5)$$

EPMs have shown tremendous potential as metal-free photocatalysts for CO_2 conversion. These materials possess two intrinsic advantages. First, EPMs consist of a single-component element, indicating that their chemical activities are determined by their structure, and the structural control can provide a uniform coordination environment to form more efficient composites with other materials. Second, the electron-rich phosphorus atoms in EPMs can effectively adsorb carbon dioxide through Lewis acid–base interactions and stabilize intermediate products, improving the photocatalytic selectivity. Recent advances in photocatalytic CO_2 reduction have leveraged these advantages of EPMs.

In 2020, Zhu *et al.* reported a hydroxyl-modified black-P monolayer showing outstanding photocatalytic efficiency, and it was capable of converting CO_2 into CO with a generation rate of 112.6 μmol h^{-1} g^{-1}.[428] This value is four times that of bulk black-P, and comparable to that of 2D g-C_3N_4. Competing reactions leading to the production of by-products such as H_2 are constantly in progress. However, hydroxyl-modified black-P exhibits a better reaction selectivity to CO (90.8%) than pristine black-P. This can be attributed to the electron-donating character of a hydroxyl group (Fig. 31a), resulting in the formation of modified black-P with a higher bandgap (~2.2 eV) than the unmodified one (2.0 eV). This elevated bandgap makes black-P more accessible to the CO_2/CO redox potential. In addition, hydroxyl-modified black-P has outstanding stability due to surface passivation, and its degradation rate is 8.8 times slower than the pristine black-P monolayer during light cycling measurements. This shows that an appropriate choice of electron-acquiring/electron-donating functional groups influences the electron distribution of the materials. Reasonable control over the reaction conditions can lead to the formation of elemental homojunction comprising mixed crystalline phases of red-P and black-P. Band alignment of red-P and black-P allows for the formation of a Z-scheme structure and introduction of another suitable semiconductor into the system results in the formation of a ternary dual Z-scheme system. Chai's group designed a dual Z-scheme homo-heterojunction of red-P/black-P@WO_3,[429] with great photocatalytic efficiency under visible light irradiation by converting CO_2 into CH_4 with a yield of 6.21 μmol g^{-1} within 6 hours, whereas the original components, red-P, WO_3, and red-P/black-P, do not produce any CH_4. In the dual Z-scheme system, red-P acts as a key bridge connecting black-P and WO_3, forming a unified and synergistic ternary homo-heterojunction composite with the appropriate bandgap energy for CO_2 reduction (Fig. 31b). Specifically, red-P has a higher

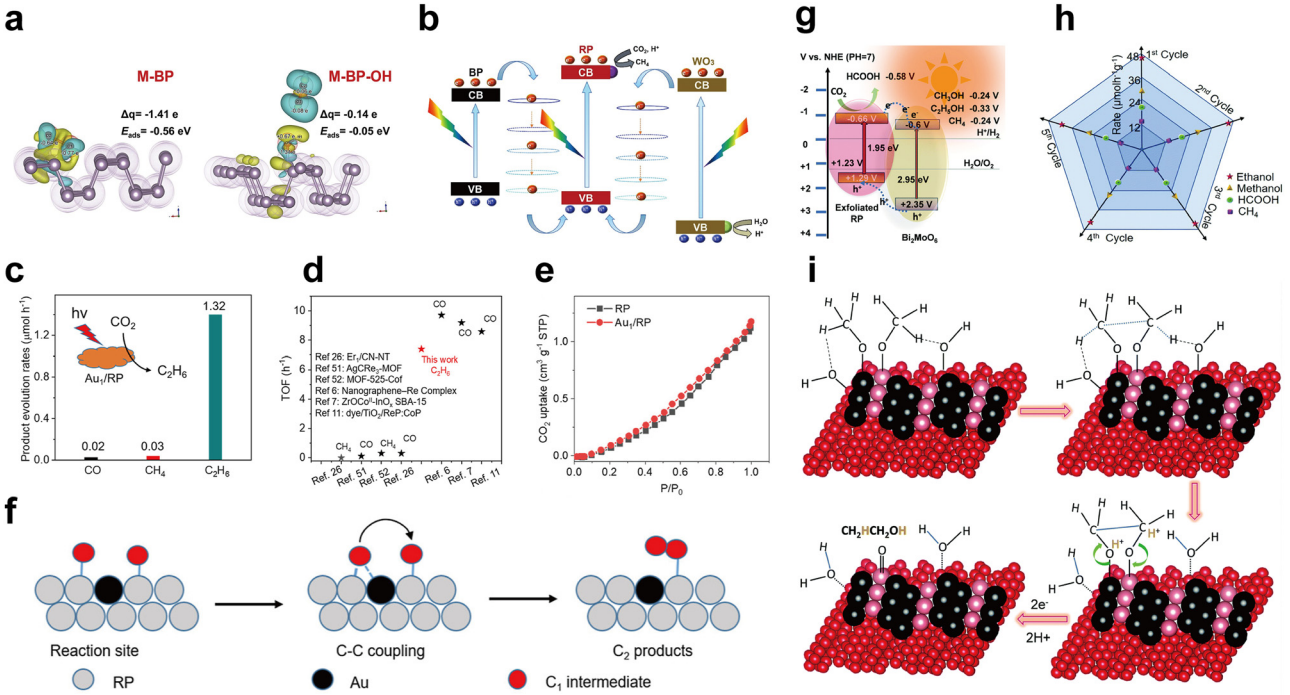

Fig. 31 Applications of elemental phosphorus materials to photocatalytic carbon dioxide conversion. (a) Charge difference of O_2 adsorbed on the black-P monolayer (M-BP) (left) and the hydroxyl-modified black-P monolayer (M-BP-OH). Reproduced with permission from ref. 428. Copyright 2020 Elsevier. (b) Scheme of the dual Z-scheme homo-heterojunction of red-P/black-P@WO_3 for photocatalytic CO_2 reduction. Reproduced with permission from ref. 429. Copyright 2022 American Chemical Society. (c) Photocatalytic CO_2 reduction rates of single-atom Au/red-P (Au_1/RP). (d) Comparison of TOF for photocatalytic CO_2 reduction of single-atom Au/red-P and other photocatalysts. (e) CO_2 adsorption curves of red-P and single-atom Au/red-P. (f) Proposed mechanism of single-atom Au/red-P for C–C coupling. Reproduced with permission from ref. 432. Copyright 2022 American Chemical Society. (g) Band structure alignment of the red-P/Bi_2MoO_6 heterostructure following the type-II mechanism. (h) The product formation rate of red-P/Bi_2MoO_6 in different cycles. (i) Proposed mechanism of photocatalytic ethanol production for red-P/Bi_2MoO_6. Reproduced with permission from ref. 434. Copyright 2022 Royal Society of Chemistry.

conduction band position than black-P and WO_3,[430] indicating its more negative reduction potential. Under visible light irradiation, black-P, red-P, and WO_3 generate charges in their respective conduction bands and valence bands. The photoinduced electrons in the conduction bands of black-P and WO_3 follow the Z-scheme vectorial transfer pathway to reach the valence band of red-P, where they recombine with holes in red-P. This effective separation and directional transport of the photoinduced electrons and holes in the ternary system contribute to the continuous progress of the photocatalytic reduction reaction.

Generating C_{1+} compounds in the photocatalytic reduction of CO_2 is typically more challenging than producing C_1 compounds (CO, CH_4, and CH_3OH). This process involves multiple electron and proton transfer reaction pathways, resulting in unsatisfactory catalytic efficiency and selectivity. Nonetheless, several C_2 compounds such as ethanol are crucial industrial chemicals and potential energy storage materials, and it is imperative to produce them in a cost-effective and environmental-friendly manner. Photocatalytic reduction of CO_2 to C_2 compounds involves a C–C coupling process, which requires overcoming a larger energy barrier during the reaction.[431] However, EPMs exhibit great potential for photocatalytic C_2 compound production based on the above discussion. From the physical perspective, EPMs are semiconducting materials with relatively narrow bandgaps, making them efficient for light harvesting in the infrared-visible light range, and they possess suitable conduction band edges for CO_2 photoreduction. From the chemical point of view, electron-rich EPMs can adsorb CO_2 on the surface through Lewis acid–base interactions, interact with O in the molecule, promote cleavage of C–O bonds, and generate large C_1 intermediates.[432,433] These physical and chemical properties have recently been exploited by some research groups.

In 2022, Li's group designed a single-atom Au loaded red-P photocatalyst for efficient ethane production.[432] The optimized single-atom Au/red-P catalyst exhibits a high ethane yield of 1.32 μmol g^{-1} h^{-1} without the need of any sacrificial agents. In contrast, the yields of CO and methane are only 0.02 and 0.03 g^{-1} h^{-1}, respectively, indicating excellent selectivity (96%) for ethane production (Fig. 31c). The turnover frequency (TOF) of the catalyst is also noteworthy, reaching as high as 7.39 h^{-1}, which exceeds those of many C_1 compound conversion photocatalysts (Fig. 31d). Various characterization techniques have been employed to demonstrate that CO_2 preferentially adsorbs on the surface of red-P (Fig. 31e) and provides active sites near each single-atom Au. This proximity effectively reduces the transfer distance of photoinduced electrons and C_1 intermediates. The presence of single-atom Au aids the desorption and movement of the C_1 intermediate at the phosphorus reactive site, followed by

C–C coupling at another phosphorus site (Fig. 31f).[432] Das *et al.* have developed a type-II red-P/Bi_2MoO_6 heterostructure photocatalyst capable of converting CO_2 into ethanol under visible light irradiation and water conditions (Fig. 31g).[434] The composite shows an excellent ethanol conversion rate of 51.8 mmol g^{-1} h^{-1}, whereas pristine red-P shows no detectable ethanol production as it mainly produces methane and formic acid after light irradiation for 10 hours. To expand the applicability of the catalyst, researchers have investigated the sunlight-directed photoreduction performance of the optimized red-P/Bi_2MoO_6 composite. The results reveal an ethanol yield of 34.1 mmol g^{-1} h^{-1}, which is 90.91% of that under Xe lamp irradiation. To evaluate the catalytic stability, the optimized composite undergoes five consecutive photocatalytic cycles and a continuous 30 hour catalytic test. The catalyst shows great recyclability and stability in CO_2 photoreduction and no noticeable change in the photoactivity (Fig. 31h). In the catalytic process, transformation of the C_1 intermediate is crucial for ethanol production. It has been found that using methane as a reactant does not lead to ethanol formation. However, a 300 mM methanol solution produces a high yield of 996.3 mmol h^{-1} g^{-1} of ethanol, indicating that methanol plays a crucial role as an intermediate in ethanol formation. A new ethanol formation mechanism has been proposed for the red-P/Bi_2MoO_6 heterostructure based on the kinetic isotope effects and *in situ* diffuse reflectance infrared Fourier transform spectroscopy, showing that one OCH_3* on the Bi atom and another OCH_3* on the Mo atom interact with the adjacent OH* groups on red-P and promote C–C coupling and C–H bond cleavage in OCH_3.[434] This leads to the formation of a $C_2H_4O_2$* intermediate with protons adsorbed on O centers (Bi) and C centers (Mo–O), ultimately resulting in ethanol production (Fig. 31i). The red-P in the composite provides strong visible light harvesting capability and abundant active sites, forms a heterojunction interface with Bi_2MoO_6 nanoparticles, prevents recombination of photoinduced charges, and improves the charge transfer efficiency of the system.

5.1.3 Electrocatalytic hydrogen evolution. Electrolysis of water ($H_2O(l) \rightarrow H_2(g) + 1/2O_2(g)$) has a rich history dating back to 1789.[435] As one of the water splitting half-cell reactions ($2H^+(aq) + 2e^- \rightarrow H_2(g)$), the hydrogen evolution reaction (HER) is an efficient and green process to convert a secondary energy source (electricity) into hydrogen fuel. Although the theoretical potential of a normal hydrogen electrode (NHE) is zero under standard conditions, the actual HER often requires a higher potential to surmount the kinetic barrier.[435] The discrepancy between the applied potential and Nernst potential in the HER is referred to as the overpotential (η).[436] Minimizing this overpotential is critical to enhancing the energy conversion efficiency and H_2 evolution rate but requires the development of exceptional electrocatalytic techniques for water splitting. Different from photocatalytic H_2 generation, the electrocatalytic HER relies on external circuit-induced carriers,[437] which enable easy regulation of the catalytic process and adjustment of catalytic efficiency by modifying the applied current.

The electrocatalytic HER mechanism is a multi-step reaction that typically takes place on the surface of the catalytic electrode layer.[438] It involves three main steps (adsorption, reduction, and desorption) and requires either hydronium ions in acidic electrolytes or water molecules in basic media (Fig. 32a).[439] The initial step in this process is the Volmer reaction (eqn (6) and (7)), in which a proton adsorbs at the active sites of the electrocatalyst and accepts an electron from the external circuit to form an adsorbed hydrogen atom (H*). Subsequently, a hydrogen molecule is generated through the Heyrovsky (eqn (8) and (9)) or Tafel (eqn (10)) routes, or both. In the Heyrovsky route, another proton migrates to the electrode surface to capture a second electron, which then combines with the adjacent H* to produce a hydrogen molecule. In contrast, in the Tafel route, two neighbouring H* interact on the electrode surface to generate H_2. Finally, hydrogen molecules are released from the surface of the catalytic electrode. The electrocatalytic HER can be written as follows:[435,440]

(1) Electrochemical hydrogen adsorption (Volmer reaction)

$$H_3O^+ + M + e^- \rightarrow M - H^* + H_2O \text{ (acidic electrolyte)} \quad (6)$$

$$H_2O + M + e^- \rightarrow M - H^* + OH^- \text{ (alkaline electrolyte)} \quad (7)$$

(2) Electrochemical desorption (Heyrovsky reaction)

$$H^+ + e^- + M - H^* \rightarrow H_2 + M \text{ (acidic electrolyte)} \quad (8)$$

$$H_2O + e^- + M - H^* \rightarrow H_2 + OH^- + M \text{ (alkaline electrolyte)} \quad (9)$$

(3) Chemical desorption (Tafel reaction)

$$2M - H^* \rightarrow H_2 + 2M \text{ (acidic and alkaline electrolytes)} \quad (10)$$

According to the Butler–Volmer equation,[441] the intrinsic exchange current density (i_0) and free energy of H adsorption (ΔG_{H^*}) are the crucial factors in catalytic reactions. The strength of the hydrogen–surface interaction can be used to determine the efficiency of an electrocatalytic surface in catalyzing the HER. Increasing the number of active sites or incorporating electron-rich groups into the electrode surface can decrease ΔG_{H^*} and increase i_0, which is particularly beneficial for proton reduction and hydrogen atom adsorption. In addition, the rate-determining step in the HER process differs between the Volmer–Heyrovsky and Volmer–Tafel pathways.[442,443] In the Volmer–Heyrovsky pathway, the Volmer reaction has a higher ΔG_{H^*} than the Heyrovsky reaction, making it the rate-determining step of the overall reaction. In contrast, in the Volmer–Tafel pathway, ΔG_{H^*} of the Tafel step is greater than that of the Volmer step, indicating that adsorbed hydrogen recombination determines the overall reaction rate.

Based on the analysis above, EPMs exhibit electron-rich properties, abundant active sites, and reasonable stability, boding well for the HER. Black-P has been extensively studied as an electrocatalyst or as a conductive scaffold with a large surface area. Luo *et al.*[444] utilized a simple solvothermal approach for preparing a 0D-2D Ni_2P@black-P heterostructure and demonstrated its excellent electrocatalytic activity for the HER. In the synthesis process, black-P nanosheets are used as precursors to react with nickel chloride, resulting in the formation of Ni_2P nanocrystals that are

monodispersed and incorporated in the black-P nanosheets to create a co-catalytic system. The electrocatalytic performance of Ni_2P@black-P was evaluated using a conventional three-electrode setup with a 0.5 M sulfuric acid solution. The overpotential of Ni_2P@black-P is only ~107 mV at 10 mA cm^{-2}, which is substantially lower than that of commercial Ni_2P particles (~311 mV) and pristine black-P nanosheets (600 mV). As shown in Fig. 32b, Ni_2P@black-P shows a small Tafel slope (38.6 mV dec^{-1}), which is comparable to that of a commercial Pt electrocatalyst (20 wt% Pt/Vulcan XC-72, 30 mV dec^{-1}), and the entire electrocatalytic process follows the Volmer–Tafel pathway.[444,445] Furthermore, the Ni_2P@black-P electrode maintains a stable current density at an overpotential of 107 mV and a well-defined crystalline morphology even after continuous scanning for 24 hours (Fig. 32c). The high performance of Ni_2P@black-P is related to the well-designed heterostructure which efficiently prevents Ni_2P nanoparticles from agglomeration and black-P nanosheets from restacking, thereby increasing the surface area and abundance of active sites. Additionally, the presence of Ni_2P tethered to the black-P surface modulates the charge carrier concentration and optimizes the HER kinetic rate. The electrocatalytic HER performance of NH_2-functionalized black-P nanosheets in alkaline electrolytes is also outstanding as exemplified by an overpotential of 290 mV at 10 mA cm^{-2} (Fig. 32d).[446] The Tafel slope of NH_2-black-P is 63 mV dec^{-1} (Fig. 32e) indicative of the Volmer–Heyrovsky mechanism. Moreover, NH_2-black-P exhibits good stability in the 12 hour chronoamperometric test, and the polarization curve remains nearly unchanged after 1000 consecutive cycles. Li *et al.*[447] have recently employed a modified CVT approach to synthesize black-P bulk crystals cost effectively, which are peeled off into nanostructured sheets for use as an HER electrocatalyst. The improved electrocatalytic activity of black-P nanosheets derived from low-cost bulk crystals can be attributed to the presence of more edge defects than in high-cost black-P, abundant exposed active sites, and promoted charge transport. Compared to the traditionally high price of black-P bulk crystals (about $600 per gram) made from ultrapure red-P,[93] there is potential to reduce the manufacturing costs of black-P and in

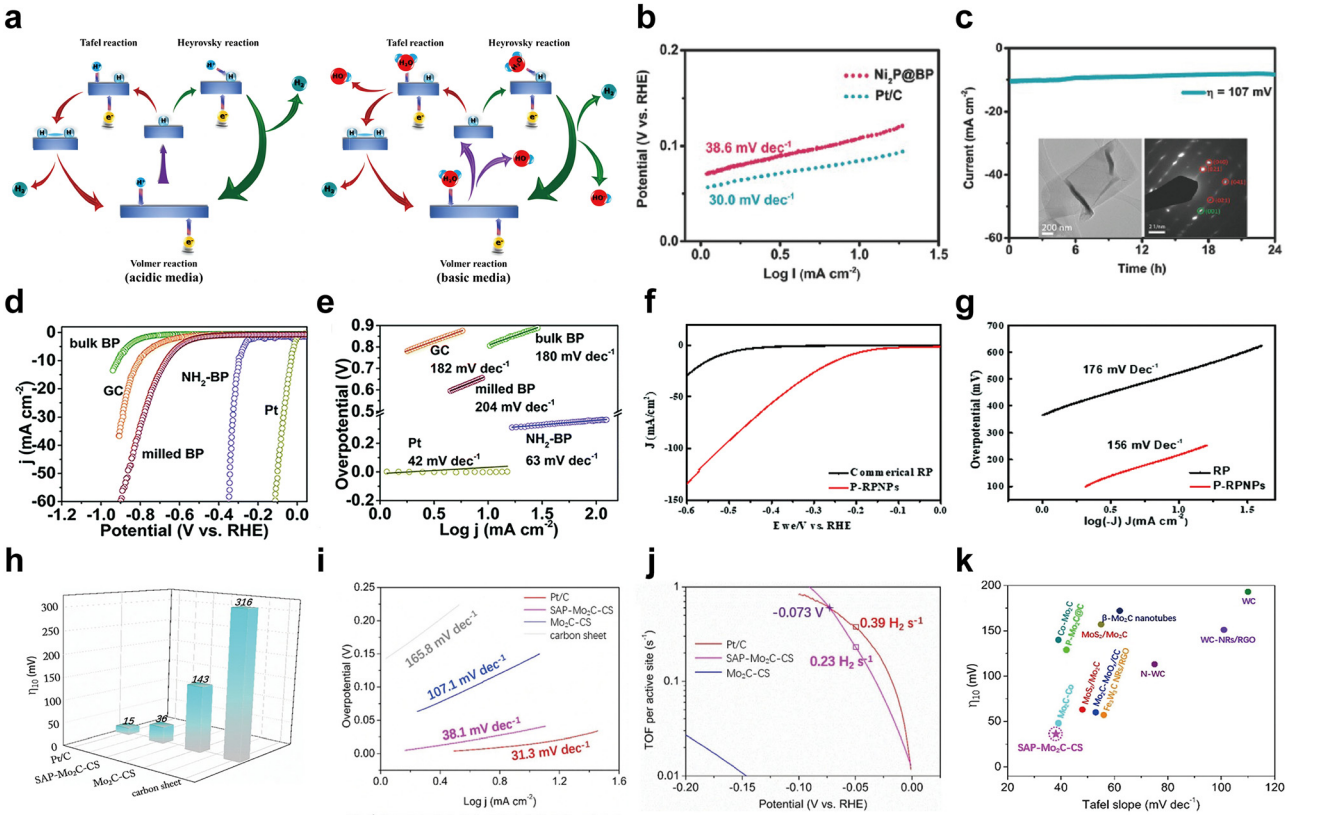

Fig. 32 Applications of elemental phosphorus materials to electrocatalytic hydrogen evolution. (a) Scheme of the hydrogen evolution mechanism on the surface of a catalyst in acidic (left) and basic (right) media. Reproduced with permission from ref. 439. Copyright 2019 Elsevier. (b) Corresponding Tafel plots for Ni_2P@black-P (BP) and Pt/C. (c) Time-dependent current density curves of Ni_2P@black-P under an overpotential of 107 mV. The inset shows the TEM image and SAED pattern after continuous sweeps for 24 hours. Reproduced with permission from ref. 444. Copyright 2016 John Wiley and Sons. (d) Voltammetry of different materials for the electrocatalytic HER at a scan rate of 5 mV s^{-1} in 1 M KOH. (e) Tafel plots derived from (d). Reproduced with permission from ref. 446. Copyright 2018 Royal Society of Chemistry. (f) Voltammetry of porous red-P nanoparticles (P-RPNPs) and commercial red-P at a scan rate of 5 mV s^{-1}. (g) Corresponding Tafel plots for porous red-P nanoparticles and red-P. Reproduced with permission from ref. 448. Copyright 2020 Royal Society of Chemistry. (h) Corresponding overpotentials at a current density of 10 mA cm^{-2} (η_{10}), (i) Tafel plots, and (j) TOF plots of four electrocatalysts. (k) The η_{10} *vs.* Tafel slope of SAP-Mo_2C-CS compared to the reported TMC-based catalysts. Reproduced with permission from ref. 454. Copyright 2020 John Wiley and Sons.

fact, cost reduction by hundreds of times will promote widespread use of black-P-based electrocatalysts in industrial production.

Porous red-P nanoparticles have been reported as a potential metal-free electrocatalyst for the HER.[448] Uniform porous red-P nanoparticles have been prepared by a simple one-pot injection method involving decomposition of the precursor P_xI_y and adding oleic acid for shape control. To evaluate the electrocatalytic performance, the nanoparticles are dissolved in toluene as ink and applied to enable red-P to stick to the surface of the working electrode. As shown in Fig. 32f, the porous red-P nanoparticles show an overpotential of 218 mV at a current density of 10 mA cm^{-2}, which is substantially lower than that of commercial red-P (523 mV), indicating that the porous morphology improves the HER electrocatalytic efficiency. At this current density, the overpotentials of most metal-free electrocatalytic materials such as CNTs[449] and N-S co-doped graphene[450] are in the range of 200–425 mV,[451] and porous red-P nanoparticles have excellent properties in this range, which are even comparable to metal catalysts such as MoS_2 nanosheets with an overpotential of 205 mV.[452] The Tafel slope is 156 mV dec^{-1} (Fig. 32g), suggesting that the overall reaction rate is controlled by diffusion.[441,448] The long-term stability of porous red-P nanoparticles is confirmed in an acidic medium after 45 hours at a static potential of −0.5 V (*vs.* RHE) and the cathode current density remains constant even after 6000 cyclic voltammetry cycles from −0.6 to 0.2 V.

Single-atom catalysts have garnered significant attention in electrocatalysis due to their exceptional atom utilization efficiency and notable reaction selectivity.[453] However, the majority of single-atom catalysts employ metal elements and the synthesis of non-metal single-atom catalysts is uncommon. Nevertheless, the electron-rich active sites of non-metal catalysts exhibit reasonable interactions with hydronium ions in acidic media, indicating their great potential for the electrocatalytic process. To maximize the utilization efficiency of phosphorus in the electrocatalytic process, Fu *et al.* prepared a highly dispersed single-atom phosphorus embedded on a single-crystal Mo_2C nanosheet array supported by a carbon sheet (SAP-Mo_2C-CS) and demonstrated the robust performance as an electrocatalyst for the HER.[454] As shown in Fig. 32h, SAP-Mo_2C-CS shows an overpotential of 36 mV at a current density of 10 mA cm^{-2}, which is comparable to that of the commercial Pt/C electrode (15 mV), and significantly lower than that of Mo_2C on carbon sheets (143 mV) and pristine carbon sheets (316 mV). The Tafel slope of SAP-Mo_2C-CS (38.1 mV dec^{-1}) indicates that the HER process mainly follows the Volmer–Tafel mechanism (Fig. 32i) and hence, recombination of the adsorbed hydrogen species determines the overall reaction rate. To elucidate the intrinsic catalytic activity of SAP-Mo_2C-CS, researchers have calculated the turnover frequency (TOF) of each active site (Fig. 32j). At an overpotential of 0.05 V, the TOF of SAP-Mo_2C-CS is 0.23 H_2s^{-1}, which is similar to the value of Pt/C (0.39 H_2s^{-1}) and considerably higher than that of Mo_2C on carbon sheets, confirming that the phosphorus single atoms are the primary active sites in SAP-Mo_2C-CS. Notably, SAP-Mo_2C-CS exhibits higher catalytic activity in acidic electrolytes than many transition metal carbides (Fig. 32k) and also maintains the stable HER activity during the chronopotentiometry test for 11 hours. To probe the mechanism for the high-performance activity of SAP-Mo_2C-CS, researchers have conducted DFT calculations to simulate the entire catalytic process. The results indicate that the presence of anchored phosphorus single atoms on Mo_2C results in chemical coupling and accompanying electron redistribution for the unique HER kinetics. This leads to a free energy of hydrogen adsorption (ΔG_{H^*}) that is almost zero and hydrogen binding strength that is sufficient to cover the surface, but weak enough to facilitate desorption of H_2 molecules for the exceptional HER activity.

5.1.4 Electrocatalytic oxygen evolution. The oxygen evolution reaction (OER), which takes place on the anodic side of the water-splitting half-cell reactions ($2H_2O(l) \rightarrow 4e^- + 4H^+(aq) + O_2(g)$), is a complex four-electron transfer process with multiple steps, making its reaction kinetics more complicated than that of the HER.[455,456] The OER requires a higher energy input to overcome the significant kinetic barriers.[457] Due to the substantial overpotential generated throughout the entire process, OER electrocatalysis imposes stricter requirements on catalysts which must possess outstanding catalytic efficiency and long-term chemical stability.

Regarding the mechanism, owing to the complexity of the basic reaction involving multi-electron transfer, a comprehensive and unified mechanism for OER electrocatalysis is yet to be established. Several studies have proposed alternative processes for the OER under different conditions. Most of the reported studies on OER electrocatalysis have been conducted under alkaline conditions, and the mechanism of OER electrocatalysis in the alkaline medium can be described as follows:[457,458]

$$M + OH^- \rightarrow MOH + e^- \quad (11)$$

$$MOH + OH^- \rightarrow MO + H_2O + e^- \quad (12)$$

$$2MO \rightarrow 2M + O_2 \quad (13)$$

$$MO + OH^- \rightarrow MOOH + e^- \quad (14)$$

$$MOOH + OH^- \rightarrow M + O_2 + H_2O \quad (15)$$

The electrocatalytic active site, denoted by M, initiates the process by adsorbing OH^- (eqn (11)). The resulting MOH intermediate then interacts with a second OH^- ion to form an intermediate MO (eqn (12)). However, researchers have differing opinions on the subsequent reaction that leads to the formation of oxygen, suggesting two possible pathways for the generation of O_2 from the MO intermediate. In one proposed route, two MO molecules combine to produce O_2 (eqn (13)) but in the other pathway, MO reacts with another OH^- to form an intermediate MOOH which subsequently decomposes to O_2 (eqn (14) and (15)). Although there may be numerous reaction pathways, it is evident that OER electrocatalysis occurs through heterogeneous catalysis, with the interaction between OH species and the active site playing a critical role in OER electrocatalysis.[459]

Significant efforts have been dedicated to investigating the OER electrocatalytic activity of EPMs. In 2016, Jiang *et al.*[460] evaluated the OER performance of black-P materials and

observed that even black-P bulk forms supported on Ti foil or carbon nanotubes required only 1.6 V (*vs.* RHE) to achieve a current density of 10 mA cm^{-2}, which is comparable to that of well-known commercial RuO_2 (1.59 V)[461] and IrO_2 (1.57 V)[462] electrocatalysts. This work demonstrates the potential of EPMs for OER electrocatalysis and encourages further research into the electrocatalytic efficiency of low-dimensional black-P and other phosphorus allotropes. Zhang's group systematically investigated the performance of few-layered black-P nanosheets in the electrocatalytic OER process.[463] The 2D structure of nanosheets has more active sites for higher electrocatalytic efficiency than the bulk counterpart, even allowing it to compete with some heterostructure materials.[460,464,465] To examine the electrocatalytic performance of black-P nanosheets, a three-electrode setup with a gradient concentration of potassium hydroxide (KOH) electrolyte is used and surprisingly, when the electrolyte concentration goes up, the electrocatalytic capability of black-P nanosheets improves approximately linearly. Under optimal conditions, *i.e.*, in 1 M KOH solution, black-P nanosheets exhibit an enhanced current density of 2.7 mA cm^{-2} at 1.6 V potential and a reduced onset potential (~1.45 V). The Tafel slopes of black-P nanosheets in 1, 0.2, 0.1, and 0.05 M KOH are 88, 138, 218, and 307 mV dec^{-1},[463] respectively, demonstrating that the OH^- concentration influences the electrocatalytic performance (Fig. 33a and b). The high-concentration hydroxide solution promotes electron transport between the electrolyte and electrode and also makes the nanosheets more stable. Fig. 33c shows the current density fluctuation of black-P nanosheets around 6.2 mA cm^{-2} in 1 M KOH. It is higher than the current densities for lower concentrations of KOH over time. After 10 000 s, the black-P nanosheets in 1 M, 0.2 M, and 0.1 M KOH show no decay in the current density, while a slight drop in the current density is observed from 0.05 M KOH. Furthermore, the polarization curves of black-P nanosheets before and after the reaction remain almost unchanged, except in 0.05 M KOH (Fig. 33d), indicating that few-layered Black-P electrocatalysts exhibit great long-term stability within a certain range of alkaline electrolyte concentrations. DFT-based theoretical calculations have shown that the oxidation level of pristine EPMs influences the electrocatalytic activity of the OER.[466] Due to the lone electron pair feature of phosphorus atoms, the catalytic site shows excessive adsorption to the reaction intermediates (MOH, MO and MOOH), blocking the subsequent reactions or impeding O_2 desorption. Changes in the local oxidation degree $\left(D^{\circ}_{\mathrm{local}}\right)$ of phosphorene can affect the adsorption energy of O*. When $D^{\circ}_{\mathrm{local}} \geq 1.8$, the O* adsorption strength decreases rapidly with increasing $D^{\circ}_{\mathrm{local}}$. Therefore, partially oxidizing the phosphorus surfaces may alleviate the adsorption strength and increase the catalytic efficiency.

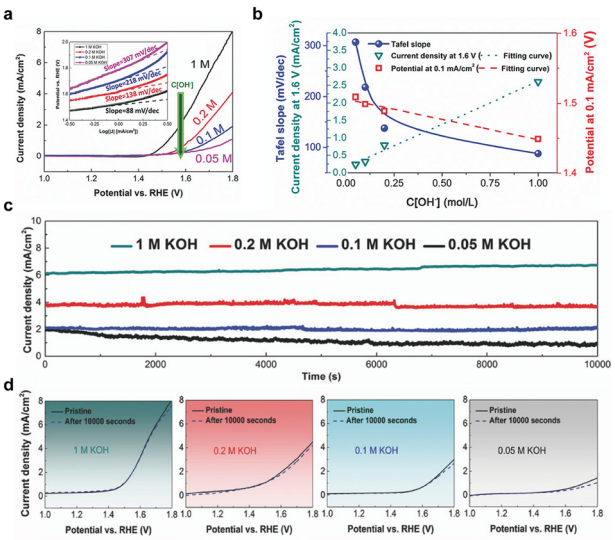

Fig. 33 Application of few-layered black-P nanosheets to electrocatalytic oxygen evolution. (a) Polarization curves of black-P nanosheets in KOH electrolyte with varied concentrations. The inset shows their corresponding Tafel plots. (b) Calculated Tafel slope, the current density at 1.6 V, and potential at 10 mV cm^{-2} in relation to the concentration of OH^-. (c) Electrocatalytic OER stability of black-P nanosheets in KOH electrolyte with varied concentrations. (d) Polarization curves of black-P nanosheets in corresponding KOH electrolytes before and after 10 000 seconds. Reproduced with permission from ref. 463. Copyright 2017 John Wiley and Sons.

Similar to HER electrocatalysis, element doping,[467] combination with other materials,[468] and designing catalyst scaffolding[469] are strategies to enhance the OER electrocatalytic activity of EPMs. Inspired by a novel photocatalyst of red-P–black-P heterostructure created by Shen and colleagues,[470] Xu's group synthesized a series of composites of red-P–black-P chemically bonded with expanded graphite (RP-BP/EG) or carbon nanotubes (RP-BP/CNTs) using a high-energy ball milling technique and compared the OER electrocatalytic activities.[471,472] The primary factors influencing the catalytic performance of the composites are the ball-milling time and relative mass ratio of the carbon-based materials. The P–C bond cannot be formed if the ball-milling time is too short but if it is too long, the heterogeneous structure collapses, and the catalyst surface is damaged, hindering O* adsorption. Excess or insufficient EG or CNTs can make it difficult for the active sites to form or be buried. Under optimum circumstances, the overpotential of RP-BP/EG reaches 328 mV *vs.* RHE at 10 mA cm^{-2}. Although this value is similar to that of some nitrogen-doped carbon materials and surface-oxidized multiwall carbon nanotubes,[471,473,474] the overpotential of RP-BP/CNTs is only 263 mV at the same current density.[472] The Tafel slope of RP-BP/EG is smaller than that of RP-BP/CNTs, indicating that the former has a faster electron transfer rate or the two systems have different rate-determining steps. However, the strength of the P–C bond varies due to the diversity of carbon nanostructures thus altering the stability of heterostructures, and the nanostructures also impact the catalytic area and density of active sites. Further investigations are required to determine the influence of composite nanostructures on OER electrocatalytic efficiency.

EPMs have shown promise in both the HER and OER, and researchers have attempted to develop these materials as bifunctional electrocatalysts for overall water splitting. In 2018, our group synthesized monodispersed in-plane black-P/Co_2P heterostructures by a simple solvothermal method in

which Co_2P nanocrystals were selectively grown on black-P edge defects.[475] Co_2P in the heterostructure not only occupies the black-P defects to improve the stability, but also provides more effective electrocatalytic active sites. Moreover, the bulging morphology alleviates agglomeration of black-P nanosheets and increases the exposure of active sites and gas effusion. The electrocatalytic activities and stability for the HER and OER are improved compared to pristine black-P and they are even comparable to those of commercial electrocatalysts (Fig. 34a–d). Given the outstanding performance of black-P/Co_2P in the HER and OER, a dual-electrode system has been constructed with black-P/Co_2P as both the cathode and anode to evaluate the overall water-splitting activity in 1.0 M KOH electrolyte (Fig. 34e).[475] The system achieves a current density of 10 mA cm^{-2} at a voltage of 1.92 V (Fig. 34f), demonstrating the great potential of this electrocatalyst for overall water splitting. Similarly, Li *et al.* prepared a bifunctional HER/OER catalyst (CoFeO@Black-P) by growing amorphous multi-transition metal (cobalt and iron) oxides on 2D black-P nanosheets.[476] The water electrolysis cell with CoFeO@Black-P electrodes reaches a current density of 10 mA cm^{-2} at a voltage of 1.58 V in 1 M KOH, and maintains 93% of the initial current density after the 24 hour of operation (Fig. 34g and h). As shown in Fig. 34i, metastable CoFe oxides can react with the phosphorus source provided by black-P to *in situ* form CoFe phosphide as the active sites in HERs. On the other hand, the rich oxygen vacancies in CoFe oxides catalyze the OER through lattice oxygen oxidation mechanism. Other effective bifunctional electrocatalysts including BPQDs/MXene nanohybrids,[477] black-P@N-doped graphene,[478] and black-P@red-P-g-C_3N_4,[479] have also been reported for overall water splitting.

5.1.5 Electrocatalytic and photocatalytic nitrogen reduction. Ammonia (NH_3) is one of the largest-output chemical products in the world,[480–482] and holds considerable importance in the global economy. For centuries, scientists have sought to convert atmospheric nitrogen into ammonia for industrial applications, and the Haber–Bosch process was developed in the early twentieth century to realize this goal. Today, the Haber–Bosch process remains widely employed and accounts for nearly 90% of global ammonia production annually.[483,484] However, the primary limitation of this technique is the high temperature (350–550 °C) and pressure (200–350 atm) required in the reaction.[485,486] Consequently, the Haber–Bosch process is a high-energy demanding process, contributing to approximately 1% of worldwide annual

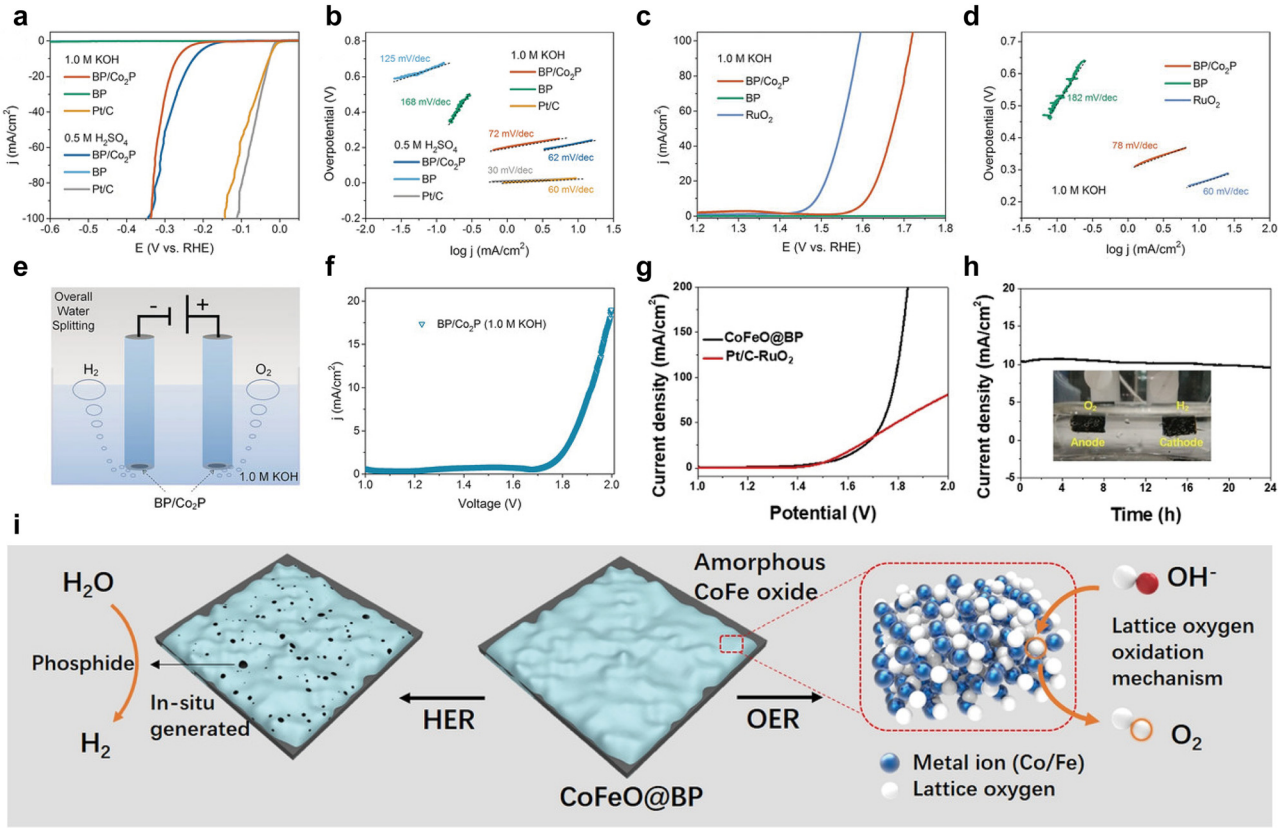

Fig. 34 Applications of elemental phosphorus materials to electrocatalytic overall water splitting. (a) HER polarization curves of pristine black-P (BP), BP/Co_2P, and Pt/C in 0.5 M H_2SO_4 and 1.0 M KOH. (b) Corresponding Tafel plots for BP, BP/Co_2P, and Pt/C in (a). (c) OER polarization curves of BP, BP/Co_2P, and RuO_2 in 1.0 M KOH. (d) Corresponding Tafel plots for BP, BP/Co_2P, and RuO_2 in (c). (e) Scheme of electrocatalytic overall water splitting for BP/Co_2P. (f) Polarization curve of BP/Co_2P for overall water splitting in 1.0 M KOH. Reproduced with permission from ref. 475. Copyright 2018 John Wiley and Sons. (g) Polarization curves of CoFeO@black-P and Pt/C-RuO_2 for overall water splitting. (h) Stability test of CoFeO@black-P. The inset shows bubble formation from both electrodes during electrolysis. (i) Proposed mechanism of CoFeO@black-P for electrocatalytic overall water splitting. Reproduced with permission from ref. 476. Copyright 2020 John Wiley and Sons.

energy consumption.[487] Inspired by the natural nitrogen fixation of rhizobia,[488] researchers are exploring milder methods to achieve an ambient nitrogen reduction reaction (NRR). Electrocatalytic and photocatalytic NRRs offer promising and sustainable strategies for future ammonia production.

Understanding the mechanism of the NRR process is critical to designing an ideal NRR catalyst. Generally, nitrogen reduction on a heterogeneous catalyst surface follows either an associative or dissociative pathway, where the primary difference between the two is the time required to break the N≡N triple bond (Fig. 35a).[484,489] In the associative process, a nitrogen molecule initially adsorbs on the catalyst surface and is then hydrogenated. Following hydrogenation, the N≡N triple bond breaks, leading to the formation of ammonia molecules. Since the nitrogen molecule contains two nitrogen atoms, hydrogenation occurs through two distinct routes: distal and alternating hydrogenation. In the distal route, hydrogenation commences on the N atom farthest from the catalyst surface, and one NH_3 molecule is formed from this N atom. The hydrogenation process then proceeds to the N atom closest to the catalyst surface, generating the second NH_3 molecule. In contrast, in the alternating route, hydrogenation occurs alternately between the two N atoms, resulting in a continuous hydrogenation cycle where the first NH_3 molecule is released immediately followed by the second NH_3 molecule. On the other hand, in the dissociative process, the N≡N triple bond breaks before hydrogenation, leaving two adsorbed N atoms on the catalyst surface. These two atoms are then hydrogenated individually before forming NH_3 molecules. It is worth mentioning that the specific NRR mechanism (associative or dissociative) followed by different NRR catalysts is mostly driven by their atomic and electronic structures,[490] which must be verified by theoretical calculations and experiments.

Developing high-performance NRR catalysts is a challenging task. The cleavage of the N≡N triple bond requires a significant amount of energy (941 kJ mol^{-1}),[491] and throughout the catalytic process, the HER always competes with the NRR at the catalytically active sites,[487,488,492] leading to a catalytic selectivity issue. Therefore, a state-of-the-art NRR catalyst must not only fulfil the conventional requirements for a high density of active sites and material stability, but also exhibit exceptional catalytic selectivity. This means that the catalyst surface binding strength of nitrogen must be greater than that of hydrogen to favour electron transfer along the NRR pathway. Due to the similar valence electronic structures of phosphorus and nitrogen ($3s^2 3p^3$ and $2s^2 2p^3$, respectively),[21,493] nitrogen has a stronger affinity for the surface of phosphorus-based materials, giving EPMs a unique advantage as NRR catalysts.

In 2019, Wang's group demonstrated that few-layered black-P nanosheets perform well as NRR electrocatalysts under ambient conditions.[494] To determine the electrocatalytic activity, they selected 0.01 M HCl as the acidic electrolyte in a standard three-electrode setup, and a few-layered black-P suspension was dropped onto carbon fibers as the working electrode. As shown in Fig. 35b and c, the catalytic electrode achieved the highest Faradaic efficiency of 5.07% at −0.6 V, with a maximum NH_3 production rate of 31.37 μg h^{-1} $mg_{cat.}{}^{-1}$ at −0.7 V. The few-layered black-P electrocatalyst outperforms its bulk counterpart (0.13% Faradaic efficiency, 0.036 μg h^{-1} $mg_{cat.}{}^{-1}$), as well as various metal-free catalysts (*e.g.*, N-doped porous carbon with a Faradaic efficiency of 1.42% and 23.8 μg h^{-1} $mg_{cat.}{}^{-1}$) and metal-based catalysts (*e.g.*, Au–TiO_2 sub-nanoclusters with a Faradaic efficiency of 8.11%and 21.4 μg h^{-1} $mg_{cat.}{}^{-1}$).[495,496] Moreover, the UV/vis absorption spectra and chromogenic reactions indicate that no obvious side-product (N_2H_4) is generated throughout the electrocatalytic process, confirming the high catalytic selectivity of few-layered black-P. Based on DFT calculations for the molecular orbitals of black-P, the NRR catalytic process follows an alternating hydrogenation pathway in an association mechanism (Fig. 35d).[494] This study not only demonstrates the feasibility of using black-P materials for the electrocatalytic NRR under ambient conditions, but also serves as a model for investigating the NRR mechanisms of EPMs. Zhu's group has reported a straightforward vdW assembly approach for loading BPQDs onto wrinkled MnO_2 nanosheets (Fig. 35e), which leads to enhanced NRR electrocatalytic activity compared to pristine materials.[497] The maximum NH_3 generation rate of BPQDs/MnO_2 is 25.3 μg h^{-1} $mg_{cat.}{}^{-1}$ and its Faradaic efficiency is 6.7% at an applied potential of −0.5 V (*vs.* RHE). The outstanding electrocatalytic performance can be ascribed to the strong synergistic effects of BPQDs/MnO_2.[497] The wrinkled MnO_2 nanosheets act as a flexible substrate to prevent severe BPQD aggregation during the catalytic process. The edges and defect sites of MnO_2 nanosheets exhibit reasonable electrocatalytic activity. Moreover, BPQDs with an abundance of active sites serve as the primary NRR catalyst and physical spacer to prevent restacking of MnO_2 nanosheets and maintain the structural stability of the composite.

Other EPMs have also shown potential for NRR electrocatalysis. Our group has conducted a series of DFT calculations and found that crystalline red-P (fibrous phase) nanoribbons have potential electrochemical nitrogen fixation activity. On the surface of crystalline red-P nanoribbons, the NRR process can be carried out through the proton-coupled electron transfer pathway, with the associative mechanism being preferable, followed by distal hydrogenation. The initial step of adsorbed N_2 hydrogenation to NNH* is proposed to be the rate-determining step due to the largest energy input required. Experimentally, we have carried out the electrocatalytic test in a gastight H-type electrolytic cell with 0.1 M Na_2SO_4 electrolyte and placed crystalline red-P nanoribbons onto a nickel foam as the catalytic electrode. The catalytic electrode delivers efficient and durable NRR performance, at an optimal NH_3 production rate of 15.4 μg h^{-1} $mg_{cat.}{}^{-1}$ at −0.4 V and a faradaic efficiency of 9.4% at −0.2 V. Compared to the few-layered black-P electrocatalyst developed by Wang's group, crystalline red-P nanoribbons exhibit a lower optimal voltage but a higher Faradaic efficiency due to the increased charge transfer and exposed-edge active sites of the quasi-1D structure.[47] However, the ammonia production rate of crystalline red-P nanoribbons is still limited and the development of red-P-based materials for NRR electrocatalysis still has a long way to go.

Compared to the deeper armchair ridges of black-P, the hexagonal lattice structure of blue-P with zigzag ridges is

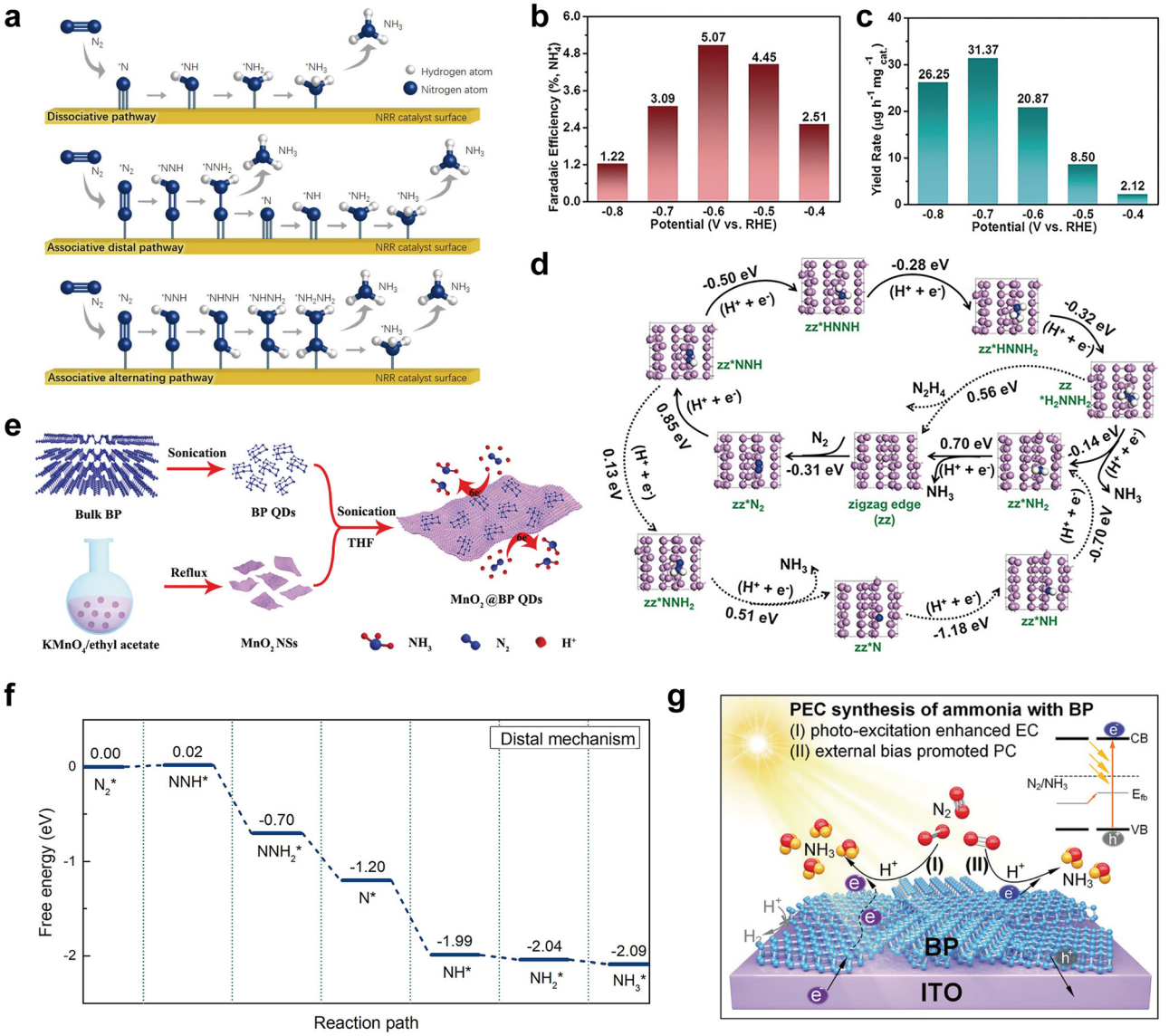

Fig. 35 Applications of elemental phosphorus materials to electrocatalytic and photocatalytic nitrogen reduction. (a) Scheme of possible mechanisms of the NRR process on the catalyst surface. Reproduced with permission from ref. 489. Copyright 2019 Elsevier. (b) Faradaic efficiency and (c) NH_3 yield rate of few-layered black-P nanosheets at different potentials. (d) Scheme of the possible reaction mechanisms (solid line: low-energy pathway and dotted line: unfavourable pathway) for the electrocatalytic NRR at the zigzag edge of few-layered black-P nanosheets under a N_2 atmosphere. Reproduced with permission from ref. 494. Copyright 2019 John Wiley and Sons. (e) Scheme of the preparation of MnO_2 nanosheets, BPQDs, and the vdW assembly of BPQDs onto MnO_2 nanosheets for NRR electrocatalysis. Reproduced with permission from ref. 497. Copyright 2020 John Wiley and Sons. (f) Free energy diagrams of the NRR process on W-N_3@blue-P along the distal mechanism. Reproduced with permission from ref. 498. Copyright 2020 Elsevier. (g) Photoelectrochemical NRR mechanisms of black-P under light irradiation and external electric field. Reproduced with permission from ref. 502. Copyright 2020 John Wiley and Sons.

relatively isotropic, making it an ideal candidate for multi-electron transfer. Recently, Zhang *et al.* have demonstrated that a kinetically stable W-N_3 center supported by blue-P exhibited great NRR catalytic activity with a limit potential of −0.02 V based on DFT calculations.[498] The W atom plays a crucial role in weakening the N≡N triple bond by accepting lone electron pairs from N_2 and donating electrons to the anti-bonding orbitals of N_2,[499] enabling N_2 molecules to readily adsorb on the composite surface. The Gibbs free energy variations of the intermediates suggest that the associative distal mechanism is the most favourable in this system (Fig. 35f). Additionally, the high selectivity of the NRR can be achieved due to the high free energy barriers for the HER (0.83 eV) and the ultralow free energy barriers for the NRR (0.02 eV). This work provides theoretical guidance for the development of blue-P-based NRR electrocatalysts.

The solar-powered photocatalytic NRR is a promising low-cost, green, and sustainable strategy for ammonia production. However, the high energy barrier of the six-electron reaction that activates and breaks the strong N≡N bond by photocatalysts,

hinders the reaction kinetics, resulting in relatively low photocatalytic NRR efficiency. Thus, developing highly active photocatalysts is crucial for achieving an efficient photocatalytic NRR. Our group has synthesized edge-rich black-P nanoflakes using a simple chemical etching exfoliation method, which achieves an efficient photocatalytic NRR without using any cocatalysts.[500] The abundant edges of the resulting nanoflakes offer numerous active sites for N_2 adsorption and complete activation of the $N\equiv N$ bond to enhance the reduction of N_2. Moreover, the black-P nanoflakes exhibit good water dispersibility, enabling full contact with the reactants. As a result, edge-rich black-P shows a high catalytic nitrogen fixation rate of 2.37 mmol h^{-1} g^{-1} under visible light irradiation, which is higher than 0.9 mmol h^{-1} g^{-1} shown by conventional black-P nanoflakes. This work highlights the impact of black-P morphology on catalytic efficiency, and the development of black-P materials with nanostructured design for NRR electrocatalysis is a promising research direction. Alternatively, incorporating co-catalysts has demonstrated acceleration of charge transfer and improvement in photocatalytic nitrogen conversion to some extent. However, controlling the interface state and studying the charge transfer at the interface remain a challenge. To address this, Shen *et al.* have selectively deposited a Ni_2P layer at the edge of black-P nanosheets, forming a 2D–2D heterojunction with plentiful Ni–P bonds.[501] The resulting Ni_2P–BP heterojunction has improved photocatalytic NRR properties such as an NH_3 generation rate of 6.14 μmol h^{-1} g^{-1} under visible light irradiation, which is 1.56 times higher than that of the Ni–P bond-free Ni_2P nanoparticle loaded black-P photocatalyst. This indicates that the interfacial Ni–P bonds plays a critical role in the catalytic process by facilitating interfacial charge transfer and enabling photoexcited electrons on the conduction band of black-P to efficiently transfer to Ni_2P and enhance the separation efficiency of electron–hole pairs. Moreover, the Ni_2P layer chemically passivates the edges of the black-P nanosheets and improves the stability of the system during the electrocatalytic process.

Compared to the electrocatalytic process with continuous and stable external bias potentials, the photocatalytic NRR faces challenges of low conversion efficiency and unstable conversion processes. However, by combining the advantages of both photocatalysis and electrocatalysis, the N_2-to-NH_3 conversion efficiency can be further improved through photoelectrochemical reactions. With these principles in mind, our group has developed a black-P photoelectrochemical electrode and investigated its catalytic nitrogen conversion activity under normal environmental conditions.[502] The electrode shows remarkable catalytic activity with an ammonia yield rate of 102.4 μg h^{-1} $mg_{cat.}^{-1}$ and a Faradaic efficiency of 23.3% at −0.4 V, outperforming most metal-free photocatalysts or electrocatalysts for the NRR.[502] Moreover, the black-P electrode exhibits great stability after 6 consecutive cycles. The exceptional NRR activity of the black-P electrode can be ascribed to the synergistic effect generated by photoexcitation and external bias (Fig. 35g), in which the photoexcitation boosts the average electron energy and charge exchange efficiency and facilitates the electrocatalytic process, while the external bias potentials improve the separation of photoexcited electron–hole pairs, promoting the photocatalytic process. Considering the excellent charge mobility of black-P and the strong visible-light absorption and chemical stability of red-P based materials such as amorphous red-P, violet-P, and fibrous-P, the future development of black-P/red-P homojunctions for photoelectrochemical ammonia production holds great promise.

This section has discussed the mechanism and performance of EPMs in photocatalytic/electrocatalytic water splitting, carbon dioxide reduction, and nitrogen fixation. It has underscored the need for a deeper understanding of reaction pathways and intermediate products in the catalytic processes involving different phosphorus materials. Attention should be given to the role of excitons in photocatalysis, the selectivity in carbon dioxide reduction, and how certain material structures lead to different products. For electrocatalysis, the establishment of standardized criteria to assess the catalytic activity of EPMs and evaluating their contributions in composite systems are areas warranting further exploration.

5.2 Energy storage applications

5.2.1 Hydrogen storage. Hydrogen is a sustainable energy carrier and plays an essential role in solving energy crises and environmental concerns. However, one of the major obstacles to its widespread use is the lack of efficient hydrogen storage technologies, particularly in fuel cell-based light-duty vehicle systems.[503,504] Currently, the most common method for hydrogen storage is compressed gas storage but this method involves storing gaseous hydrogen in an alloyed tank at a pressure of 700 bar with a gravimetric density of 4.2 wt%.[505] Although this approach is simple and efficient, it poses safety concerns such as gas leakages, high-pressure operations, and vessel explosions. Another widely used technology for hydrogen storage is liquefaction which was developed in the 1990s. This approach involves cooling hydrogen to −253 °C to produce liquefied hydrogen.[506] The liquefaction storage density (70.8 kg m^{-3}) is much higher than that of compressed gas (35 kg m^{-3}), but it suffers from evaporation loss and high energy consumption problems.

Solid-state storage technologies such as metal hydride techniques, physisorption, and chemical adsorption have garnered considerable attention as a potential alternative to conventional hydrogen storage technologies.[507] The search for suitable solid-state storage materials is ongoing and promises to yield exciting possibilities.[508–510] According to the US Department of Energy (USDOE) targets for 2020,[511–513] high-efficiency hydrogen storage materials with a gravimetric density of 5.5 wt% should be employed with hydrogen reversibility occurring at temperatures ranging from −40 to 60 °C at a filling/releasing rate of 1.5 kg H_2 min^{-1}. This criterion requires that the energy associated with adsorbing each hydrogen molecule must be within an appropriate range to regulate the adsorption/desorption kinetics. To date, many publications have demonstrated that carbonaceous materials can be used for hydrogen storage.[514–516] However, pure carbon atoms have a low affinity for hydrogen, and therefore, metal doping is a viable strategy for enhancing hydrogen adsorption. Nonetheless, metal atoms are prone to clustering on

the carbon matrix, resulting in low reversibility and an inability to meet the long-term hydrogen storage requirement.

In comparison to carbonaceous materials, metal atoms on phosphorene exhibit significantly lower tendencies for cluster formation. Although phosphorene is heavier than graphene, it is lighter than many other prominent 2D materials, including MXenes and TMDs, resulting in a high gravimetric density. In 2014, Li *et al.*[517] conducted the first study on Li-decorated monolayer black-P using theoretical calculations. Li-decorated black phosphorene exhibits a hydrogen storage capacity of 8.11 wt% and average adsorption energy of 0.18 eV per H_2, exceeding the hydrogen storage targets established by USDOE. Luo *et al.*[513] have demonstrated better hydrogen storage performance for Li-decorated single-layered blue-P. At a Li/P ratio of 1:1, the interaction between Li atoms and blue-P is sufficiently strong, maintaining the Li atom dispersion. Due to the space constraint surrounding Li atoms, double-layer adsorption occurred, and each atom can adsorb two molecules of H_2, leading to a hydrogen storage capacity of 9.52 wt%. This can be attributed to blue phosphorene having a flatter in-plane structure than black phosphorene, and the zigzag ridges aiding in the dispersion of Li atoms. Recently, Xu *et al.*[518] have used a solvothermal approach to prepare Co-doped black-P nanosheets and evaluated their efficacy in electrochemical hydrogen storage. The optimal hydrogen storage capacity of Co-doped black-P reaches 6200 mA h g^{-1} (*i.e.*, 18 wt% of composite weight), and the average capacity is ~10.3 times that of pristine black-P nanosheets. The active catalytic sites of Co atoms that facilitate hydrogen transfer are primarily responsible for the electrochemical hydrogen storage ability of the composite. Additionally, Co doping reduces the bandgap and increases the conductivity to provide favourable conditions for electrochemical hydrogen storage. However, most of the research on hydrogen storage in phosphorene is still in the theoretical stage, and several studies based on DFT calculations have been conducted to investigate the hydrogen capture capability of phosphorene.[519–523]

5.2.2 Lithium-ion batteries. Lithium-ion batteries (LIBs) are one of the most potent electrochemical energy storage devices capable of reversibly converting chemical energy into electrical energy.[524–527] They are widely employed in a variety of electronic devices, including cell phones, laptops, and electric vehicles. In 2019, John B. Goodenough, M. Stanley Whittingham, and Akira Yoshino, who made revolutionary breakthroughs in the development of LIBs, were awarded the Nobel Prize in Chemistry in recognition of their achievements.[528] Lithium atoms possess the lightest mass and smallest radius among all metal atoms,[529] and these remarkable properties enable LIBs to have energy densities 2–3 times greater and power densities 5–6 times higher than conventional nickel–chromium and lead–acid batteries.[526]

In LIBs, the specific capacities of anode and cathode materials primarily determine the energy capacity and charge/discharge rate. Commercially available LIBs often employ graphite anodes and lithium metal oxide cathodes, resulting in a theoretical energy capacity of approximately 400 W h kg^{-1} and a practical capacity of around 200 W h kg^{-1}.[530] However, this performance falls short of the increasing requirements for electrochemical energy storage devices, thus necessitating enhancements in the specific capacity of LIBs. Beyond graphite anodes, considerable efforts have been devoted to layered materials, which can be divided into four categories: 2D monoelemental materials (Xenes),[531] metal nitrides/carbides (MXenes),[532] transition metal dichalcogenides (TMDs),[533] and transition metal oxides (TMOs).[534] Low-dimensional EPMs have garnered significant interest as potential LIB anodes among the Xenes. For example, black-P possesses a low diffusion energy barrier for lithium ions (0.08 eV),[535] enabling it to exhibit 10^2 and 10^4 times faster lithium ion diffusion rates than MoS_2 and graphene, respectively, thereby suggesting a rapid charge/discharge rate. Moreover, the theoretical specific capacities of EPMs reach 2596 mA h g^{-1} surpass those of most TMOs and TMDs.[536,537] These characteristics render EPMs a promising anode material for the next-generation LIBs and other electrochemical energy storage devices (Table 3).

The working mechanism of LIBs is characterized by two primary phases: lithiation and delithiation.[538,539] During the charging process, energy is stored as chemical energy and an external current drives lithium ions to the anode, where they are intercalated into the phosphorus interlayer, forming a new phase of Li_3P. During the charging process, the thermodynamically favourable delithiation continues. Li_3P progressively decomposes, and the intercalated Li atoms contribute their valence electrons to the external circuit, resulting in the formation of Li^+. Eventually, the contributed electrons congregate at the cathode, dragging Li^+ across the electrolyte and accumulating in the cathode materials. Given the significant volume changes that occur during each lithiation/delithiation process, maintaining the anode structure is critical to achieving long-cycle performance in LIBs.

Experimental studies have been conducted on black-P, amorphous red-P, violet-P, and fibrous-P as anode materials for LIBs, with blue-P and green-P LIBs being theoretically proven to be viable.[74,540] In the past few years, black-P has garnered significant interest, and the mechanism of the lithiation/delithiation process in black-P has been more explicitly defined. The structure of black-P is highly anisotropic, and lithium ions prefer diffusing along the shallower zigzag ridges rather than the armchair ridges with a relatively higher energy barrier of 0.68 eV.[535] Moreover, a semiconductor-to-metallic transition occurs during the Li^+ intercalation process,[541] leading to increased electronic conductivity of the black-P anode. Parker *et al.*[542] were the first to report the black-P-based anodes for LIBs and found that bulk black-P exhibited a reversible rated charge capacity of 1279 mA h g^{-1}. While this value exceeds that of commercial graphite (372 mA h g^{-1}), it only reaches half of the theoretical capacity, and the initial cycle efficiency remains relatively low (57%). In 2019, Chen *et al.*[305] synthesized fibrous-P and violet-P bulk crystals through a CVD method and demonstrated that these two EPMs have the potential to be LIB anodes as well. The first discharge capacity of the fibrous-P anode is 1783 mA h g^{-1} and that of the violet-P anode is 2113.8 mA h g^{-1}, with Coulombic efficiencies of 81.04% and 75.76%, respectively. However, fibrous-P and violet-P anodes display irreversible capacities after several dozen cycles, limiting their long-term

Table 3 Summary of electrochemical energy storage devices made of elemental phosphorus-based materials

Allotropes	Materials	Applications	Methodology	Capacity	Capacity retention rate (%) (cycle number, rate or current density)	Ref.
Black phosphorus	BP-Graphite	LIB	High energy mechanical milling	Initial discharge capacity of 2786 mA h g^{-1} at 0.2C	80 (100, 0.2C)	549
	Sandwich-structure G-BPGO	LIB	Vacuum-filtration	Initial discharge specific capacity of 2587 mA h g^{-1} at 0.1 A g^{-1}	1401 mA h g^{-1} (200, 0.1 A g^{-1})	550
	Bi–P/C	LIB	Ball-milling method	High-rate discharge capacities of 1788.2 mA h g^{-1} at 13 A g^{-1}	86.3 (300, 7.8 A g^{-1})	551
	BP/NiCo MOF	LIB	Solution reaction route	Reversible capacity of 853 mA h g^{-1} at 0.5 A g^{-1}	91.3 (1000, 5 A g^{-1})	552
	BP/G/CNTs	LIB	Ball-milling method	Initial reversible capacity of 1375 mA h g^{-1} at 0.15 A g^{-1}	79 (1000, 1 A g^{-1})	553
	(BP-G)/PANI	LIB	Sonication and ball milling	Reversible discharge capacity of 1520 mA h g^{-1} at 0.26 A g^{-1}	440 mA h g^{-1} (2000, 13 A g^{-1})	554
	PCNF/S/BPQD	LSB	Sonication and wet chemistry	Rate capacity of 784 mA h g^{-1} at 4C	~90 (200, 0.1C)	555
	BP-coated separator	LSB	Vacuum-filtration	Specific capacity of 725 mA h g^{-1} at 1.8 A g^{-1}	86 (100, 0.4 A g^{-1})	556
	BPQD/δ-MnO_2	LAB	Hydrothermal route	Discharge capacity of 8463 mA h g^{-1} at 0.1 A g^{-1}	1000 mA h g^{-1} (182, 0.4 A g^{-1})	557
	Phosphorene-coated Li metal	LAB	Ultrasonication and spin coating	Constant discharge capacity 1000 mA h g^{-1} at 0.25 A g^{-1}	100 (50, 0.25 A g^{-1})	558
	BP–CNT	LIB and SIB	Surface oxidation-assisted chemical bonding procedure	LIB: Initial discharge capacity of ~1922 mA h g^{-1} at 0.2C SIB: Initial discharge capacity of ~2073 mA h g^{-1} at 0.2C	LIB: 87.5 (400, 0.2C) SIB: 75.3 (200, 0.2C)	559
	BPQD/TNS	LIB and SIB	Interfacial assembly strategy	LIB: Reversible capacity of 828 mA h g^{-1} at 0.1 A g^{-1} SIB: Initial discharge capacity of ≈723 mA h g^{-1} at 0.2 A g^{-1}	LIB: over 100% (2400, 1 A g^{-1}) SIB: nearly 100% (1000, 1 A g^{-1})	560
	4-RBP	SIB	4-NBD modification and solvothermal reaction	Initial discharge specific capacity of 2500 mA h g^{-1} at 0.1 A g^{-1}	1472 mA h g^{-1} (50, 0.1 A g^{-1})	561
	Layered BP/graphene	SIB	Flash-heat-treatment and straightforward pressure synthesis	Specific charge capacity of 1377.6 and 720.8 mA h g^{-1} at 1 and 40 A g^{-1}, respectively	1250 mA h g^{-1} (500, 1 A g^{-1}) 640 mA h g^{-1} (500, 40 A g^{-1})	562
	RP@BP/3DNG	SIB	Solvothermal strategy	Reversible capacity of 1440.2 and 521.3 mA h g^{-1} at 0.05 and 10 A g^{-1}, respectively	89.3 (1200, 10.0 A g^{-1})	563
	Few-layer black phosphorene	SIB	Electrochemical exfoliation	Activated capacity of 1968 mA h g^{-1} at 0.1 A g^{-1}	60.5 (50, 0.1 A g^{-1})	564
	Phosphorene–graphene	SIB	Self-assembly	Specific capacity of 2440 mA h g^{-1} at 0.05 A g^{-1}	84 (100, 8 A g^{-1})	565
	Phosphorene/MXene	SIB	Self-assembly	Reversible capacity of 535 mA h g^{-1} at 0.1 A g^{-1}	87 (1000, 1 A g^{-1})	566
	MoS_2/BP	SIB	Hydrothermal method	Reversible capacity of 435.5 mA h g^{-1} at 1.0 A g^{-1} after 150 cycles	263.2 mA h g^{-1} (1000, 10 A g^{-1})	567
	BP–C	PIB	Ball-milling method	Initial specific capacity of 617 mA h g^{-1} at 0.05 A g^{-1}	~30 mA h g^{-1} (50, 0.05 A g^{-1})	568
	(P-CNTs)/PANI	PIB	Ball-milling and *in situ* solution polymerization	Reversible capacity of 642.7 mA h g^{-1} at 50 mA g^{-1}	94 (500, 0.5 A g^{-1})	569
	Restacked BP nanoflakes	SC	Liquid exfoliation	Specific capacitance of 13.75 F cm^{-3} at 0.01 V s^{-1}	71.8 (30 000, 0.5 V s^{-1})	570
	BP sponges	SC	Electrochemical technique	Specific capacitance of 80 F g^{-1} at 0.01 V s^{-1}	80 (15 000, 0.1 V s^{-1})	571
	BP/CNTs	SC	High-heat treatment and microfluidic-spinning technique	Specific volumetric capacitance of 308.7 F cm^{-3} at 0.1 A cm^{-3}	90.2 (10 000, 0.4 A cm^{-3})	572
	E-BP/ZIF-67	SC	Droplet microfluidic	Specific capacitance of 506 F cm^{-3} at 500 mA cm^{-3}	89.3 (12 000, 2 A cm^{-3})	573
Amorphous red phosphorus	RP/A-TiO_2	LIB	*In situ* hydrolyzation	Rate capacity of 202 mA h g^{-1} at 1 A g^{-1}	89.3 (100, 0.1 A g^{-1})	574
	P/C	LIB	Vaporization-adsorption method	Specific capacity of 2173 mA h g^{-1} at 1C	90 (500, 0.2C)	29
	RPN/rGF	LIB	Evaporation–condensation method	Rate capacity of 1073 mA h g^{-1} at 3C	78.4 (300, 0.3C)	575
	RP/TiN/CNT	LIB	High-energy ball milling method	Reversible capacity of 868.7 mA h g^{-1} at 2.3 A g^{-1}	96.9 (3rd ~ 850th, 2.3 A g^{-1})	576
	HPNs	LIB and SIB	Wet solvothermal method	Specific capacity of 1285.7 and 1364.7 mA h g^{-1} at 0.2C for LIBs and SIBs, respectively	LIB: 1048.4 mA h g^{-1} (600, 1C)	577

Table 3 (*continued*)

Allotropes	Materials	Applications	Methodology	Capacity	Capacity retention rate (%) (cycle number, rate or current density)	Ref.
					SIB: 969.8 mA h g^{-1} (600, 1C)	
	P@CMK-3	LIB and SIB	Vaporization–condensation–conversion process	LIB: Specific capacity of 2185 mA h g^{-1} at 1.2C SIB: Specific capacity of 2331 mA h g^{-1} at 0.6C	LIB: ~80 (1000, 1.2C) SIB: 1600 mA h g^{-1} (140, 1C)	578
	BP/RP	LIB and SC	Sono-chemical process	LIB: Initial discharge capacity of 2449 mA h g^{-1} at 0.05 A g^{-1} SC: Specific capacitance of ≈60.1 F g^{-1} at 0.5 A g^{-1}	LIB: 491 mA h g^{-1} (100, 0.05 A g^{-1}) SC: 83.3 (2000, 1 A g^{-1})	579
	RP_{EN}@CF	LSB	Laser-assisted exfoliation	Specific capacity of 782.3 mA h g^{-1} at 3C	769.5 mA h g^{-1} (500, 1C)	580
	P@C	SIB	Shear emulsifying and electrospinning	Reversible capacity of 1308 mA h g^{-1} at 0.2 A g^{-1}	81 (1000, 2 A g^{-1})	581
	P-CNT	SIB	Ball-milling method	Specific capacity of 2134 mA h g^{-1} at 0.26 A g^{-1}	~91 (100, 0.52 A g^{-1})	582
	P@RGO	SIB	Physical vapor deposition	Specific capacity of 1165.4 mA h g^{-1} at 159.4 mA g^{-1}	87.9 (300, 1.5939 A g^{-1})	583
	P_{red}@CNF	SIB	Vaporization–condensation method	Specific capacities of ~1850 mA h g^{-1} over 500 cycles at 0.1 A g^{-1}	>1000 mA h g^{-1} (5000, 1 A g^{-1})	584
	NPRP@RGO	SIB	Redox reaction and boiling process	Specific capacity of 1848.67 mA h g^{-1} at 0.2563 A g^{-1} after 150 cycles	775.3 mA h g^{-1} (1500, 5.12 A g^{-1})	585
	RP@Ni–P	SIB	Electroless deposition and chemical dealloying	Reversible specific capacity of 1256.2 mA h g^{-1} at 0.26 A g^{-1}	409.1 mA h g^{-1} (2000, 5 A g^{-1})	586
	P@N-MPC	SIB	Vaporization-condensation method	Specific capacity of ≈600 mA h g^{-1} at 0.15 A g^{-1}	~450 mA h g^{-1} (1000, 1 A g^{-1})	587
	P_2@N-SGCNT	SIB and PIB	High-temperature infiltration	SIB: Reversible capacity of 2480 mA h g^{-1} at 0.1 A g^{-1} PIB: Reversible capacity of 762 mA h g^{-1} at 0.05 A g^{-1}	SIB: 1936 mA h g^{-1} (2000, 1 A g^{-1}) PIB: 319 mA h g^{-1} (1000, 2 A g^{-1})	588
	P50@ZRCod-0.025	PIB	Solvothermal synthesis	Reversible capacity of 595.8 mA h g^{-1} at 50 m A g^{-1}	150.7 mA h g^{-1} (400, 2.5 A g^{-1})	589
	Red P@N-PHCNFs	PIB	Vaporization–condensation	Reversible capacity of 650 mA h g^{-1} at 0.1 A g^{-1}	84 (200, 1 A g^{-1})	590
	H-P@NCNS/NCNT	PIB	Magnetic field assisted methodology	Reversible charge capacity of ≈527 mA h g^{-1} at 2.0 A g^{-1}	≈85% (500, 2 A g^{-1})	591
	R-BP/SPC	SC	Sonochemical process	Specific capacitance of 364.5 F g^{-1} at 500 mA g^{-1}	89 (10 000, 2 A g^{-1})	592
	P-rGO	SC	Potentiodyna-mic deposition	Specific capacitance of 334.2 F g^{-1} at 1 A g^{-1}	99.2 (10 000, 1 A g^{-1})	593
Fibrous phosphorus	Fibrous phosphorus	LIB	Iodine-assisted CVD	Initial discharge capacity of 1783 mA h g^{-1} at 0.1 A g^{-1}	75 (10, 0.1 A g^{-1})	305
	FP-C	LIB	CVT	Reversible specific capacity of 1621 mA h g^{-1} at 0.2 A g^{-1}	742.4 mA h g^{-1} (700, 2 A g^{-1})	594
	MWCNT@f-RP@BP hybrid	LIB	CVD	Initial discharge capacity of ~1333 mA h g^{-1} at 0.5 A g^{-1}	560 mA h g^{-1} (250, 0.5 A g^{-1})	595
Violet phosphorus	Hittorf's phosphorus	LIB	Iodine-assisted CVD	Initial discharge capacity of 2113.8 mA h g^{-1} at 0.1 A g^{-1}	558 mA h g^{-1} (40, 0.1 A g^{-1})	305
	Hittorf's violet phosphorene	LIB and SIB	DFT calculations	Adsorption energies of 1.65 eV for Li and 1.32 eV for Na (theoretical)	—	596
Blue phosphorus	Single-layer blue phosphorus	LIB	DFT calculations	Charge capacity of 865 mA h g^{-1} (theoretical)	—	597
	Double-layer blue phosphorus	LIB	DFT calculations	Charge capacity of 649 mA h g^{-1} (theoretical)	—	597
	BlueP/graphene heterostructure	LIB	DFT calculations	Specific capacity of 626 mA h g^{-1} (theoretical)	—	598
	BlueP/MS_2 hetero-structures (M = Nb, Ta)	LIB	DFT calculations	Specific capacities of 528.257 mA h g^{-1} for BlueP/NbS_2 and 392.154 mA h g^{-1} for BlueP/TaS_2 (theoretical)	—	599
	Blue phosphorene	LSB	DFT calculations	Adsorption energies in the range of −0.86 to 2.45 eV for lithium polysulfides	—	600

Table 3 (*continued*)

Allotropes	Materials	Applications	Methodology	Capacity	Capacity retention rate (%) (cycle number, rate or current density)	Ref.
	2D-N-doped blue phosphorus	LAB	DFT calculations	Storage capacity of >314.22 mA h g^{-1} (theoretical)	—	601
	h-BN/blue-P heterostructure	LIB and SIB	DFT calculations	Specific capacities of 801 mA h g^{-1} for Li and 541 mA h g^{-1} for Na (theoretical)	—	602
	C_3N/blue-P heterostructure	LIB and SIB	DFT calculations	Specific capacities of 333 mA h g^{-1} for Li and 658 mA h g^{-1} for Na (theoretical)	—	603
	Monolayer blue phosphorene	SIB and PIB	DFT calculations	Specific capacities of 865 mA h g^{-1} in both cases (theoretical)	—	540
Green phosphorus	Single-layer GP	LIB	DFT calculations	Specific capacity of 432.7 mA h g^{-1} (theoretical)	—	74
	2D green phosphorene	SC	DFT calculations	Specific capacitance of $\approx$90 F g^{-1} (theoretical)	—	604

capacity retention. Generally, pristine bulk materials lack rational structural designs,[543] and abrupt pulverization of the anode materials during the delithiation process leads to undulation of the lattice structure, resulting in a substantial volume expansion of up to 300%.[544] This can lead to the loss of electrical contact within the active material, resulting in a rapid decay of the battery capacity.

Nanostructured design can enhance electrochemical reactions and improve active material utilization.[545,546] Among various nanostructured strategies, exfoliating the bulk phase into 2D nanosheets is a widely adopted method that can decrease electrode thickness, reduce electron and ion diffusion distances within the electrode layer, and ultimately enhance the volumetric energy density of LIBs. However, 2D phosphorene nanosheets with large specific surface areas suffer from restacking and detrimental parasitic reactions with the electrolyte. These reactions often occur at the edge of the phosphorene zigzag diffusion channel, resulting in the distortion of the surrounding phosphorus atoms.[547] Alternatively, the development of 3D electrode architectures is another design option for enhancing performance. Zhu *et al.* have developed a green and template-free hydrothermal approach to synthesize honeycomb-like micron-sized red-P with a tunable porous architecture.[548] The optimal porous red-P anode delivers exceptional lithium storage performance, achieving a substantial reversible capacity of 2587.4 mA h g^{-1} at 50 mA g^{-1} and a capacity retention of $\sim$81.9% at 500 mA g^{-1} after 500 cycles. The results from *in situ* TEM and *ex situ* SEM measurements indicate that the porous structure buffers the volume variations throughout the lithiation/delithiation process, improving the long-cycle stability of the anode materials.

Currently, commercial LIBs offer limited power densities typically ranging from 100 to 300 W kg^{-1} and require long charging time to ensure safe operation.[605,606] To enhance battery utilization efficiency in portable electronics and electric vehicles, it is crucial to develop high-energy-density LIBs that possess superior fast-charging capabilities. EPMs are promising candidates as anode materials due to their high theoretical specific capacity (2596 mA h g^{-1}) and moderate lithiation potential (0.7 V *vs.* Li^+/Li). However, challenges such as limited conductivity, sluggish reaction kinetics, and unstable solid-electrolyte interphase (SEI) impede the high-rate capability of the phosphorus anode during the lithiation/delithiation process. Despite self-structure redesign efforts, there are still limitations, and new strategies are required to optimize the performance of EPMs as anode materials in fast-charging LIBs.[526] Carbonaceous materials possess good electrical conductivity and material stability and their incorporation into the anode can effectively improve the fast-charging capabilities of EPMs. In carbon–phosphorus (P/C) composites, the presence of high-conductive carbon-rich materials amplifies lithium ion diffusion in the anode by reducing the polarization effect,[607] and carbon-rich materials also act as an external buffer layer to control volume changes.[608] Cui's group designed a red-P/C nanocomposite for fast-charging LIBs by an adsorption and surface cleaning approach.[29] The average thickness of red-P/C electrodes is 21.5 μm, featuring an industrial-

grade areal capacity of around 3.5 mA h cm^{-2} at 0.5 mA cm^{-2}. This thickness is considerably less than that of the commercial graphite (76.3 μm) and $Li_4Ti_5O_{12}$ (124.5 μm) electrodes at the same areal capacity (Fig. 36a). Consequently, the total volumetric capacity of the red-P/C electrode is 1628 mA h cm^{-3}, far surpassing that of graphite (459 mA h cm^{-3}) and $Li_4Ti_5O_{12}$ (281 mA h cm^{-3}) electrodes (Fig. 36b). The red-P/C nanocomposite also exhibits an extended cycle life. After 500 discharge–charge cycles, the red-P/C electrode shows a specific capacity of 1625 mA h g^{-1} and retention rate of around 90% at 0.86 mA cm^{-2} (0.2C). Following long-cycling, the red-P/C electrode retains its morphological integrity and electrical connectivity without fractures or contact losses after long-cycling tests. A uniform and thin solid-electrolyte interphase layer (<50 nm) is formed on the surface of a red-P/C nanoparticle, while the interior nanoscale void spaces are well preserved to buffer the volume changes after 100 cycles.[29] These findings demonstrate that the red-P/C nanocomposite is structurally robust at both the electrode and particle levels, enabling stable battery cycling and high specific capacity at relatively high current densities.

Sun *et al.* have proposed that the formation of robust P–C bonds in P/C composites can minimize electrical contact loss between the active materials and the carbon conductor and improve the cyclic stability of P/C composites.[549] They evaluated

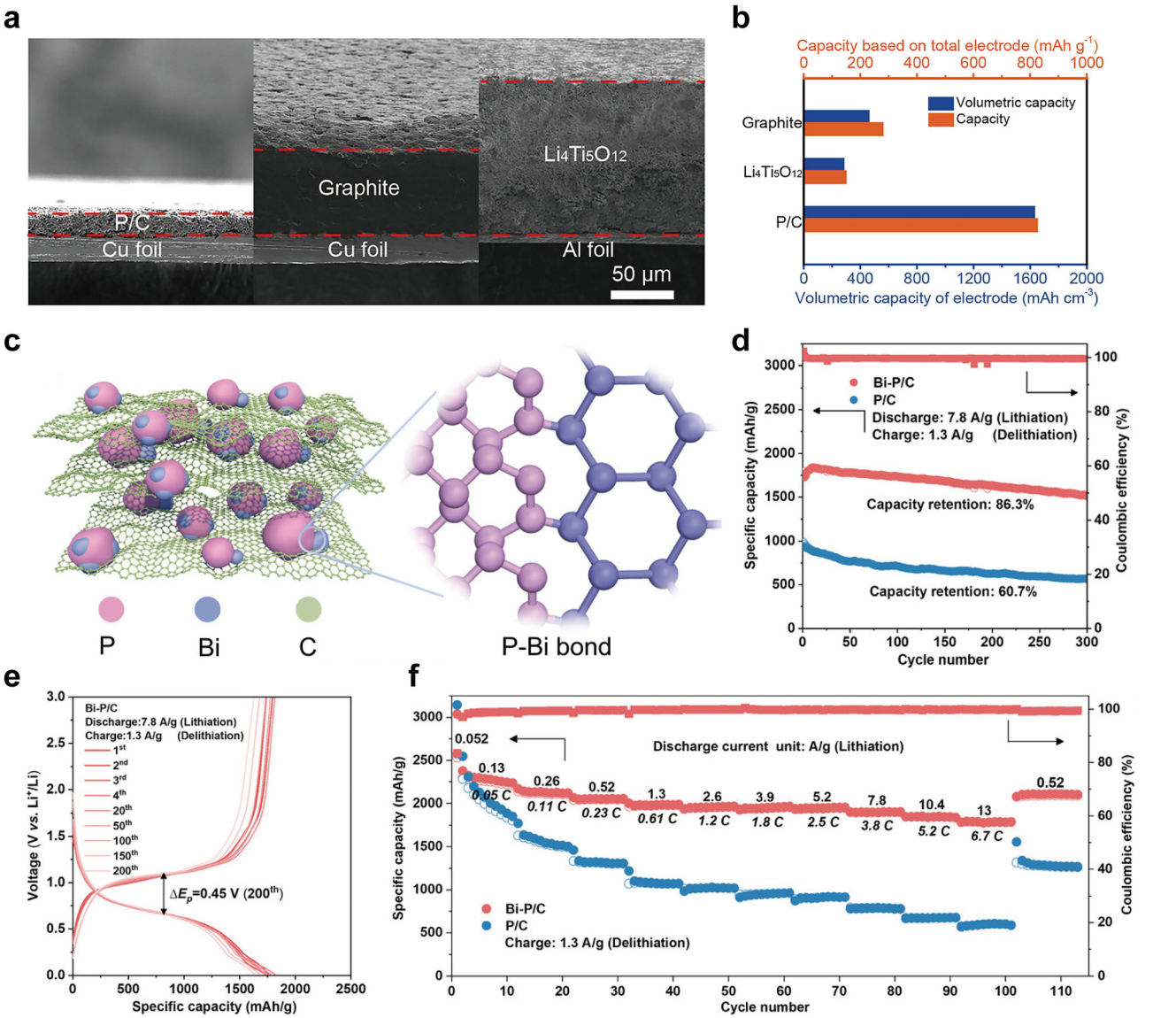

Fig. 36 Applications of elemental phosphorus materials to LIBs. (a) Cross-sectional SEM images of P/C, graphite, and $Li_4Ti_5O_{12}$ anodes with the same areal capacity of 3.5 mA h cm^{-2} at 0.5 mA cm^{-2}. (b) Comparison of capacities and volumetric capacities of P/C, graphite, and $Li_4Ti_5O_{12}$ anodes with the same areal capacity of 3.5 mA h cm^{-2} at 0.5 mA cm^{-2}. Reproduced with permission from ref. 29. Copyright 2019 Elsevier. (c) Scheme of the synthesis of Bi–P/C composites. (d) Long-cycling stability of Bi–P/C and P/C at 7.8 A g^{-1}. (e) Corresponding voltage profiles of Bi–P/C at 7.8 A g^{-1}. (f) Rate performance comparison between Bi–P/C and P/C anodes across a range of rates from 0.052 to 13 A g^{-1}. Reproduced with permission from ref. 551. Copyright 2022 John Wiley and Sons.

the impact of the carbon structure on stable P–C bond formation by comparing four common carbon materials: graphite, graphite oxide, carbon black, and fullerene. Their findings demonstrate that the black-P–graphite composite has the greatest proportion of P–C bonds, making it an optimal choice as a LIB anode material with extended cycle life and high-rate performance. At a constant current of 0.2C, the black-P–graphite composite displays an impressive initial discharge capacity of 2786 mA h g^{-1} and excellent stability. Specifically, it maintains a remarkable capacity of 1849 mA h g^{-1} after 100 cycles, whereas the capacity of black-P/graphite without robust P–C bonds declines rapidly after only 40 cycles. However, the fast-charging capabilities of P/C composites are limited by the high lithium diffusion barrier (0.34 eV) of carbon carriers and the heterogeneous interface.[609] To address these issues, Sun *et al.* have recently incorporated electrochemically active bismuth nanoparticles into P/C composites by ball milling (Fig. 36c) to improve fast-charging and cycling.[551] In principle, Bi possesses a slightly higher initial lithiation potential than P, enabling it to act as a modest Li reservoir that traps Li during lithiation. Meanwhile, initial delithiation potential of Bi is slightly lower than that of P, allowing it to emit Li before P during delithiation. Moreover, the Bi anode exhibits a low Li^+ diffusion barrier (0.08 eV) and excellent electron transfer ability. Its strong interaction with P promotes Li^+ transport while reducing large transient stress and capturing dissolvable polyphosphide at elevated current densities. The optimized Bi–P/C anode delivers excellent electrochemical performance, with a substantial fast-charging capacity of 1755.7 mA h g^{-1} at 7.8 A g^{-1} (5.2C) and it maintains a capacity retention rate of 86.3% after 300 cycles, which is better than the 60.7% retention rate of the pristine P/C anode after 300 cycles (Fig. 36d).[551] Morphological studies reveal that the Bi–P/C anode maintains a smooth and dense surface with a volume expansion of ~164.7% after 300 cycles, while the P/C anode has huge surface cracks with a larger volume expansion of ~268.2%. Moreover, the discharge platform of the Bi–P/C anode is around 0.66 V at the 200th cycle (Fig. 36e), effectively inhibiting Li dendrite formation. The ΔE_p of the Bi–P/C anode (0.45 V) at the 200th cycle is considerably lower than that of P/C (0.91 V) at 7.8 A g^{-1}, suggesting that the Bi–P/C electrode provides ultrafast lithiation/delithiation reaction kinetics. As depicted in Fig. 36f, the Bi–P/C anode exhibits remarkably high-rate discharge capacities at rates ranging from 0.052 to 13 A g^{-1}, while the P/C anode shows inferior discharge capacities. Additionally, both Bi and LiBi are calculated to have high adsorption energies for LiP_7 and LiP_5, indicating their ability to capture and facilitate the conversion of soluble lithium polyphosphides, resulting in increased reversible capacity and improved cycle stability.

Introduction of a conductive polymer coating layer into P/C composites has been shown to be effective in stabilizing the solid–electrolyte interphase and preventing the formation of low-conductivity by-products during fast charging. Ji's group has developed a covalently bonded black-P/graphite anode coated with a thin polyaniline gel ((BP-G)/PANI), which has a high rate, high capacity, and robust cycling stability.[554] The covalent bonding to graphite inhibits edge reconstruction of layered black-P and maintains the structure of phosphorus atoms surrounding the zigzag diffusion channel, while the conductive PANI facilitates charge transfer at the electrode–electrolyte interface (Fig. 37a). After 2000 cycles at current densities of 2.6, 5.2 and 13 A g^{-1}, the reversible capacities reach 910, 790 and 440 mA h g^{-1}, respectively (Fig. 37b). The high-rate performance of (BP-G)/PANI exceeds that of conventional carbon anodes and advanced silicon anodes and is comparable to that of several well-known high-rate materials (Fig. 37c). To probe the role of different components in (BP-G)/PANI composites, researchers have prepared several composite materials for comparison (Fig. 37d). The (BP-G)/PANI composite exhibits a reversible capacity of 1520 mA h g^{-1} at 0.26 A g^{-1}, which is 10 times higher than that of BP-G without the PANI coating at the same rate. Furthermore, the discharge capacity of (BP-G)/PANI is ~3 times that of (RP-G)/PANI, indicating the significant contribution of black-P to the capacity of (BP-G)/PANI. The synergistic effects of the composite enable excellent Li^+ transport kinetics and high-rate and high-capacity lithium storage.

5.2.3 Sodium-ion batteries. While LIBs are efficient and powerful, the restricted and uneven distribution of elemental lithium renders them unsuitable for future rechargeable batteries.[610–612] With the rising prominence of electric vehicles and swift advancement of energy storage devices, lithium resources will become increasingly rare.[613] Consequently, researchers have turned their attention to LIB alternatives such as sodium-ion batteries (SIBs), which possess similar electrochemical features and offer outstanding theoretical capacity.[614] In particular, SIBs provide the following advantages: (i) Sodium is naturally abundant, with a concentration of 2.83 wt% in the earth's crust, which is approximately 435 times greater than that of lithium (0.0065 wt%).[615] (ii) Aluminium foil can replace copper as the anode current collector in SIBs, which not only reduces the manufacturing cost but also makes the battery lighter and more portable.[616] (iii) The Na^+ electrolyte has a stronger ion conductivity than Li^+ electrolyte, which helps to enhance battery performance. Kuratani *et al.* have compared the molar conductivity of $NaClO_4$ and $LiClO_4$ solutions with that of aprotic solvents and found that $NaClO_4$ solutions have a lower viscosity and higher conductivity (10–20%) than $LiClO_4$ solutions due to the solvation energy and size difference between Na and Li.[617] However, due to the significantly larger ionic radius of Na^+ (1.02 Å) compared to Li^+ (0.69 Å),[618] electrode structural fluctuations and ion insertion behaviour in SIBs become more uncontrollable, leading to slower electrochemical reaction kinetics and increased volume expansion. For this reason, high-performance SIBs necessitate more stringent electrode materials. Recent research on SIB cathodes has demonstrated that $NaMnO_2$, $NaFePO_4$, and $Na_3V_2(PO_4)_3$ are promising cathode materials owing to their substantial storage capacity and reliable safety.[19] Nevertheless, the advancement of SIB anodes continues to rely on traditional carbon materials, metal oxide/sulphide and sodium-based alloys, whose specific capabilities and cycle life remain unsatisfactory.

Graphene is typically arranged in a layered honeycomb-like pattern, which enables ion insertion and extraction. However,

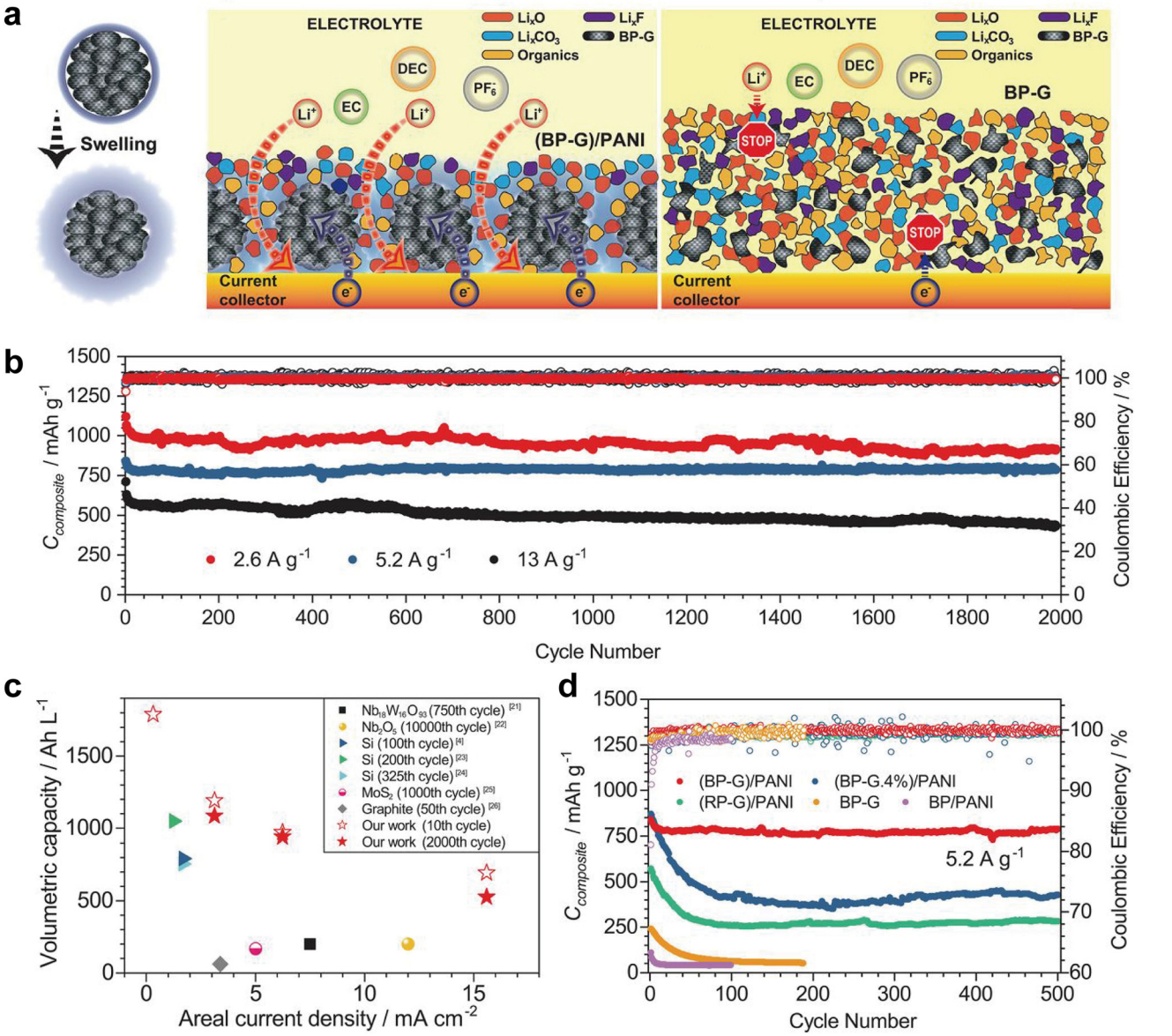

Fig. 37 Engineered interface black-P composites designed for high-rate and high-capacity lithium storage. (a) Scheme of electrolyte-swollen (BP-G)/PANI that retains the solid–electrolyte interphase and pristine BP-G that suffers from the formation of less-conductive by-products during lithiation/delithiation. (b) Long-cycling tests of (BP-G)/PANI at current densities of 2.6, 5.2 and 13 A g^{-1}. (c) Volumetric performance metrics of the (BP-G)/PANI composite in comparison to a range of high-rate materials. (d) Cycling performance comparison between the (BP-G)/PANI composite and various control samples. Reproduced with permission from ref. 554. Copyright 2020 Science.

the limited interlayer spacing in graphene is insufficient for sodium ions, significantly constraining the gravimetric capacity of graphene-based anode materials. In contrast, black-P exhibits a considerably larger interlayer spacing than graphene (3.08 Å *vs.* 1.86 Å), indicating its potential to accommodate more sodium ions per gram, resulting in a higher theoretical specific capacity (2596 mA h g^{-1}). The sodiation mechanism in black-P involves two processes: intercalation and alloying (Fig. 38a).[565] *In situ* TEM and *ex situ* XRD studies have revealed that intercalation occurs within interlayer spaces of black-P, where Na^+ preferentially diffuses along the one-dimensional pore channels (zigzag ridges) due to the wide channel size. The channel along the zigzag direction has a sufficient width of 3.08 Å to permit Na^+ (2.04 Å) diffusion, whereas the channel width along the armchair direction is only 1.16 Å and cannot accommodate Na^+ diffusion. During the intercalation process, the host structure of black-P remains largely unaltered, resulting in a highly reversible cycle in the 0.54–1.5 V range. However, the specific capacity is limited to 150 mA h g^{-1} at this point, with a spatial conformation of $Na_{0.17}P$. Further sodiation below 0.54 V proceeds to the alloying reaction stage, where the P–P bond is broken, leading to the formation of amorphous Na_xP. Eventually, as the potential reaches 0.1 V, the Na_3P phase is formed, and the alloying reaction is almost complete. However, this is

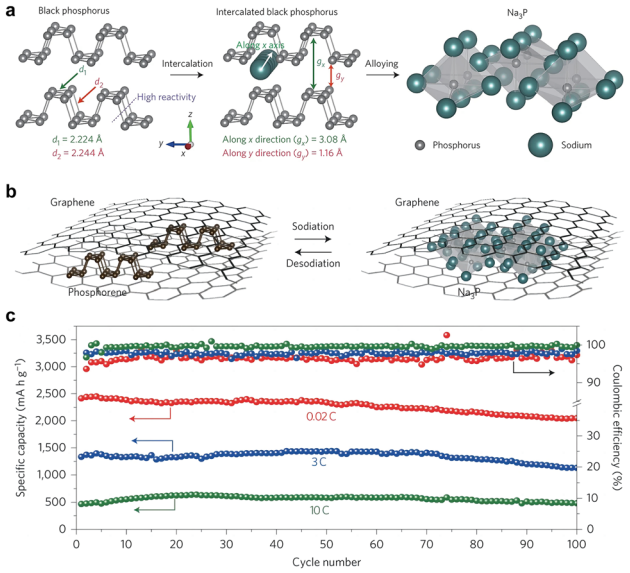

Fig. 38 Sodiation process and electrochemical performance in black-P-based anodes. (a) Scheme of the mechanism of sodiation in black-P. (b) Scheme of sandwich-like phosphorene–graphene nanohybrids during sodiation/desodiation. (c) Cycling performance of phosphorene–graphene nanohybrids evaluated at different current densities. Reproduced with permission from ref. 565. Copyright 2015 Nature Publishing Group.

accompanied by a significant volume expansion of over 500%. First-principles calculations also support this proposed mechanism. The diffusion energy barriers for sodium atoms along the zigzag, armchair, and interlayer directions are 0.18, 0.76, and 4.2 eV, respectively.[619] These values indicate that sodium atoms primarily follow one-dimensional pathways along the zigzag ridges in black-P. This diffusion behaviour is similar to that observed in nanotube materials along their pores, suggesting that black-P could potentially exhibit exceptional rate capacity when employed as an anode material for SIBs.[619,620]

Huang *et al.* have electrochemically exfoliated black-P bulk crystals into few-layered phosphorene and directly utilized the obtained phosphorene as an anode material for SIBs.[564] Electrochemical tests reveal that few-layered phosphorene exhibited an activation capacity of up to 1968 mA h g^{-1} at 100 mA g^{-1} and a capacity retention of 60.5% after 50 cycles. At a higher current density of 1500 mA g^{-1}, the retained capacity is 603.3 mA h g^{-1} after 100 cycles, suggesting the great potential of phosphorene as an SIB anode material. Given that phosphorene is directly used in this work, the electrochemical performance can be further enhanced by doping and compositing strategies. As a representative example, Cui's group has prepared sandwich-like phosphorene–graphene nanohybrids using a self-assembly method (Fig. 38b).[565] In this hybrid material, phosphorene nanosheets reduce the diffusion distance for both sodium ions and electrons to improve the rate performance. Simultaneously, the graphene nanosheets facilitate electron transport from phosphorene to the current collector and provide a buffer space for the anisotropic expansion of phosphorene during Na_3P alloy formation. These lead to exceptional electrochemical performance with a high specific capacity, rate capability, and capacity retention. Specifically, the phosphorene–graphene composite shows a specific capacity of 2440 mA h g^{-1} at 0.02C (50 mA g^{-1}) and maintains a reversible capacity of 2080 mA h g^{-1} after 100 cycles (with a decay of only 0.16% per cycle). Moreover, even at the significantly higher rate of 10C (10 A g^{-1}), a specific capacity of 645 mA h g^{-1} can be achieved (Fig. 38c).

As one of the most prevalent phosphorus allotropes, cost-effective red-P possesses a high theoretical sodium capacity and a relatively low safe working potential (0.4 V for Na^+/Na),[621] which promotes fast charging without the risk of dendrite formation. However, the fundamental mechanism behind its long-cycle capacity decay remains a subject of debate. It has been assumed that electrochemical fading of red-P-based anodes is similar to the decay process of silicon anodes in LIBs, wherein the anode undergoes significant volume expansion during long-term cycling, leading to severe particle pulverization and active material losses.[583,622,623] Nevertheless, Liu *et al.* have discovered the "liquefication" phenomenon of red-P in SIBs by *in situ* TEM and chemo-mechanical simulations.[584] This finding suggests that red-P should be less susceptible to volume fluctuation and fracture compared to the silicon anodes in LIBs. Instead, the primary cause of capacity decay in red-P-based anodes stems from side reactions that occur during the formation of reactive sodium phosphides. To mitigate capacity decay, researchers have developed an effective encapsulation technique, that is, synthesis of red-P-impregnated carbon nanofiber composites (P_{red}@CNF), which has been confirmed to prevent undesirable side reactions in red-P anodes. They employed a dry-format electrochemical cell setup (Fig. 39a) for real-time observation of the sodiation process.[584] Fig. 39b illustrates the "liquid-like" material behaviour of red-P during sodiation, where red-P may produce low-yielding stress and exhibit low stiffness (*i.e.*, softening) as sodiation continues, thus allowing red-P to flow plastically inside the CNF like a fluid.[584] Model stimulations in the various states of sodiation (Fig. 39c) align well with the longitudinal flow of red-P observed by *in situ* TEM. The average longitudinal expansion of red-P along the CNF is ~330% during the complete sodiation process (Fig. 39d and e). Another series of cropped time-lapse STEM images display two distorted and blended red-P segments during the sodiation expansion (Fig. 39f), resembling two droplets and directly confirming the sodiation induced red-P softening effect. In contrast to a free-standing red-P segment, the CNF-encapsulated red-P exhibits reduced tensile stresses near the segment surface and is mechanically constrained by the CNF shell (Fig. 39g and h) to prevent fracture formation in the red-P segments. The designed P_{red}@CNF anode demonstrates a specific capacity of 1850 mA h g^{-1} at 0.1 A g^{-1} after 500 cycles, and over 1000 mA h g^{-1} after 5000 cycles at 1 A g^{-1}.

Heterojunction construction can enhance the electrochemical stability and conductivity of phosphorus-based electrodes.[578,624,625] However, the incorporation of another component in these heterojunctions often results in a lower theoretical capacity (*e.g.*, carbon materials with a theoretical capacity of 530 mA h g^{-1}),[626] sacrificing a part of the total electrode capacity. To optimize the stability of phosphorus-based electrodes while preserving the theoretical

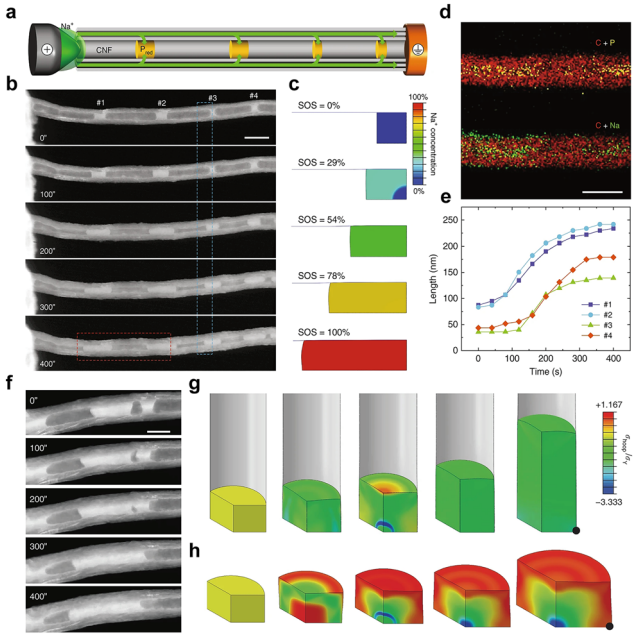

Fig. 39 *In situ* TEM analysis and corresponding chemo-mechanical simulations of P_{red}@CNF composites. (a) Scheme of *in situ* TEM experimental setup of a dry-format electrochemical cell. (b) STEM image series captured in real-time showing red-P volume expansion during sodiation. The scale bar is 200 nm. (c) Simulated state of sodiation (SOS) corresponding to the morphological changes in red-P in the region labelled with a blue box in (b). (d) Energy dispersive spectroscopy mapping of phosphorus (green), sodium (yellow), and carbon (red) elements of the region labelled with a red box in (b). The scale bar is 200 nm. (e) The length change of four red-P segments marked in (b) over time during sodiation. (f) STEM image series captured in real-time showing two red-P segments merging during sodiation. The scale bar is 100 nm. (g) Simulated hoop stress distribution of P_{red}@CNF and (h) a free-standing red-P particle. Reproduced with permission from ref. 584. Copyright 2020 Nature Publishing Group.

capacity as much as possible, it is beneficial to develop mono-elemental phosphorus heterojunctions. Recently, Ma *et al.* have fabricated RP@BP core–shell heterostructures on 3D nitrogen-doped graphene using a straightforward one-step solvothermal method.[563] The resulting RP@BP core–shell heterogeneous structure features a crystalline black-P shell tightly enclosing an amorphous red-P core. The internal electric field at the heterojunction not only provides exceptional electron conductivity and an extremely low Na^+ diffusion barrier, but also induces electron cloud transfer from black-P to red-P. This suppresses the reactivity of lone-pair electrons in black-P atoms, resulting in excellent air stability of the composite. Electrochemical tests reveal that the composite anode exhibits an impressive capacity of 1440.2 mA h g^{-1} at 0.05 A g^{-1}, superior to that of both pristine red-P (1137.9 mA h g^{-1}) and black-P (713.3 mA h g^{-1}) supported on 3D nitrogen-doped graphene.[563] The composite anode also delivers an exceptional rate performance with a reversible capacity of 521.3 mA h g^{-1} achievable at 10.0 A g^{-1}. Moreover, the electrode displays great electrochemical and air stability with a retention rate of 89.3% after 1200 cycles at 10.0 A g^{-1} and stable cycling over 500 cycles at 10.0 A g^{-1} after exposure to air.

The synthesis of crystalline red-P phases, such as fibrous-P and Violet-P, remains a challenging endeavour with limited reports on their utilization for SIBs. Nevertheless, the crystalline phase offers several distinct advantages over its amorphous counterpart. First, the crystalline lattice structure enhances charge mobility and electrode conductivity.[33] Second, crystalline red-P generates polymeric chains,[351] which mitigate the occurrence of side reactions during the charge/discharge process. Third, the crystalline structural phase enables a more comprehensive understanding of the sodiation mechanism in red-P anodes. Yan *et al.*[627] have synthesized a 3D structured nanocomposite by incorporating highly dispersed crystalline red-P (violet-P phase) nanorods within a reduced graphite oxide aerogel matrix. This composite anode has a remarkable initial specific capacity of 2427 mA h g^{-1} with an initial Coulombic efficiency of 82% at 0.1 A g^{-1} and capacity retention even at higher current densities. This investigation highlights the potential of crystalline red-P as promising anode materials for SIBs.

5.2.4 Potassium-ion batteries. Potassium, which belongs to the same group as lithium and sodium in the periodic table of elements, is receiving increasing attention as a potential candidate to supplement or even replace LIBs due to its similar properties. Potassium ion batteries (PIBs) offer numerous advantages, including the following: (i) potassium (1.5 wt%) is abundant in the earth's crust, more than lithium (0.0017 wt%) and comparable to sodium (2.3 wt%),[628] ensuring a reliable supply. (ii) Potassium does not react with aluminium, allowing for cheaper aluminium foil as current collectors, reducing cost, and improving energy density. (iii) Potassium has a low redox potential, making it suitable for high-voltage and high-energy-density devices. As shown in Fig. 40a, PIBs exhibit a wider electrochemical voltage window than LIBs and SIBs in carbonate electrolyte solutions.[629] (iv) Potassium ions have the smallest Stokes radii among Li^+, Na^+, and K^+ (Fig. 40b) and low desolvation energy (119.2 kJ mol^{-1}) in propylene carbonate,[630] leading to fast diffusion rates and high conductivity in electrolyte solutions. This results in excellent rate performance.

However, the large ion radius of K^+ leads to sluggish potassiation kinetics,[631] which poses a challenge in selecting suitable electrode materials. For example, silicon-based materials that exhibit a high capacity for LIBs are inactive in PIBs.[632] The commercial graphite anode for KIBs only achieves a capacity of 279 mA h g^{-1}.[633] Despite various modification strategies being developed for graphite, the capacity improvement has remained limited due to the intrinsic properties of carbonous materials. In contrast, the theoretical capacities of EPMs upon K_4P_3 and KP formation are 1154 and 843 mA h g^{-1}, respectively.[590,634] To the best of our knowledge, these are the highest specific capacities among all elements for PIB anodes, indicating that phosphorus-based anodes have a higher upper limit for PIB development. However, the existence of potassium phosphide-rich polymorphisms (such as K_3P, KP, K_4P_3, and K_3P_{11}) makes it difficult to investigate the potassium storage mechanism of phosphorus.[635] Currently, research on PIBs for phosphorus-based anodes mainly focuses on well-established EPMs including amorphous red-P and black-P, as well as their heterostructures with carbon or metal species.

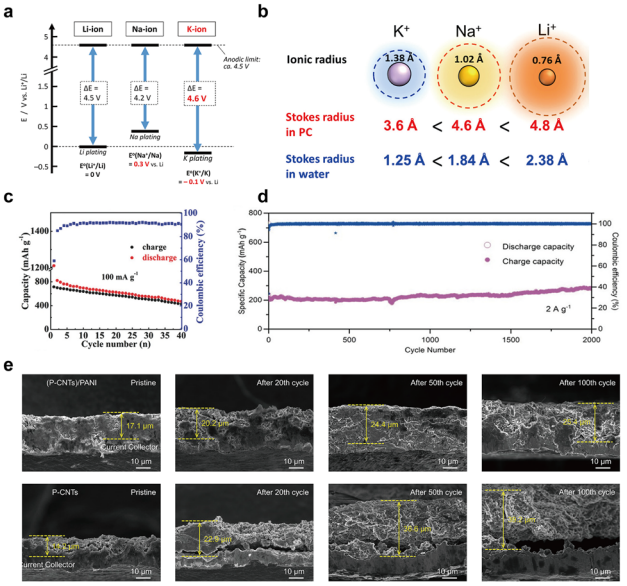

Fig. 40 Applications of elemental phosphorus materials to PIBs. (a) Electrochemical voltage windows of LIBs, SIBs, and PIBs in carbonate electrolyte solutions. (b) Comparison of ionic radii and Stokes radii in propylene carbonate and water among Li^+, Na^+, and K^+. Reproduced with permission from ref. 629. Copyright 2020 American Chemical Society. (c) Cycling performance of the red-P/3D carbon nanosheet framework nanocomposite at 100 mA g^{-1}. Reproduced with permission from ref. 634. Copyright 2018 John Wiley and Sons. (d) Long-term cycling performance of red-P/3D sulphur and nitrogen co-doped carbon nanofiber electrodes at 2 A g^{-1}. Reproduced with permission from ref. 637. Copyright 2022 John Wiley and Sons. (e) SEM images of the thickness of (P-CNTs)/PANI (top) and P-CNTs without PANI coating (bottom) in the initial and depotassiation states after 20, 50, and 100 cycles at 1000 mA g^{-1}. Reproduced with permission from ref. 569. Copyright 2022 John Wiley and Sons.

Amorphous red-P has been investigated for PIBs due to its non-toxicity and cost-effectiveness for mass production. However, its intrinsic low conductivity ($\sim 10^{-14}$ S cm^{-1}) and significant volume expansion during the potassiation/depotassiation make pure red-P unsuitable as electrodes. To address this issue, researchers have explored the incorporation of highly conductive carbon materials into the phosphorus anode to enhance its storage performance. In 2017, Zhang *et al.* measured the K^+ storage capacity of red-P-based composites.[636] They utilized red-P and carbon black as precursors to prepare the P/C anode *via* ball milling and electrochemical tests showed that this P/C anode exhibited an initial discharge capacity of 2171.7 mA h g^{-1} at 50 mA g^{-1}, significantly surpassing the performance of the Sn_4P_3/C anode (588.7 mA h g^{-1}). However, the P/C anode displayed rapid capacity fading, experiencing a 91% reversible capacity decay by the 20th cycle and reaching near-zero capacity by the 50th cycle. This capacity fading arose from the disordered microstructure of the composite, which impeded interfacial charge transport. To address the significant structural changes during the potassiation/depotassiation process, Xiong *et al.* anchored red-P nanoparticles to a 3D porous carbon nanosheet framework.[634] This approach yielded an initial charge capacity of 715.2 mA h g^{-1} at 100 mA g^{-1} through KP alloy formation, with a capacity retention of 427.4 mA h g^{-1} after 40 cycles (Fig. 40c). Although this method demonstrates improved cycle stability compared to Zhang's work,[636] there are limitations. Yu's group has further addressed the aggregation and pulverization issues of red-P particles by incorporating them into free-standing nitrogen-doped porous hollow carbon nanofibers, achieving a remarkable reversible capacity and exceptionally long cycle life (465 mA h g^{-1} at 2 A g^{-1} after 800 cycles).[590] Compared to nitrogen, lower electronegativity of sulphur leads to stronger chemical interactions with phosphorus atoms, increasing the adsorption energy of phosphorus atoms on sulphur-doped carbon matrices. Feng and colleagues have demonstrated that encapsulating strain-relaxed red-P within 3D interconnected multi-channel sulphur and nitrogen co-doped carbon nanofibers can enhance potassium ion capture and promote electrochemical reaction kinetics.[637] This composite structure not only buffers the stress and strain caused by significant volume expansion, but also utilizes the defect sites and high electronic conductivity generated by the synergistic effects of dual heteroatom doping. Impressively, the composite sustains a reversible capacity of 282 mA h g^{-1} after 2000 continuous cycles even at a high current rate of 2 A g^{-1} (Fig. 40d). In addition, employing metallic Bi as an electrochemically active coating has recently been shown to boost the electrical conductivity and cycle stability of red-P-based composites.[638]

The unique thermodynamically stable structure and high electronic conductivity ($\sim 10^2$ S cm^{-1}) of black-P make it a potential anode material for PIBs. However, pristine black-P is not practical for PIBs, and engineering is necessary to achieve reasonable electrochemical stability. Sultana *et al.*[568] have synthesized a black-P-carbon nanocomposite by ball milling and compacted the nanocomposites into dense aggregates to improve packaging of the black-P active surface. The nanocomposite shows a first cycle capacity of 617 mA h g^{-1} at 50 mA g^{-1} in 0.75 M KPF_6 in ethylene carbonate/diethyl carbonate (1 : 1 by vol.), which is more than twice that of the graphite anode (270 mA h g^{-1}). However, the cycle stability of the nanocomposite is relatively limited. After 50 cycles at the same current rate, the anode capacity decays to around 30 mA h g^{-1}. The gradual degradation of black-P during the cycle is responsible for the destruction of the solid electrolyte interphase layer and subsequent effects on the heterogeneous charge transfer kinetics. To improve the cycle stability of black-P-based materials, Lu's group has recently proposed the use of a PANI coating layer to alleviate black phosphorene degradation and replacement of graphite with regular nanostructured carbon materials to improve electrode conductivity.[569] They have assembled carbon nanotubes and black-P flakes by ball milling and performed *in situ* polymerization of PANI to obtain a phosphorene–carbon nanotubes/polyaniline ((P-CNTs)/PANI) composite. In 3 M KFSI/dimethoxyethane electrolyte, (-CNTs)/PANI shows a maximum charge capacity of 417.6 mA h g^{-1} at 500 mA g^{-1} and maintains a reversible capacity of 392.5 mA h g^{-1} and an impressive retention rate of 94% after 500 cycles. Morphological studies show that the (P-CNTs)/PANI electrode has good structural stability during the potassiation/depotassiation process (Fig. 40e). After 20, 50, and 100 cycles at 1000 mA g^{-1}, the thickness of the (P-CNTs)/PANI electrode shows a slight increase with the number of cycles, but

the overall electrode structure remains largely unchanged. In contrast, the P-CNT electrode without the PANI coating undergoes significant alterations in thickness and there are noticeable cracks in the electrode material. These observations suggest that the PANI coating mitigates volume expansion of the composite and prevents contact loss with the current collector during the charge/discharge process. Zhang *et al.*[639] have demonstrated that the incorporation of a localized high-concentration electrolyte enhances the ionic conductivity of the electrolyte and facilitates the formation of a robust solid electrolyte interphase for improved long-cycling stability of black-P/C electrodes. This finding emphasizes the role of the electrolyte in determining the electrochemical performance of KIBs and motivates further exploration to develop electrolytes that complement the characteristics of phosphorus-based electrodes.

5.2.5 Supercapacitors. As another important electrochemical energy storage device, supercapacitors (SCs) have high power density ($\sim 10^3$ W kg^{-1}), long cycling time, and an ultrafast charge/discharge rate (~ 1 s) when compared to rechargeable batteries.[640–642] A typical SC is composed of flexible substrates, current collectors, separators, electrolytes, and electrode materials.[643] In general, SCs can be divided into three types based on their charge storage mechanisms: electric double-layer capacitors, pseudocapacitors, and hybrid capacitors.[644] During the charging process of electric double-layer capacitors, electrolyte ions are adsorbed on the polarized electrode surface, generating an electric double layer between the electrode and electrolyte. Unrestricted by electrochemical charge transfer kinetics, the SCs can operate at charge/discharge rates within seconds. Pseudocapacitors involve fast, reversible Faradaic redox reactions at the electrode–electrolyte interfacial active sites. Hybrid capacitors store charges through a combination of electric double layers and Faradaic redox processes. Among the three types of capacitors, electric double-layer capacitors currently hold the largest market share due to the simplicity of the electric double-layer mechanism and the maturity of manufacturing technology.[645]

The electrode is a critical component of SCs and the material selection and structural design impact the electrochemical and cycling properties.[642] EPMs comprise various phosphorus allotropes and corresponding nanostructures boding well for electrodes. EPMs have the following advantages as SC electrodes: (i) both black-P derivatives and red-P modifications feature nanoscale channels within their structures, allowing for shorter charge transfer paths and facilitating electrochemical reaction kinetics. (ii) Low-dimensional EPMs exhibit great mechanical flexibility and packing density,[643] suggesting their potential use in fabricating sophisticated and flexible SCs. (iii) Low-dimensional EPMs possess large lateral dimensions and exposed active-site surfaces. In comparison with chemically inert carbon materials, EPMs are more likely to form composites with metal/non-metal species, enhancing electrochemical performance.

In 2016, Hao *et al.*[570] investigated the electrochemical performance of liquid-exfoliated black-P nanoflakes in all-solid-state SCs. The fabricated flexible electrodes achieved a high stack volumetric capacitance of 13.75 F cm^{-3} (48.5 F g^{-1}) at a scan rate of 0.01 V s^{-1} and a great capacitance retention of 71.8% at 0.5 V s^{-1} over 30 000 cycles (Fig. 41a and b). Although this charge storage performance is better than that of several graphene-based and multi-walled carbon nanotube electrodes,[646–648] the as-fabricated SCs still have some limitations, including a rapid volumetric capacitance reduction with increased charge/discharge rates, which is due to morphological degradation caused by long-term sonication. Yang *et al.*[649] have described a modified electrochemical exfoliation approach for the production of high-quality few-layered black-P nanoflakes. Vacuum filtering of the black-P nanoflake dispersion yields free-standing thin films for flexible quasi-solid-state micro-SCs. The as-prepared micro-SCs show excellent steady electrochemical performance at a high scanning rate of even up to 100 V s^{-1} (Fig. 41c) comparable to that of MXene-based quasi-solid-state micro-SCs at the same scanning rate.[649] The micro-SCs have a remarkable energy density of 3.63 mW h cm^{-3} at a power density of 0.247 W cm^{-3}, surpassing that of many 2D metal/non-metal materials (Fig. 41d). The device also exhibits an ultralong cycling lifetime of over 50 000 cycles at 0.2 A cm^{-3} and remarkable flexibility by retaining more than 91.3% of capacity after 500 bending cycles (Fig. 41e). Using 2D nanosheets as the building blocks in the 3D architecture can enhance the electrochemical performance of electrode materials, particularly for LIBs. To expand this strategy to SC electrodes, our group has reported the synthesis of a semi-connected 3D black-P sponge in three minutes under ambient conditions using a facile and simple electrochemical approach.[571] As an electrode material for all-solid-state SCs, black-P sponge shows a specific capacitance of 80 F g^{-1} at 10 mV s^{-1}, which is better than those of bulk black-P and black-P nanosheets. On the one hand, the high-quality ultrathin nanosheets as a basic unit of the black-P sponge offer expanded active sites and lateral dimensions and remove the high energy barrier of individual nanosheets to promote the charge transfer kinetics. On the other hand, the pores and channels inside the sponge allow contact with the electrolyte for better ion diffusion.

Nanostructures can enhance the specific capacitances of pure black-P electrodes, but achieving capacitance values in the hundreds or thousands remains highly challenging. To fabricate flexible SCs with a high energy density, the development of black-P-based multicomponent materials is necessary. Chen's group has chemically engineered black-P with carbon nanotubes to produce heterostructure composites.[572] With the aid of the microfluidic spinning technique, the composites are assembled into non-woven fabrics (Fig. 41f) for high-performance SC electrodes. The optimal flexible SC shows an outstanding volumetric capacitance of 308.7 F cm^{-3} at 0.1 A cm^{-3}, an energy density of 96.5 mW h cm^{-3}, cycle stability with a 90.2% retention rate after 10 000 cycles (Fig. 41g), and sustained bending durability. This enhancement stems from the open network structure of the composites featuring abundant well-defined micro/mesopores for enhanced conduction, rapid ion transport, and mechanical stability. Recently, Wu *et al.* have employed a droplet microfluidics method to fabricate an anisotropic black-P/ZIF-67 heterostructure composite and utilized 3D printing to construct fully integrated solid-state flexible SCs.[573] The SC has a high volumetric energy

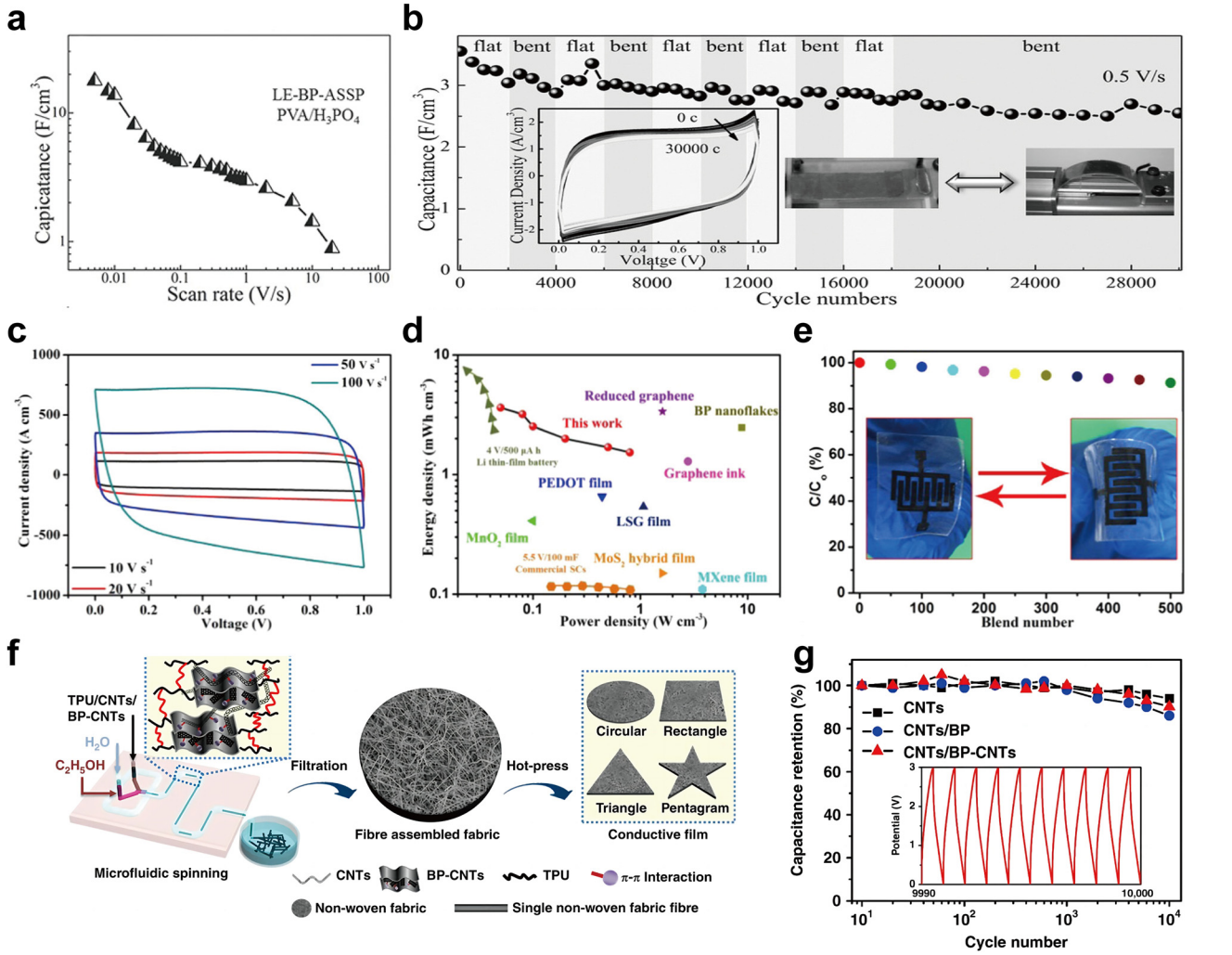

Fig. 41 Applications of elemental phosphorus materials to SCs. (a) Stack capacitances of the liquid-exfoliated black-P based all-solid-state SC (LE-BP-ASSP) with PVA/H_3PO_4 gel electrolyte at different scan rates. (b) Cycle stability of LE-BP-ASSP at 0.5 V s^{-1} in alternating flat and bent configurations. The inset shows representative cyclic voltammetry curves and photographs of the device in both flat and bent configurations. Reproduced with permission from ref. 570. Copyright 2016 John Wiley and Sons. (c) Cyclic voltammetry curves of the as-prepared micro-SCs at various scan rates. (d) Energy densities and power densities of the micro-SCs compared to those of various previously reported SC devices. (e) The capacitance retention rate of different bending cycles for the micro-SCs. Reproduced with permission from ref. 649. Copyright 2019 American Chemical Society. (f) Microfluidic spinning technique for the assembly of non-woven fabrics, which can be tailored into various shapes. (g) Cycle stability of black-P-carbon nanotube based SCs at 0.4 A cm^{-3}. The inset shows galvanostatic charge/discharge curves after 10 000 cycles. CNTs refer to pristine carbon nanotubes. CNTs/BP refers to a physical mixture of carbon nanotubes and black-P. CNTs/BP–CNTs refer to the physical mixture of carbon nanotubes and carbon nanotubes chemical-bridged black-P, which achieved the best electrochemical performance among the three materials. Reproduced with permission from ref. 572. Copyright 2018 Nature Publishing Group.

density of 109.8 mW h cm^{-3} at a power density of 0.675 W cm^{-3}, a capacitance of 506 F cm^{-3}, and long-term stability for 12 000 cycles. These research findings demonstrate the significant potential of SCs in next-generation wearable devices.

Researchers have also shown interests in red-P as an electrode material for SCs due to its environmental-friendless, cost-effectiveness, chemical stability, and high theoretical capacitance similar to that of black-P.[650] However, as previously stated, the poor electrical conductivity of pristine red-P limits the charge storage effectiveness. To enhance the conductivity, red-P is often coupled with carbon materials such as graphene and carbon nanotubes through chemical bonding or vdW interactions.[593] However, the main drawback of carbon materials is the low specific capacitance that impacts the energy storage efficiency. In this regard, black-P owns high conductivity and theoretical capacitance as well as compatibility with red-P. In 2017, Chen *et al.* reported the *in situ* synthesis of red-P/black-P composites using a facile sonication method and their application as SC electrodes.[579] The cyclic voltammetry curves of the resulting electrode exhibited a rectangular-like shape, indicating the electric double-layer charge mechanism at the electrolyte/electrode interface.[651] At a current density of 0.5 A g^{-1}, the hybrid composite showed a specific capacitance of around 60.1 F g^{-1} and 83.3% capacity retention for 2000 cycles.

This work not only establishes the excellent energy storage properties of red-P/black-P hybrids, but also provides a straightforward and cost-effective preparation method. Inspired by Chen's work, Gopalakrishnan and colleagues incorporated sulfonated porous carbon materials into red-P/black-P hybrids to boost the electrochemical performance of elemental phosphorus hybrids.[592] As an SC electrode, the ternary composite has a high specific capacitance of 364.5 F g^{-1} and maintains long-cycling stability retaining 89% of capacity after 10 000 charge/discharge cycles. The improved capacitive properties are associated with the synergistic effects between elemental phosphorus hybrids and porous carbon materials. The highly stable carbon frameworks featuring phosphorus bonding and heteroatom doping provide numerous active sites for ionic interactions and improve the surface wettability for seamless electrode/electrolyte interactions. Other EPMs such as blue-P and green-P have recently also shown promising theoretical potential as electrodes in SCs.[604]

5.2.6 Other energy storage applications. Lithium–sulphur batteries (LSBs) represent a promising type of rechargeable battery with significant development potential. They offer advantages such as low mass density (Li: 0.534 g cm^{-3} and S: 2.07 g cm^{-3}),[652] high theoretical energy density (2600 W h kg^{-1}),[653] and cost-effectiveness. However, several critical challenges associated with sulphur cathode materials have impeded the practical application of LSBs. First of all, both sulphur and polysulfides have poor electrical conductivity. The conductivities of sulphur monomers and their final discharge product Li_2S are approximately 5×10^{-30} S cm^{-1} and 3×10^{-17} S cm^{-1} at room temperature, respectively.[654,655] Second, the chain polysulfide (Li_2S_x, $4 \leq x \leq 8$) generated during the cathode reaction upon discharge can dissolve in the liquid electrolyte, leading to diffusion and migration within the battery. This process contributes to degradation of LSBs. In addition, owing to the substantial density disparity between monomeric sulphur (2.07 g cm^{-3}) and Li_2S (1.66 g cm^{-3}), the cathode experiences a volume change of around 80% during charging and discharging cycles.[656,657] The primary strategies to address these issues involve encapsulating sulphur within suitable materials and modifying the separator.

Few-layered black-P nanosheets offer several advantages such as large interlayer spacing (~3.08 Å), high sulfophilicity, and high lithium-ion mobility, rendering them ideal encapsulating materials for sulphur cathodes. Zhou *et al.* have constructed a 2D heterostructure of black-P/graphene for encapsulating sulphur species to provide catalytic and chemisorptive benefits for electrolyte-lean Li–S batteries.[658] The 2D heterostructure not only enhances the electrochemical stability of black-P nanosheets, but also facilitates electronic regulation between black-P and graphene. The electric field generated at the heterostructure interface increases the intrinsic conductivity of the materials and accelerates electron transfer in the redox conversion of polysulfides. Concurrently, it promotes chemisorption of polysulfides and reduces the migration barrier for lithium ions to catalyze the conversion of polysulfides. These features contribute to low capacity fading with an average decline as low as 0.021% per cycle after 600 cycles at 2C. Xu *et al.*[555] have demonstrated that BPQDs have a higher lithium polysulfide adsorption capacity and more substantial Li_2S precipitation capacity than large black-P flakes (Fig. 42a and b). BPQDs show strong interactions with lithium polysulphide through P–S and P–Li bonds and the abundant active sites at the edges of BPQDs catalyze the conversion of lithium polysulphide. As a result, the porous carbon nanofibers/sulphur cathodes containing a small amount (2 wt% of the cathode weight) of BPQDs exhibit fast reaction kinetics, no polysulphide shuttling, and excellent cycling stability. The porous carbon nanofibers/sulphur cathode with BPQDs has an initial capacity of 1234 mA h g^{-1} at 0.1C and after 200 cycles, it retains a capacity of 1072 mA h g^{-1} (Fig. 42c) and shows a small capacity decay rate of 0.06% per cycle. In comparison, the porous carbon nanofibers/sulphur cathode without BPQDs has an initial capacity of only 1036 mA h g^{-1} and a decay rate of 2% per cycle. The BPQD containing cathode also delivers greater rate performance than the BPQD-free cathode (Fig. 42d).

While both the component and structural design of the cathode materials discussed above inhibit polysulfide shuttling and enhance the cycle stability, they do not eliminate shuttling, particularly during extended cycling. Consequently, researchers have explored separator modification by introducing active materials to physically restrict polysulfides or chemically anchoring polysulfides.[656,659,660] The modified separators also decrease the impedance between the cathode and separator, enhance the wettability between the separator and electrolyte, and improve the electrochemical performance. Cui's group has prepared a uniform, dense black-P nanoflake coating on a Celgard commercial polypropylene separator by vacuum filtration deposition.[556] The black-P coating intercepts and combines the polysulfides to prevent diffusion through the separator to the anode. The binding energy of the black-P coating to lithium polysulfide ranges from 1.32 to 2.82 eV (without vdW interaction) and 1.86 to 3.05 eV (with vdW interaction) and increases as the Li_2S_x molecular chain shortens (x decreasing from 8 to 1). This energy is higher than that of the graphene coating (0.21–0.79 eV). The capacity of the cells with a conventional separator decays to below 100 mA h g^{-1} at 0.4 A g^{-1} after 100 cycles, while the capacity retention of separators modified with classical graphene is around 66%. In contrast, the black-P modified separator displays an initial discharge capacity of 930 mA h g^{-1} and retains a capacity of 800 mA h g^{-1} after 100 cycles. In further high-rate cycling studies, the specific capacity of the black-P modified separator remains at 623 mA h g^{-1} even at a high rate of 3.5 A g^{-1}.

In addition to black-P, red-P is used in separator modification. Red-P is a weak Lewis base agent that can undergo reasonable Lewis acid–base interactions with weak Lewis acids of lithium polysulphide, allowing it to chemically anchor the polysulphide. Concurrently, red-P can anchor polysulphides through sulphur chain interactions to inhibit shuttling and the interaction between red-P and polysulfide leads to the production of a high-conductivity by-product Li_3PO_4 which aids in Li^+ transport in the separator and promotes the sulphur reaction kinetics. Wang *et al.* were the first to utilize red-P nanoparticles to modify conventional polypropylene separators, capturing and reusing lithium polysulphide through strong chemical interactions between red-P and

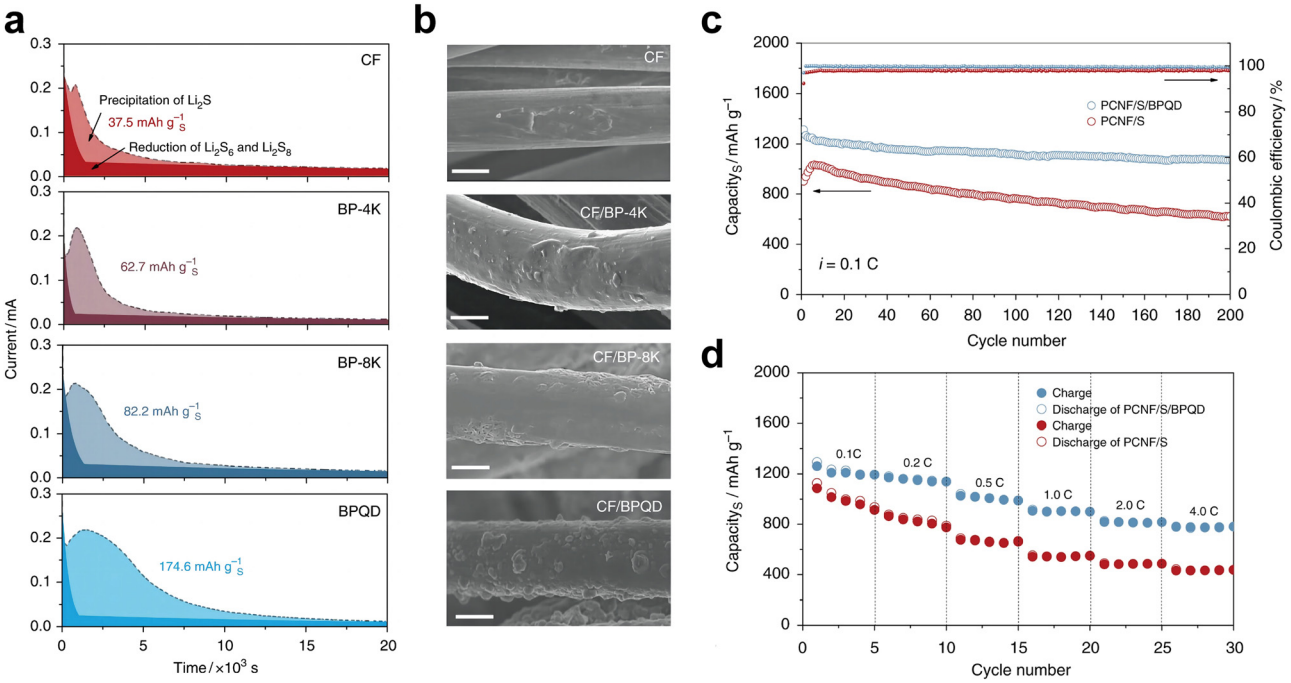

Fig. 42 Applications of BPQDs to LSBs. (a) Potentiostatic discharge curves of Li_2S_8 tetraglyme solution on various substrates at 2.05 V. The dark/light colours denote the reduction of Li_2S_8/Li_2S_6 and the precipitation of Li_2S, respectively. CF refers to carbon fibers. BP-4K and BP-8K refer to 4000 rpm and 8000 rpm centrifugated black-P products, respectively. (b) SEM images of the precipitation of Li_2S on various substrates as indicated in (a). The scale bar is 5 μm. (c) Cyclic capacities and Coulombic efficiencies of porous carbon nanofibers/sulphur cathode containing BPQDs (PCNF/S/BPQD) and pristine PCNF/S at 0.1C for 200 cycles. (d) Cyclic capacities of PCNF/S/BPQD and PCNF/S at various rates. Reproduced with permission from ref. 555. Copyright 2018 Nature Publishing Group.

polysulfides.[661] The LSBs based on red-P modified separators have excellent cycling properties. The unmodified polypropylene separators experienced substantial pore blockage due to polysulfide penetration with polysulphide decomposing, precipitating, and obstructing the pores. In contrast, the red-P modified separator maintained a highly porous surface to inhibit polysulfide penetration. The surface of lithium after cycling with the red-P modified separator was the smoothest, while the surface of lithium with the pristine polypropylene separators exhibited a large number of cracks and dendrites. This result suggests that red-P-based separators inhibit polysulphides and safeguard the lithium anode from corrosion. Consequently, the red-P modified separators achieved a high capacity retention of 82% during a long cycle test of 500 cycles at a current density of 1C, better than that of super P-coated separators (65%) and pristine polypropylene separators (43%). The red-P-based separators also had an excellent rate capability of 809 mA h g^{-1} at a high rate of 2C. Moreover, incorporating an independent functional interlayer between the cathode and separator of LSBs can physically block and chemically absorb lithium polysulfide. An interlayer with exceptional conductivity can function as a secondary current collector to improve the cathode conductivity. Lee *et al.*[662] prepared a red-P nanoparticle-coated carbon nanotube film as an interlayer by pulsed laser ablation and direct spinning. The interlayer provides efficient Li^+ and electron transport as well as strong chemical anchoring of lithium polysulfide. Consequently, the interlayer has a superior specific capacity of 782.3 mA h g^{-1} at 3C, long-term cycle stability, and high Coulombic efficiency. At a rate of 1C, the specific capacity initially reaches 1050.2 mA h g^{-1} and remains at 769.5 mA h g^{-1} after 500 cycles, with a Coulomb efficiency exceeding 99%.

Lithium-air batteries (LABs), which operate through the reversible reaction of Li + O_2 ↔ Li_2O_2, have the potential to offer an impressive theoretical energy density of around 3500 W h kg^{-1}. However, the sluggish kinetics of the cathode leads to high overpotentials, substantial polarization, and poor reversibility. As discussed in Section 5.1.4, EPMs inherently offer several benefits for electrocatalytic oxygen evolution, rendering them promising candidates to enhance the reaction kinetics of LABs. Cheng *et al.*[557] have designed a BPQD-modified δ-MnO_2 catalyst and prepared it on carbon cloth using a hydrothermal method as a binder-free cathode for LABs. The Li–O_2 cell with this BPQD modification shows a high capacity of 8463 mA h g^{-1} at 100 mA g^{-1} (Fig. 43a) which is greater than the capacity of 2965 mA h g^{-1} without BPQD modification (Fig. 43b), demonstrating the high catalytic activity of BPQD/δ-MnO_2 in the oxygen reduction reaction (ORR). In the cyclic voltammetry test (Fig. 43c), the BPQD/δ-MnO_2 electrode exhibits a higher onset potential for the ORR (2.64 V) and a lower onset potential for the OER (3.04 V) than the δ-MnO_2 electrode without BPQD modification.[557] Additionally, the peak OER current of the BPQD/δ-MnO_2 electrode increases significantly, suggesting that the introduction of BPQDs enhances the electrochemical reaction kinetics. Cycling stability tests (Fig. 43d–f) reveal that BPQD/δ-MnO_2 polarization gradually increases with the cycle

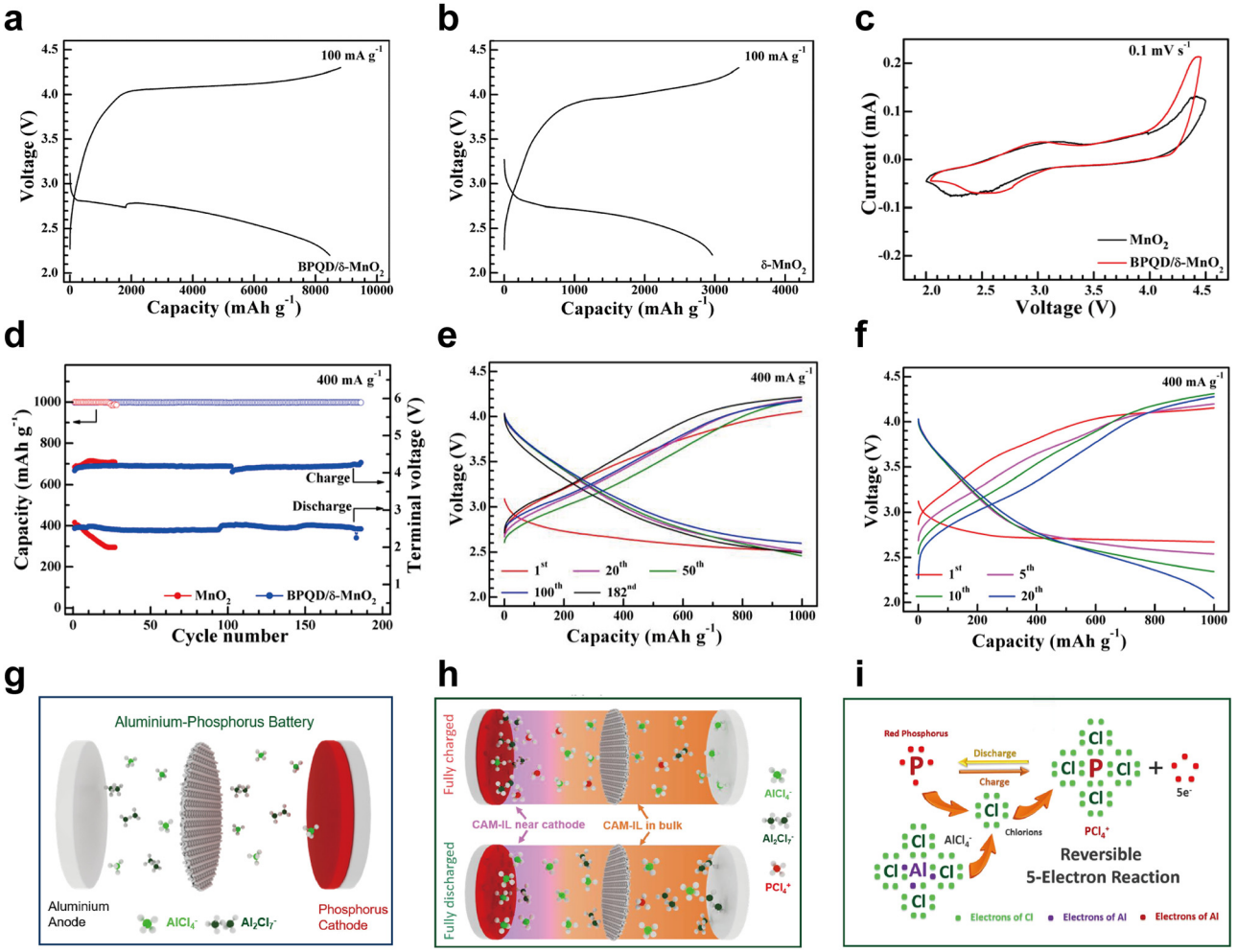

Fig. 43 Applications of elemental phosphorus materials to other energy storage applications. (a) Voltage curves of BPQD/δ-MnO_2 and (b) δ-MnO_2-catalyzed Li–O_2 cells at 100 mA g^{-1}. (c) Cyclic voltammetry curves of BPQD/δ-MnO_2 and δ-MnO_2-catalyzed Li–O_2 cells at 0.1 mV s^{-1}. (d) Cycling performance of Li–O_2 cells with BPQD/δ-MnO_2 and δ-MnO_2 cathodes at 400 mA g^{-1} with a capacity limit of 1000 mA h g^{-1}, and (e) voltage curves of BPQD/δ-MnO_2 and (f) δ-MnO_2-catalyzed Li–O_2 cells. Reproduced with permission from ref. 557. Copyright 2019 Elsevier. (g) Scheme of an aluminium–phosphorus battery comprising a phosphorus cathode, aluminium anode, and CAM-IL electrolyte. (h) Scheme of the distribution of AlCl, Al_2Cl, and PCl in an Al–P battery under a fully charged/discharged state. (i) Scheme of the reversible phosphorus-based five-electron transfer processes. Reproduced with permission from ref. 664. Copyright 2022 Elsevier.

number, whereas δ-MnO_2 polarization increases rapidly. These findings indicate that BPQDs enhance the ORR/OER catalytic activity, leading to superior discharge capacity and cycling stability for LABs. Moreover, researchers have identified black phosphorene and nitrogen-doped blue-P as highly effective catalysts for cathodic reactions through theoretical calculations.[601,663]

Recent advances have shown that EPMs are being developed for new types of energy storage devices. Cai *et al.* have reported an innovative aluminium–phosphorus battery which incorporates red-P as the cathode, aluminium as the anode, and CAM-IL as the electrolyte (Fig. 43g).[664] This battery boasts a high theoretical capacity of 4325 mA h g^{-1} due to the reversible, phosphorus-based five-electron transfer reaction as shown in Fig. 43h and i. The researchers have assembled a prototype aluminium–phosphorus battery showing a capacity of 1512 mA h g^{-1} and an energy density of 1176 W h kg^{-1}, which surpass those of many alkaline metal ion batteries. By employing modification strategies, the cutting-edge aluminium–phosphorus battery is anticipated to have large potential in low-cost, high-performance energy storage applications due to the multiple electron transfer reactions and abundant availability of both phosphorus and aluminium.

In summary, EPMs possess many intrinsic advantages including high theoretical capacity, resource abundance, and environmental compatibility and are promising candidates for various energy storage devices such as hydrogen storage systems, alkali metal batteries, and supercapacitors. As researchers delve deeper into various modification strategies including structural design and nanosizing, practical application challenges such as structural and electrochemical stability degradation stemming from the volume expansion of phosphorus allotrope materials must be addressed. The development of innovative energy storage devices with various phosphorus allotropes like aluminium–phosphorus batteries will offer more viable alternatives for energy

storage systems. Arguably, the most prominent potential application of EPMs currently lies in the realm of energy storage. However, all these applications are still in their infancy and lack industrial-grade standardized testing. Therefore, further efforts are necessary to transition from research to commercial application.

5.3. Environmental remediation applications

5.3.1 Pollutant sensing. The hazardous pollutants released from industrial processes, transportation, and other human activities have detrimental effects on the environment and human health and in particular, monitoring and regulating air quality are becoming more critical. Gas sensors are devices that generate a measurable output in response to a specific gaseous stimulus. The typical device structure is similar to that of a field effect transistor, where the sensing materials serve as a channel between the source and drain electrodes modulated by the gate voltage.[665] The fundamental principle of gas sensors is based on the detection of changes in the electrical resistance induced by gas molecules adsorbed onto the sensing materials.[666–668] NO_2 is a common air contaminant released by locomotive exhaust and industrial combustion and the United States Environmental Protection Agency has stated that exposure to NO_2 concentrations exceeding 53 parts per billion (ppb) can lead to health problems.[669] Chronic inhalation of high concentration of NO_2 can irritate the cough mucosal membranes and pulmonary tract to produce dyspnoea and can even lead to lung cancer. Various sensors made of metal oxides have been reported to be highly sensitive to NO_2.[670] However, these metal oxide sensors often require a high operating temperature and in order to make them wearable and portable, it is critical to develop a high-sensitivity gas sensor capable of real-time NO_2 detection at room temperature.

Previous theoretical studies have demonstrated that EPMs exhibit ultra-high sensitivity and selectivity for NO_2 detection at room temperature. The strong interaction between the frontier orbitals of NO_2 molecules and p_z orbitals of phosphorus atoms leads to charge transfer, enabling NO_2 to act as an oxidant and remove electrons from EPMs.[671–673] Among the various allotropes of phosphorus, black phosphorene is currently the predominantly used sensing material. In 2015, Abbas *et al.*[674] developed a multilayer black-P field-effect transistor for gas sensing (Fig. 44a) showing an NO_2 detection limit of 5 ppb (Fig. 44b). Cho *et al.*[675] have investigated the sensing characteristics of black-P, graphene, and MoS_2 and found that black-P has an intrinsic sensing capacity that is 20 times greater than that of graphene and MoS_2 (Fig. 44c). Furthermore, only black-P shows selective response to NO_2 while being unresponsive to oxygen-functionalized molecules.[675] A plausible explanation for the superior NO_2 detecting capability of black-P has been postulated. First, since NO_2 molecules are paramagnetic, their adsorption on black-P can provoke spin polarization, leading to the production of a spin-polarized current in the channel. Second, black-P has larger molecular adsorption energy than the other two materials rendering it more sensitive to NO_2 (Fig. 44d).

To further improve the detection ability of NO_2, Sang's group has recently prepared a few-layered black-P microribbon-based gas sensor that achieves sub-ppb level detection under nitrogen and ambient conditions.[676] As shown in Fig. 44e, the gas sensor shows response ($\Delta G/G_0$) to different concentrations of NO_2 over time at room temperature and zero relative humidity. After exposing the sensor to 0.4 ppb of NO_2, the response is about 8.09%. The specific adsorption capacity of the black-P microribbon for NO_2 is assessed by comparing the response to 100 ppb NO_2 and other common indoor air pollutants under dry ambient conditions (Fig. 44f). When the sensor is exposed to 10 ppm NO_2 for five cycles (on–off mode) under dry conditions at room temperature (Fig. 44g), good repeatability is demonstrated and the selective detection limit is 0.4 ppb for NO_2 at room temperature and zero relative humidity. However, in practical applications, ambient humidity often complicates the calibration process and reduces the sensor accuracy. If the relative humidity goes up from 0 to 80%, the response of the black-P microribbon sensor to NO_2 is no longer evident in the range of 100 ppb to 20 ppm (Fig. 44h) because adsorbed water molecules capture electrons and degrade the sensitivity.[677] Therefore, gas sensors made of black-P need to be surface passivated.

An alternative strategy is to select a relatively chemically stable allotrope of phosphorus. Zhu *et al.*[30] deposited a red-P thin film on an Au electrode-patterned SiO_2/Si substrate. The film is composed of micrometer-scale particles assembled from amorphous red-P nanoclusters with different sizes (10 or 100 nm). As shown in Fig. 44i, the sensor shows dynamic response-recovery curves for different concentrations of NO_2 (40 to 200 ppm) at room temperature in nitrogen. The sensor has high sensitivity (229%) to 200 ppm NO_2, but due to the poor conductivity of amorphous red-P, the bias stress and high noise levels (0.107%) reduce the detection limit.[30] The conductivity of red-P can be improved by modulating the internal structure. The selectivity of the sensor is evaluated in the presence of potentially interfering gases (Fig. 44j) and the response to NO_2 is significantly stronger, even though the concentration of the other gases is higher (1000 ppm) compared to NO_2 (200 ppm). This selectivity originates from the intrinsic physicochemical properties of elemental phosphorus. Amorphous red-P has several unique sensing features, including amphoteric sensing that allows it to respond negatively to both oxidizing and reducing gas species. In addition, unlike the adsorption mechanism of black-P,[674] the adsorption process on amorphous red-P is dominated by synergistic Langmuir isotherm adsorption and P–P bond expansion (Fig. 44k).

DFT calculations show that other EPMs are also promising gas sensors. Montes *et al.* investigated the adsorption of inorganic gas molecules (CO, CO_2, NH_3, NO, and NO_2) on blue-P nanotubes (Fig. 44l).[678] In comparison with black phosphorene, blue-P nanotubes exhibit better selectivity and sensitivity for N-containing gases. The current change before and after adsorption of NO_2 is 294% at a voltage of 0.2 V, which is more than 2.4 times higher than those of other materials such as phosphorene (122%),[679] MoS_2 (57%),[680] and $PtSe_2$ (12%).[681] Singsen *et al.* have observed that silicon-doped green phosphorene exhibits high selectivity towards carbonyl-containing volatile organic compounds such as acetone, propane, and formaldehyde because the pi and lone pairs of electrons in the carbonyl group interact

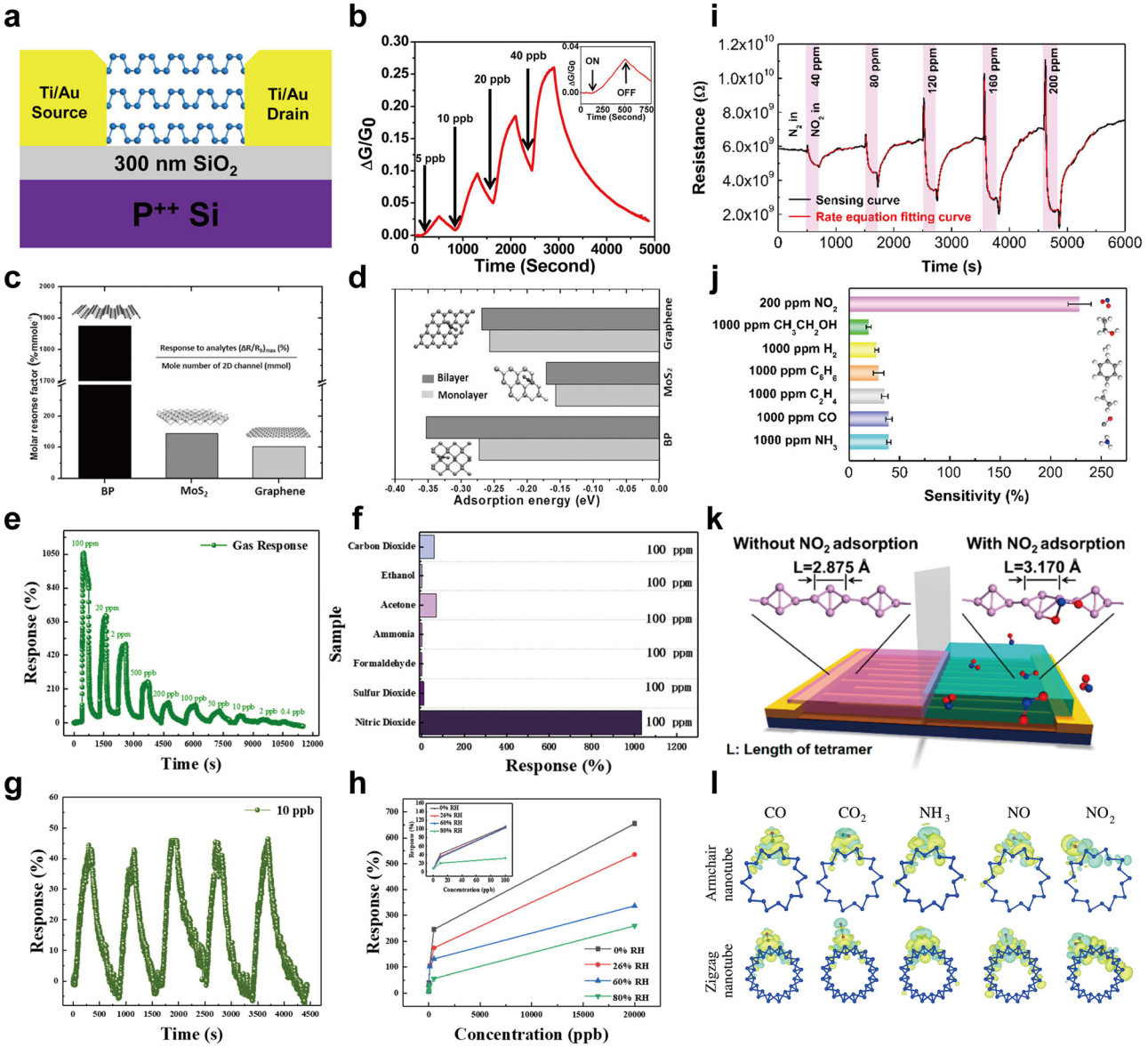

Fig. 44 Applications of elemental phosphorus materials to pollutant sensing. (a) Scheme of a multilayer black-P field-effect transistor. (b) A plot of the time-dependent relative conductance change ($\Delta G/G_0$) is presented for a multilayer black-P sensor, which exhibits sensitivity to NO_2 concentrations ranging from 5 ppb to 40 ppb. The inset displays an enlarged image of the response to a 5 ppb NO_2 exposure, with marked time points denoting the activation and deactivation of the NO_2 gas. Reproduced with permission from ref. 674. Copyright 2015 American Chemical Society. (c) Calculated molar response factor of the black-P sensor and comparison with that of MoS_2 and graphene. (d) Minimum NO_2 adsorption energy for monolayer and bilayer for black-P, MoS_2, and graphene. Reproduced with permission from ref. 675. Copyright 2016 John Wiley and Sons. (e) A plot of the time-dependent relative conductance change ($\Delta G/G_0$) is presented for a black-P microribbon sensor under zero relative humidity, which exhibits sensitivity to NO_2 concentrations ranging from 0.4 ppb to 100 ppm. (f) Black-P microribbon sensor response to NO_2 and other common indoor air pollutants under dry room temperature conditions. (g) Five cycles of the on–off switching mode through the black-P microribbon sensor to 10 ppb NO_2 under dry room temperature conditions. (h) Plots of the black-P microribbon sensor response to NO_2 concentrations are presented under various relative humidity conditions of 0%, 26%, 60%, and 80% in air. The inset displays the response to concentrations of NO_2 in the range of 0.4 ppb to 100 ppb under the same relative humidity conditions. Reproduced with permission from ref. 676. Copyright 2022 American Chemical Society. (i) Dynamic sensing response-recovery curves (black) measured for different NO_2 concentrations ranging from 40 to 200 ppm. A fitting function based on an adsorption rate is used to fit the data, and the results are shown in red. (j) Red-P based sensor response to NO_2 (200 ppm) and other gas molecules (1000 ppm). (k) Expansion of the amorphous red-P tetramer induced by NO_2 adsorption. Reproduced with permission from ref. 30. Copyright 2018 American Chemical Society. (l) The adsorption of different molecules on the armchair and zigzag blue-P nanotubes with variances in electron density. Reproduced with permission from ref. 678. Copyright 2017 Royal Society of Chemistry.

with electron-deficient Si atoms in the doped green phosphorene to produce strong adsorption.[682] Dharani *et al.*[683] and Bhuvaneswari *et al.*[684] have studied the adsorption characteristics of hexanal, benzyl chloride, and chlorobenzene on violet phosphorene. Zhang *et al.*[685] have conducted spin-polarized first-principles computations with vdW correction to investigate the properties of

fibrous phosphorene in air pollution monitoring. Fibrous phosphorene with a lone pair of electrons in the p orbital shows strong attraction to electron-deficient substances, giving rise to high detection sensitivity for NO, NO_2, O_3, and SO_2. However, gas sensors made of blue, green, violet, and fibrous phosphorus are still in the theoretical stage.

5.3.2 Gas phase degradation of pollutants. As aforementioned, air pollution is a pressing concern for the modern society due to acid rain, photochemical smog, stratospheric ozone depletion, greenhouse effects, and other environmental issues.[686,687] Combustion of fossil fuels in thermal power plants results in exhaust emissions with high concentrations of SO_x and NO_x that often exceed the permissible limits.[688] Among the various sulphur and nitrogen oxide species, SO_2 and NO are the most abundant and hazardous air pollutants and so accurate purification is crucial.[689]

Yellow phosphorus, also known as white phosphorus, is typically unsuitable for energy storage and catalysis due to its high reactivity. However, its cost-effective and efficient reducing properties make it a popular in flue gas treatment. In the 1990s, Chang and Liu utilized a yellow phosphorus/alkaline emulsion to remove NO_x and SO_2 from the flue gas.[690] The emulsified yellow phosphorus droplets come in contact with O_2 in the flue gas, releasing O_3 and O, which oxidize NO into water-soluble NO_2, and convert SO_2 into $(NH_4)_2SO_4$ and $CaSO_4$.[691] The alkaline buffer in the yellow phosphorus emulsion plays a crucial role in maintaining an appropriate pH range for NO_x absorption to enhance the adsorption efficiency. Ning's group has reported that red mud could replace $CaCO_3$ as the alkaline buffer in the yellow phosphorus emulsion and suggested economic benefits in removing insoluble NO and reducing the ecological risk of red mud accumulation.[692] The primary reaction products between NO and yellow phosphorus are high-priced NO_3^-, NO_2^-, and PO_4^{3-}, which have potential applications in the production of nitrogen and phosphorus fertilizers. Subsequently, an improved oxidation process has been developed to simultaneously remove NO_x and SO_2 using yellow phosphorus and red mud and the removal capabilities are 97.9% and 100%, respectively.[693] This method is more cost-effective than traditional oxidative denitrification and desulfurization techniques while achieving the purpose of "waste control by waste".

Photo-oxidation is an innovative and promising technique for the degradation of gaseous pollutants, and Lu's group has developed photocatalytic black-P composites for NO removal. The 2D heterojunction of black-P/monolayer Bi_2WO_6 is prepared by integrating Bi_2WO_6 into the surface of black-P nanosheets (Fig. 45a).[388] Active radicals are identified by DMPO-ESR spin-trap measurements and a charge transfer mechanism for photodegradation is postulated based on the Z-scheme. In the process, the electron in the valence band of black-P reduces O_2 to $^{\bullet}O_2^-$, which then oxidizes NO to NO_3^- (Fig. 45b). Owing to the excellent electron transfer ability and broader absorption range (from UV to NIR) of black-P, the NO removal efficiency goes up to 67% after irradiation for 30 minutes, which is 2.6 times greater than that of the pristine monolayer Bi_2WO_6 (26%). A type I heterojunction of black-P/porous g-C_3N_4-HKUST-1 has also been designed (Fig. 45c).

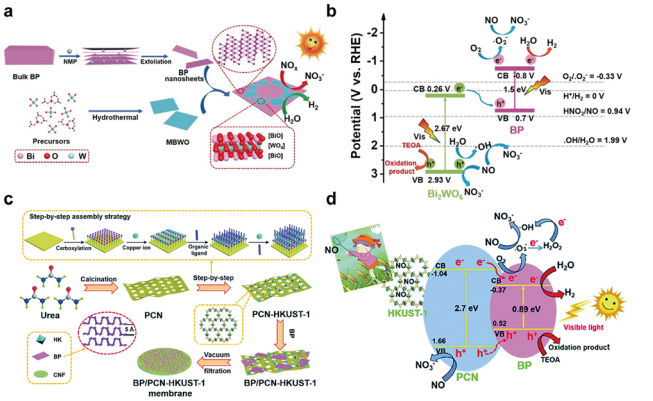

Fig. 45 Applications of elemental phosphorus materials to gaseous pollutant degradation. (a) Scheme of the fabrication of a 2D heterojunction black-P/monolayer Bi_2WO_6. (b) Photocatalytic mechanism of the black-P/monolayer Bi_2WO_6 heterojunction under visible-light irradiation. Reproduced with permission from ref. 388. Copyright 2019 John Wiley and Sons. (c) Scheme of fabrication of the black-P/porous g-C_3N_4-HKUST-1 membrane. (d) Photocatalytic mechanism of the black-P/porous g-C_3N_4-HKUST-1 membrane under visible-light irradiation. Reproduced with permission from ref. 387. Copyright 2019 Royal Society of Chemistry.

HKUST-1 is a copper benzene tricarboxylate metal–organic framework (MOF) with good NO adsorption properties and visible light response.[694] The ternary composite is employed to photocatalyze the oxidation of NO at the ppb level under visible-light irradiation (Fig. 45d).[387] The optimal composite membrane achieves an NO removal ratio of 74%, which is better than those of previously reported g-C_3N_4-based heterojunctions.[695–697] This high photo-oxidation performance can be ascribed to the synergistic effects of the heterojunction as well as superior NO adsorption capability of the MOF.

5.3.3 Liquid phase degradation of pollutants. Water pollution caused by chemical pollutants such as organic dyes, antibiotics, and heavy metals causes significant environmental and health concerns because these liquid pollutants have adverse effects on aquatic organisms, even at ecologically relevant concentrations between ng L^{-1} and g L^{-1}. Moreover, these toxins can enter the human body through the food chain, posing significant health risks.[698–700] Traditional wastewater treatment techniques are divided into physical and chemical ones. Physical methods typically encompass adsorption, membrane filtration, and ion exchange and chemical methods include chemical deposition and advanced oxidation. However, most of these treatments are designed to remove either organic pollutants or heavy metals, but both types of contaminants normally exist in wastewater. Therefore, there is a pressing need to develop pollutant removal technologies capable of degrading both organic pollutants and heavy metal ions simultaneously. Low-dimensional EPMs have great physical adsorption capabilities for wastewater pollutants due to the large surface area and semiconductor characteristics, and they can also efficiently photo-degrade pollutants under visible light illumination.[701–703]

Synthetic organic dyes which are widely used industrially have become a growing concern due to their impact on the ecosystem. Azo dyes containing the azo-functional group R–N=N–R′

(R and R′ can be aryl or alkyl) constitute more than 70% of synthetic organic dyes.[28,704] Methyl orange is a representative azo dye that can be used to evaluate the effectiveness of degradation for other azo dyes. Zhang *et al.* have investigated the photo-degradation efficiency of 50 mL of methyl orange (100 ppm) using amorphous red-P, crystalline red-P ([P12(4)]P2[phase) microbelts and violet-P microrods.[396] Both crystalline red-P and violet-P exhibit higher efficiency under visible light irradiation compared to the amorphous red-P sample. Crystalline red-P degrades 90% of the methyl orange within 40 minutes and the rate is twice that of violet-P. The transient photocurrents of crystalline red-P microbelts, which have a bigger surface area, are higher than those of the violet-P microrods, indicating that the former has superior photo-induced charge separation and transfer efficiency.

Ag_2CO_3 has attracted the attention of many researchers due to the unique photocatalytic mechanism. Ag^+ in Ag_2CO_3 can react with photo-induced electrons to form the Ag/Ag_2CO_3 system,[705] in which an appropriate amount of Ag can lead to the production of surface plasmon resonance for enhanced light absorption and photocatalytic efficiency,[706] but excessive Ag may cause photo-corrosion and suppress the photocatalytic activity.[707] Therefore, precise control of the Ag concentration on the surface is critical. By taking advantage of the conduction band and valence band positions of Ag_2CO_3 and black-P, a Z-scheme black-P/Ag_2CO_3 heterojunction can be constructed to avoid excessive formation of Ag nanoparticles and improve the photocatalytic activity to degrade organic dyes. Wang *et al.* have synthesized a direct Z-scheme heterojunction photocatalyst composed of PDDA-functionalized black-P nanosheets and Ag_2CO_3 by co-precipitation.[708] The black-P/Ag_2CO_3 composite has a high degradation efficiency as exemplified by the mineralization of 94.1% of methyl orange into CO_2 and H_2O within 30 minutes, which is better than that of Ag_2CO_3 (43.3%). After four irradiation cycles, the activity of the black-P/Ag_2CO_3 composite photocatalytic activity is 87.1%, whereas the pristine Ag_2CO_3 shows a 19.2% degradation rate (Fig. 46a). Ag_2CO_3 has a lower conduction band potential than the $^{\bullet}O_2^-$ redox potential and the conduction band of Ag_2CO_3 is incapable of reducing O_2 to $^{\bullet}O_2^-$ based on the type-II mechanism. However, capture experiments show that both $^{\bullet}O_2^-$ and $^{\bullet}OH$ play important roles in the photocatalytic degradation of methyl orange (Fig. 46b and c), confirming that it is not a type-II heterojunction but rather a direct Z-scheme photocatalytic mechanism. The amount of black-P affects the photocatalytic activity, because excess black-P obstructs the photoactive sites on the Ag_2CO_3 surface but insufficient black-P cannot mitigate photo-corrosion. Therefore, the Ag concentration must be controlled to optimize the transfer and separation of photo-induced charges to function as an ''electron sink'' to enhance the stability of the black-P/Ag_2CO_3 heterojunction.

Rhodamine B is a well-known hydrophilic industrial colorant used in food processing, textile dyeing, and fluorescent labelling. Rhodamine B is classified as a group 3 carcinogen by The International Agency for Research on Cancer in 1987,[709] and it is considered a carcinogenic, genotoxic, and neurotoxic inducer or toxin in animals.[710] Jeong *et al.* synthesized amorphous partial oxidized violet-P through an open-air ball milling approach with controlled mechanical energy and the materials have excellent catalytic activity for the removal of rhodamine B in a light-free environment.[711] In contrast to crystalline violet-P prepared by conventional CVD, violet-P is amorphous. When 10 mg of partially oxidized violet-P is added to 40 mL of 30 mg L^{-1} rhodamine B solution, complete reduction occurs within 15 minutes and the fastest rate occurs in the first 5 minutes. Violet-P with strong electron affinity and surface P═O as the redox-active species are responsible for the outstanding activity.[711] Removal of the oxidized phosphorus moiety normally decreases the catalytic reduction rate, but amorphous violet-P retains the reducing ability due to the substantial negative charge on the surface which persists in a highly unstable state.

Inadvertent discharge of antibiotics is detrimental to the environment and organisms with antibiotic resistance and superbugs can develop, which pose threats to human beings.[712–714] Fe-based MOFs are a unique class of MOFs exhibiting excellent stability, large porosity, large surface area, ease of production, and environmental friendliness.[715–717] Among them, MIL-101(Fe) has found many applications in photocatalysis, although the fundamental limitation is fast electron–hole recombination that decreases the photocatalytic efficiency. In this respect, red-P is an excellent dopant to improve the photocatalytic activity of MOF-based photocatalysts. Lei *et al.* have prepared tunable red-P/MIL-101(Fe) composites by a low-temperature solvothermal technique and investigated the efficacy in photo-degradation of tetracycline.[718] Morphological analysis reveals that the purified red-P is evenly anchored on MIL-101(Fe) in the form of tiny particles thus producing a rough surface. At a pH of 5, tetracycline concentration of 50 mg L^{-1}, catalyst dosage of 0.50 g L^{-1}, and full-range wavelength exposure, the photocatalytic efficiency of the Red-P (15 wt%)/MIL-101(Fe) composite towards tetracycline is 90.1% in 80 minutes (Fig. 46d), which is higher than those of pristine MIL-101(Fe) (51.1%), red-P (29.2%), and red-P (1.5 wt%)/TiO_2 (75.9%) under the same conditions.[718] Furthermore, the composite has remarkable stability (Fig. 46e) and the photocurrent of red-P (15 wt%)/MIL-101(Fe) is also higher than that of the pristine MIL-101(Fe) (Fig. 46f).

Besides organic pollutants, inorganic pollutants such as lead, mercury, arsenic, and chromium contribute to water pollution. Cr(VI), a by-product of electroplating and leather manufacturing, can cause liver and renal disorders in humans.[719] The metal-free photocatalyst g-C_3N_4 with a bandgap of ~2.7 eV shows good chemical stability but its poor electroconductivity limits the catalytic activity.[720] Introduction of black-P with a smaller bandgap can improve the conductivity of g-C_3N_4 and the stability of black-P can be enhanced by covering the noncovalent surface with unreactive g-C_3N_4. Meng *et al.* have synthesized a ternary heterojunction photocatalyst of g-C_3N_4/Black-P/MoS_2 by the solvent-free high-energy ball milling method.[721] The grinding balls deliver high-temperature pulses to g-C_3N_4, black-P, and MoS_2 causing chemical bond breakage and formation and creating good interfacial contact to reduce the interfacial charge transfer impedance and facilitate carrier migration and separation, making g-C_3N_4/Black-P/MoS_2 an efficient photocatalyst. Under light illumination, the optimal g-C_3N_4/Black-P/MoS_2

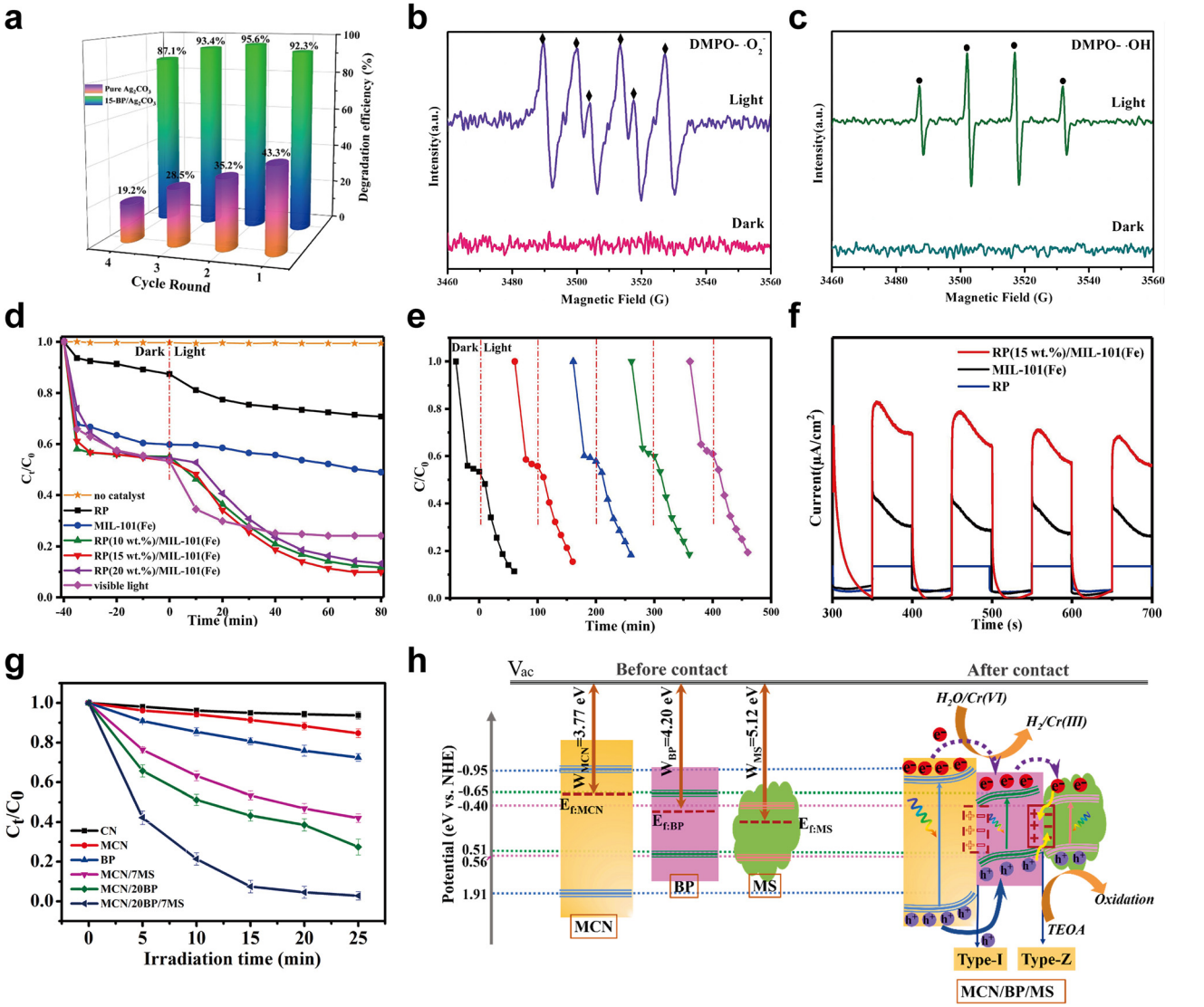

Fig. 46 Applications of elemental phosphorus materials to liquid phase pollutant degradation. (a) Cycling performance of Ag_2CO_3 and optimal black-P/Ag_2CO_3 composite for methyl orange degradation. (b) Electron spin resonance spectra of the black-P/Ag_2CO_3 composite for DMPO-$^{\bullet}O_2^-$ and (c) DMPO-$^{\bullet}$OH. Reproduced with permission from ref. 708. Copyright 2021 Springer. (d) The degradation of tetracycline using various photocatalysts. (e) The cycling stability of red-P/MIL-101(Fe) for tetracycline degradation. (f) Photocurrent responses of red-P/MIL-101(Fe), pristine MIL-101(Fe), and red-P. Reproduced with permission from ref. 718. Copyright 2020 Elsevier. (g) Photocatalytic Cr(VI) reduction rate curves in the presence of g-C_3N_4 (CN), ball-milled g-C_3N_4 (MCN), black phosphorus (BP), and binary and ternary composites. (h) The band energy alignment scheme and photocatalytic reaction mechanism of the g-C_3N_4/black-P/MoS_2 composite (MCN/BP/MS). Reproduced with permission from ref. 721. Copyright 2021 Elsevier.

composite eliminates nearly 100% Cr(VI) after 25 minutes (Fig. 46g). However, the reduction efficiency of Cr(VI) by black-P is inadequate with only 27.5% of Cr(VI) reduced in the same time. Hence, light absorption by the ternary composite increases considerably throughout the UV–vis range and charge transfer in the ternary composite shows the mixed type-I/Z scheme (Fig. 46h). This uncommon scheme allows integration of the electric field at the interface, making it difficult for photogenerated electrons to migrate from the high conduction band to the low conduction band or to recombine with valence band holes. As a result, more photogenerated electrons with the strong reducing capacity remain in the conduction band of g-C_3N_4 and black-P to boost the photocatalytic Cr(VI) reduction efficacy.[722]

5.3.4 Bacterial disinfection. Drinking water safety is a worldwide concern, particularly in developing countries that are experiencing rapid industrialization and urbanization.[719,723,724] According to the WHO, water contaminated with pathogenic microorganisms is responsible for 80% infections in developing countries.[725] To address this issue, various methods have been developed to disinfect water, for example, UV irradiation, ozonation, chlorination, and high-temperature treatment.[726] However, these traditional technologies have drawbacks such as insufficient disinfection, production of hazardous by-products, and high energy consumption and it is essential to develop high-efficiency and eco-friendly methods for bacterial disinfection. In recent years, semiconductor-based photocatalysis has

emerged as a promising alternative for disinfection.[727–729] The materials generate reactive oxygen species (ROS) that act as powerful oxidants to inactivate a wide range of pathogens.

Amorphous red-P has been extensively studied in photocatalysis as an inexpensive and ambient-stable semiconductor.[28] More importantly, it has low toxicity and can be used to disinfect drinking water.[730] In 2015, Xia *et al.*[731] reported inactivation of *Escherichia coli* by amorphous red-P under visible light irradiation. The purified amorphous red-P has superior bacterial inactivation efficiency due to the water stability and moderate bandgap (1.42 eV). At a concentration of 100 mg L^{-1}, the cell loss is 2×10^7 cfu mL^{-1} within 90 minutes during visible light irradiation (Fig. 47a), outperforming C_3N_4 and even metal-based B-Ni-*co*-doped TiO_2.[732,733] The disinfection

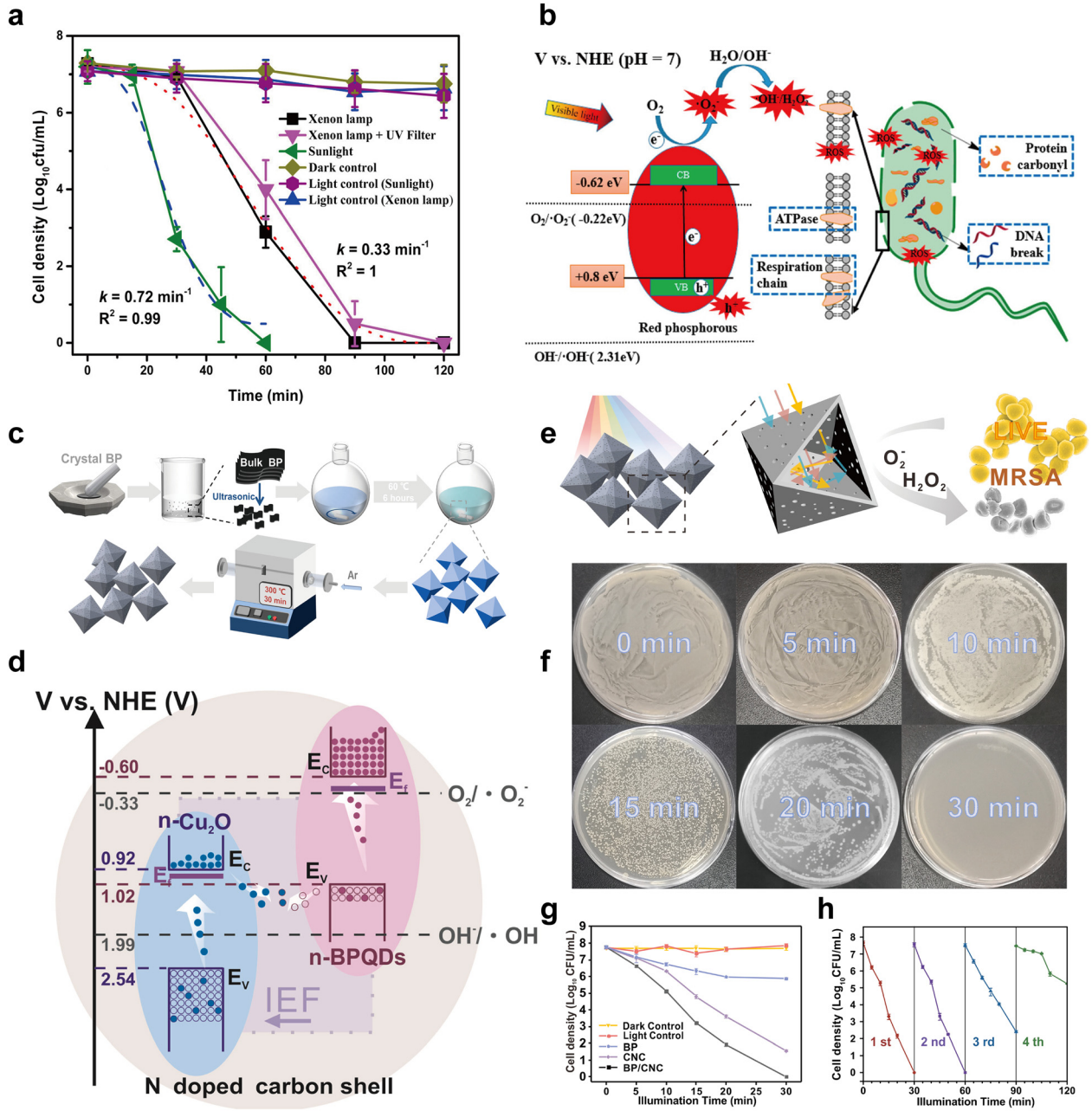

Fig. 47 Applications of elemental phosphorus materials to bacterial disinfection. (a) Photocatalytic inactivation kinetics under different irradiation conditions in the presence of amorphous red-P. (b) The proposed mechanism for bacterial disinfection by amorphous red-P under visible-light irradiation. Reproduced with permission from ref. 731. Copyright 2015 American Chemical Society. (c) The synthetic process for preparing BPQDs/Cu_2O/N-doped hollow porous carbon composite. (d) Z-scheme band structure and electron transfer pathway of the composite. (e) Scheme of the photo-responsive multidrug-resistant bacterial disinfection of BPQDs/Cu_2O/N-doped hollow porous carbon composites. (f) Photographs of the agar plates with the composite (10 mg L^{-1}) at different illumination times. (g) Disinfection efficiency of materials under different conditions. (h) The cycling stability of BPQDs/Cu_2O/N-doped hollow porous carbon composite for photocatalytic disinfection. Reproduced with permission from ref. 741. Copyright 2021 Elsevier.

mechanism of amorphous red-P has been studied by monitoring the leakage of membrane-functional enzymes and biomolecules. ROS attacks the cell membrane as the primary target, increases the cell membrane permeability, and ultimately kills the bacteria *via* intracellular protein carboxylation and DNA destruction (Fig. 47b). Athira *et al.*[734] have investigated the photocatalytic efficiency of commercial red-P in inactivating *Escherichia coli* using direct sunlight. The photo-induced ROS, mostly $O_2^{\bullet-}$ and $HO_2^{\bullet}$, sterilizes the bacteria within 50 minutes with a red-P concentration of 150 mg L^{-1}. The conduction band potential is −0.497 V, which is more negative than the potential required for the generation of $O_2^{\bullet-}$ by single-electron transfer reduction (−0.16 V *vs.* NHE) and it is also adequate for the production of $HO_2^{\bullet}$. These findings suggest that amorphous red-P has promising prospects in photocatalytic bacterial disinfection and is suitable for outdoor sterilization of water under natural light.

On the heels of the development of CVD for fibrous-P, several studies have focused on the photocatalytic performance pertaining to bacterial disinfection. Roshith and colleagues have prepared urchin-like fibrous-P with a bandgap of 1.9 eV and an absorption edge extending to 650 nm for more efficient sunlight absorption.[304] Under direct sunlight irradiation, a high capacity to inactivate *Escherichia coli* is at 10^8 cfu mL^{-1} in 30 minutes is demonstrated by urchin-like fibrous-P, which is more effective than most red-P-based systems. An optofluidic reactor capable of continuous flow photocatalytic disinfection of *Escherichia coli* has been developed by immobilizing fibrous-P to the inner wall of a quartz capillary.[735] After sunlight exposure for 14 minutes, the immobilized photocatalyst reduces the bacterial concentration by 6.7 log 10 (>99.9999%). This continuous photocatalytic disinfection technique is promising for purposes as it can be scaled up. Zhang *et al.* have reported a two-step approach to prepare a crystalline red-P/graphene oxide layer on Ti for rapid microbial inactivation.[736] An irregular pyramidal crystalline red-P layer is first prepared on a Ti plate by CVD and then a graphene oxide layer is deposited on the red-P layer *via* the shellac heating transition. After exposure to simulated sunlight for 20 minutes, the composite film shows an inactivation rate of 99.9% against *Staphylococcus aureus* and *Escherichia coli* and also has good antibacterial properties upon exposure to visible (>410 nm), infrared (808 nm), and LED light.

The sharp edges of 2D nanosheets can physically damage bacterial membranes producing leakage of intracellular contents and bacterial death, the so-called "nanoknife" effect.[737–739] Hence, black-P nanosheets used as photocatalysts also produce physical antibacterial effects. He *et al.*[740] have constructed a metal-free 2D/2D black-P and graphitic carbon nitride heterojunction for efficient photocatalytic water disinfection under visible light. The disinfection activity against *Escherichia coli* is about 7 times higher than that of pristine graphitic carbon nitride, and bacterial cells (10^7 cfu mL^{-1}) can be completely inactivated within 60 minutes. Both black-P and graphitic carbon nitride nanosheets are 2D materials with synergistic physical antibacterial properties, and graphitic carbon nitride can further mitigate the recombination of photoinduced electrons/holes during the photocatalytic process to give electrons sufficient time to form $^{\bullet}OH$ and H_2O_2 to attack bacteria.

A stable and well-ordered hierarchical structure can improve the sunlight usage and lifespan of photo-induced charge carriers. In particular, porous hollow structures have excellent light-harvesting properties because of the longer light path. Luo *et al.* have reported an MOF-derived BPQDs/Cu_2O/N-doped hollow porous carbon structure for inactivation of methicillin-resistant *Staphylococcus aureus*.[741] The synthesis involves cross-linking copper ions with trimesic acid through coordination assembly to form Cu-BTC MOFs. Benzimidazole is added to the solution to control the MOF shape and introduce the N source.[742] Cu-BTC MOFs are then used as the self-sacrificial templates in the annealing process to generate Cu_2O/N-doped hollow porous carbon. The sonicated BPQDs interact with Cu_2O/N-doped hollow porous carbon to produce a regular octahedral-like ternary composite (Fig. 47c). Cu_2O nanoparticles and BPQDs are evenly distributed throughout the hollow sphere to form an indirect Z-type heterojunction (Fig. 47d). This heterojunction constitutes a broad spatial barrier to prevent charge congestion and recombination thus allowing unimpeded transmission of photo-induced carriers and preserving the high redox potential. Upon visible light irradiation, the ternary composite shows photo-responsive multidrug-resistant bacterial disinfection (Fig. 47e) and completely inactivates 10^8 cfu mL^{-1} *Staphylococcus aureus* within 30 minutes with a dosage of only 10 mg L^{-1} (Fig. 47f). Control experiments show that visible light irradiation or the photocatalyst alone has no disinfection effects on drug-resistant bacteria and the disinfection efficiency of single BPQD or Cu_2O/N-doped hollow porous carbon is thus not significant (Fig. 47g).[741] The photocatalytic stability of BPQDs/Cu_2O/N-doped hollow porous carbon is very good in the first three cycles, but the efficiency decreases in the 4th cycle (Fig. 47h) on account of photo-corrosion of Cu_2O.[743] Future research should aim at developing more stable and efficient hierarchical photocatalysts.

5.3.5 Soil remediation. In recent decades, the global population growth has spurred the demand for food and intensified agriculture resulting in soil degradation. This is a critical global issue that poses lasting harm to non-renewable soil resources with severe economic and environmental consequences.[744–746] Saline-alkali soil is a significant type of salt-induced degraded soil that covers an area of over 900 million hectares worldwide.[747] Typically, it is characterized by high salinity, poor water permeability, and inadequate aeration leading to nutrient deficiencies, decreased crop yields, and low quality.[748–750] Biochar is a solid carbonaceous residue produced by thermal decomposition of biomass.[751] It is utilized as a soil pollutant adsorbent and conditioner with significant potential in improving saline-alkali soil. However, pristine biochar faces challenges in soil remediation. For example, it contains a large amount of soluble alkali ions such as Na^+, K^+, Mg^{2+}, Ca^{2+}, and excessive use of alkaline biochar materials can increase the susceptibility of soil salinization and impede plant growth.[752,753] Therefore, modifying the biochar is necessary for saline-alkali soil reclamation.

Introducing phosphorus-containing substances (phosphate, phosphorus oxide, and phosphorus allotrope) into biochar has been proven to be effective modification technology to improve remediation of saline-alkali soil. Phosphorus-containing substances undergo biodegradation in the soil to generate

phosphate groups which can neutralize the soluble alkaline ions in biochar.[754] Moreover, phosphorus acts as a nutrient element for soil microorganisms and plant growth and enhances plant phosphorus absorption, soil microbial activity, and metal-ion immobilization.[755] In 2019, Li's group reported that $Ca(H_2PO_4)_2$ engineered swine manure biochar could immobilize toxic metal ions in smelting contaminated soil by forming insoluble phosphate precipitates.[756] The application of this modified biochar not only reduced the accumulation of toxic metals in the plants, but also increased the plant biomass to simultaneously promote remediation and crop production. Red-P is a possible fertilizer that slowly converts to phosphate in the presence of H_2O and O_2.[757] Recently, Sun's group has developed red-P-modified biochar through a ball milling approach for saline-alkali soil remediation.[750] The ball milling process converts red-P powder into nanoparticles that are evenly distributed on the biochar surface with a portion being oxidized into phosphorus oxide and phosphate. The biochar is further ground into submicron particles to increase the specific surface area and enhance soil remediation. Through a series of experiments in amended soil, researchers have proposed a remediation mechanism for red-P-modified biochar (Fig. 48). First, biochar has a strong salt adsorption capacity to allay saline-alkali stress or stress responses in plants. Both biochar-based materials and ball-milled red-P reduce the soil electrical conductivity. Second, biochar improves the physical and chemical properties of saline-alkali soil by increasing the organic carbon content, cation exchange capacity, and water storage while reducing the soil pH. Red-P-modified biochar can reduce the soil pH to 7.36 and maintain it at a near-neutral pH because phosphoric acid in red-P neutralizes hydroxyl ions in soil.[758] Third, biochar is nutrient-rich and improves soil fertility for plant growth. For the same level of phosphorus addition, red-P-modified biochar contains more available phosphorus than ball-milled red-P, suggesting its high potential as a fertilizer with the ability to accumulate and release soil nutrients beneficial for microorganisms and plant reproduction. Overall, red-P-modified biochar is a promising soil amendment to enhance the soil productivity and biological activity and in turn to promote the growth of plants in saline-alkali soils.

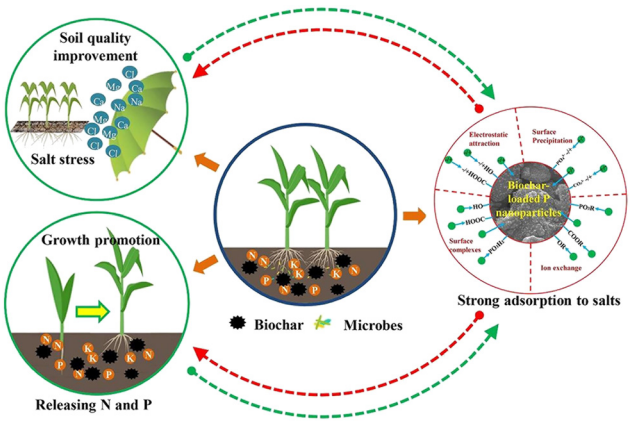

Fig. 48 Mechanism of red-P-modified biochar for saline-alkali soil remediation. Reproduced with permission from ref. 750. Copyright 2021 Elsevier.

The use of EPMs in soil remediation is still in its early stages and only red-P has been directly applied for this purpose. Zhang *et al.* have found that black-P nanosheets have no significant effects on the enzyme activity in black soil during 60 day exposure, demonstrating that black-P nanosheets are eco-friendly compared with many other nanomaterials.[759] This study highlights the potential of black-P nanomaterials in soil remediation. Black-P nanomaterials possess a larger specific surface area and higher chemical activity than nanoscale red-P, so that black-P can quickly deposit oxidized metal ions in contaminated soil and release high-valence phosphate in a shorter time. Therefore, it is anticipated that modified black-P nanomaterials have superior soil remediation characteristics compared to red-P. Moreover, the current production cost of black-P-based materials has been reduced to 0.235 Euros per gram, boding well for more widespread use in soil remediation.[385]

In summary, EPMs have developed distinctive applications in the field of sensing and environmental remediation. Among these, black-P exhibits superior conductivity in comparison to other EPMs, rendering it an optimal choice for the development of highly sensitive sensors. For pollutant treatment and bacterial disinfection, amorphous red-P, crystalline fibrous-P, and violet-P have demonstrated notable performance. This is largely due to their appropriate bandgaps and environmental stability, making them highly promising for sustained roles in environmental catalysis. Furthermore, given that phosphorus serves as a suitable fertilizer, exploring the application of EPMs in soil remediation could prove to be a strategy with dual benefits, both repairing the soil and enhancing its fertility. However, research in this particular domain is still relatively sparse at the present.

6. Conclusions and outlook

This review presents a comprehensive and up-to-date overview of the progress pertaining to the development, fundamental properties, synthetic methodologies, and applications of EPMs to energy conversion, storage, and environmental remediation. Significant progress has been made in understanding the structure–property–function relationships of various phosphorus allotropes to provide insights into the optimal constituent materials and systems for specific applications. Although considerable achievements have been made in the design and engineering of EPMs, there are still ample opportunities for further advancements. To facilitate sustained development of EPMs in the post-graphene era, this review provides critical information about the four important aspects: (1) new allotrope discovery, (2) fundamental property exploration, (3) synthetic methods and optimization, and (4) applications and performance improvement.

The synergistic integration of artificial intelligence-based theoretical calculations and chemical synthesis presents a promising avenue for the discovery of new phosphorus allotropes. Theoretically, phosphorus allotropes can be obtained by the mixed assembly of distinct phosphorus cluster motifs. However, as the range of EPMs continues to expand, the challenge of identifying new allotropes becomes increasingly

complex. Traditional reliance on experience and intuition may no longer be sufficient to uncover intricate phosphorus allotrope structures. This is where the evolving realm of artificial intelligence steps in. With its potential applications in structural prediction, functional forecasting, performance analysis, and structural optimization, artificial intelligence offers a plethora of opportunities for improving both efficiency and accuracy in these areas. Implementation of machine learning-driven theoretical predictions can screen different phosphorus cluster motifs with high throughput in order to reduce the need for substantial human labour and computing resources.[56] We anticipate that more advanced and sophisticated artificial intelligence algorithms will be developed, especially structural prediction of new EPMs, in the future to expedite discovery and enhance our understanding of these materials.

The primary aim of exploring fundamental properties is to elucidate the precise structures of existing phosphorus allotropes and the microscopic and nanoscopic interactions between EPMs and exotic materials. Currently, the research on properties focuses on black-P based materials but there is an urgent need to characterize the fundamental properties of other EPMs. It is imperative to conduct a comprehensive examination of the structures of all five red-P modifications and evaluate the associated structure–property relationships. Furthermore, it is essential to investigate the alloying and dealloying mechanisms of different crystalline phosphorus for alkaline metal ion batteries. To observe these interactions, appropriate *in situ* characterization techniques should be employed in conjunction with *ex situ* methods.

Optimization of the synthetic methods and conditions is crucial to both bulk crystals and low-dimensional nanomaterials of EPMs. Developing high-quality, cost-effective synthesis for bulk crystal production is important. Although several techniques have been reported for the preparation of gram-level black-P single crystals, the high production cost, elevated temperature, and high pressure have impeded widespread adoption in many laboratories. Successful synthesis of blue and green phosphorus bulk crystals remains elusive but presents a potential avenue for future inorganic synthesis. Although crystalline red-P bulk crystals can be prepared by chemical vapor transport and other methods, contamination from other crystalline forms is prevalent necessitating improvements in quality control. The synthesis of nanostructured EPMs grapples with challenges such as low yield and inadequate quality control. The liquid-phase exfoliation method shows promise for large-scale EPMs nanosheet production, but often encounters issues like edge defects. In the synthesis of blue phosphorene, molecular beam epitaxy is the only reported technique so far. It typically produces domain sizes ranging from a few nanometers to several tens of nanometers, which is significantly smaller than that required for practical device fabrication. Additionally, there is a need to optimize the synthesis of 1D nanoribbons and 0D quantum dots for different phosphorus allotropes.

The current state of EPM application is primarily in the proof-of-concept stage. The majority of applications are confined to laboratory settings with insufficient attention being paid to the cost, processability, and scalability of the synthesized EPMs. Among the various EPMs, black-P and amorphous red-P have greater potential for industrialization due to more advanced development. Energy storage is one of the most promising applications of EPMs and the construction of 3D hierarchical structures represents a promising approach to enhance the EPM energy storage capability by promoting ion diffusion and accommodating volume changes during charging-discharging cycles. Furthermore, a deeper understanding of the intercalation processes involving multivalent ions and organic ions will be useful for the development of EPM-based electrodes in next-generation batteries and supercapacitors.

In conclusion, substantial advancements have been made in the field of EPMs in the past decade. Cutting-edge analytical methodologies, computational chemistry, and nano-techniques have fueled this progress and deepened our understanding of the intricate structure–property–function relationships of EPMs. At the same time, it is important to keep in mind that phosphorus is a critical resource. Application of phosphorus beyond its dominant use for fertilizers should be critically evaluated for sustainability, including in the field of EPMs. Future progress is anticipated from extensive characterization of phosphorus allotropes and development of a diverse range of micro and nanostructures, with an increasing focus on sustainable usage and recycling of phosphorus. This balanced approach will open new opportunities for the practical application of EPMs.

Author contributions

J. Wang, G. Qu, and X.-F. Yu proposed the topic of the review. H. Tian surveyed the literature and compiled the manuscript. G. Lai supplemented the tables and figures. P. K. Chu, G. Jiang, S. Zhuang, and J. Shi refined the manuscript and provided constructive insight. J. Gao, Q. Wu, L. Yao, L. Zeng, Y. Liu, and X. Yang discussed and revised the tables and figures. Y. Dou, Z. Duan, X. Feng, X. He, and J. Zhao discussed and revised the text.

Conflicts of interest

There are no conflicts to declare.

Acknowledgements

This work was supported by National Natural Science Foundation of China (92143301, 92043302, and 21975280), National Key Research and Development Program of China (2020YFA0907500), Shenzhen Science and Technology Program Grant (JCYJ20220818100806014), and Youth Innovation Promotion Association of the Chinese Academy of Sciences (2020354).

References

1 H. Tiessen, P. White and J. Hammond, *The Ecophysiology of Plant-Phosphorus Interactions*, Springer, 2008, **https://www.springer.com/gp/book/9781402084348**.

2 C. T. Reinhard, N. J. Planavsky, B. C. Gill, K. Ozaki, L. J. Robbins, T. W. Lyons, W. W. Fischer, C. Wang, D. B. Cole and K. O. Konhauser, *Nature*, 2017, **541**, 386–389.
3 A. R. Jupp, S. Beijer, G. C. Narain, W. Schipper and J. C. Slootweg, *Chem. Soc. Rev.*, 2021, **50**, 87–101.
4 M. Pasek and K. Block, *Nat. Geosci.*, 2009, **2**, 553–556.
5 S. Duhamel, J. M. Diaz, J. C. Adams, K. Djaoudi, V. Steck and E. M. Waggoner, *Nat. Geosci.*, 2021, **14**, 359–368.
6 A. C. Martiny, C. T. A. Pham, F. W. Primeau, J. A. Vrugt, J. K. Moore, S. A. Levin and M. W. Lomas, *Nat. Geosci.*, 2013, **6**, 279–283.
7 X. Wei, Y. Hu, B. S. Razavi, J. Zhou, J. Shen, P. Nannipieri, J. Wu and T. Ge, *Soil Biol. Biochem.*, 2019, **131**, 62–70.
8 C. M. Moore, M. M. Mills, K. R. Arrigo, I. Berman-Frank, L. Bopp, P. W. Boyd, E. D. Galbraith, R. J. Geider, C. Guieu, S. L. Jaccard, T. D. Jickells, J. La Roche, T. M. Lenton, N. M. Mahowald, E. Maranon, I. Marinov, J. K. Moore, T. Nakatsuka, A. Oschlies, M. A. Saito, T. F. Thingstad, A. Tsuda and O. Ulloa, *Nat. Geosci.*, 2013, **6**, 701–710.
9 M. Delgado-Baquerizo, F. T. Maestre, A. Gallardo, M. A. Bowker, M. D. Wallenstein, J. L. Quero, V. Ochoa, B. Gozalo, M. García-Gómez, S. Soliveres, P. García-Palacios, M. Berdugo, E. Valencia, C. Escolar, T. Arredondo, C. Barraza-Zepeda, D. Bran, J. A. Carreira, M. Chaieb, A. A. Conceição, M. Derak, D. J. Eldridge, A. Escudero, C. I. Espinosa, J. Gaitán, M. G. Gatica, S. Gómez-González, E. Guzman, J. R. Gutiérrez, A. Florentino, E. Hepper, R. M. Hernández, E. Huber-Sannwald, M. Jankju, J. Liu, R. L. Mau, M. Miriti, J. Monerris, K. Naseri, Z. Noumi, V. Polo, A. Prina, E. Pucheta, E. Ramírez, D. A. Ramírez-Collantes, R. Romão, M. Tighe, D. Torres, C. Torres-Díaz, E. D. Ungar, J. Val, W. Wamiti, D. Wang and E. Zaady, *Nature*, 2013, **502**, 672–676.
10 S. Huang and X. Ling, *Small*, 2017, **13**, 1700823.
11 Y. Yi, Z. Sun, J. Li, P. K. Chu and X.-F. Yu, *Small Methods*, 2019, **3**, 1900165.
12 H. Liu, Y. Du, Y. Deng and P. D. Ye, *Chem. Soc. Rev.*, 2015, **44**, 2732–2743.
13 G. Qu, T. Xia, W. Zhou, X. Zhang, H. Zhang, L. Hu, J. Shi, X. F. Yu and G. Jiang, *Chem. Rev.*, 2020, **120**, 2288–2346.
14 X. Shao, Z. Ding, W. Zhou, Y. Li, Z. Li, H. Cui, X. Lin, G. Cao, B. Cheng, H. Sun, M. Li, K. Liu, D. Lu, S. Geng, W. Shi, G. Zhang, Q. Song, L. Chen, G. Wang, W. Su, L. Cai, L. Fang, D. T. Leong, Y. Li, X. F. Yu and H. Li, *Nat. Nanotechnol.*, 2021, **16**, 1150–1160.
15 J. Shao, H. Xie, H. Huang, Z. Li, Z. Sun, Y. Xu, Q. Xiao, X. F. Yu, Y. Zhao, H. Zhang, H. Wang and P. K. Chu, *Nat. Commun.*, 2016, **7**, 12967.
16 E. T. Alori, B. R. Glick and O. O. Babalola, *Front. Microbiol.*, 2017, **8**, 971.
17 A. Seweryn and T. Bujak, *ACS Sustainable Chem. Eng.*, 2018, **6**, 17294–17301.
18 J. Xiong, P. Cui, X. Chen, J. Wang, K. Parida, M.-F. Lin and P. S. Lee, *Nat. Commun.*, 2018, **9**, 4280.
19 H. Liu, K. Hu, D. Yan, R. Chen, Y. Zou, H. Liu and S. Wang, *Adv. Mater.*, 2018, **30**, 1800295.
20 J. Pang, A. Bachmatiuk, Y. Yin, B. Trzebicka, L. Zhao, L. Fu, R. G. Mendes, T. Gemming, Z. Liu and M. H. Rummeli, *Adv. Energy Mater.*, 2018, **8**, 1702093.
21 W. Gao, Y. Zhou, X. Wu, Q. Shen, J. Ye and Z. Zou, *Adv. Funct. Mater.*, 2021, **31**, 2005197.
22 Y. Duan, R. Li, Q. Liu and Z. Shen, *Green Chem.*, 2022, **24**, 3475–3501.
23 Y. Zhu, J. Ren, X. Zhang and D. Yang, *Nanoscale*, 2020, **12**, 13297–13310.
24 L. Zeng, L. Huang, J. Zhu, P. Li, P. K. Chu, J. Wang and X. F. Yu, *Small*, 2022, **18**, 2201808.
25 N. A. Giffin and J. D. Masuda, *Coord. Chem. Rev.*, 2011, **255**, 1342–1359.
26 L. Zeng, X. Zhang, Y. Liu, X. Yang, J. Wang, Q. Liu, Q. Luo, C. Jing, X.-F. Yu, G. Qu, P. K. Chu and G. Jiang, *Chem*, 2021, **8**, 632–662.
27 K. Song, Q. Li, Y. Yuan, S. Hu, J. Liu, Y. Zhang, Y.-T. Pan, W. Zhao and J. He, *ACS Appl. Nano Mater.*, 2022, **5**, 18080–18092.
28 C. M. Fung, C. C. Er, L. L. Tan, A. R. Mohamed and S. P. Chai, *Chem. Rev.*, 2021, **122**, 3879–3965.
29 Y. Sun, L. Wang, Y. Li, Y. Li, H. R. Lee, A. Pei, X. He and Y. Cui, *Joule*, 2019, **3**, 1080–1093.
30 Q. Zhu, H. Wang, J. Yang, C. Xie, D. Zeng and N. Zhao, *ACS Sens.*, 2018, **3**, 2629–2636.
31 J. Zhang, X. Liu, G. Neri and N. Pinna, *Adv. Mater.*, 2016, **28**, 795–831.
32 W. Hittorf, *Ann. Phys.*, 1865, **202**, 193–228.
33 H. Thurn and H. Krebs, *Acta Crystallogr., Sect. B: Struct. Sci.*, 1969, **25**, 125–135.
34 W. L. Roth, T. W. DeWitt and A. J. Smith, *J. Am. Chem. Soc.*, 1947, **69**, 2881–2885.
35 C. C. Stephenson, R. L. Potter, T. G. Maple and J. C. Morrow, *J. Chem. Thermodyn.*, 1969, **1**, 59–76.
36 L. Du, Y. Zhao, L. Wu, X. Hu, L. Yao, Y. Wang, X. Bai, Y. Dai, J. Qiao, M. G. Uddin, X. Li, J. Lahtinen, X. Bai, G. Zhang, W. Ji and Z. Sun, *Nat. Commun.*, 2021, **12**, 4822.
37 A. G. Ricciardulli, Y. Wang, S. Yang and P. Samori, *J. Am. Chem. Soc.*, 2022, **144**, 3660–3666.
38 A. J. Mannix, B. Kiraly, M. C. Hersam and N. P. Guisinger, *Nat. Rev. Chem.*, 2017, **1**, 0014.
39 P. W. Bridgman, *J. Am. Chem. Soc.*, 1914, **36**, 1344–1363.
40 P. W. Bridgman, *Proc. Am. Acad. Arts Sci.*, 1937, **71**, 387–460.
41 I. Shirotani, R. Maniwa, H. Sato, A. Fukizawa, N. Sato, Y. Maruyama, T. Kajiwara, H. Inokuchi and S.-I. Akimoto, *Nippon Kagaku Kaishi*, 1981, **10**, 1604–1609.
42 S. Lange, P. Schmidt and T. Nilges, *Inorg. Chem.*, 2007, **46**, 4028–4035.
43 T. Nilges, M. Kersting and T. Pfeifer, *J. Solid State Chem.*, 2008, **181**, 1707–1711.
44 M. Köpf, N. Eckstein, D. Pfister, C. Grotz, I. Krüger, M. Greiwe, T. Hansen, H. Kohlmann and T. Nilges, *J. Cryst. Growth*, 2014, **405**, 6–10.
45 L. Li, Y. Yu, G. J. Ye, Q. Ge, X. Ou, H. Wu, D. Feng, X. H. Chen and Y. Zhang, *Nat. Nanotechnol.*, 2014, **9**, 372–377.
46 H. Liu, A. T. Neal, Z. Zhu, Z. Luo, X. Xu, D. Tománek and P. D. Ye, *ACS Nano*, 2014, **8**, 4033–4041.

47 Q. Liu, X. Zhang, J. Wang, Y. Zhang, S. Bian, Z. Cheng, N. Kang, H. Huang, S. Gu, Y. Wang, D. Liu, P. K. Chu and X.-F. Yu, *Angew. Chem., Int. Ed.*, 2020, **59**, 14383–14387.
48 L. Zhang, H. Huang, B. Zhang, M. Gu, D. Zhao, X. Zhao, L. Li, J. Zhou, K. Wu, Y. Cheng and J. Zhang, *Angew. Chem., Int. Ed.*, 2020, **59**, 1074–1080.
49 Z. Zhu and D. Tománek, *Phys. Rev. Lett.*, 2014, **112**, 176802.
50 W. H. Han, S. Kim, I.-H. Lee and K. J. Chang, *J. Phys. Chem. Lett.*, 2017, **8**, 4627–4632.
51 L. Craco, T. A. d S. Pereira, S. R. Ferreira, S. S. Carara and S. Leoni, *Phys. Rev. B*, 2018, **98**, 035114.
52 J. L. Zhang, S. Zhao, C. Han, Z. Wang, S. Zhong, S. Sun, R. Guo, X. Zhou, C. D. Gu, K. D. Yuan, Z. Li and W. Chen, *Nano Lett.*, 2016, **16**, 4903–4908.
53 H. Wang, C. Liu, H. Wang, X. Han, S. Zhang, J. Sun, Y. Zhang, Y. Cao, Y. Yao and J. Sun, *Chem. Commun.*, 2021, **57**, 3975–3978.
54 V. L. Deringer, D. M. Proserpio, G. Csanyi and C. J. Pickard, *Faraday Discuss.*, 2018, **211**, 45–59.
55 V. L. Deringer, M. A. Caro and G. Csanyi, *Nat. Commun.*, 2020, **11**, 5461.
56 V. L. Deringer, C. J. Pickard and D. M. Proserpio, *Angew. Chem., Int. Ed.*, 2020, **59**, 15880–15885.
57 A. Koneru, R. Batra, S. Manna, T. D. Loeffler, H. Chan, M. Sternberg, A. Avarca, H. Singh, M. J. Cherukara and S. Sankaranarayanan, *J. Phys. Chem. Lett.*, 2022, **13**, 1886–1893.
58 Y. Zhou, W. Kirkpatrick and V. L. Deringer, *Adv. Mater.*, 2022, **34**, 2107515.
59 A. Hirsch, *Nat. Mater.*, 2010, **9**, 868–871.
60 S. Lewis Nathan and G. Nocera Daniel, *Proc. Natl. Acad. Sci. U. S. A.*, 2006, **103**, 15729–15735.
61 D. G. Nocera, *2007 Renewable Energy: Solar Fuels Gordon Research Conference-January 21-26*, Gordon Research Conferences, 2008.
62 S. L. Suib, *New and Future Developments in Catalysis: Solar Photocatalysis*, Elsevier Science, 2013.
63 R. Showstack, *World's Heavy Dependence on Fossil Fuels Projected to Continue*, EOS, 2017, DOI: 10.1029/2017EO082549.
64 C. Stewart and M.-A. Hessami, *Energy Convers Manage.*, 2005, **46**, 403–420.
65 H. Zhou, T. Fan and D. Zhang, *ChemSusChem*, 2011, **4**, 1344–1387.
66 N. S. Diffenbaugh and M. Burke, *Proc. Natl. Acad. Sci. U. S. A.*, 2019, **116**, 9808–9813.
67 A. Carleton Tamma and M. Hsiang Solomon, *Science*, 2016, **353**, aad9837.
68 F. Zhang, W. Zhang, D. Wexler and Z. Guo, *Adv. Mater.*, 2022, **34**, 2107965.
69 J. Qiao, X. Kong, Z. X. Hu, F. Yang and W. Ji, *Nat. Commun.*, 2014, **5**, 4475.
70 P. E. M. Amaral, G. P. Nieman, G. R. Schwenk, H. Jing, R. Zhang, E. B. Cerkez, D. Strongin and H. F. Ji, *Angew. Chem., Int. Ed.*, 2019, **58**, 6766–6771.
71 F. Xia, H. Wang, J. C. M. Hwang, A. H. C. Neto and L. Yang, *Nat. Rev. Phys.*, 2019, **1**, 306–317.
72 K. L. Kuntz, R. A. Wells, J. Hu, T. Yang, B. Dong, H. Guo, A. H. Woomer, D. L. Druffel, A. Alabanza, D. Tománek and S. C. Warren, *ACS Appl. Mater. Interfaces*, 2017, **9**, 9126–9135.
73 B. Ghosh, S. Nahas, S. Bhowmick and A. Agarwal, *Phys. Rev. B: Condens. Matter Mater. Phys.*, 2015, **91**, 115433.
74 H. Wang, C. Liu, Y. Cao, S. Liu, B. Zhang, Z. Hu and J. Sun, *ACS Appl. Energy Mater.*, 2022, **5**, 2184–2191.
75 S. Kaur, A. Kumar, S. Srivastava, K. Tankeshwar and R. Pandey, *J. Phys. Chem. C*, 2018, **122**, 26032–26038.
76 J. Guan, Z. Zhu and D. Tománek, *Phys. Rev. Lett.*, 2014, **113**, 226801.
77 H. Huang, L. Zhang, B. Xiao, Y. Cheng and J. Zhang, *Appl. Phys. Lett.*, 2019, **115**, 163101.
78 H. Guo, N. Lu, J. Dai, X. Wu and X. C. Zeng, *J. Phys. Chem. C*, 2014, **118**, 14051–14059.
79 F. Krafft, *Angew. Chem., Int. Ed. Engl.*, 1969, **8**, 660–671.
80 J. Emsley, *13th element*, John Wiley & Sons, Inc., 2000.
81 The Nobel Foundation, Percy W. Bridgman – Biographical, 1946.
82 J. Xiao, M. Long, C.-S. Deng, J. He, L.-L. Cui and H. Xu, *J. Phys. Chem. C*, 2016, **120**, 4638–4646.
83 A. Singh, H. Bae, S. Lee, K. Shabbiri, T. Hussain and H. Lee, *Appl. Surf. Sci.*, 2020, **512**, 145641.
84 K. Ashley, D. Cordell and D. Mavinic, *Chemosphere*, 2011, **84**, 737–746.
85 M. F. Crass, *J. Chem. Educ.*, 1941, **18**, 316.
86 M. B. Geeson and C. C. Cummins, *Science*, 2018, **359**, 1383–1385.
87 M. Kohn, *J. Chem. Educ.*, 1944, **21**, 522.
88 M. Ruck, D. Hoppe, B. Wahl, P. Simon, Y. Wang and G. Seifert, *Angew. Chem., Int. Ed.*, 2005, **44**, 7616–7619.
89 P. F. McMillan, *Nat. Mater.*, 2005, **4**, 715–718.
90 J. Wittig and B. T. Matthias, *Science*, 1968, **160**, 994–995.
91 W. Tao, N. Kong, X. Ji, Y. Zhang, A. Sharma, J. Ouyang, B. Qi, J. Wang, N. Xie, C. Kang, H. Zhang, O. C. Farokhzad and J. S. Kim, *Chem. Soc. Rev.*, 2019, **48**, 2891–2912.
92 A. Favron, E. Gaufres, F. Fossard, A. L. Phaneuf-L'Heureux, N. Y. Tang, P. L. Levesque, A. Loiseau, R. Leonelli, S. Francoeur and R. Martel, *Nat. Mater.*, 2015, **14**, 826–832.
93 R. Gusmão, Z. Sofer and M. Pumera, *Angew. Chem., Int. Ed.*, 2017, **56**, 8052–8072.
94 T. Gorkan, E. Aktürk and S. Ciraci, *Phys. Rev. B*, 2019, **100**, 125306.
95 M. Wu, H. Fu, L. Zhou, K. Yao and X. C. Zeng, *Nano Lett.*, 2015, **15**, 3557–3562.
96 K. Burke, *J. Chem. Phys.*, 2012, **136**, 150901.
97 V. L. Deringer, M. A. Caro and G. Csanyi, *Adv. Mater.*, 2019, **31**, 1902765.
98 J. Behler, *Angew. Chem., Int. Ed.*, 2017, **56**, 12828–12840.
99 Z. Wang, Z. Sun, H. Yin, X. Liu, J. Wang, H. Zhao, C. H. Pang, T. Wu, S. Li, Z. Yin and X.-F. Yu, *Adv. Mater.*, 2022, **34**, 2104113.
100 N. B. Goodman, L. Ley and D. W. Bullett, *Phys. Rev. B: Condens. Matter Mater. Phys.*, 1983, **27**, 7440–7450.
101 M. Häser and O. Treutler, *J. Chem. Phys.*, 1995, **102**, 3703–3711.
102 N. J. Brassington, H. G. M. Edwards and D. A. Long, *J. Raman Spectrosc.*, 1981, **11**, 346–348.

103 L. R. Maxwell, S. B. Hendricks and V. M. Mosley, *J. Chem. Phys.*, 1935, **3**, 699–709.
104 N. A. Giffin and J. D. Masuda, *Coord. Chem. Rev.*, 2011, **255**, 1342–1359.
105 A. Simon, H. Borrmann and J. Horakh, *Chem. Ber.*, 2006, **130**, 1235–1240.
106 H. Okudera, R. E. Dinnebier and A. Simon, *Z. Kirchenges.*, 2005, **220**, 259–264.
107 R. R. Hart, M. B. Robin and N. A. Kuebler, *J. Chem. Phys.*, 1965, **42**, 3631–3638.
108 L. Pauling and M. Simonetta, *J. Chem. Phys.*, 1952, **20**, 29–34.
109 F. Xia, H. Wang and Y. Jia, *Nat. Commun.*, 2014, **5**, 4458.
110 J. C. Jamieson, *Science*, 1963, **139**, 1291–1292.
111 L. Cartz, S. R. Srinivasa, R. J. Riedner, J. D. Jorgensen and T. G. Worlton, *J. Chem. Phys.*, 1979, **71**, 1718–1721.
112 A. Carvalho, M. Wang, X. Zhu, A. S. Rodin, H. Su and A. H. Castro Neto, *Nat. Rev. Mater.*, 2016, **1**, 16061.
113 S. Zhou, C. Bao, B. Fan, H. Zhou, Q. Gao, H. Zhong, T. Lin, H. Liu, P. Yu, P. Tang, S. Meng, W. Duan and S. Zhou, *Nature*, 2023, **614**, 75–80.
114 X. Ling, H. Wang, S. Huang, F. Xia and M. S. Dresselhaus, *Proc. Natl. Acad. Sci. U. S. A.*, 2015, **112**, 4523.
115 J. Dai and X. C. Zeng, *J. Phys. Chem. Lett.*, 2014, **5**, 1289–1293.
116 Y. Cai, G. Zhang and Y.-W. Zhang, *Phosphorene: Physical Properties, Synthesis, and Fabrication*, Jenny Standford Publishing, 2019.
117 J. M. Zaug, A. K. Soper and S. M. Clark, *Nat. Mater.*, 2008, **7**, 890–899.
118 D. J. Olego, J. A. Baumann, M. A. Kuck, R. Schachter, C. G. Michel and P. M. Raccah, *Solid State Commun.*, 1984, **52**, 311–314.
119 R. O. Jones and D. Hohl, *J. Chem. Phys.*, 1990, **92**, 6710–6721.
120 B. V. Shanabrook and J. S. Lannin, *Phys. Rev. B: Condens. Matter Mater. Phys.*, 1981, **24**, 4771–4780.
121 G. E. Jellison, *Solid State Commun.*, 1979, **30**, 481–485.
122 H. Farman, J. C. Dore and S. R. Elliott, *Phys. Lett. A*, 1994, **186**, 410–414.
123 S. Zhang, H. J. Qian, Z. Liu, H. Ju, Z. Y. Lu, H. Zhang, L. Chi and S. Cui, *Angew. Chem., Int. Ed.*, 2019, **58**, 1659–1663.
124 M. Hart, E. R. White, J. Chen, C. M. McGilvery, C. J. Pickard, A. Michaelides, A. Sella, M. S. P. Shaffer and C. G. Salzmann, *Angew. Chem., Int. Ed.*, 2017, **56**, 8144–8148.
125 S. Böcker and M. Häser, *Z. Anorg. Allg. Chem.*, 1995, **621**, 258–286.
126 M. Häser, U. Schneider and R. Ahlrichs, *J. Am. Chem. Soc.*, 1992, **114**, 9551–9559.
127 M. Rubenstein and F. M. Ryan, *J. Electrochem. Soc.*, 1966, **113**, 1063.
128 V. V. Nechaeva, N. D. Talanov and A. I. Soklakov, *Zh. Neorg. Khim.*, 1979, **24**, 1979–1981.
129 Z. Sun, B. Zhang and Q. Yan, *Inorg. Chem. Front.*, 2022, **9**, 4385–4393.
130 G. Schusteritsch, M. Uhrin and C. J. Pickard, *Nano Lett.*, 2016, **16**, 2975–2980.
131 Z. Hu and W. Guo, *Small*, 2021, **17**, 2008004.
132 Y. L. Lu, S. Dong, J. Li, Y. Wu, L. Wang and H. Zhao, *Phys. Chem. Chem. Phys.*, 2020, **22**, 13713–13720.
133 Z. Zhu, X. Cai, S. Yi, J. Chen, Y. Dai, C. Niu, Z. Guo, M. Xie, F. Liu, J.-H. Cho, Y. Jia and Z. Zhang, *Phys. Rev. Lett.*, 2017, **119**, 106101.
134 X. Huang, J. Guan, Z. Lin, B. Liu, S. Xing, W. Wang and J. Guo, *Nano Lett.*, 2017, **17**, 4619–4623.
135 L. Xian, A. Pérez Paz, E. Bianco, P. M. Ajayan and A. Rubio, *2D Mater.*, 2017, **4**, 041003.
136 G. Cicirello, M. Wang, Q. P. Sam, J. L. Hart, N. L. Williams, H. Yin, J. J. Cha and J. Wang, *J. Am. Chem. Soc.*, 2023, **145**, 8218–8230.
137 T. Nilges, P. Schmidt and R. Weihrich, *Encycl. Inorg. Bioinorg. Chem.*, 2018, DOI: 10.1002/9781119951438.eibc2643.
138 M. Hermes and F. Scholz, *Electrochem. Commun.*, 2000, **2**, 845–850.
139 V. Tran, R. Soklaski, Y. Liang and L. Yang, *Phys. Rev. B: Condens. Matter Mater. Phys.*, 2014, **89**, 235319.
140 L. Liang, J. Wang, W. Lin, B. G. Sumpter, V. Meunier and M. Pan, *Nano Lett.*, 2014, **14**, 6400–6406.
141 W. J. Ong, L. L. Tan, Y. H. Ng, S. T. Yong and S. P. Chai, *Chem. Rev.*, 2016, **116**, 7159–7329.
142 J. Zhou, T.-Y. Cai and S. Ju, *Phys. Rev. B*, 2021, **104**, 245401.
143 R. B. Pontes, R. H. Miwa, A. J. R. da Silva, A. Fazzio and J. E. Padilha, *Phys. Rev. B*, 2018, **97**, 235419.
144 J. Zhuang, C. Liu, Q. Gao, Y. Liu, H. Feng, X. Xu, J. Wang, J. Zhao, S. X. Dou, Z. Hu and Y. Du, *ACS Nano*, 2018, **12**, 5059–5065.
145 C. Gu, S. Zhao, J. L. Zhang, S. Sun, K. Yuan, Z. Hu, C. Han, Z. Ma, L. Wang, F. Huo, W. Huang, Z. Li and W. Chen, *ACS Nano*, 2017, **11**, 4943–4949.
146 J. K. Ellis, M. J. Lucero and G. E. Scuseria, *Appl. Phys. Lett.*, 2011, **99**, 261908.
147 W. Zhao, Z. Ghorannevis, L. Chu, M. Toh, C. Kloc, P.-H. Tan and G. Eda, *ACS Nano*, 2013, **7**, 791–797.
148 I. G. Lezama, A. Arora, A. Ubaldini, C. Barreteau, E. Giannini, M. Potemski and A. F. Morpurgo, *Nano Lett.*, 2015, **15**, 2336–2342.
149 T. Low, A. S. Rodin, A. Carvalho, Y. Jiang, H. Wang, F. Xia and A. H. Castro Neto, *Phys. Rev. B: Condens. Matter Mater. Phys.*, 2014, **90**, 075434.
150 G. Zhang, S. Huang, A. Chaves, C. Song, V. O. Özçelik, T. Low and H. Yan, *Nat. Commun.*, 2017, **8**, 14071.
151 Q. Liu, X. Zhang, L. B. Abdalla, A. Fazzio and A. Zunger, *Nano Lett.*, 2015, **15**, 1222–1228.
152 T. Kaewmaraya, L. Ngamwongwan, P. Moontragoon, W. Jarernboon, D. Singh, R. Ahuja, A. Karton and T. Hussain, *J. Hazard. Mater.*, 2021, **401**, 123340.
153 X. Peng, Q. Wei and A. Copple, *Phys. Rev. B: Condens. Matter Mater. Phys.*, 2014, **90**, 085402.
154 K. S. Novoselov, A. K. Geim, S. V. Morozov, D. Jiang, M. I. Katsnelson, I. V. Grigorieva, S. V. Dubonos and A. A. Firsov, *Nature*, 2005, **438**, 197–200.
155 L. Liao, Y.-C. Lin, M. Bao, R. Cheng, J. Bai, Y. Liu, Y. Qu, K. L. Wang, Y. Huang and X. Duan, *Nature*, 2010, **467**, 305–308.

156 B. Radisavljevic, A. Radenovic, J. Brivio, V. Giacometti and A. Kis, *Nat. Nanotechnol.*, 2011, **6**, 147–150.
157 M. Buscema, D. J. Groenendijk, S. I. Blanter, G. A. Steele, H. S. van der Zant and A. Castellanos-Gomez, *Nano Lett.*, 2014, **14**, 3347–3352.
158 J. L. Hart, K. Hantanasirisakul, A. C. Lang, B. Anasori, D. Pinto, Y. Pivak, J. T. van Omme, S. J. May, Y. Gogotsi and M. L. Taheri, *Nat. Commun.*, 2019, **10**, 522.
159 Y. Xu, J. Dai and X. C. Zeng, *J. Phys. Chem. Lett.*, 2016, **7**, 302–307.
160 Z. Sun, B. Zhang, Y. Zhao, M. Khurram and Q. Yan, *Chem. Mater.*, 2021, **33**, 6240–6248.
161 E. Golias, M. Krivenkov, A. Varykhalov, J. Sanchez-Barriga and O. Rader, *Nano Lett.*, 2018, **18**, 6672–6678.
162 R. Fei, A. Faghaninia, R. Soklaski, J.-A. Yan, C. Lo and L. Yang, *Nano Lett.*, 2014, **14**, 6393–6399.
163 T. Yin, L. Long, X. Tang, M. Qiu, W. Liang, R. Cao, Q. Zhang, D. Wang and H. Zhang, *Adv. Sci.*, 2020, **7**, 2001431.
164 X. Qian, J. Zhou and G. Chen, *Nat. Mater.*, 2021, **20**, 1188–1202.
165 X. Zhang, X. F. Qiao, W. Shi, J. B. Wu, D. S. Jiang and P. H. Tan, *Chem. Soc. Rev.*, 2015, **44**, 2757–2785.
166 Y. Zhang, J. Wang, Q. Liu, S. Gu, Z. Sun, P. K. Chu and X. Yu, *APL Mater.*, 2020, **8**, 120903.
167 N. Mao, S. Zhang, J. Wu, J. Zhang and L. Tong, *Small Methods*, 2018, **2**, 1700409.
168 J. Hlinka, T. Ostapchuk, E. Buixaderas, C. Kadlec, P. Kuzel, I. Gregora, J. Kroupa, M. Savinov, A. Klic, J. Drahokoupil, I. Etxebarria and J. Dec, *Phys. Rev. Lett.*, 2014, **112**, 197601.
169 S. Sugai and I. Shirotani, *Solid State Commun.*, 1985, **53**, 753–755.
170 C. Kaneta, H. Katayama-Yoshida and A. Morita, *J. Phys. Soc. Jpn.*, 1986, **55**, 1213–1223.
171 N. Suzuki and M. Aoki, *Solid State Commun.*, 1987, **61**, 595–600.
172 J. Ribeiro-Soares, R. M. Almeida, L. G. Cançado, M. S. Dresselhaus and A. Jorio, *Phys. Rev. B: Condens. Matter Mater. Phys.*, 2015, **91**, 205421.
173 L. Zhang, H. Huang, Z. Lv, L. Li, M. Gu, X. Zhao, B. Zhang, Y. Cheng and J. Zhang, *ACS Appl. Electron. Mater.*, 2021, **3**, 1043–1049.
174 A. Impellizzeri, A. A. Vorfolomeeva, N. V. Surovtsev, A. V. Okotrub, C. P. Ewels and D. V. Rybkovskiy, *Phys. Chem. Chem. Phys.*, 2021, **23**, 16611–16622.
175 B. Smith, B. Vermeersch, J. Carrete, E. Ou, J. Kim, N. Mingo, D. Akinwande and L. Shi, *Adv. Mater.*, 2017, **29**, 1603756.
176 S. Lee, F. Yang, J. Suh, S. Yang, Y. Lee, G. Li, H. Sung Choe, A. Suslu, Y. Chen, C. Ko, J. Park, K. Liu, J. Li, K. Hippalgaonkar, J. J. Urban, S. Tongay and J. Wu, *Nat. Commun.*, 2015, **6**, 8573.
177 X.-J. Ge, K.-L. Yao and J.-T. Lü, *Phys. Rev. B: Condens. Matter Mater. Phys.*, 2016, **94**, 165433.
178 Y. Zhao, H. Wang, H. Huang, Q. Xiao, Y. Xu, Z. Guo, H. Xie, J. Shao, Z. Sun, W. Han, X. F. Yu, P. Li and P. K. Chu, *Angew. Chem., Int. Ed.*, 2016, **55**, 5003–5007.
179 D. K. Sang, H. Wang, Z. Guo, N. Xie and H. Zhang, *Adv. Funct. Mater.*, 2019, **29**, 1903419.
180 L. Zhao, X. Chao, N. Xu, G. Ling and P. Zhang, *Adv. Eng. Mater.*, 2021, **23**, 2100450.
181 X. Liu, K. Chen, X. Li, Q. Xu, J. Weng and J. Xu, *Adv. Mater.*, 2021, **33**, 2005924.
182 H. Lyu, W. Wilwin, Z. Lin and H. Su, *J. Phys. Chem. C*, 2022, **126**, 8883–8888.
183 J. K. Burdett, P. Haaland and T. J. McLarnan, *J. Chem. Phys.*, 1981, **75**, 5774–5781.
184 L. Radom, W. J. Hehre and J. A. Pople, *J. Am. Chem. Soc.*, 1972, **94**, 2371–2381.
185 S. F. Nelsen and J. M. Buschek, *J. Am. Chem. Soc.*, 1973, **95**, 2011–2013.
186 F. Bachhuber, J. von Appen, R. Dronskowski, P. Schmidt, T. Nilges, A. Pfitzner and R. Weihrich, *Angew. Chem., Int. Ed.*, 2014, **53**, 11629–11633.
187 K. Ding, L. Wen, S. Huang, Y. Li, Y. Zhang and Y. Lu, *RSC Adv.*, 2016, **6**, 80872–80884.
188 S. Kuriakose, T. Ahmed, S. Balendhran, V. Bansal, S. Sriram, M. Bhaskaran and S. Walia, *2D Mater.*, 2018, **5**, 032001.
189 J.-S. Kim, Y. Liu, W. Zhu, S. Kim, D. Wu, L. Tao, A. Dodabalapur, K. Lai and D. Akinwande, *Sci. Rep.*, 2015, **5**, 8989.
190 F. Alsaffar, S. Alodan, A. Alrasheed, A. Alhussain, N. Alrubaiq, A. Abbas and M. R. Amer, *Sci. Rep.*, 2017, **7**, 44540.
191 M. T. Edmonds, A. Tadich, A. Carvalho, A. Ziletti, K. M. O'Donnell, S. P. Koenig, D. F. Coker, B. Özyilmaz, A. H. C. Neto and M. S. Fuhrer, *ACS Appl. Mater. Interfaces*, 2015, **7**, 14557–14562.
192 Q. Zhou, Q. Chen, Y. Tong and J. Wang, *Angew. Chem., Int. Ed.*, 2016, **55**, 11437–11441.
193 A. Fali, M. Snure and Y. Abate, *Appl. Phys. Lett.*, 2021, **118**, 163105.
194 Y. Huang, J. Qiao, K. He, S. Bliznakov, E. Sutter, X. Chen, D. Luo, F. Meng, D. Su, J. Decker, W. Ji, R. S. Ruoff and P. Sutter, *Chem. Mater.*, 2016, **28**, 8330–8339.
195 Z. Hu, Q. Li, B. Lei, Q. Zhou, D. Xiang, Z. Lyu, F. Hu, J. Wang, Y. Ren, R. Guo, E. Goki, L. Wang, C. Han, J. Wang and W. Chen, *Angew. Chem., Int. Ed.*, 2017, **56**, 9131–9135.
196 W. Yu, J. Xu, F. Chen, Y. Wang, S. Tang, F. Geng, J. Lv, G. Qu, L. Zhao and Y. Wang, *Angew. Chem., Int. Ed.*, 2022, **61**, e202213595.
197 Y. Zhao, Z. Sun, B. Zhang and Q. Yan, *ACS Appl. Mater. Interfaces*, 2022, **14**, 9925–9932.
198 T. Zhang, Y. Wan, H. Xie, Y. Mu, P. Du, D. Wang, X. Wu, H. Ji and L. Wan, *J. Am. Chem. Soc.*, 2018, **140**, 7561–7567.
199 L. Li, M. Engel, D. B. Farmer, S.-J. Han and H. S. P. Wong, *ACS Nano*, 2016, **10**, 4672–4677.
200 J. R. Brent, N. Savjani, E. A. Lewis, S. J. Haigh, D. J. Lewis and P. O'Brien, *Chem. Commun.*, 2014, **50**, 13338–13341.
201 C. R. Ryder, J. D. Wood, S. A. Wells, Y. Yang, D. Jariwala, T. J. Marks, G. C. Schatz and M. C. Hersam, *Nat. Chem.*, 2016, **8**, 597–602.
202 W. Lv, B. Yang, B. Wang, W. Wan, Y. Ge, R. Yang, C. Hao, J. Xiang, B. Zhang, Z. Zeng and Z. Liu, *ACS Appl. Mater. Interfaces*, 2018, **10**, 9663–9668.
203 Z. Guo, S. Chen, Z. Wang, Z. Yang, F. Liu, Y. Xu, J. Wang, Y. Yi, H. Zhang, L. Liao, P. K. Chu and X. F. Yu, *Adv. Mater.*, 2017, **29**, 1703811.

204 R. W. Keyes, *Phys. Rev.*, 1953, **92**, 580–584.
205 H. Krebs, H. Weitz and K. H. Worms, *Z. Anorg. Allg. Chem.*, 1955, **280**, 119–133.
206 A. Brown and S. Rundqvist, *Acta Crystallogr.*, 1965, **19**, 684–685.
207 Y. Maruyama, S. Suzuki, K. Kobayashi and S. Tanuma, *Phys. B*, 1981, **105**, 99–102.
208 M. Binnewies, M. Schmidt and P. Schmidt, *Z. Anorg. Allg. Chem.*, 2017, **643**, 1295–1311.
209 M. R. P. Pielmeier and T. Nilges, *Angew. Chem., Int. Ed.*, 2021, **60**, 6816–6823.
210 M. Liu, S. Feng, Y. Hou, S. Zhao, L. Tang, J. Liu, F. Wang and B. Liu, *Mater. Today*, 2020, **36**, 91–101.
211 A. Castellanos-Gomez, L. Vicarelli, E. Prada, J. O. Island, K. L. Narasimha-Acharya, S. I. Blanter, D. J. Groenendijk, M. Buscema, G. A. Steele, J. V. Alvarez, H. W. Zandbergen, J. J. Palacios and H. S. J. van der Zant, *2D Mater.*, 2014, **1**, 025001.
212 Z. Duan, Y. Wang, S. Bian, D. Liu, Y. Zhang, X. Zhang, R. He, J. Wang, G. Qu, P. K. Chu and X. F. Yu, *Nanoscale*, 2022, **14**, 2599–2604.
213 X. Zhu, T. Zhang, Z. Sun, H. Chen, J. Guan, X. Chen, H. Ji, P. Du and S. Yang, *Adv. Mater.*, 2017, **29**, 1605776.
214 W. Liu, Y. Zhu, X. Xu, S. Wang and X. Zhang, *J. Mater. Sci.: Mater. Electron.*, 2020, **31**, 9543–9549.
215 L. Yang, D. Wang, M. Liu, H. Liu, J. Tan, Z. Wang, H. Zhou, Q. Yu, J. Wang, J. Lin, X. Zou, L. Qiu, H.-M. Cheng and B. Liu, *Mater. Today*, 2021, **51**, 145–154.
216 X. Liu, B. Gaihre, M. N. George, Y. Li, M. Tilton, M. J. Yaszemski and L. Lu, *Biomater. Sci.*, 2021, **9**, 2768–2803.
217 J. N. Coleman, M. Lotya, A. O'Neill, S. D. Bergin, P. J. King, U. Khan, K. Young, A. Gaucher, S. De, R. J. Smith, I. V. Shvets, S. K. Arora, G. Stanton, H. Y. Kim, K. Lee, G. T. Kim, G. S. Duesberg, T. Hallam, J. J. Boland, J. J. Wang, J. F. Donegan, J. C. Grunlan, G. Moriarty, A. Shmeliov, R. J. Nicholls, J. M. Perkins, E. M. Grieveson, K. Theuwissen, D. W. McComb, P. D. Nellist and V. Nicolosi, *Science*, 2011, **331**, 568–571.
218 Z. Guo, H. Zhang, S. Lu, Z. Wang, S. Tang, J. Shao, Z. Sun, H. Xie, H. Wang, X.-F. Yu and P. K. Chu, *Adv. Funct. Mater.*, 2015, **25**, 6996–7002.
219 H. Wang, S. Jiang, W. Shao, X. Zhang, S. Chen, X. Sun, Q. Zhang, Y. Luo and Y. Xie, *J. Am. Chem. Soc.*, 2018, **140**, 3474–3480.
220 G. Abellan, V. Lloret, U. Mundloch, M. Marcia, C. Neiss, A. Gorling, M. Varela, F. Hauke and A. Hirsch, *Angew. Chem., Int. Ed.*, 2016, **55**, 14557–14562.
221 D. Hanlon, C. Backes, E. Doherty, C. S. Cucinotta, N. C. Berner, C. Boland, K. Lee, A. Harvey, P. Lynch, Z. Gholamvand, S. Zhang, K. Wang, G. Moynihan, A. Pokle, Q. M. Ramasse, N. McEvoy, W. J. Blau, J. Wang, G. Abellan, F. Hauke, A. Hirsch, S. Sanvito, D. D. O'Regan, G. S. Duesberg, V. Nicolosi and J. N. Coleman, *Nat. Commun.*, 2015, **6**, 8563.
222 J. Kang, J. D. Wood, S. A. Wells, J.-H. Lee, X. Liu, K.-S. Chen and M. C. Hersam, *ACS Nano*, 2015, **9**, 3596–3604.
223 S. Lin, S. Liu, Z. Yang, Y. Li, T. W. Ng, Z. Xu, Q. Bao, J. Hao, C.-S. Lee, C. Surya, F. Yan and S. P. Lau, *Adv. Funct. Mater.*, 2016, **26**, 864–871.
224 H. Mu, S. Lin, Z. Wang, S. Xiao, P. Li, Y. Chen, H. Zhang, H. Bao, S. P. Lau, C. Pan, D. Fan and Q. Bao, *Adv. Opt. Mater.*, 2015, **3**, 1447–1453.
225 M. Qiu, D. Wang, W. Liang, L. Liu, Y. Zhang, X. Chen, D. K. Sang, C. Xing, Z. Li, B. Dong, F. Xing, D. Fan, S. Bao, H. Zhang and Y. Cao, *Proc. Natl. Acad. Sci. U. S. A.*, 2018, **115**, 501–506.
226 Z. Sofer, D. Bousa, J. Luxa, V. Mazanek and M. Pumera, *Chem. Commun.*, 2016, **52**, 1563–1566.
227 A. H. Woomer, T. W. Farnsworth, J. Hu, R. A. Wells, C. L. Donley and S. C. Warren, *ACS Nano*, 2015, **9**, 8869–8884.
228 J. Y. Xu, L. F. Gao, C. X. Hu, Z. Y. Zhu, M. Zhao, Q. Wang and H. L. Zhang, *Chem. Commun.*, 2016, **52**, 8107–8110.
229 P. Yasaei, B. Kumar, T. Foroozan, C. Wang, M. Asadi, D. Tuschel, J. E. Indacochea, R. F. Klie and A. Salehi-Khojin, *Adv. Mater.*, 2015, **27**, 1887–1892.
230 B. Zhang, F. Lou, R. Zhao, J. He, J. Li, X. Su, J. Ning and K. Yang, *Opt. Lett.*, 2015, **40**, 3691–3694.
231 J.-W. Jiang and H. S. Park, *J. Phys. D: Appl. Phys.*, 2014, **47**, 385304.
232 M. B. Erande, S. R. Suryawanshi, M. A. More and D. J. Late, *Eur. J. Inorg. Chem.*, 2015, 3102–3107.
233 L. Li, D. Zhang, J. Deng, Y. Gou and J. Fang, *J. Energy Chem.*, 2020, **49**, 365–374.
234 F. Luo, D. Wang, J. Zhang, X. Li, D. Liu, H. Li, M. Lu, X. Xie, L. Huang and W. Huang, *ACS Appl. Nano Mater.*, 2019, **2**, 3793–3801.
235 J. S. Mayell and A. J. Bard, *J. Am. Chem. Soc.*, 1963, **85**, 421–425.
236 C. Wang, Q. He, U. Halim, Y. Liu, E. Zhu, Z. Lin, H. Xiao, X. Duan, Z. Feng, R. Cheng, N. O. Weiss, G. Ye, Y.-C. Huang, H. Wu, H.-C. Cheng, I. Shakir, L. Liao, X. Chen, W. A. Goddard Iii, Y. Huang and X. Duan, *Nature*, 2018, **555**, 231–236.
237 X. Jiang, Z. e Lin, X. Zeng, J. He, F. Xu, P. Deng, J. Jia, X. Jiang, X. Hou and Z. Long, *Chem. Commun.*, 2019, **55**, 12192–12195.
238 H. Huang, M. Gao, Y. Kang, J. Li, J. Wang, L. Wu, P. K. Chu, Y. Huang, M. R. Ibarra and X. F. Yu, *Chem. Commun.*, 2019, **56**, 221–224.
239 W. Lu, H. Nan, J. Hong, Y. Chen, C. Zhu, Z. Liang, X. Ma, Z. Ni, C. Jin and Z. Zhang, *Nano Res.*, 2014, **7**, 853–859.
240 H. Kwon, S. W. Seo, T. G. Kim, E. S. Lee, P. T. Lanh, S. Yang, S. Ryu and J. W. Kim, *ACS Nano*, 2016, **10**, 8723–8731.
241 X. Liu, K. S. Chen, S. A. Wells, I. Balla, J. Zhu, J. D. Wood and M. C. Hersam, *Adv. Mater.*, 2017, **29**, 1604121.
242 R. Garcia, A. W. Knoll and E. Riedo, *Nat. Nanotechnol.*, 2014, **9**, 577–587.
243 Z. Cai, B. Liu, X. Zou and H.-M. Cheng, *Chem. Rev.*, 2018, **118**, 6091–6133.
244 J. B. Smith, D. Hagaman and H. F. Ji, *Nanotechnology*, 2016, **27**, 215602.

245 Y. Xu, X. Shi, Y. Zhang, H. Zhang, Q. Zhang, Z. Huang, X. Xu, J. Guo, H. Zhang, L. Sun, Z. Zeng, A. Pan and K. Zhang, *Nat. Commun.*, 2020, **11**, 1330.
246 C. Chen, Y. Yin, R. Zhang, Q. Yuan, Y. Xu, Y. Zhang, J. Chen, Y. Zhang, C. Li, J. Wang, J. Li, L. Fei, Q. Yu, Z. Zhou, H. Zhang, R. Cheng, Z. Dong, X. Xu, A. Pan, K. Zhang and J. He, *Nat. Mater.*, 2023, **22**, 717–724.
247 H. Lowndes Douglas, D. B. Geohegan, A. A. Puretzky, D. P. Norton and C. M. Rouleau, *Science*, 1996, **273**, 898–903.
248 P. Shriber, A. Samanta, G. D. Nessim and I. Grinberg, *J. Phys. Chem. Lett.*, 2018, **9**, 1759–1764.
249 Z. Wu, Y. Lyu, Y. Zhang, R. Ding, B. Zheng, Z. Yang, S. P. Lau, X. H. Chen and J. Hao, *Nat. Mater.*, 2021, **20**, 1203–1209.
250 Z. Yang, J. Hao, S. Yuan, S. Lin, H. M. Yau, J. Dai and S. P. Lau, *Adv. Mater.*, 2015, **27**, 3748–3754.
251 C. Tan and H. Zhang, *Nat. Commun.*, 2015, **6**, 7873.
252 B. Tian, B. Tian, B. Smith, M. C. Scott, Q. Lei, R. Hua, Y. Tian and Y. Liu, *Proc. Natl. Acad. Sci. U. S. A.*, 2018, **115**, 4345–4350.
253 Y. Zhang, X. Rui, Y. Tang, Y. Liu, J. Wei, S. Chen, W. R. Leow, W. Li, Y. Liu, J. Deng, B. Ma, Q. Yan and X. Chen, *Adv. Energy Mater.*, 2016, **6**, 1502409.
254 G. Zhao, T. Wang, Y. Shao, Y. Wu, B. Huang and X. Hao, *Small*, 2017, **13**, 1602243.
255 N. Wei, Y. Chen, Y. Zhang, C. Zhou, X. Hao, K. Xu, K. Cai and J. Chen, *Nanoscale*, 2018, **10**, 4385–4390.
256 P. Masih Das, G. Danda, A. Cupo, W. M. Parkin, L. Liang, N. Kharche, X. Ling, S. Huang, M. S. Dresselhaus, V. Meunier and M. Drndic, *ACS Nano*, 2016, **10**, 5687–5695.
257 X. W. Feng, X. Huang, L. Chen, W. C. Tan, L. Wang and K. W. Ang, *Adv. Funct. Mater.*, 2018, **28**, 1801524.
258 M. C. Watts, L. Picco, F. S. Russell-Pavier, P. L. Cullen, T. S. Miller, S. P. Bartus, O. D. Payton, N. T. Skipper, V. Tileli and C. A. Howard, *Nature*, 2019, **568**, 216–220.
259 Y. C. Cheng, Y. H. Zhu, Y. Han, Z. Y. Liu, B. C. Yang, A. M. Nie, W. Huang, R. Shahbazian-Yassar and F. Mashayek, *Chem. Mater.*, 2017, **29**, 1350–1356.
260 G. Abellan, C. Neiss, V. Lloret, S. Wild, J. C. Chacon-Torres, K. Werbach, F. Fedi, H. Shiozawa, A. Gorling, H. Peterlik, T. Pichler, F. Hauke and A. Hirsch, *Angew. Chem., Int. Ed.*, 2017, **56**, 15267–15273.
261 T. J. Macdonald, A. J. Clancy, W. Xu, Z. Jiang, C. T. Lin, L. Mohan, T. Du, D. D. Tune, L. Lanzetta, G. Min, T. Webb, A. Ashoka, R. Pandya, V. Tileli, M. A. McLachlan, J. R. Durrant, S. A. Haque and C. A. Howard, *J. Am. Chem. Soc.*, 2021, **143**, 21549–21559.
262 Z. Liu, Y. Sun, H. Cao, D. Xie, W. Li, J. Wang and A. K. Cheetham, *Nat. Commun.*, 2020, **11**, 3917.
263 W. Yu, J. Yang, J. Li, K. Zhang, H. Xu, X. Zhou, W. Chen and K. P. Loh, *Adv. Mater.*, 2021, **33**, 2102083.
264 Y. Yu, J. Yao, X. Niu, B. Xing, Y. Liu, X. Wu, M. Li, X. Yan, J. Sha and Y. Wang, *CrystEngComm*, 2020, **22**, 3824–3830.
265 L. Macewicz, K. Pyrchla, R. Bogdanowicz, G. Sumanasekera and J. B. Jasinski, *J. Phys. Chem. Lett.*, 2021, **12**, 8347–8354.
266 K. A. Ritter and J. W. Lyding, *Nat. Mater.*, 2009, **8**, 235–242.
267 X. Zhang, H. Xie, Z. Liu, C. Tan, Z. Luo, H. Li, J. Lin, L. Sun, W. Chen, Z. Xu, L. Xie, W. Huang and H. Zhang, *Angew. Chem., Int. Ed.*, 2015, **54**, 3653–3657.
268 M. Ozhukil Valappil, S. Alwarappan and V. K. Pillai, *Nanoscale*, 2022, **14**, 1037–1053.
269 Z. Sun, H. Xie, S. Tang, X. F. Yu, Z. Guo, J. Shao, H. Zhang, H. Huang, H. Wang and P. K. Chu, *Angew. Chem., Int. Ed.*, 2015, **54**, 11526–11530.
270 Z. Sun, Y. Zhao, Z. Li, H. Cui, Y. Zhou, W. Li, W. Tao, H. Zhang, H. Wang, P. K. Chu and X. F. Yu, *Small*, 2017, **13**, 1602896.
271 L. Chan, P. Gao, W. Zhou, C. Mei, Y. Huang, X. F. Yu, P. K. Chu and T. Chen, *ACS Nano*, 2018, **12**, 12401–12415.
272 S. Geng, L. Wu, H. Cui, W. Tan, T. Chen, P. K. Chu and X. F. Yu, *Chem. Commun.*, 2018, **54**, 6060–6063.
273 M. Meng, Z. Gan, J. Zhang, K. Liu, L. Wang, S. Li, Y. Yao, Y. Zhu and J. Li, *Phys. Status Solidi B*, 2017, **254**, 1700011.
274 W. Chen, K. Li, Y. Wang, X. Feng, Z. Liao, Q. Su, X. Lin and Z. He, *J. Phys. Chem. Lett.*, 2017, **8**, 591–598.
275 W. Wang, X. Niu, H. Qian, L. Guan, M. Zhao, X. Ding, S. Zhang, Y. Wang and J. Sha, *Nanotechnology*, 2016, **27**, 505204.
276 C. C. Mayorga-Martinez, N. Mohamad Latiff, A. Y. S. Eng, Z. Sofer and M. Pumera, *Anal. Chem.*, 2016, **88**, 10074–10079.
277 X. Tang, H. Chen, J. S. Ponraj, S. C. Dhanabalan, Q. Xiao, D. Fan and H. Zhang, *Adv. Sci.*, 2018, **5**, 1800420.
278 X. Ren, X. Yang, G. Xie and J. Luo, *ACS Appl. Nano Mater.*, 2020, **3**, 4799–4809.
279 C. Zhu, F. Xu, L. Zhang, M. Li, J. Chen, S. Xu, G. Huang, W. Chen and L. Sun, *Chem. – Eur. J.*, 2016, **22**, 7357–7362.
280 S. Ge, L. Zhang, P. Wang and Y. Fang, *Sci. Rep.*, 2016, **6**, 27307.
281 X. Ren, F. Zhang and X. Zhang, *Chem. – Asian J.*, 2018, **13**, 1842–1846.
282 T. W. DeWitt and S. Skolnik, *J. Am. Chem. Soc.*, 1946, **68**, 2305–2309.
283 M. Serrano-Ruiz, A. Romerosa and P. Lorenzo-Luis, *Eur. J. Inorg. Chem.*, 2014, 1587–1598.
284 A. Pedler, *J. Chem. Soc., Trans.*, 1890, **57**, 599–613.
285 G. Rathenau, *Physica*, 1937, **4**, 503–514.
286 N. P. Tarasova, Y. V. Smetannikov, I. M. Artemkina, I. A. Lavrov, M. A. Sinaiskii and V. I. Ermakov, *Dokl. Chem.*, 2006, **410**, 189–191.
287 A. Piro Nicholas, S. Figueroa Joshua, T. McKellar Jessica and C. Cummins Christopher, *Science*, 2006, **313**, 1276–1279.
288 M. E. Barr, B. R. Adams, R. R. Weller and L. F. Dahl, *J. Am. Chem. Soc.*, 1991, **113**, 3052–3060.
289 M. Grayson, *Pure Appl. Chem.*, 1964, **9**, 193–204.
290 D. Perner and A. Henglein, *Z. Naturforsch. B*, 1962, **17**, 703–711.
291 R. Saravanan, E. Thirumal, V. K. Gupta, V. Narayanan and A. Stephen, *J. Mol. Liq.*, 2013, **177**, 394–401.
292 Y. Sun, Z. Ren, Y. Liu and R. Fu, *Mater. Lett.*, 2019, **236**, 542–546.
293 F. Chen, K. Mu, D. Zhang, X. Mi, Y. Li, Z. Shen and S. Zhan, *Top. Catal.*, 2021, **64**, 559–566.

294 M. Zhang, J. Liu, L. Liu, K. Sun, X. Liang, J. Wan and F. Fu, *Ceram. Int.*, 2020, **46**, 23165–23172.
295 L. Liu, J. Shen, K. Wu and N. Yang, *Small Methods*, 2021, **5**, 2100720.
296 Y. Li, S. Jiang, Y. Qian, Y. Han, J. Zhou, T. Li, L. Xi, N. Lin and Y. Qian, *Chem. Commun.*, 2019, **55**, 6751–6754.
297 W. Liu, S. Ju and X. Yu, *ACS Nano*, 2020, **14**, 974–984.
298 J. Mo, Y. Xu, L. Zhu, W. Wei and J. Zhao, *Angew. Chem., Int. Ed.*, 2021, **60**, 12524–12531.
299 H. Song, J. Wang, B. Xiong, J. Hu, P. Zeng, X. Liu and H. Liang, *Angew. Chem., Int. Ed.*, 2022, **134**, e202117679.
300 G. Jia, M. Sun, Y. Wang, X. Cui, B. Huang and J. C. Yu, *Adv. Funct. Mater.*, 2022, **33**, 2212051.
301 G. H. Han, D. L. Duong, D. H. Keum, S. J. Yun and Y. H. Lee, *Chem. Rev.*, 2018, **118**, 6297–6336.
302 J. B. Smith, D. Hagaman, D. DiGuiseppi, R. Schweitzer-Stenner and H. F. Ji, *Angew. Chem., Int. Ed.*, 2016, **55**, 11829–11833.
303 N. Eckstein, A. Hohmann, R. Weihrich, T. Nilges and P. Schmidt, *Z. Anorg. Allg. Chem.*, 2013, **639**, 2741–2743.
304 M. Roshith, M. S. Kumar, A. K. Nanda Kumar, S. Ramasubramanian, J. Stanley, T. G. Satheesh Babu and D. V. Ravi Kumar, *J. Photochem. Photobiol., A*, 2019, **384**, 112034.
305 Z. Chen, Y. Zhu, Q. Wang, W. Liu, Y. Cui, X. Tao and D. Zhang, *Electrochim. Acta*, 2019, **295**, 230–236.
306 S. Zhang, S. Ma, B. Cao, Q. Zhuang, Y. Xu, J. Wang, X. Zhang, X. Nan, X. Hao and B. Xu, *Angew. Chem., Int. Ed.*, 2023, **62**, e202217127.
307 H. W. Ban, J. G. Oh, S. Jo, H. Jeong, D. H. Gu, S. Baek, S. Y. Lee, Y. I. Park, J. Jang and J. S. Son, *Chem. Mater.*, 2019, **31**, 5909–5918.
308 G. Cunningham, M. Lotya, C. S. Cucinotta, S. Sanvito, S. D. Bergin, R. Menzel, M. S. P. Shaffer and J. N. Coleman, *ACS Nano*, 2012, **6**, 3468–3480.
309 V. Sresht, A. A. H. Pádua and D. Blankschtein, *ACS Nano*, 2015, **9**, 8255–8268.
310 G. Zhang, D. Liu, N. Tian, X. Wang, W. Yan, Z. Huang and Y. Zhang, *Inorg. Chem.*, 2021, **60**, 4883–4890.
311 D. Nakamura and H. Nakano, *Chem. Mater.*, 2018, **30**, 5333–5338.
312 P. E. M. Amaral, D. C. Hall, Jr., R. Pai, J. E. Krol, V. Kalra, G. D. Ehrlich and H.-F. Ji, *ACS Appl. Nano Mater.*, 2020, **3**, 752–759.
313 D. Geng, B. Wu, Y. Guo, L. Huang, Y. Xue, J. Chen, G. Yu, L. Jiang, W. Hu and Y. Liu, *Proc. Natl. Acad. Sci. U. S. A.*, 2012, **109**, 7992.
314 Y. Liu, Z. Hu and J. C. Yu, *Appl. Catal., B*, 2019, **247**, 100–106.
315 F. Wang and W. E. Buhro, *ACS Nano*, 2017, **11**, 12526–12535.
316 J. Li, Z. Wang and F. L. Deepak, *ACS Nano*, 2017, **11**, 5590–5597.
317 Y. Li, B. R. Bunes, L. Zang, J. Zhao, Y. Li, Y. Zhu and C. Wang, *ACS Nano*, 2016, **10**, 2386–2391.
318 D. Wang, F. Luo, M. Lu, X. Xie, L. Huang and W. Huang, *Small*, 2019, **15**, 1804404.
319 L. Zhang, M. Gu, L. Li, X. Zhao, C. Fu, T. Liu, X. Xu, Y. Cheng and J. Zhang, *Chem. Mater.*, 2020, **32**, 7363–7369.
320 H.-S. Tsai, C.-C. Lai, C.-H. Hsiao, H. Medina, T.-Y. Su, H. Ouyang, T.-H. Chen, J.-H. Liang and Y.-L. Chueh, *ACS Appl. Mater. Interfaces*, 2015, **7**, 13723–13727.
321 Y. Zhang, D. Zhang, Y. Wang, Q. Liu, Q. Li and M. Dong, *ACS Appl. Nano Mater.*, 2021, **4**, 9932–9937.
322 B. Zhang, L. Zhang, Z. Wang, Y. Li, Y. Cheng, L. Ma and J. Zhang, *J. Mater. Chem. A*, 2021, **9**, 13855–13860.
323 F. Baumer, Y. Ma, C. Shen, A. Zhang, L. Chen, Y. Liu, D. Pfister, T. Nilges and C. Zhou, *ACS Nano*, 2017, **11**, 4105–4113.
324 R. Zhao, S. Liu, X. Zhao, M. Gu, Y. Zhang, M. Jin, Y. Wang, Y. Cheng and J. Zhang, *J. Mater. Chem. A*, 2022, **10**, 245–250.
325 W. M. Girma, M. Z. Fahmi, A. Permadi, M. A. Abate and J.-Y. Chang, *J. Mater. Chem. B*, 2017, **5**, 6193–6216.
326 L. Long, X. Niu, K. Yan, G. Zhou, J. Wang, X. Wu and P. K. Chu, *Small*, 2018, **14**, 1803132.
327 W. Dai, H. Dong, B. Fugetsu, Y. Cao, H. Lu, X. Ma and X. Zhang, *Small*, 2015, **11**, 4158–4164.
328 S. H. C. Askes, G. U. Reddy, R. Wyrwa, S. Bonnet and A. Schiller, *J. Am. Chem. Soc.*, 2017, **139**, 15292–15295.
329 R. Zhao, S. Liu, X. Zhao, Y. Cheng and J. Zhang, *Adv. Mater. Interfaces*, 2022, **9**, 2200705.
330 R. Zhao, X. Zhao, X. Xu, Y. Zhang, Y. Wang, M. Jin, Z. Liu, Y. Cheng, H. Zheng and J. Zhang, *J. Phys. Chem. Lett.*, 2022, **13**, 8236–8244.
331 H. Tian, J.-Q. Zhang, W. Ho, J.-P. Xu, B. Xia, Y. Xia, J. Fan, H. Xu, M. Xie and S. Y. Tong, *Matter*, 2020, **2**, 111–118.
332 F.-F. Zhu, W.-J. Chen, Y. Xu, C.-L. Gao, D.-D. Guan, C.-H. Liu, D. Qian, S.-C. Zhang and J.-F. Jia, *Nat. Mater.*, 2015, **14**, 1020–1025.
333 J. L. Zhang, C. Han, Z. Hu, L. Wang, L. Liu, A. T. S. Wee and W. Chen, *Adv. Mater.*, 2018, **30**, 1802207.
334 J. L. Zhang, S. Zhao, S. Sun, H. Ding, J. Hu, Y. Li, Q. Xu, X. Yu, M. Telychko, J. Su, C. Gu, Y. Zheng, X. Lian, Z. Ma, R. Guo, J. Lu, Z. Sun, J. Zhu, Z. Li and W. Chen, *ACS Nano*, 2020, **14**, 3687–3695.
335 S. Yang, Z. Hu, W. Wang, P. Cheng, L. Chen and K. Wu, *Chin. Phys. Lett.*, 2020, **37**, 096803.
336 M. Schaal, J. Picker, F. Otto, M. Gruenewald, R. Forker and T. Fritz, *J. Phys.: Condens. Matter*, 2021, **33**, 485002.
337 R. Forker, M. Meissner and T. Fritz, *Soft Matter*, 2017, **13**, 1748–1758.
338 Y. Yin, V. Gladkikh, Q. Yuan and F. Ding, *Chem. Mater.*, 2022, **34**, 8230–8236.
339 S. Zhao and Z. Li, *J. Phys. Chem. C*, 2020, **125**, 675–679.
340 J. Zeng, P. Cui and Z. Zhang, *Phys. Rev. Lett.*, 2017, **118**, 046101.
341 Y. Yin, V. Gladkikh, P. Li, L. Zhang, Q. Yuan and F. Ding, *Chem. Mater.*, 2021, **33**, 9447–9453.
342 A. Sala, M. Caporali, M. Serrano-Ruiz, F. Armillotta, E. Vesselli, F. Genuzio, T. O. Mentes, A. Locatelli, G. Comelli, C. Africh and A. Verdini, *Nanoscale*, 2022, **14**, 16256–16261.

343 W. Nunn, T. K. Truttmann and B. Jalan, *J. Mater. Res.*, 2021, **36**, 4846–4864.
344 G. Barik and S. Pal, *Phys. Chem. Chem. Phys.*, 2021, **23**, 26547–26560.
345 P. G. Demingos and A. R. Muniz, *J. Phys. Chem. C*, 2020, **124**, 21207–21214.
346 C. Dai, X. Cai, Y. Ni, Y. Chen and H. Wang, *Phys. Chem. Chem. Phys.*, 2022, **24**, 22572–22579.
347 L. Qiu, J. Dong and F. Ding, *Nanoscale*, 2019, **11**, 7135–7139.
348 A. Pfitzner, S. Reiser and T. Nilges, *Angew. Chem., Int. Ed.*, 2000, **39**, 4160–4162.
349 S. Nilges, T. Nilges, H. Haeuseler and A. Pfitzner, *J. Mol. Struct.*, 2004, **706**, 89–94.
350 A. Pfitzner, *Chem. – Eur. J.*, 2000, **6**, 1891–1898.
351 A. Pfitzner, M. F. Bräu, J. Zweck, G. Brunklaus and H. Eckert, *Angew. Chem., Int. Ed.*, 2004, **43**, 4228–4231.
352 Y. Zhao, Z. Xie, H. Gu, C. Zhu and Z. Gu, *Chem. Soc. Rev.*, 2012, **41**, 3297–3317.
353 M. Hart, J. Chen, A. Michaelides, A. Sella, M. S. P. Shaffer and C. G. Salzmann, *Inorg. Chem.*, 2019, **58**, 15216–15224.
354 J. Urquhart, *Chem. World*, 2017, 31.
355 J. Zhang, D. Zhao, D. Xiao, C. Ma, H. Du, X. Li, L. Zhang, J. Huang, H. Huang, C. L. Jia, D. Tománek and C. Niu, *Angew. Chem., Int. Ed.*, 2017, **56**, 1850–1854.
356 J. Zhang, C. Fu, S. Song, H. Du, D. Zhao, H. Huang, L. Zhang, J. Guan, Y. Zhang, X. Zhao, C. Ma, C. L. Jia and D. Tománek, *Nano Lett.*, 2020, **20**, 1280–1285.
357 D. V. Rybkovskiy, V. O. Koroteev, A. Impellizzeri, A. A. Vorfolomeeva, E. Y. Gerasimov, A. V. Okotrub, A. Chuvilin, L. G. Bulusheva and C. P. Ewels, *ACS Nano*, 2022, **16**, 6002–6012.
358 N. Kittner, F. Lill and D. M. Kammen, *Nat. Energy*, 2017, **2**, 17125.
359 K. Liu, P. Cao, W. Chen, C. I. Ezeh, Z. Chen, Y. Luo, Q. Liu, H. Zhao, Z. Rui, S. Gao, Z. Yin, X. Sun and X. Yu, *Mater. Adv.*, 2022, **3**, 1359–1400.
360 Y. Shang, X. Xu, B. Gao, S. Wang and X. Duan, *Chem. Soc. Rev.*, 2021, **50**, 5281–5322.
361 E. Shayan, V. Zare and I. Mirzaee, *Energy Convers Manage.*, 2018, **159**, 30–41.
362 H. Wang, W. Fu, X. Yang, Z. Huang, J. Li, H. Zhang and Y. Wang, *J. Mater. Chem. A*, 2020, **8**, 6926–6956.
363 J. M. Ogden, *Annu. Rev. Energy Environ.*, 1999, **24**, 227–279.
364 A. Turner John, *Science*, 2004, **305**, 972–974.
365 C. Wu and R. Liu, *Int. J. Hydrogen Energy*, 2011, **36**, 2860–2868.
366 S. Kumar, N. L. Reddy, H. S. Kushwaha, A. Kumar, M. V. Shankar, K. Bhattacharyya, A. Halder and V. Krishnan, *ChemSusChem*, 2017, **10**, 3588–3603.
367 N. Zhu, X. Dong, Z. Liu, G. Zhang, W. Jin and N. Xu, *Chem. Commun.*, 2012, **48**, 7137–7139.
368 A. Fujishima and K. Honda, *Nature*, 1972, **238**, 37–38.
369 C. Xu, P. Ravi Anusuyadevi, C. Aymonier, R. Luque and S. Marre, *Chem. Soc. Rev.*, 2019, **48**, 3868–3902.
370 D. Ravelli, D. Dondi, M. Fagnoni and A. Albini, *Chem. Soc. Rev.*, 2009, **38**, 1999–2011.
371 A. Meng, L. Zhang, B. Cheng and J. Yu, *Adv. Mater.*, 2019, **31**, 1807660.
372 Z. Li, X. Meng and Z. Zhang, *J. Photochem. Photobiol., C*, 2018, **35**, 39–55.
373 S. A. Ansari, M. S. Ansari and M. H. Cho, *Phys. Chem. Chem. Phys.*, 2016, **18**, 3921–3928.
374 X. J. Zhu, T. M. Zhang, Z. J. Sun, H. L. Chen, J. Guan, X. Chen, H. X. Ji, P. W. Du and S. F. Yang, *Adv. Mater.*, 2017, **29**, 1605776.
375 Y. Zhu, C. Lv, Z. Yin, J. Ren, X. Yang, C. L. Dong, H. Liu, R. Cai, Y. C. Huang, W. Theis, S. Shen and D. Yang, *Angew. Chem., Int. Ed.*, 2020, **59**, 868–873.
376 A. Maibam, S. K. Das, P. P. Samal and S. Krishnamurty, *RSC Adv.*, 2021, **11**, 13348–13358.
377 Z. Shen, Z. Hu, W. Wang, S.-F. Lee, D. K. L. Chan, Y. Li, T. Gu and J. C. Yu, *Nanoscale*, 2014, **6**, 14163–14167.
378 J. Xiao, M. Q. Long, X. J. Zhang, D. Zhang, H. Xu and K. S. Chan, *J. Phys. Chem. Lett.*, 2015, **6**, 4141–4147.
379 B. Li, C. C. Ren, S. F. Zhang, W. X. Ji, C. W. Zhang, P. Li and P. J. Wang, *J. Nanomater.*, 2019, **2019**, 4020762.
380 X. Wang, K. Maeda, A. Thomas, K. Takanabe, G. Xin, J. M. Carlsson, K. Domen and M. Antonietti, *Nat. Mater.*, 2009, **8**, 76–80.
381 S. K. Muduli, E. Varrla, Y. Xu, S. A. Kulkarni, A. Katre, S. Chakraborty, S. Chen, T. C. Sum, R. Xu and N. Mathews, *J. Mater. Chem. A*, 2017, **5**, 24874–24879.
382 W. Lei, Y. Mi, R. Feng, P. Liu, S. Hu, J. Yu, X. Liu, J. A. Rodriguez, J.-O. Wang, L. Zheng, K. Tang, S. Zhu, G. Liu and M. Liu, *Nano Energy*, 2018, **50**, 552–561.
383 A. Chouat, D. T. Nguyen, S. Mohan and T.-O. Do, *ACS Appl. Nano Mater.*, 2022, **5**, 13078–13089.
384 Y.-J. Yuan, P. Wang, Z. Li, Y. Wu, W. Bai, Y. Su, J. Guan, S. Wu, J. Zhong, Z.-T. Yu and Z. Zou, *Appl. Catal., B*, 2019, **242**, 1–8.
385 M. Wen, J. Wang, R. Tong, D. Liu, H. Huang, Y. Yu, Z. K. Zhou, P. K. Chu and X. F. Yu, *Adv. Sci.*, 2019, **6**, 1801321.
386 J. Ran, B. Zhu and S. Z. Qiao, *Angew. Chem., Int. Ed.*, 2017, **56**, 10373–10377.
387 J. Hu, Y. Ji, Z. Mo, N. Li, Q. Xu, Y. Li, H. Xu, D. Chen and J. Lu, *J. Mater. Chem. A*, 2019, **7**, 4408–4414.
388 J. Hu, D. Chen, Z. Mo, N. Li, Q. Xu, H. Li, J. He, H. Xu and J. Lu, *Angew. Chem., Int. Ed.*, 2019, **58**, 2073–2077.
389 Y.-P. Yuan, S.-W. Cao, Y.-S. Liao, L.-S. Yin and C. Xue, *Appl. Catal., B*, 2013, **140–141**, 164–168.
390 F. Wang, C. Li, Y. Li and J. C. Yu, *Appl. Catal., B*, 2012, **119–120**, 267–272.
391 W. Wang, G. Li, T. An, D. K. L. Chan, J. C. Yu and P. K. Wong, *Appl. Catal., B*, 2018, **238**, 126–135.
392 C. Li, M. Fu, Y. Wang, E. Liu, J. Fan and X. Hu, *Catal. Sci. Technol.*, 2020, **10**, 2221–2230.
393 Z. Hu, L. Yuan, Z. Liu, Z. Shen and J. C. Yu, *Angew. Chem., Int. Ed.*, 2016, **55**, 9580–9585.
394 L. Jing, R. Zhu, D. L. Phillips and J. C. Yu, *Adv. Funct. Mater.*, 2017, **27**, 1703484.
395 M. Gu, L. Zhang, S. Mao, Y. Zou, D. Ma, J. Shi, N. Yang, C. Fu, X. Zhao, X. Xu, Y. Cheng and J. Zhang, *Chem. Commun.*, 2022, **58**, 12811–12814.

396 S. Zhang, S. Ma, X. Hao, Y. Wang, B. Cao, B. Han, H. Zhang, X. Kong and B. Xu, *Nanoscale*, 2021, **13**, 18955–18960.
397 Y. Zhu, C. Lv, Z. Yin, J. Ren, X. Yang, C. L. Dong, H. Liu, R. Cai, Y. C. Huang, W. Theis, S. Shen and D. Yang, *Angew. Chem., Int. Ed.*, 2020, **59**, 868–873.
398 S. Thurakkal and X. Y. Zhang, *Adv. Sci.*, 2020, **7**, 1902359.
399 H. Huang, Q. L. Xiao, J. H. Wang, X. F. Yu, H. Y. Wang, H. Zhang and P. K. Chu, *npj 2D Mater. Appl.*, 2017, **1**, 20.
400 G. B. Tang, F. H. Hsu, X. Xu and P. K. Chu, *Chem. Eng. J.*, 2020, **392**, 123631.
401 A. Marjani, M. Ghambarian and M. Ghashghaee, *Sci. Rep.*, 2021, **11**, 842.
402 W. Y. Lei, G. Liu, J. Zhang and M. H. Liu, *Chem. Soc. Rev.*, 2017, **46**, 3492–3509.
403 M. Zhu, S. Kim, L. Mao, M. Fujitsuka, J. Zhang, X. Wang and T. Majima, *J. Am. Chem. Soc.*, 2017, **139**, 13234–13242.
404 M. Zhu, Z. Sun, M. Fujitsuka and T. Majima, *Angew. Chem., Int. Ed.*, 2018, **57**, 2160–2164.
405 M. Zhu, X. Cai, M. Fujitsuka, J. Zhang and T. Majima, *Angew. Chem., Int. Ed.*, 2017, **56**, 2064–2068.
406 H. Wang, W. Liu, X. He, P. Zhang, X. Zhang and Y. Xie, *J. Am. Chem. Soc.*, 2020, **142**, 14007–14022.
407 H. Wang, X. Zhang and Y. Xie, *ACS Nano*, 2018, **12**, 9648–9653.
408 W. Shao, L. Wang, H. Wang, Z. Zhao, X. Zhang, S. Jiang, S. Chen, X. Sun, Q. Zhang and Y. Xie, *J. Phys. Chem. Lett.*, 2019, **10**, 2904–2910.
409 H. Wang, S. Jin, X. Zhang and Y. Xie, *Angew. Chem., Int. Ed.*, 2020, **59**, 22828–22839.
410 Y. Li, H. Wang, X. Zhang, S. Wang, S. Jin, X. Xu, W. Liu, Z. Zhao and Y. Xie, *Angew. Chem., Int. Ed.*, 2021, **60**, 12891–12896.
411 Z. Hu, L. Yuan, Z. Liu, Z. Shen and J. C. Yu, *Angew. Chem., Int. Ed.*, 2016, **55**, 9580–9585.
412 C. Wu, R. Zhu, W. Y. Teoh, Y. Liu, J. Deng, H. Dai, L. Jing, Y. H. Ng and J. C. Yu, *Appl. Catal., B*, 2022, **312**, 121428.
413 S. Li, Y. H. Ng, R. Zhu, S. Lv, C. Wu, Y. Liu, L. Jing, J. Deng and H. Dai, *Appl. Catal., B*, 2021, **297**, 120412.
414 Y. Zhu, C. Lv, Z. Yin, J. Ren, X. Yang, C.-L. Dong, H. Liu, R. Cai, Y.-C. Huang, W. Theis, S. Shen and D. Yang, *Angew. Chem., Int. Ed.*, 2020, **59**, 868–873.
415 B. J. Wang, X. H. Li, X. L. Cai, W. Y. Yu, L. W. Zhang, R. Q. Zhao and S. H. Ke, *J. Phys. Chem. C*, 2018, **122**, 7075–7080.
416 X. Zhan, Z. Deng, J. Nie, Y. Du, L. Li and X. Zu, *J. Phys.: Condens. Matter*, 2021, **33**, 485703.
417 M. Tahir and N. S. Amin, *Renewable Sustainable Energy Rev.*, 2013, **25**, 560–579.
418 S. N. Habisreutinger, L. Schmidt-Mende and J. K. Stolarczyk, *Angew. Chem., Int. Ed.*, 2013, **52**, 7372–7408.
419 C. D. Windle and R. N. Perutz, *Coord. Chem. Rev.*, 2012, **256**, 2562–2570.
420 J. Anjali, V. K. Jose and J.-M. Lee, *J. Mater. Chem. A*, 2019, **7**, 15491–15518.
421 G. Fu, Y. Liu, Z. Wu and J.-M. Lee, *ACS Appl. Nano Mater.*, 2018, **1**, 1904–1911.
422 T. Inoue, A. Fujishima, S. Konishi and K. Honda, *Nature*, 1979, **277**, 637–638.
423 T. Sakakura, J.-C. Choi and H. Yasuda, *Chem. Rev.*, 2007, **107**, 2365–2387.
424 J. Schneider, H. Jia, J. T. Muckerman and E. Fujita, *Chem. Soc. Rev.*, 2012, **41**, 2036–2051.
425 P. Prabhu, V. Jose and J. M. Lee, *Adv. Funct. Mater.*, 2020, **30**, 1910768.
426 Y. Jiang, X. Li, Z. Wu, C. Cao, Y. Mei and P. Lian, *Inorg. Chem. Ind.*, 2021, **53**, 59–71.
427 C. Wang, Z. Sun, Y. Zheng and Y. H. Hu, *J. Mater. Chem. A*, 2019, **7**, 865–887.
428 X. Zhu, S. Huang, Q. Yu, Y. She, J. Yang, G. Zhou, Q. Li, X. She, J. Deng, H. Li and H. Xu, *Appl. Catal., B*, 2020, **269**, 118760.
429 C.-M. Fung, B.-J. Ng, C.-C. Er, X. Y. Kong, L.-L. Tan, A. R. Mohamed and S.-P. Chai, *ACS Appl. Energy Mater.*, 2022, **5**, 15257–15268.
430 B. Wan, B. Yang, Y. Wang, J. Zhang, Z. Zeng, Z. Liu and W. Wang, *Nanotechnology*, 2015, **26**, 435702.
431 J. Albero, Y. Peng and H. García, *ACS Catal.*, 2020, **10**, 5734–5749.
432 H. Ou, G. Li, W. Ren, B. Pan, G. Luo, Z. Hu, D. Wang and Y. Li, *J. Am. Chem. Soc.*, 2022, **144**, 22075–22082.
433 M. Wang, S. Xu, Z. Zhou, C.-L. Dong, X. Guo, J.-L. Chen, Y.-C. Huang, S. Shen, Y. Chen, L. Guo and C. Burda, *Angew. Chem., Int. Ed.*, 2022, **61**, e202204711.
434 R. Das, K. Das, B. Ray, C. P. Vinod and S. C. Peter, *Energy Environ. Sci.*, 2022, **15**, 1967–1976.
435 J. Zhu, L. S. Hu, P. X. Zhao, L. Y. S. Lee and K. Y. Wong, *Chem. Rev.*, 2020, **120**, 851–918.
436 J. Li, M. N. Banis, Z. Ren, K. R. Adair, K. Doyle-Davis, D. M. Meira, Y. Z. Finfrock, L. Zhang, F. Kong, T. K. Sham, R. Li, J. Luo and X. Sun, *Small*, 2021, **17**, 2007245.
437 W. Qian, S. Xu, X. Zhang, C. Li, W. Yang, C. R. Bowen and Y. Yang, *Nano-Micro Lett.*, 2021, **13**, 156.
438 J. Di, C. Yan, A. D. Handoko, Z. W. Seh, H. Li and Z. Liu, *Mater. Today*, 2018, **21**, 749–770.
439 P. Yu, F. Wang, T. A. Shifa, X. Zhan, X. Lou, F. Xia and J. He, *Nano Energy*, 2019, **58**, 244–276.
440 J. Janata, *Angew. Chem., Int. Ed.*, 2011, **50**, 9538.
441 T. Shinagawa, A. T. Garcia-Esparza and K. Takanabe, *Sci. Rep.*, 2015, **5**, 13801.
442 Y. Jiao, Y. Zheng, K. Davey and S.-Z. Qiao, *Nat. Energy*, 2016, **1**, 16130.
443 D. Liu, X. Li, S. Chen, H. Yan, C. Wang, C. Wu, Y. A. Haleem, S. Duan, J. Lu, B. Ge, P. M. Ajayan, Y. Luo, J. Jiang and L. Song, *Nat. Energy*, 2019, **4**, 512–518.
444 Z.-Z. Luo, Y. Zhang, C. Zhang, H. T. Tan, Z. Li, A. Abutaha, X.-L. Wu, Q. Xiong, K. A. Khor, K. Hippalgaonkar, J. Xu, H. H. Hng and Q. Yan, *Adv. Energy Mater.*, 2017, **7**, 1601285.
445 C. Xu, S. Peng, C. Tan, H. Ang, H. Tan, H. Zhang and Q. Yan, *J. Mater. Chem. A*, 2014, **2**, 5597–5601.
446 L. Shao, H. Sun, L. Miao, X. Chen, M. Han, J. Sun, S. Liu, L. Li, F. Cheng and J. Chen, *J. Mater. Chem. A*, 2018, **6**, 2494–2499.

447 W. Li, M. Li, J. Li, J. Liang, K. R. Adair, Y. Hu, Q. Xiao, X. Cui, R. Li, F. Brandys, R. Divigalpitiya, T.-K. Sham and X. Sun, *ACS Appl. Nano Mater.*, 2020, **3**, 7508–7515.
448 C. Y. Chan, C. H. Chang and H. Y. Tuan, *Chem. Commun.*, 2020, **56**, 2937–2940.
449 W. Cui, Q. Liu, N. Cheng, A. M. Asiri and X. Sun, *Chem. Commun.*, 2014, **50**, 9340–9342.
450 Y. Ito, W. Cong, T. Fujita, Z. Tang and M. Chen, *Angew. Chem., Int. Ed.*, 2015, **54**, 2131–2136.
451 M. Zeng and Y. Li, *J. Mater. Chem. A*, 2015, **3**, 14942–14962.
452 D. Voiry, M. Salehi, R. Silva, T. Fujita, M. Chen, T. Asefa, V. B. Shenoy, G. Eda and M. Chhowalla, *Nano Lett.*, 2013, **13**, 6222–6227.
453 A. Wang, J. Li and T. Zhang, *Nat. Rev. Chem.*, 2018, **2**, 65–81.
454 W. Fu, Y. Wang, W. Tian, H. Zhang, J. Li, S. Wang and Y. Wang, *Angew. Chem., Int. Ed.*, 2020, **59**, 23791–23799.
455 H. F. Wang, L. Chen, H. Pang, S. Kaskel and Q. Xu, *Chem. Soc. Rev.*, 2020, **49**, 1414–1448.
456 M. Tahir, L. Pan, F. Idrees, X. W. Zhang, L. Wang, J. J. Zou and Z. L. Wang, *Nano Energy*, 2017, **37**, 136–157.
457 N. T. Suen, S. F. Hung, Q. Quan, N. Zhang, Y. J. Xu and H. M. Chen, *Chem. Soc. Rev.*, 2017, **46**, 337–365.
458 H. Dau, C. Limberg, T. Reier, M. Risch, S. Roggan and P. Strasser, *ChemCatChem*, 2010, **2**, 724–761.
459 Y. C. Liu, J. A. Koza and J. A. Switzer, *Electrochim. Acta*, 2014, **140**, 359–365.
460 Q. Jiang, L. Xu, N. Chen, H. Zhang, L. Dai and S. Wang, *Angew. Chem., Int. Ed.*, 2016, **55**, 13849–13853.
461 T. T. Sun, L. B. Xu, Y. S. Yan, A. A. Zakhidov, R. H. Baughman and J. F. Chen, *ACS Catal.*, 2016, **6**, 1446–1450.
462 F. Song and X. Hu, *J. Am. Chem. Soc.*, 2014, **136**, 16481–16484.
463 X. Ren, J. Zhou, X. Qi, Y. Liu, Z. Huang, Z. Li, Y. Ge, S. C. Dhanabalan, J. S. Ponraj, S. Wang, J. Zhong and H. Zhang, *Adv. Energy Mater.*, 2017, **7**, 1700396.
464 Y. Liang, Y. Li, H. Wang, J. Zhou, J. Wang, T. Regier and H. Dai, *Nat. Mater.*, 2011, **10**, 780–786.
465 S. Chen, J. Duan, M. Jaroniec and S. Z. Qiao, *Angew. Chem., Int. Ed.*, 2013, **52**, 13567–13570.
466 X. X. Xue, S. Shen, X. Jiang, P. Sengdala, K. Chen and Y. Feng, *J. Phys. Chem. Lett.*, 2019, **10**, 3440–3446.
467 R. Li, Z. D. Wei and X. L. Gou, *ACS Catal.*, 2015, **5**, 4133–4142.
468 T. Wu, S. N. Zhang, K. J. Bu, W. Zhao, Q. Y. Bi, T. Q. Lin, J. Huang, Y. S. Li and F. Q. Huang, *J. Mater. Chem. A*, 2019, **7**, 22063–22069.
469 H. Qiao, H. Liu, Z. Huang, Q. Ma, S. Luo, J. Li, Y. Liu, J. Zhong and X. Qi, *Adv. Energy Mater.*, 2020, **10**, 2002424.
470 Z. Shen, S. Sun, W. Wang, J. Liu, Z. Liu and J. C. Yu, *J. Mater. Chem. A*, 2015, **3**, 3285–3288.
471 K. Bai, J.-C. Fan, P.-H. Shi, Y.-L. Min and Q.-J. Xu, *J. Power Sources*, 2020, **456**, 228003.
472 C. Gao, Z. Zhao, X. Qin, J. Teng, J. Fan, P. Shi, Q. Xu and Y. Min, *Compos. Commun.*, 2021, **24**, 100624.
473 Y. Zhao, R. Nakamura, K. Kamiya, S. Nakanishi and K. Hashimoto, *Nat. Commun.*, 2013, **4**, 2390.
474 X. Lu, W.-L. Yim, B. H. R. Suryanto and C. Zhao, *J. Am. Chem. Soc.*, 2015, **137**, 2901–2907.
475 J. Wang, D. Liu, H. Huang, N. Yang, B. Yu, M. Wen, X. Wang, P. K. Chu and X. F. Yu, *Angew. Chem., Int. Ed.*, 2018, **57**, 2600–2604.
476 X. Li, L. Xiao, L. Zhou, Q. Xu, J. Weng, J. Xu and B. Liu, *Angew. Chem., Int. Ed.*, 2020, **59**, 21106–21113.
477 X.-D. Zhu, Y. Xie and Y.-T. Liu, *J. Mater. Chem. A*, 2018, **6**, 21255–21260.
478 Z. Yuan, J. Li, M. Yang, Z. Fang, J. Jian, D. Yu, X. Chen and L. Dai, *J. Am. Chem. Soc.*, 2019, **141**, 4972–4979.
479 F. Shiravani, J. Tashkhourian and B. Haghighi, *Sustain. Energy Fuels*, 2021, **5**, 3229–3239.
480 D. R. MacFarlane, P. V. Cherepanov, J. Choi, B. H. R. Suryanto, R. Y. Hodgetts, J. M. Bakker, F. M. F. Vallana and A. N. Simonov, *Joule*, 2020, **4**, 1186–1205.
481 K. H. R. Rouwenhorst, A. G. J. Van der Ham, G. Mul and S. R. A. Kersten, *Renewable Sustainable Energy Rev.*, 2019, **114**, 109339.
482 R. Lan, J. T. S. Irvine and S. W. Tao, *Int. J. Hydrogen Energy*, 2012, **37**, 1482–1494.
483 Y. Yao, S. Zhu, H. Wang, H. Li and M. Shao, *J. Am. Chem. Soc.*, 2018, **140**, 1496–1501.
484 C. Guo, J. Ran, A. Vasileff and S.-Z. Qiao, *Energy Environ. Sci.*, 2018, **11**, 45–56.
485 S. Mukherjee, D. A. Cullen, S. Karakalos, K. Liu, H. Zhang, S. Zhao, H. Xu, K. L. More, G. Wang and G. Wu, *Nano Energy*, 2018, **48**, 217–226.
486 M. Kitano, Y. Inoue, Y. Yamazaki, F. Hayashi, S. Kanbara, S. Matsuishi, T. Yokoyama, S.-W. Kim, M. Hara and H. Hosono, *Nat. Chem.*, 2012, **4**, 934–940.
487 C. J. M. van der Ham, M. T. M. Koper and D. G. H. Hetterscheid, *Chem. Soc. Rev.*, 2014, **43**, 5183–5191.
488 S. L. Foster, S. I. P. Bakovic, R. D. Duda, S. Maheshwari, R. D. Milton, S. D. Minteer, M. J. Janik, J. N. Renner and L. F. Greenlee, *Nat. Catal.*, 2018, **1**, 490–500.
489 Y. Wan, J. Xu and R. Lv, *Mater. Today*, 2019, **27**, 69–90.
490 X. Zhao, G. Hu, G. F. Chen, H. Zhang, S. Zhang and H. Wang, *Adv. Mater.*, 2021, **33**, 2007650.
491 Y. Pang, C. Su, G. Jia, L. Xu and Z. Shao, *Chem. Soc. Rev.*, 2021, **50**, 12744–12787.
492 X. Guo, H. Du, F. Qu and J. Li, *J. Mater. Chem. A*, 2019, **7**, 3531–3543.
493 D. W. Boukhvalov, *Phys. Chem. Chem. Phys.*, 2015, **17**, 27210–27216.
494 L. Zhang, L. X. Ding, G. F. Chen, X. Yang and H. Wang, *Angew. Chem., Int. Ed.*, 2019, **58**, 2612–2616.
495 Y. Liu, Y. Su, X. Quan, X. Fan, S. Chen, H. Yu, H. Zhao, Y. Zhang and J. Zhao, *ACS Catal.*, 2018, **8**, 1186–1191.
496 M.-M. Shi, D. Bao, B.-R. Wulan, Y.-H. Li, Y.-F. Zhang, J.-M. Yan and Q. Jiang, *Adv. Mater.*, 2017, **29**, 1606550.
497 C. Wang, J. Gao, J. G. Zhao, D. J. Yan and X. D. Zhu, *Small*, 2020, **16**, 1907091.
498 Z. M. Zhang, X. Yao, X. Y. Lang, Y. F. Zhu, W. Gao and Q. Jiang, *Appl. Surf. Sci.*, 2021, **536**, 147706.

499 M.-A. Légaré, G. Bélanger-Chabot, D. Dewhurst Rian, E. Welz, I. Krummenacher, B. Engels and H. Braunschweig, *Science*, 2018, **359**, 896–900.
500 S. Bian, M. Wen, J. Wang, N. Yang, P. K. Chu and X. F. Yu, *J. Phys. Chem. Lett.*, 2020, **11**, 1052–1058.
501 Z.-K. Shen, M. Cheng, Y.-J. Yuan, L. Pei, J. Zhong, J. Guan, X. Li, Z.-J. Li, L. Bao, X. Zhang, Z.-T. Yu and Z. Zou, *Appl. Catal., B*, 2021, **295**, 120274.
502 D. Liu, J. Wang, S. Bian, Q. Liu, Y. Gao, X. Wang, P. K. Chu and X. F. Yu, *Adv. Funct. Mater.*, 2020, **30**, 2002731.
503 D. J. Durbin and C. Malardier-Jugroot, *Int. J. Hydrogen Energy*, 2013, **38**, 14595–14617.
504 W. Lubitz and W. Tumas, *Chem. Rev.*, 2007, **107**, 3900–3903.
505 E. Rivard, M. Trudeau and K. Zaghib, *Materials*, 2019, **12**, 1973.
506 P. Kumar, S. Singh, S. A. R. Hashmi and K.-H. Kim, *Nano Energy*, 2021, **85**, 105989.
507 R. Lotfi and Y. Saboohi, *Phys. E*, 2014, **60**, 104–111.
508 R. Mohtadi and S.-i Orimo, *Nat. Rev. Mater.*, 2016, **2**, 16091.
509 M. Darvish Ganji, S. M. Hosseini-khah and Z. Amini-tabar, *Phys. Chem. Chem. Phys.*, 2015, **17**, 2504–2511.
510 K.-F. Aguey-Zinsou and J.-R. Ares-Fernández, *Energy Environ. Sci.*, 2010, **3**, 526–543.
511 Y. F. Zhang and X. L. Cheng, *Chem. Phys.*, 2018, **505**, 26–33.
512 R. Y. Sathe and T. J. D. Kumar, *Int. J. Hydrogen Energy*, 2020, **45**, 12940–12948.
513 D. Luo, J. Y. Li, Y. Zhang, Y. Song and H. S. Chen, *Int. J. Hydrogen Energy*, 2018, **43**, 8415–8425.
514 M. Sevilla and R. Mokaya, *Energy Environ. Sci.*, 2014, **7**, 1250–1280.
515 R. Nagar, B. P. Vinayan, S. S. Samantaray and S. Ramaprabhu, *J. Mater. Chem. A*, 2017, **5**, 22897–22912.
516 S. A. Shevlin and Z. X. Guo, *Chem. Soc. Rev.*, 2009, **38**, 211–225.
517 Q.-F. Li, X. G. Wan, C.-G. Duan and J.-L. Kuo, *J. Phys. D: Appl. Phys.*, 2014, **47**, 465302.
518 J. Xu, H. Li, Y. Li, M. Wang, Z. Li, F. Mo, C. Zhang, L. Zhu, R. Nan and P. Wang, *Mater. Lett.*, 2021, **303**, 130422.
519 M. Ghambarian, Z. Azizi and M. Ghashghaee, *Int. J. Hydrogen Energy*, 2020, **45**, 16298–16309.
520 M. Garara, H. Benzidi, M. Lakhal, M. Louilidi, H. Ez-Zahraouy, A. El Kenz, M. Hamedoun, A. Benyoussef, A. Kara and O. Mounkachi, *Int. J. Hydrogen Energy*, 2019, **44**, 24829–24838.
521 H.-P. Zhang, W. Hu, A. Du, X. Lu, Y.-P. Zhang, J. Zhou, X. Lin and Y. Tang, *Appl. Surf. Sci.*, 2018, **433**, 249–255.
522 M. Nagpal and R. Kakkar, *Int. J. Hydrogen Energy*, 2018, **43**, 12168–12188.
523 S. Haldar, S. Mukherjee, F. Ahmed and C. V. Singh, *Int. J. Hydrogen Energy*, 2017, **42**, 23018–23027.
524 B. Dunn, H. Kamath and J. M. Tarascon, *Science*, 2011, **334**, 928–935.
525 G. Harper, R. Sommerville, E. Kendrick, L. Driscoll, P. Slater, R. Stolkin, A. Walton, P. Christensen, O. Heidrich, S. Lambert, A. Abbott, K. Ryder, L. Gaines and P. Anderson, *Nature*, 2019, **575**, 75–86.
526 L. Ji, Z. Lin, M. Alcoutlabi and X. Zhang, *Energy Environ. Sci.*, 2011, **4**, 2682–2699.
527 D. Larcher and J. M. Tarascon, *Nat. Chem.*, 2015, **7**, 19–29.
528 E. Pomerantseva, F. Bonaccorso, X. L. Feng, Y. Cui and Y. Gogotsi, *Science*, 2019, **366**, 969.
529 H. Jin, H. Wang, Z. Qi, D.-S. Bin, T. Zhang, Y. Wan, J. Chen, C. Chuang, Y.-R. Lu, T.-S. Chan, H. Ju, A.-M. Cao, W. Yan, X. Wu, H. Ji and L.-J. Wan, *Angew. Chem., Int. Ed.*, 2020, **59**, 2318–2322.
530 M. Qiu, Z. T. Sun, D. K. Sang, X. G. Han, H. Zhang and C. M. Niu, *Nanoscale*, 2017, **9**, 13384–13403.
531 T. T. Wang, H. D. Wang, Z. K. Kou, W. Y. Liang, X. L. Luo, F. Verpoort, Y. J. Zeng and H. Zhang, *Adv. Funct. Mater.*, 2020, **30**, 2002885.
532 J. B. Pang, R. G. Mendes, A. Bachmatiuk, L. Zhao, H. Q. Ta, T. Gemming, H. Liu, Z. F. Liu and M. H. Rummeli, *Chem. Soc. Rev.*, 2019, **48**, 72–133.
533 M. Chhowalla, H. S. Shin, G. Eda, L. J. Li, K. P. Loh and H. Zhang, *Nat. Chem.*, 2013, **5**, 263–275.
534 M. Zheng, H. Tang, L. Li, Q. Hu, L. Zhang, H. Xue and H. Pang, *Adv. Sci.*, 2018, **5**, 1700592.
535 W. Li, Y. Yang, G. Zhang and Y.-W. Zhang, *Nano Lett.*, 2015, **15**, 1691–1697.
536 Y. Q. Fu, Q. L. Wei, G. X. Zhang and S. H. Sun, *Adv. Energy Mater.*, 2018, **8**, 1703058.
537 S. A. Ansari, Z. Khan, M. O. Ansari and M. H. Cho, *RSC Adv.*, 2016, **6**, 44616–44629.
538 M. Winter, J. O. Besenhard, M. E. Spahr and P. Novak, *Adv. Mater.*, 1998, **10**, 725–763.
539 F. Wu, J. Maier and Y. Yu, *Chem. Soc. Rev.*, 2020, **49**, 1569–1614.
540 S. Mukherjee, L. Kavalsky and C. V. Singh, *ACS Appl. Mater. Interfaces*, 2018, **10**, 8630–8639.
541 S. Zhao, W. Kang and J. Xue, *J. Mater. Chem. A*, 2014, **2**, 19046–19052.
542 C. M. Park and H. J. Sohn, *Adv. Mater.*, 2007, **19**, 2465–2468.
543 Y. Sun, F. Zeng, Y. Zhu, P. Lu and D. Yang, *J. Energy Chem.*, 2021, **61**, 531–552.
544 W. W. Xia, Q. B. Zhang, F. Xu, H. Y. Ma, J. Chen, K. Qasim, B. H. Ge, C. Y. Zhu and L. T. Sun, *J. Phys. Chem. C*, 2016, **120**, 5861–5868.
545 C. K. Chan, H. Peng, G. Liu, K. McIlwrath, X. F. Zhang, R. A. Huggins and Y. Cui, *Nat. Nanotechnol.*, 2008, **3**, 31–35.
546 Z. W. Seh, Y. Sun, Q. Zhang and Y. Cui, *Chem. Soc. Rev.*, 2016, **45**, 5605–5634.
547 Y. Lee, J.-Y. Yoon, D. Scullion, J. Jang, E. J. G. Santos, H. Y. Jeong and K. Kim, *J. Phys. D: Appl. Phys.*, 2017, **50**, 084003.
548 J. Zhu, Z. Liu, W. Wang, L. Yue, W. Li, H. Zhang, L. Zhao, H. Zheng, J. Wang and Y. Li, *ACS Nano*, 2021, **15**, 1880–1892.
549 J. Sun, G. Zheng, H. W. Lee, N. Liu, H. Wang, H. Yao, W. Yang and Y. Cui, *Nano Lett.*, 2014, **14**, 4573–4580.
550 H. Liu, Y. Zou, L. Tao, Z. Ma, D. Liu, P. Zhou, H. Liu and S. Wang, *Small*, 2017, **13**, 1700758.
551 S. Zhang, Y. Zhang, Z. Zhang, H. Wang, Y. Cao, B. Zhang, X. Liu, C. Mao, X. Han, H. Gong, Z. Yang and J. Sun, *Adv. Energy Mater.*, 2022, **12**, 2103888.

552 J. Jin, Y. Zheng, S.-Z. Huang, P.-P. Sun, N. Srikanth, L. B. Kong, Q. Yan and K. Zhou, *J. Mater. Chem. A*, 2019, **7**, 783–790.
553 M. Li, W. Li, Y. Hu, A. A. Yakovenko, Y. Ren, J. Luo, W. M. Holden, M. Shakouri, Q. Xiao, X. Gao, F. Zhao, J. Liang, R. Feng, R. Li, G. T. Seidler, F. Brandys, R. Divigalpitiya, T. K. Sham and X. Sun, *Adv. Mater.*, 2021, **33**, 2101259.
554 H. Jin, S. Xin, C. Chuang, W. Li, H. Wang, J. Zhu, H. Xie, T. Zhang, Y. Wan, Z. Qi, W. Yan, Y.-R. Lu, T.-S. Chan, X. Wu, B. Goodenough John, H. Ji and X. Duan, *Science*, 2020, **370**, 192–197.
555 Z. L. Xu, S. Lin, N. Onofrio, L. Zhou, F. Shi, W. Lu, K. Kang, Q. Zhang and S. P. Lau, *Nat. Commun.*, 2018, **9**, 4164.
556 J. Sun, Y. Sun, M. Pasta, G. Zhou, Y. Li, W. Liu, F. Xiong and Y. Cui, *Adv. Mater.*, 2016, **28**, 9797–9803.
557 H. Cheng, J. Xie, G. Cao, Y. Lu, D. Zheng, Y. Jin, K. Wang and X. Zhao, *Energy Storage Mater.*, 2019, **23**, 684–692.
558 Y. Kim, D. Koo, S. Ha, S. C. Jung, T. Yim, H. Kim, S. K. Oh, D. M. Kim, A. Choi, Y. Kang, K. H. Ryu, M. Jang, Y. K. Han, S. M. Oh and K. T. Lee, *ACS Nano*, 2018, **12**, 4419–4430.
559 S. Haghighat-Shishavan, M. Nazarian-Samani, M. Nazarian-Samani, H.-K. Roh, K.-Y. Chung, B.-W. Cho, S. F. Kashani-Bozorg and K.-B. Kim, *J. Mater. Chem. A*, 2018, **6**, 10121–10134.
560 R. Meng, J. Huang, Y. Feng, L. Zu, C. Peng, L. Zheng, L. Zheng, Z. Chen, G. Liu, B. Chen, Y. Mi and J. Yang, *Adv. Energy Mater.*, 2018, **8**, 1801514.
561 H. Liu, L. Tao, Y. Zhang, C. Xie, P. Zhou, H. Liu, R. Chen and S. Wang, *ACS Appl. Mater. Interfaces*, 2017, **9**, 36849–36856.
562 Y. Liu, Q. Liu, A. Zhang, J. Cai, X. Cao, Z. Li, P. D. Asimow and C. Zhou, *ACS Nano*, 2018, **12**, 8323–8329.
563 X. Ma, C. Ji, X. Li, Y. Liu and X. Xiong, *Mater. Today*, 2022, **59**, 36–45.
564 Z. Huang, H. Hou, Y. Zhang, C. Wang, X. Qiu and X. Ji, *Adv. Mater.*, 2017, **29**, 1702372.
565 J. Sun, H. W. Lee, M. Pasta, H. Yuan, G. Zheng, Y. Sun, Y. Li and Y. Cui, *Nat. Nanotechnol.*, 2015, **10**, 980–985.
566 X. Guo, W. Zhang, J. Zhang, D. Zhou, X. Tang, X. Xu, B. Li, H. Liu and G. Wang, *ACS Nano*, 2020, **14**, 3651–3659.
567 C. Zhang, T. Liang, H. Dong, J. Li, J. Shen, W. Yang, X. Wang, H. Geng and Z. Zhang, *Mater. Chem. Front.*, 2021, **5**, 6639–6647.
568 I. Sultana, M. M. Rahman, T. Ramireddy, Y. Chen and A. M. Glushenkov, *J. Mater. Chem. A*, 2017, **5**, 23506–23512.
569 J. Guan, A. M. Rao, J. Zhou, X. Yu and B. Lu, *Adv. Funct. Mater.*, 2022, **32**, 2203522.
570 C. Hao, B. Yang, F. Wen, J. Xiang, L. Li, W. Wang, Z. Zeng, B. Xu, Z. Zhao, Z. Liu and Y. Tian, *Adv. Mater.*, 2016, **28**, 3194–3201.
571 M. Wen, D. Liu, Y. Kang, J. Wang, H. Huang, J. Li, P. K. Chu and X.-F. Yu, *Mater. Horiz.*, 2019, **6**, 176–181.
572 X. Wu, Y. Xu, Y. Hu, G. Wu, H. Cheng, Q. Yu, K. Zhang, W. Chen and S. Chen, *Nat. Commun.*, 2018, **9**, 4573.
573 T. Wu, Z. Ma, Y. He, X. Wu, B. Tang, Z. Yu, G. Wu, S. Chen and N. Bao, *Angew. Chem., Int. Ed.*, 2021, **60**, 10366–10374.
574 H. Xiao, Y. Xia, Y. Gan, H. Huang, C. Liang, X. Tao, L. Xu and W. Zhang, *RSC Adv.*, 2014, **4**, 60914–60919.
575 T. Wang, F. Cheng, N. Zhang, W. Tian, J. Zhou, R. Zhang, J. Cao, M. Luo, N. Li, L. Jiang, D. Li, Y. Li, K. Liang, H. Liu, P. Chen and B. Kong, *Adv. Eng. Mater.*, 2021, **23**, 2001507.
576 X. Han, Z. Zhang, M. Han, Y. Cui and J. Sun, *Energy Storage Mater.*, 2020, **26**, 147–156.
577 J. Zhou, X. Liu, W. Cai, Y. Zhu, J. Liang, K. Zhang, Y. Lan, Z. Jiang, G. Wang and Y. Qian, *Adv. Mater.*, 2017, **29**, 1700214.
578 W. Li, Z. Yang, M. Li, Y. Jiang, X. Wei, X. Zhong, L. Gu and Y. Yu, *Nano Lett.*, 2016, **16**, 1546–1553.
579 X. Chen, G. Xu, X. Ren, Z. Li, X. Qi, K. Huang, H. Zhang, Z. Huang and J. Zhong, *J. Mater. Chem. A*, 2017, **5**, 6581–6588.
580 J. Lee, H. Song, K. A. Min, Q. Guo, D. Kim, Z. Zheng, B. Han, Y. Jung and L. Y. S. Lee, *Small Methods*, 2021, **5**, 2100215.
581 Y. Liu, N. Zhang, X. Liu, C. Chen, L.-Z. Fan and L. Jiao, *Energy Storage Mater.*, 2017, **9**, 170–178.
582 J. Song, Z. Yu, M. L. Gordin, X. Li, H. Peng and D. Wang, *ACS Nano*, 2015, **9**, 11933–11941.
583 Y. Liu, A. Zhang, C. Shen, Q. Liu, X. Cao, Y. Ma, L. Chen, C. Lau, T.-C. Chen, F. Wei and C. Zhou, *ACS Nano*, 2017, **11**, 5530–5537.
584 Y. Liu, Q. Liu, C. Jian, D. Cui, M. Chen, Z. Li, T. Li, T. Nilges, K. He, Z. Jia and C. Zhou, *Nat. Commun.*, 2020, **11**, 2520.
585 S. Liu, H. Xu, X. Bian, J. Feng, J. Liu, Y. Yang, C. Yuan, Y. An, R. Fan and L. Ci, *ACS Nano*, 2018, **12**, 7380–7387.
586 S. Liu, J. Feng, X. Bian, J. Liu, H. Xu and Y. An, *Energy Environ. Sci.*, 2017, **10**, 1222–1233.
587 W. Li, S. Hu, X. Luo, Z. Li, X. Sun, M. Li, F. Liu and Y. Yu, *Adv. Mater.*, 2017, **29**, 1605820.
588 J. Ruan, F. Mo, Z. Long, Y. Song, F. Fang, D. Sun and S. Zheng, *ACS Nano*, 2020, **14**, 12222–12233.
589 X. Sui, X. Huang, H. Pu, Y. Wang and J. Chen, *Nano Energy*, 2021, **83**, 105797.
590 Y. Wu, S. Hu, R. Xu, J. Wang, Z. Peng, Q. Zhang and Y. Yu, *Nano Lett.*, 2019, **19**, 1351–1358.
591 G. Qin, Y. Liu, F. Liu, X. Sun, L. Hou, B. Liu and C. Yuan, *Adv. Energy Mater.*, 2020, **11**, 2003429.
592 A. Gopalakrishnan and S. Badhulika, *Chem. Commun.*, 2020, **56**, 7096–7099.
593 M. Khalid and H. Varela, *J. Mater. Chem. A*, 2018, **6**, 3141–3150.
594 L. Liu, X. Gao, X. Cui, B. Wang, F. Hu, T. Yuan, J. Li, L. Zu, H. Lian and X. Cui, *Nanomaterials*, 2023, **13**, 1060.
595 D. Zhao, L. Zhang, C. Fu, J. Huang, H. Huang, Z. Li, J. Zhang and C. Niu, *Carbon*, 2018, **139**, 1057–1062.
596 B. Cai, S. Dong, Z. Mao, Y.-L. Lu, Z. Pan, Y. Ou and J. Li, *Solid State Commun.*, 2021, **330**, 114276.
597 Q.-F. Li, C.-G. Duan, X. G. Wan and J.-L. Kuo, *J. Phys. Chem. C*, 2015, **119**, 8662–8670.
598 Y. Li, W. Wu and F. Ma, *J. Mater. Chem. A*, 2019, **7**, 611–620.
599 Q. Peng, Z. Wang, B. Sa, B. Wu and Z. Sun, *ACS Appl. Mater. Interfaces*, 2016, **8**, 13449–13457.
600 S. Mukherjee, L. Kavalsky, K. Chattopadhyay and C. V. Singh, *Nanoscale*, 2018, **10**, 21335–21352.
601 Y. Xiao, J. Wang, Y. Wang and W. Zhang, *Appl. Surf. Sci.*, 2019, **488**, 620–628.

602 J. Bao, L. Zhu, H. Wang, S. Han, Y. Jin, G. Zhao, Y. Zhu, X. Guo, J. Hou, H. Yin and J. Tian, *J. Phys. Chem. C*, 2018, **122**, 23329–23335.
603 J. Bao, H. Li, Q. Duan, D. Jiang, W. Liu, X. Guo, J. Hou and J. Tian, *Solid State Ion.*, 2020, **345**, 115160.
604 S. Hajibaba and Y. Abdi, *J. Energy Storage*, 2021, **33**, 102062.
605 J. B. Goodenough and K.-S. Park, *J. Am. Chem. Soc.*, 2013, **135**, 1167–1176.
606 Y. Gogotsi and P. Simon, *Science*, 2011, **334**, 917–918.
607 G.-C. Guo, D. Wang, X.-L. Wei, Q. Zhang, H. Liu, W.-M. Lau and L.-M. Liu, *J. Phys. Chem. Lett.*, 2015, **6**, 5002–5008.
608 J. Cheng, L. Gao, T. Li, S. Mei, C. Wang, B. Wen, W. Huang, C. Li, G. Zheng, H. Wang and H. Zhang, *Nano-Micro Lett.*, 2020, **12**, 179.
609 E. Olsson, G. Chai, M. Dove and Q. Cai, *Nanoscale*, 2019, **11**, 5274–5284.
610 S. Y. Chu, S. H. Guo and H. S. Zhou, *Chem. Soc. Rev.*, 2021, **50**, 13189–13235.
611 A. K. Thakur, M. S. Ahmed, G. Oh, H. Kang, Y. Jeong, R. Prabakaran, M. P. Vikram, S. W. Sharshir, J. Kim and J. Y. Hwang, *J. Mater. Chem. A*, 2021, **9**, 2628–2661.
612 M. M. Lao, Y. Zhang, W. B. Luo, Q. Y. Yan, W. P. Sun and S. X. Dou, *Adv. Mater.*, 2017, **29**, 1700622.
613 W. Zhang, J. Lu and Z. Guo, *Mater. Today*, 2021, **50**, 400–417.
614 T. Jin, Q. Q. Han and L. F. Jiao, *Adv. Mater.*, 2020, **32**, 1806304.
615 M. S. Balogun, Y. Luo, W. T. Qiu, P. Liu and Y. X. Tong, *Carbon*, 2016, **98**, 162–178.
616 Y. M. Li, Y. X. Lu, C. L. Zhao, Y. S. Hu, M. M. Titirici, H. Li, X. J. Huang and L. Q. Chen, *Energy Storage Mater.*, 2017, **7**, 130–151.
617 K. Kuratani, N. Uemura, H. Senoh, H. T. Takeshita and T. Kiyobayashi, *J. Power Sources*, 2013, **223**, 175–182.
618 X. D. Xiang, K. Zhang and J. Chen, *Adv. Mater.*, 2015, **27**, 5343–5364.
619 K. P. S. S. Hembram, H. Jung, B. C. Yeo, S. J. Pai, S. Kim, K.-R. Lee and S. S. Han, *J. Phys. Chem. C*, 2015, **119**, 15041–15046.
620 X. Liu, Y. Wen, Z. Chen, B. Shan and R. Chen, *Phys. Chem. Chem. Phys.*, 2015, **17**, 16398–16404.
621 C. Liu, X. Han, Y. Cao, S. Zhang, Y. Zhang and J. Sun, *Energy Storage Mater.*, 2019, **20**, 343–372.
622 W.-J. Li, S.-L. Chou, J.-Z. Wang, H.-K. Liu and S.-X. Dou, *Nano Lett.*, 2013, **13**, 5480–5484.
623 W. Li, S. Hu, X. Luo, Z. Li, X. Sun, M. Li, F. Liu and Y. Yu, *Adv. Mater.*, 2017, **29**, 1605820.
624 Y. Kim, Y. Park, A. Choi, N.-S. Choi, J. Kim, J. Lee, J. H. Ryu, S. M. Oh and K. T. Lee, *Adv. Mater.*, 2013, **25**, 3045–3049.
625 C. Zhang, X. Wang, Q. Liang, X. Liu, Q. Weng, J. Liu, Y. Yang, Z. Dai, K. Ding, Y. Bando, J. Tang and D. Golberg, *Nano Lett.*, 2016, **16**, 2054–2060.
626 M. Lao, Y. Zhang, W. Luo, Q. Yan, W. Sun and S. X. Dou, *Adv. Mater.*, 2017, **29**, 1700622.
627 Y. Yan, S. Xia, H. Sun, Y. Pang, J. Yang and S. Zheng, *Chem. Eng. J.*, 2020, **393**, 124788.
628 X. L. Huang, F. Zhao, Y. Qi, Y.-A. Qiu, J. S. Chen, H. K. Liu, S. X. Dou and Z. M. Wang, *Energy Storage Mater.*, 2021, **42**, 193–208.
629 T. Hosaka, K. Kubota, A. S. Hameed and S. Komaba, *Chem. Rev.*, 2020, **120**, 6358–6466.
630 M. Okoshi, Y. Yamada, S. Komaba, A. Yamada and H. Nakai, *J. Electrochem. Soc.*, 2017, **164**, A54.
631 Y. Xu, C. Zhang, M. Zhou, Q. Fu, C. Zhao, M. Wu and Y. Lei, *Nat. Commun.*, 2018, **9**, 1720.
632 D. Yang, C. Liu, X. Rui and Q. Yan, *Nanoscale*, 2019, **11**, 15402–15417.
633 J. Zhao, X. Zou, Y. Zhu, Y. Xu and C. Wang, *Adv. Funct. Mater.*, 2016, **26**, 8103–8110.
634 P. Xiong, P. Bai, S. Tu, M. Cheng, J. Zhang, J. Sun and Y. Xu, *Small*, 2018, **14**, 1802140.
635 Y. Wu, H. B. Huang, Y. Feng, Z. S. Wu and Y. Yu, *Adv. Mater.*, 2019, **31**, 1901414.
636 W. Zhang, J. Mao, S. Li, Z. Chen and Z. Guo, *J. Am. Chem. Soc.*, 2017, **139**, 3316–3319.
637 W. Feng, H. Wang, Y. Jiang, H. Zhang, W. Luo, W. Chen, C. Shen, C. Wang, J. Wu and L. Mai, *Adv. Energy Mater.*, 2022, **12**, 2103343.
638 X. Liu, J. Zhu, X. Wang, L. Yue, W. Wang, B. Wang, D. Shen and Y. Li, *Adv. Funct. Mater.*, 2022, **33**, 2209388.
639 X. Du and B. Zhang, *ACS Nano*, 2021, **15**, 16851–16860.
640 M. Yu and X. Feng, *Joule*, 2019, **3**, 338–360.
641 C. Zhong, Y. Deng, W. Hu, J. Qiao, L. Zhang and J. Zhang, *Chem. Soc. Rev.*, 2015, **44**, 7484–7539.
642 M. Hu, H. Zhang, T. Hu, B. Fan, X. Wang and Z. Li, *Chem. Soc. Rev.*, 2020, **49**, 6666–6693.
643 Y. Wu, W. Yuan, M. Xu, S. Bai, Y. Chen, Z. Tang, C. Wang, Y. Yang, X. Zhang, Y. Yuan, M. Chen, X. Zhang, B. Liu and L. Jiang, *Chem. Eng. J.*, 2021, **412**, 128744.
644 D. P. Dubal, N. R. Chodankar, D.-H. Kim and P. Gomez-Romero, *Chem. Soc. Rev.*, 2018, **47**, 2065–2129.
645 X. Tian, *2D Mater.*, 2021, **9**, 012001.
646 S.-K. Kim, H.-J. Koo, A. Lee and P. V. Braun, *Adv. Mater.*, 2014, **26**, 5108–5112.
647 Z. S. Wu, K. Parvez, X. Feng and K. Müllen, *Nat. Commun.*, 2013, **4**, 2487.
648 F. El-Kady Maher, V. Strong, S. Dubin and B. Kaner Richard, *Science*, 2012, **335**, 1326–1330.
649 J. Yang, Z. Pan, Q. Yu, Q. Zhang, X. Ding, X. Shi, Y. Qiu, K. Zhang, J. Wang and Y. Zhang, *ACS Appl. Mater. Interfaces*, 2019, **11**, 5938–5946.
650 J. S. Shaikh, N. S. Shaikh, S. Sabale, N. Parveen, S. P. Patil, Y. K. Mishra, P. Kanjanaboos, S. Praserthdam and C. D. Lokhande, *Mater. Today Chem.*, 2021, **21**, 100480.
651 R. Yi, S. Chen, J. Song, M. L. Gordin, A. Manivannan and D. Wang, *Adv. Funct. Mater.*, 2014, **24**, 7433–7439.
652 J. Chang, J. Shang, Y. Sun, L. K. Ono, D. Wang, Z. Ma, Q. Huang, D. Chen, G. Liu, Y. Cui, Y. Qi and Z. Zheng, *Nat. Commun.*, 2018, **9**, 4480.
653 T. Tao, S. Lu, Y. Fan, W. Lei, S. Huang and Y. Chen, *Adv. Mater.*, 2017, **29**, 1700542.
654 T. Wang, J. He, X.-B. Cheng, J. Zhu, B. Lu and Y. Wu, *ACS Energy Lett.*, 2022, **8**, 116–150.
655 Z. Pan, D. J. L. Brett, G. He and I. P. Parkin, *Adv. Energy Mater.*, 2022, **12**, 2103483.

656 Z. W. Seh, Y. Sun, Q. Zhang and Y. Cui, *Chem. Soc. Rev.*, 2016, **45**, 5605–5634.
657 H. J. Peng, J. Q. Huang and Q. Zhang, *Chem. Soc. Rev.*, 2017, **46**, 5237–5288.
658 J. Zhou, T. Wu, Y. Pan, J. Zhu, X. Chen, C. Peng, C. Shu, L. Kong, W. Tang and S. L. Chou, *Adv. Funct. Mater.*, 2021, **32**, 2106966.
659 H. Hao, T. Hutter, B. L. Boyce, J. Watt, P. Liu and D. Mitlin, *Chem. Rev.*, 2022, **122**, 8053–8125.
660 C. Li, R. Liu, Y. Xiao, F. Cao and H. Zhang, *Energy Storage Mater.*, 2021, **40**, 439–460.
661 Z. Wang, M. Feng, H. Sun, G. Li, Q. Fu, H. Li, J. Liu, L. Sun, A. Mauger, C. M. Julien, H. Xie and Z. Chen, *Nano Energy*, 2019, **59**, 390–398.
662 J. Lee, H. Song, K. A. Min, Q. Guo, D. Kim, Z. Zheng, B. Han, Y. Jung and L. Y. S. Lee, *Small Methods*, 2021, **5**, 2100215.
663 L. Kavalsky, S. Mukherjee and C. V. Singh, *ACS Appl. Mater. Interfaces*, 2019, **11**, 499–510.
664 T. Cai, T. Li, B. Li, Y. Hu, X. Li, T. Lin, H. Hu, B. Luo, Y. Zhang, X. Zhu, Y. Cui, L. Zhao, W. Xing, Z. Yan and L. Wang, *Energy Storage Mater.*, 2022, **53**, 415–423.
665 H. S. Tsai, Y. Wang, C. Liu, T. Wang and M. Huo, *J. Hazard. Mater.*, 2022, **423**, 127148.
666 H.-J. Kim and J.-H. Lee, *Sens. Actuators, B*, 2014, **192**, 607–627.
667 J. Zhang, X. H. Liu, G. Neri and N. Pinna, *Adv. Mater.*, 2016, **28**, 795–831.
668 S. Deng, V. Tjoa, H. M. Fan, H. R. Tan, D. C. Sayle, M. Olivo, S. Mhaisalkar, J. Wei and C. H. Sow, *J. Am. Chem. Soc.*, 2012, **134**, 4905–4917.
669 K. Belanger, T. R. Holford, J. F. Gent, M. E. Hill, J. M. Kezik and B. P. Leaderer, *Epidemiol.*, 2013, **24**, 320–330.
670 Y.-H. Choi, D.-H. Kim and S.-H. Hong, *ACS Appl. Mater. Interfaces*, 2018, **10**, 14901–14913.
671 Y. Cai, Q. Ke, G. Zhang and Y.-W. Zhang, *J. Phys. Chem. C*, 2015, **119**, 3102–3110.
672 E. Montes and U. Schwingenschlögl, *J. Mater. Chem. C*, 2017, **5**, 5365–5371.
673 D. An, X. Zhang, Z. Bi, W. Shan, H. Zhang, S. Xia and M. Qiu, *Adv. Funct. Mater.*, 2021, **31**, 2106484.
674 A. N. Abbas, B. L. Liu, L. Chen, Y. Q. Ma, S. Cong, N. Aroonyadet, M. Köpf, T. Nilges and C. W. Zhou, *ACS Nano*, 2015, **9**, 5618–5624.
675 S. Y. Cho, Y. Lee, H. J. Koh, H. Jung, J. S. Kim, H. W. Yoo, J. Kim and H. T. Jung, *Adv. Mater.*, 2016, **28**, 7020–7028.
676 D. Han, X. Han, L. Liu, D. Li, Y. Liu, Z. Liu, D. Liu, Y. Chen, K. Zhuo and S. Sang, *ACS Appl. Mater. Interfaces*, 2022, **14**, 13942–13951.
677 H. Chen, Y. Chen, H. Zhang, D. W. Zhang, P. Zhou and J. Huang, *Adv. Funct. Mater.*, 2018, **28**, 1801035.
678 E. Montes and U. Schwingenschlogl, *J. Mater. Chem. C*, 2017, **5**, 5365–5371.
679 L. Kou, T. Frauenheim and C. Chen, *J. Phys. Chem. Lett.*, 2014, **5**, 2675–2681.
680 J. Sun, N. Lin, H. Ren, C. Tang, L. Yang and X. Zhao, *RSC Adv.*, 2016, **6**, 17494–17503.
681 M. Sajjad, E. Montes, N. Singh and U. Schwingenschlögl, *Adv. Mater. Interfaces*, 2017, **4**, 1600911.
682 S. Singsen, A. Watwiangkham, L. Ngamwongwan, I. Fongkaew, S. Jungthawan and S. Suthirakun, *ACS Appl. Nano Mater.*, 2023, **6**, 1496–1506.
683 S. Dharani, V. Nagarajan and R. Chandiramouli, *J. Mol. Graphics Modell.*, 2019, **91**, 22–29.
684 R. Bhuvaneswari, V. Nagarajan and R. Chandiramouli, *Comput. Theor. Chem.*, 2019, **1165**, 112563.
685 B. Zhang, Z. Mao and P. Wu, *Appl. Surf. Sci.*, 2021, **565**, 150546.
686 Y. X. Liu, J. Zhang, C. D. Sheng, Y. C. Zhang and L. A. Zhao, *Chem. Eng. J.*, 2010, **162**, 1006–1011.
687 R. Chen, T. S. Zhang, Y. Q. Guo, J. W. Wang, J. X. Wei and Q. J. Yu, *Chem. Eng. J.*, 2021, **420**, 127588.
688 F. Rezaei, A. A. Rownaghi, S. Monjezi, R. P. Lively and C. W. Jones, *Energy Fuels*, 2015, **29**, 5467–5486.
689 Y. Sun, E. Zwolińska and A. G. Chmielewski, *Crit. Rev. Environ. Sci. Technol.*, 2015, **46**, 119–142.
690 S. G. Chang and D. K. Liu, *Nature*, 1990, **343**, 151–153.
691 D. K. Liu, D.-X. Shen and S.-G. Chang, *Environ. Sci. Technol.*, 1991, **25**, 55–60.
692 B. Li, Y. Liu, X. Zhao, P. Ning, X. Liu and T. Zhu, *J. Hazard. Mater.*, 2021, **403**, 123971.
693 Y. Liu, B. Li, X. Lei, S. Liu, H. Zhu, E. Ding and P. Ning, *Chem. Eng. J.*, 2022, **428**, 131991.
694 B. Xiao, P. S. Wheatley, X. Zhao, A. J. Fletcher, S. Fox, A. G. Rossi, I. L. Megson, S. Bordiga, L. Regli, K. M. Thomas and R. E. Morris, *J. Am. Chem. Soc.*, 2007, **129**, 1203–1209.
695 Z. Wang, Y. Huang, W. Ho, J. Cao, Z. Shen and S. C. Lee, *Appl. Catal., B*, 2016, **199**, 123–133.
696 W. Wan, S. Yu, F. Dong, Q. Zhang and Y. Zhou, *J. Mater. Chem. A*, 2016, **4**, 7823–7829.
697 W. Cui, J. Li, F. Dong, Y. Sun, G. Jiang, W. Cen, S. C. Lee and Z. Wu, *Environ. Sci. Technol.*, 2017, **51**, 10682–10690.
698 X. Wu, S. J. Cobbina, G. Mao, H. Xu, Z. Zhang and L. Yang, *Environ. Sci. Pollut. Res.*, 2016, **23**, 8244–8259.
699 E. Nilsen, K. L. Smalling, L. Ahrens, M. Gros, K. S. B. Miglioranza, Y. Picó and H. L. Schoenfuss, *Environ. Toxicol. Chem.*, 2019, **38**, 46–60.
700 P. Morcillo, M. Á. Esteban and A. Cuesta, *Chemosphere*, 2016, **144**, 225–233.
701 M. Feng, D. D. Dionysiou and V. K. Sharma, *Chem. Eng. J.*, 2020, **389**, 123460.
702 C. Wu, L. Jing, J. Deng, Y. Liu, S. Li, S. Lv, Y. Sun, Q. Zhang and H. Dai, *Chemosphere*, 2021, **274**, 129793.
703 Y. Zheng, Y. Chen, B. Gao, B. Lin and X. Wang, *Engineering*, 2021, **7**, 991–1001.
704 M. S. Tsuboy, J. P. F. Angeli, M. S. Mantovani, S. Knasmüller, G. A. Umbuzeiro and L. R. Ribeiro, *Toxicol. Vitro*, 2007, **21**, 1650–1655.
705 Z. Zhang, W. Wang, E. Gao, S. Sun and L. Zhang, *J. Phys. Chem. C*, 2012, **116**, 25898–25903.
706 S. Linic, P. Christopher and D. B. Ingram, *Nat. Mater.*, 2011, **10**, 911–921.
707 Y. Liu, J. Kong, J. Yuan, W. Zhao, X. Zhu, C. Sun and J. Xie, *Chem. Eng. J.*, 2018, **331**, 242–254.
708 P. Wang, H. Zhao, S. Li, R. Jing, Y. Liu, N. Jiang, F. Bian, Y. Liu, H. Liu and Q. Zhang, *J. Mater. Sci.*, 2021, **56**, 8060–8078.

709 Q. Lu, W. Gao, J. Du, L. Zhou and Y. Lian, *J. Agric. Food Chem.*, 2012, **60**, 4773–4778.
710 Y. Y. Cheng and T. H. Tsai, *J. Agric. Food Chem.*, 2017, **65**, 1078–1085.
711 R. H. Jeong, D. I. Kim, J. W. Lee, J.-H. Yu, B. G. Jeong, H. M. Oh, M. S. Jeong and J.-H. Boo, *2D Mater.*, 2019, **6**, 045039.
712 F. Yu, Y. Li, S. Han and J. Ma, *Chemosphere*, 2016, **153**, 365–385.
713 Y. Xiang, Z. Xu, Y. Wei, Y. Zhou, X. Yang, Y. Yang, J. Yang, J. Zhang, L. Luo and Z. Zhou, *J. Environ. Manage.*, 2019, **237**, 128–138.
714 M.-F. Li, Y.-G. Liu, G.-M. Zeng, N. Liu and S.-B. Liu, *Chemosphere*, 2019, **226**, 360–380.
715 Q. Wu, H. Yang, L. Kang, Z. Gao and F. Ren, *Appl. Catal., B*, 2020, **263**, 118282.
716 D. Wang and Z. Li, *Res. Chem. Intermed.*, 2017, **43**, 5169–5186.
717 K. G. M. Laurier, F. Vermoortele, R. Ameloot, D. E. De Vos, J. Hofkens and M. B. J. Roeffaers, *J. Am. Chem. Soc.*, 2013, **135**, 14488–14491.
718 X. Lei, J. Wang, Y. Shi, W. Yao, Q. Wu, Q. Wu and R. Zou, *Appl. Surf. Sci.*, 2020, **528**, 146963.
719 Z. Zhao, H. An, J. Lin, M. Feng, V. Murugadoss, T. Ding, H. Liu, Q. Shao, X. Mai, N. Wang, H. Gu, S. Angaiah and Z. Guo, *Chem. Rec.*, 2019, **19**, 873–882.
720 N. Tian, H. Huang, X. Du, F. Dong and Y. Zhang, *J. Mater. Chem. A*, 2019, **7**, 11584–11612.
721 A. Meng, W. Tian, H. Yang, X. Wang, X. Wang and Z. Li, *J. Hazard. Mater.*, 2021, **413**, 125400.
722 D. Wang, L. Huang, Z. Guo, S. Jin, C. Liu, W. Wang and W. Yuan, *ACS Appl. Nano Mater.*, 2018, **1**, 4594–4601.
723 S. Sharma and A. Bhattacharya, *Appl. Water Sci.*, 2017, **7**, 1043–1067.
724 Z. Teng, N. Yang, H. Lv, S. Wang, M. Hu, C. Wang, D. Wang and G. Wang, *Chem*, 2019, **5**, 664–680.
725 W. Wang, C. Zhou, Y. Yang, G. Zeng, C. Zhang, Y. Zhou, J. Yang, D. Huang, H. Wang, W. Xiong, X. Li, Y. Fu, Z. Wang, Q. He, M. Jia and H. Luo, *Chem. Eng. J.*, 2021, **404**, 126540.
726 E. M. Anastasi, T. D. Wohlsen, H. M. Stratton and M. Katouli, *Water Res.*, 2013, **47**, 6670–6679.
727 Y. Li, X. Liu, L. Tan, Z. Cui, D. Jing, X. Yang, Y. Liang, Z. Li, S. Zhu, Y. Zheng, K. W. K. Yeung, D. Zheng, X. Wang and S. Wu, *Adv. Funct. Mater.*, 2019, **29**, 1900946.
728 X. Zhang, J. Zhang, J. Yu, Y. Zhang, Z. Cui, Y. Sun and B. Hou, *Appl. Catal., B*, 2018, **220**, 57–66.
729 B. Zhang, S. Zou, R. Cai, M. Li and Z. He, *Appl. Catal., B*, 2018, **224**, 383–393.
730 J. A. Young, *J. Chem. Educ.*, 2004, **81**, 945.
731 D. Xia, Z. Shen, G. Huang, W. Wang, J. C. Yu and P. K. Wong, *Environ. Sci. Technol.*, 2015, **49**, 6264–6273.
732 W. Wang, Y. Yu, T. An, G. Li, H. Y. Yip, J. C. Yu and P. K. Wong, *Environ. Sci. Technol.*, 2012, **46**, 4599–4606.
733 W. Wang, J. C. Yu, D. Xia, P. K. Wong and Y. Li, *Environ. Sci. Technol.*, 2013, **47**, 8724–8732.
734 T. K. Athira, M. Roshith, R. Kadrekar, A. Arya, M. S. Kumar, G. Anantharaj, L. Gurrala, V. Saranyan, T. G. S. Babu and V. R. K. Darbha, *Mater. Res. Express*, 2020, **7**, 104002.
735 M. Roshith, A. Pathak, A. K. Nanda Kumar, G. Anantharaj, V. Saranyan, S. Ramasubramanian, T. G. Satheesh Babu and D. V. Ravi Kumar, *Appl. Surf. Sci.*, 2021, **540**, 148398.
736 Q. Zhang, X. Liu, L. Tan, Z. Cui, Z. Li, Y. Liang, S. Zhu, K. W. K. Yeung, Y. Zheng and S. Wu, *Chem. Eng. J.*, 2020, **383**, 123088.
737 T. Guo, S. Zhuang, H. Qiu, Y. Guo, L. Wang, G. Jin, W. Lin, G. Huang and H. Yang, *Part. Part. Syst. Charact.*, 2020, **37**, 2000169.
738 H. Ji, H. Sun and X. Qu, *Adv. Drug Delivery Rev.*, 2016, **105**, 176–189.
739 M. D. Rojas-Andrade, G. Chata, D. Rouholiman, J. Liu, C. Saltikov and S. Chen, *Nanoscale*, 2017, **9**, 994–1006.
740 D. He, Z. Zhang, Y. Xing, Y. Zhou, H. Yang, H. Liu, J. Qu, X. Yuan, J. Guan and Y.-N. Zhang, *Chem. Eng. J.*, 2020, **384**, 123258.
741 S. Luo, R. Liu, X. Zhang, R. Chen, M. Yan, K. Huang, J. Sun, R. Wang and J. Wang, *J. Hazard. Mater.*, 2022, **424**, 127281.
742 X. Han, X. He, L. Sun, X. Han, W. Zhan, J. Xu, X. Wang and J. Chen, *ACS Catal.*, 2018, **8**, 3348–3356.
743 Y. Kwon, A. Soon, H. Han and H. Lee, *J. Mater. Chem. A*, 2015, **3**, 156–162.
744 Z. Bao, C. Shi, W. Tu, L. Li and Q. Li, *Environ. Pollut.*, 2022, **313**, 120184.
745 X. Pan, M. Shi, X. Chen, S. Kuang, H. Ullah, H. Lu and L. Riaz, *Front. Environ. Sci.*, 2022, **10**, 1057384.
746 X. Zheng, W. Xu, J. Dong, T. Yang, Z. Shangguan, J. Qu, X. Li and X. Tan, *J. Hazard. Mater.*, 2022, **438**, 129557.
747 X. Li, A. Wang, W. Wan, X. Luo, L. Zheng, G. He, D. Huang, W. Chen and Q. Huang, *Appl. Environ. Microbiol.*, 2021, **87**, e01366.
748 L. Stille, E. Smeets, B. Wicke, R. Singh and G. Singh, *Energy Sustain. Dev.*, 2011, **15**, 388–397.
749 S. Ullah, S. Dahlawi, A. Naeem, Z. Rengel and R. Naidu, *Sci. Total Environ.*, 2018, **625**, 320–335.
750 P. Zhang, X. Bing, L. Jiao, H. Xiao, B. Li and H. Sun, *Chem. Eng. J.*, 2022, **431**, 133904.
751 H. Tang, M. Chen, P. Wu, M. Faheem, Q. Feng, X. Lee, S. Wang and B. Wang, *Chemosphere*, 2022, **311**, 137025.
752 S. K. Das, G. K. Ghosh and R. Avasthe, *Biomass Conv. Bioref.*, 2023, **13**, 1359–1369.
753 J.-H. Yuan, R.-K. Xu and H. Zhang, *Bioresour. Technol.*, 2011, **102**, 3488–3497.
754 A. M. Puziy, O. I. Poddubnaya, B. Gawdzik and J. M. D. Tascon, *Carbon*, 2020, **157**, 796–846.
755 H. Zhang, J. G. Shao, S. H. Zhang, X. Zhang and H. P. Chen, *J. Hazard. Mater.*, 2020, **390**, 121349.
756 J. Ren, Z. Zhao, A. Ali, W. Guan, R. Xiao, J. J. Wang, S. Ma, D. Guo, B. Zhou, Z. Zhang and R. Li, *J. Soils Sediments*, 2020, **20**, 3041–3052.
757 H. P. Rothbaum, *Outlook Agric.*, 1966, **5**, 123–128.
758 H. Lyu, B. Gao, F. He, C. Ding, J. Tang and J. C. Crittenden, *ACS Sustainable Chem. Eng.*, 2017, **5**, 9568–9585.
759 X. Zhang, Z. Xiong, S. Zhang, Y. Ge, W. Ma, L. Yan, D. Li, D. Wang, S. Deng, Q. Zhao, W. Wang and B. Xing, *Environ. Sci.: Nano*, 2020, **7**, 404–413.

